Journey to the centre of the earthquake: how does frictional stability affect earthquake source properties?

Thesis submitted in accordance with the requirements of the University of Liverpool for the degree of Doctor of Philosophy by

Louisa Olivia Brotherson

June 2023

ABSTRACT

Journey to the centre of the earthquake: how does frictional stability affect earthquake source properties?

Louisa Brotherson

Earthquakes remain a significant natural hazard. Reducing uncertainty in peak ground motion models (GMMs) of earthquakes is essential for improving risk mitigation. Earthquake source properties, such as stress drop, corner frequency and rupture velocity, describe the dynamic evolution of slip over the fault area during an earthquake, known as the earthquake source. While the earthquake source controls the magnitude and radiated wavefield of the earthquake, it is the most variable and uncertain term in GMMs, used to predict peak ground motions for seismic hazard analysis. Laboratory friction studies have the potential to improve our understanding of the earthquake source, but largely neglect the impact of the evolution of fault frictional properties. This thesis addresses this by simulating faulting using triaxial deformation experiments, observing how changes in fault stability affect the source properties of laboratory analogues for earthquakes.

Spontaneous stick-slip behaviour, generated in laboratory frictional sliding experiments, are useful analogues for natural earthquakes. Previous laboratory studies have shown that stick-slips and earthquakes are extremely similar: stick-slip waveforms visually resemble earthquake seismograms, with P- and S- wave arrivals and codas. However, the piezoelectric crystals held within the seismic sample assembly which record radiated P- and S-waves are uncalibrated. The recorded wavefield is therefore subject to frequency-dependent amplitude fluctuations, which means that only relative source property estimates of stick-slips can be determined. The absolute acoustic sensor calibration method of McLaskey et al. (2015) is adapted to calibrate the seismic sample assembly. Calibration enables stick-slip source spectra to be recovered, removing the effect of the instrument geometry so that source properties can be estimated.

The validity of this calibration is tested by comparing mechanical and seismic estimates of seismic moment and stress drop in frictional sliding experiments of poly(methyl methacrylate) (PMMA), a useful analogue for crustal rocks. Initial results suggest that both seismic moment and stress drop decrease with increased cumulative displacement, which coincides with increased pre-seismic slip and smaller, slower precursory stress drop events similar to natural slow slip. While there is a good correlation between both mechanical and seismic estimates, there are limitations in using a simple earthquake source model (Brune's model) to fit stick-slip source spectra.

The role of roughness and normal stress on source property evolution is investigated in a broader study with PMMA. Stabilisation with increased cumulative displacement is observed with a transition from unstable stick-slip to quasi-stable and stable sliding, in line with previous studies. New findings are that smoother surfaces exhibit more quasi-stable sliding and precursory events, which lead to lower stress drop, seismic moment and average rupture velocity. This supports field and modelling studies of fault maturity in natural faults and implies that fault maturity should be incorporated into GMMs to reduce uncertainty in peak ground motion.

For Grandma Ina, Grandma Mary,

Grandad Vinel and Grandad Henry

CONTENTS

LIST OF FIGURES AND TABLES

ACKNOWLEDGEMENTS

It's difficult to know where to begin with writing these acknowledgements. Finishing a PhD thesis is no mean feat. People associate the proverb "it takes a village" with having children, but I also think that it applies in the case of my PhD…?

Firstly, I'd like to thank my supervisors Ben Edwards and Dan Faulkner for supporting me and my work for the last 4 or so years. Both of you have been such valuable sources of knowledge and we've solved seemingly endless problems together. I have learned a lot from you both and I am very grateful for that.

Next, I'd like to thank all the members of Liverpool's Rock Deformation Laboratory, past and present. In no particular order: Betty, Dave, John W, Joe G, John B, Gary, Mike, Pier, Mahesh, Sam, and everyone else who has passed through in my time there. Gary, Mike and Joe – your technical support has saved me countless times! Thank you for being an ever-constant, supportive presence, especially when my experiments weren't working. An extra special thanks go to Izzy and Elliot, my PhD cohort peers who have been on this journey alongside me. I really wouldn't have finished without you both! I will miss our conversations and lab lunches at Shiraz dearly.

As my PhD is interdisciplinary, my thanks also goes to the other Seismology PhDs who have supported me along the way: Jaleena, Pungky and Leslie. Venturing around Seattle for SSA 2022 will always be one of the highlights of my PhD. Further thanks goes to the wider cohort of PhDs, postdocs, academics and support staff in the Department and DTP who enhanced my experience immensely. Shout-out to everyone who has put up with my nattering as an officemate over the past few years!

Thank you to Dave and Silvio for a fantastic viva. I was so nervous beforehand but you settled my nerves whilst guiding a fascinating discussion. Your enthusiasm and depth of knowledge made it a great experience that I will never forget!

Outside of university, I have the BEST support network who have quite literally kept me sane throughout my PhD. I am immeasurably grateful to my Mum, Dad, sister Courtney and Grandma for always being a WhatsApp call away when times were tough. I would not be where I am now if it was not for you all. Thanks also go to my extended family, friends and housemates who kept me going, particularly during the COVID-19 pandemic. The African Caribbean Research Collective (ACRC-UK) has been a source of positivity and strength over the past 4 years, so thank you to members of the collective for being the realest!

Finally, I would like to thank Matt for being incredible during some of the toughest times of my life so far. Your support knows no bounds and I am forever grateful for you.

1 INTRODUCTION

Reducing the adverse effects of natural disasters, including earthquakes, is one of the UN's Sustainable Development Goals (SDG 11: Sustainable Cities and Communities; *The Sustainable Development Goals Report 2022*). Earthquakes remain a significant natural hazard, threatening lives and livelihoods. Earthquakes can cause severe damage to infrastructure, with the economic impacts of earthquakes ranging from $100 million to $100 billion depending on the magnitude of the earthquake and economic model used to calculate losses (Kazimi and Mackenzie, 2016). As rapid urbanisation increases the risk of exposure of human populations to seismic hazards, understanding the origin and mechanics of earthquakes is becoming increasingly important. Probabilistic seismic hazard analysis (PSHA) consists of using short-term probabilistic earthquake forecasting models to characterise seismic hazard risk through the prediction of peak ground motion (e.g. peak ground acceleration). PSHA uses historic earthquake strong motion data and assesses the probability of exceeding a given shaking intensity in a particular location. However, peak ground motion estimates continue to have high levels of uncertainty, with discrepancies between predicted and observed ground motion (Baltay et al., 2017; Strasser et al., 2009).

Peak ground motion at a site is generally predicted using empirical ground motion prediction equations (GMPEs), which are often derived through regression analysis of strong motion data recorded during an earthquake. The discrepancy between predicted and observed ground motion can be reduced by either incorporating more physical constraints into empirical GMPEs or developing physics-based numerical simulations to predict ground motions (Bommer and Scherbaum, 2005; Lee et al., 2020). In particular, earthquake source properties, i.e. physical parameters that describe the area of a fault that slips during an earthquake or stress drop, are highly uncertain because processes occur at several kilometres' depth. Before recent developments in geodesy, seismology was one of the only modes of observing rock deformation at depth. While the relationship between radiated wavefields of earthquakes and earthquake source properties has been studied and modelled in depth, it can be difficult to test the accuracy of earthquake source properties and modelling. Understanding the underlying physical processes involved in natural faults and the earthquake cycle is key to reliable modelling of earthquake rupture and improved characterisation of earthquake source properties.

A key question that remains is how earthquake source properties evolve during the earthquake cycle. Earthquake nucleation has been described through a variety of models. For example, Beroza and Ellsworth (1996) outline how the seismic nucleation phase starts abruptly, but weakly, at the arrival of the P-wave with a lower moment rate than the following mainshock. They

propose two models that describe how earthquakes nucleate: 1) the cascade model, where a small earthquake triggers a cascade of increasingly larger slip events (Wyss and Brune, 1967; Brune, 1979; Abercrombie and Mori, 1994); 2) the pre-slip model, where failure initiates aseismically with slow, stable sliding over a limited area of a fault (Dieterich, 1992, 1986; Okubo, 1989; Shibazaki and Matsu'ura, 1992). Conversely, Lambert, Lapusta and Faulkner (2021) describe earthquake nucleation as the stage of a developing rupture before runaway instability occurs. Before this, if stress increase were to cease, the system would remain in a state of equilibrium. As frictional fault processes evolve during the earthquake cycle, stress evolves, controlling the magnitude, frequency and ground motion associated with earthquakes (Rice et al., 2005). While seismology provides vital inferences of stress, such as stress drop, through which earthquake processes can be interpreted, geological field observations are crucial additions to interpretations to establish the broad range of fault structures and materials that exist. While closer range, below-surface observation of the seismic wavefield is possible (e.g. Abercrombie, 1995), it is often less pragmatic. This difficulty has motivated an increasing number of experimental investigations to connect seismological observations with models of fault processes (e.g. Brace and Byerlee, 1966; Passelègue et al., 2013; Ikari et al., 2015; Leeman et al., 2016). Laboratory experiments are advantageous as conditions such as temperature, pressure and displacement can be carefully controlled and accurately measured, providing physical constraints for uncertainties in processes such as earthquake rupture (Tobin et al., 2007).

To this end, this thesis aims to constrain the source properties of laboratory-generated instabilities (analogues for earthquakes) known as stick-slip, to understand how the source properties of these instabilities, some of which are readily measurable in the laboratory, affect radiated seismic waves. In this chapter, following a brief introduction of several fundamental concepts behind earthquakes, friction and faulting, the thesis's aims, objectives and structure are outlined.

1.1 PLATE TECTONICS, FAULTS AND GLOBAL SEISMICITY

Earthquakes nucleate due to the accumulation of tectonic stress in the Earth's lithosphere. Plate tectonics drive stress accumulation, building up elastic strain through the deformation of the lithosphere. Large earthquakes primarily occur along tectonic plate boundaries (Figure 1.1). Depending on pressure and temperature conditions, the lithosphere may deform through the formation of shear zones (ductile behaviour; associated with fault creep) or fractures (brittle behaviour; associated with seismicity). In the upper lithosphere, pressure and temperature conditions are relatively low, leading to a brittle regime that broadly follows linear elasticity until the point of failure (Paterson and Wong, 2005). Brittle failure of rocks results from the initiation,

growth and coalescence of microcracks and fractures, which leads to macroscopic failure i.e. brittle faults. Natural faults are quasi-planar fractures or discontinuities in rock volumes which have been displaced due to plate tectonic stresses. Fault properties control the magnitude of an earthquake. The seismic moment M_0 (in Nm), which describes the size of an earthquake, can be derived using the following equation (Aki, 1966):

$$M_0 = GAD. \tag{1.1}$$

G is the shear modulus of the fault rocks involved in earthquake nucleation (Pa(, A is the rupture area along the fault (m^2) and D is the average fault slip on fault area A (m). Seismic moment can be converted to moment magnitude M_W using the following relation (Hanks and Kanamori, 1979):

$$M_W = \frac{2}{3} \times \log_{10} M_0 - 6.033. \tag{1.2}$$

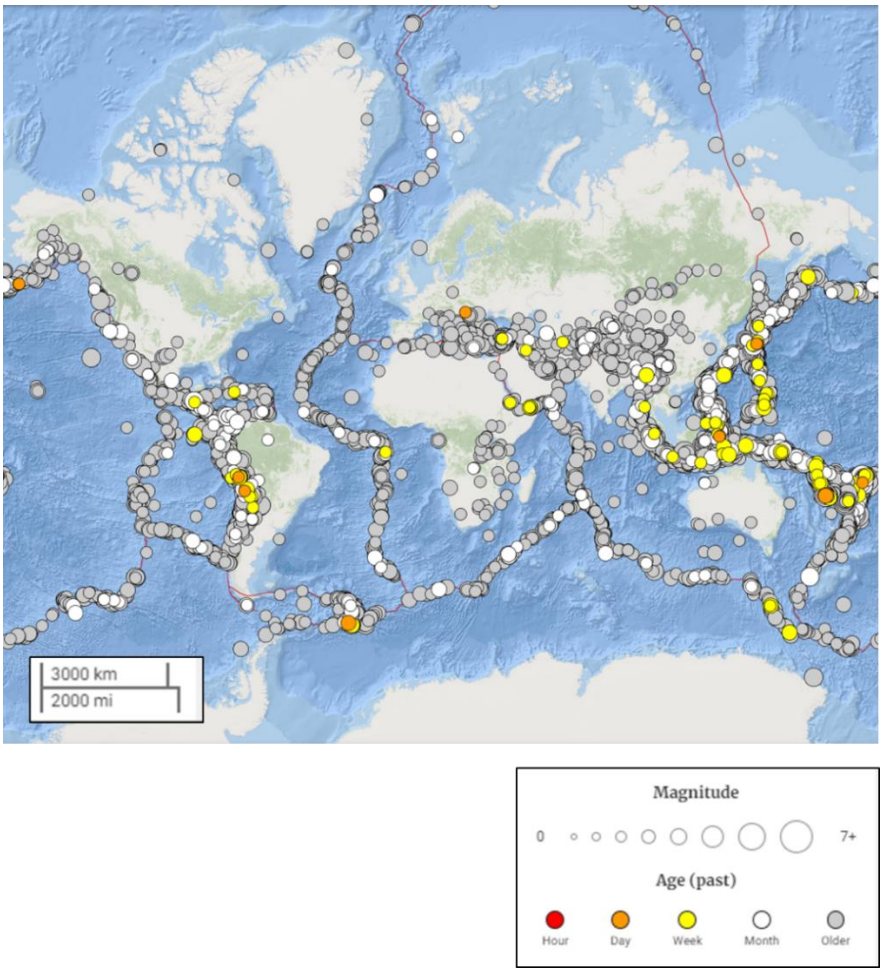

***Figure 1.1**: Global seismicity map of all earthquakes (filled circles) greater than M_W 4.5 (Equation 1.2) from 01/01/22 until 07/06/23. Major tectonic plates are outlined by the red line. The size of the circle represents*

the earthquake magnitude, fill colour represents the age of the earthquake from 07/06/23 (U.S. Geological Survey, 2023).

1.2 EARTHQUAKE NUCLEATION

1.2.1 Rock friction

Understanding how earthquakes nucleate is important as they may produce measurable precursory events that could be used in short-term probabilistic earthquake models (Ellsworth and Beroza, 1995). Earthquakes form due to slow deformation (mm/yr) caused by tectonic stresses, where elastic strain energy slowly increases until peak strength is reached and the material fails, releasing stored energy (stress) suddenly and causing the fault to slip (m/s; Scholz, 2019). Earthquakes are dynamic frictional instabilities, with faults sliding unstably during earthquake slip due to variations in frictional resistance.

Faults can also release stored elastic strain through aseismic creep (mm/yr), where faults slide stably (Scholz, 1998). These two types of frictional behaviour (unstable earthquakes and stable aseismic creep) arise from the complexities of fault friction, structure, composition, stiffness, pore fluids, dynamic interactions and changes to the energy balance throughout the earthquake cycle.

Fault stability has been an area of experimental study since the 1960s when Brace and Byerlee (1966) related natural fault behaviour to laboratory friction experiments. In their study, they found that simulated faults would either: 1) slide stably at a relatively constant level of stress, or; 2) slide unstably as regular stick-slip with repeated cycles of a build-up of stress and strain ('stick') followed by a sudden failure, associated with stress release ('slip').

The stick-slip mechanism can be described schematically by a simple slider-spring model (Figure 1.2; Brace and Byerlee, 1966; Dieterich, 1992; Gao, Kuhlmann-Wilsdorf and Makel, 1993; Bowden, Bowden and Tabor, 2001). A slider block is pulled with frictional resistance force F by a spring with elastic loading stiffness k against a fixed surface and slips with displacement u. During the 'stick' phase, the slider block is fixed, the spring lengthens and elastic strain energy is stored. During the 'slip' phase, the shear stress between the slide block and fixed surface is equal to the contact strength which causes the block to slip suddenly. The spring shortens, releasing the stored elastic strain energy and releasing stress (stress drop). Stick-slip instability can also be described considering the case when frictional resistance force decreases with slip at a faster rate than the spring's stiffness (point i), Figure 1.2b). In this case, the imbalance in force produces a slider acceleration, creating instability. Once point ii) is reached, the force is greater than the spring's force, decelerating the slider and bringing it to rest at point iii). If the slider remains stationary, the areas under the curves, between i) to ii) and ii) to iii), are equal (Scholz, 2019).

This frictional behaviour is known as slip weakening behaviour (Ida, 1972; Palmer and Rice, 1973) and requires the following condition for instability:

$$\left|\frac{\partial F}{\partial u}\right| > k. \tag{1.3}$$

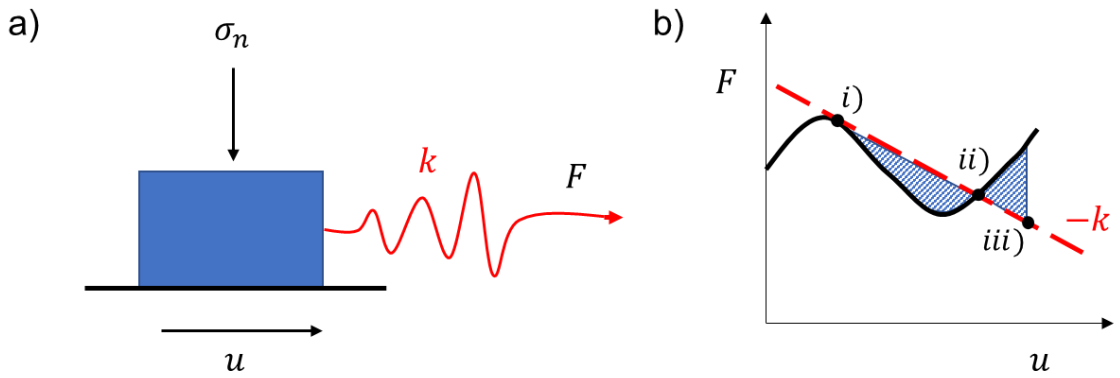

Figure 1.2: *a) Spring-slider system describing stick (build-up of elastic strain) and slip (sudden stress release) when frictional resistance force F is applied to a sample. k is the elastic loading stiffness, σ_n is normal stress and u is displacement in the slip direction. b) Frictional resistance force as a function of slip (black line) before, during and after stick-slip instability. $-k$ is the gradient of the red line. After Scholz (2019).*

Brace and Byerlee (1966) interpreted stick-slip behaviour as an analogue for natural fault behaviour, finding that normal stress affected frictional behaviour. Subsequent studies found that fault structure (Byerlee et al., 1978; Byerlee and Summers, 1976) and rock composition (Summers and Byerlee, 1977) also affected fault stability.

However, there are fundamental differences between stick-slip and earthquakes. For example, Beeler et al., (2012) found that the relation of rupture duration Δt to fault length L and shear wave velocity β ($\Delta t \approx 1.1\frac{L}{\beta}$, assuming a crack-like rupture expanding with a speed of 0.85β) breaks down for laboratory stick-slip. This is because for laboratory stick-slip (and in some natural cases, e.g. Campbell et al., 2020), the ends of the fault are unconfined, meaning that rupture propagation speed is not solely controlled by the elastic properties of the surrounding material. Instead, slip continues when rupture fronts propagate to the unconfined ends of the fault. Other factors to consider in natural earthquakes include higher temperatures, pore fluid pressure, slower strain rates and lithological variation (Kilgore et al., 2017; McGarr, 2012). Elastic loading stiffness will also affect whether a laboratory system stick-slips or creeps: Rabinowicz (1958) found that the stiffer a system, the smaller the stress drop magnitude, reducing to zero for the stiffest loading systems. This observation can be related to Figure 1.2: as the spring stiffness is increased, there

is no capacity for acceleration. Instability is a function of both slip weakening frictional resistance and the critical stiffness of the system.

1.2.1.1 Slip weakening friction

A way to consider how a material weakens with slip and how earthquake rupture nucleates is the linear slip weakening model of friction. Assuming a stability criterion according to Griffith's (1921) crack theory, a pre-existing weak patch (either a crack or a slipping region on a pre-existing crack) of finite size is present in a material. Irwin (1957) extended Griffith's theory, introducing a cohesive crack tip which explains the loss of strength at a crack tip (Figure 1.3). Elastic stored energy that accumulates during the interseismic period is released as radiated energy and dissipated energy in the fault vicinity (Paglialunga et al., 2022). Dissipated energy can be subdivided into two contributions: frictional dissipation (Kanamori, 1977; Kanamori and Brodsky, 2004) and fracture energy. Fracture energy (E_f, Figure 1.3) is equivalent to frictional work, which dissipates during crack growth and strength loss over a characteristic distance, δ_c (Andrews, 1976; Barenblatt, 1962; Ida, 1972; Palmer and Rice, 1973). Tinti et al. (2005) described fracture energy as the critical energy release rate required to expand a rupture. Breakdown work, defined as the energy expended at the rupture tip to propagate the rupture by a unit area, has been proposed as a proxy for fracture energy in seismological studies (e.g. Venkataraman and Kanamori, 2004; Abercrombie and Rice, 2005). However, more recent studies have found that breakdown work is only analogous to fracture energy if fault weakening is concentrated near the propagating rupture tip (Brener and Bouchbinder, 2021; Lambert and Lapusta, 2020). In this work, fracture energy is defined by the Tinti et al. (2005) definition and is likely a small portion of the breakdown work.

Assuming that a fault's stress state is close to the peak stress ($\tau_0 \approx \tau_p = \sigma_n \mu_p$, where τ_0 is a fault's stress state, τ_p is the peak shear stress, σ_n is the normal stress and μ_p is the peak coefficient of friction), the nucleation length of an event L_c can be defined by the following equation:

$$L_c \approx C \frac{G\delta_c}{\sigma_n(\mu_p - \mu_r)}. \qquad (1.4)$$

C is the crack shape factor (typically $7\pi/24$ for a circular crack), G is the shear modulus, δ_c is a characteristic slip distance (m), σ_n is the normal stress (Pa), μ_p is the peak friction level and μ_r is the residual friction level (Andrews, 1976; Palmer and Rice, 1973). Friction decreases from μ_p to μ_r (and from τ_p to τ_r) over characteristic slip distance, δ_c. Energy is consumed by crack growth and released from slip weakening, which releases strain energy.

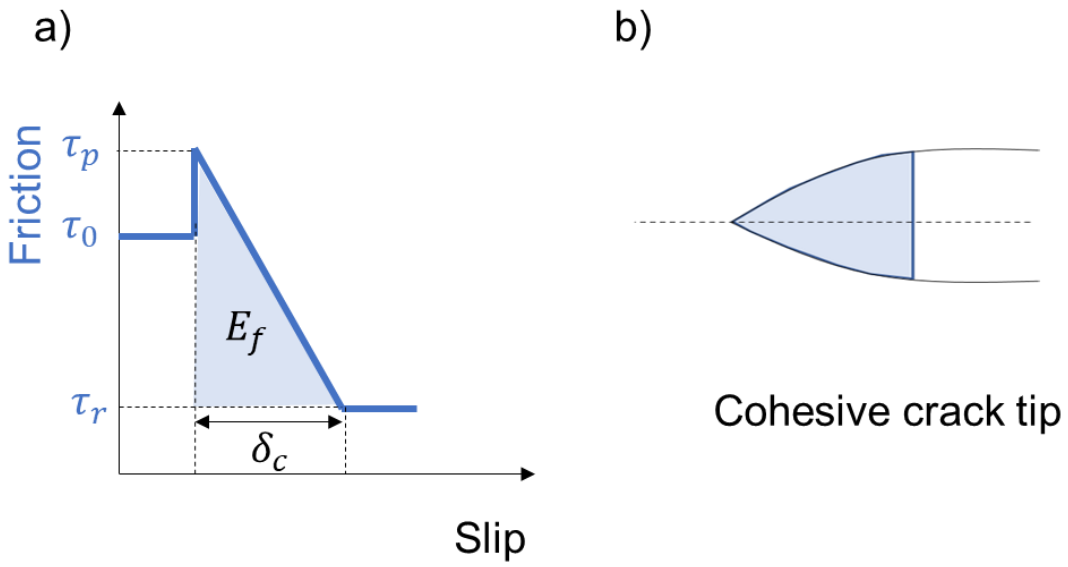

Figure 1.3: *a) Schematic diagram of the cohesive crack tip model which describes a growing cohesive crack (b) that weakens as a function of slip. τ_p is the peak shear stress (Pa), τ_r is the weakened (residual) shear stress (Pa), τ_0 is the initial shear stress (Pa) and δ_c is the characteristic slip weakening distance (m). E_f is the fracture energy released from slip weakening (J).*

Slip weakening has been used to explain experimental stick-slip instability (Byerlee, 1970). Nevertheless, slip weakening friction does not provide a physical 'healing' mechanism for frictional strength to regain its initial value. Rabinowicz (1951, 1958) made the first observation of a healing mechanism to explain how frictional strength can return to its original level and also found stick-slip systems to be velocity weakening, leading to rate-and-state friction laws (Dieterich, 1972; Ruina, 1983; Scholz et al., 1972).

1.2.1.2 Rate-and-State Friction

As highlighted by the slip weakening friction framework, instability occurs due to the minimisation of potential energy, which is due to slip weakening frictional resistance. However, Dieterich (1979) found through velocity stepping tests that friction also depends on applied velocity (rate) and previous slip episodes (state), not just fault slip (Rice and Ruina, 1983; Ruina, 1983; Marone, 1998). This conceptualisation of frictional instability has been formalised in rate-and-state friction laws, which describe how velocity affects frictional stability (Dieterich and Kilgore, 1996; Faulkner et al., 2010; Marone, 1998a).

Rate-and-state dependent friction laws describe frictional stability using empirical parameters, derived from laboratory experiments. The laws are defined as follows:

$$\mu = \mu_0 + a \log\left(\frac{V}{V_0}\right) + b \log\left(\frac{V_0 \theta}{D_c}\right). \quad (1.5)$$

μ is the coefficient of friction ($\mu = \frac{\tau}{\sigma_n}$, where τ is the shear stress and σ_n is the normal stress on the fault, both in Pa), μ_0 is the coefficient of friction at reference velocity V_0 (m/s), V is the sliding velocity (m/s), θ is the state variable (s), D_c is the critical slip distance (m), and a and b are dimensionless constants that relate to the rate- and state-dependence of friction respectively (Dieterich, 1979b; Marone, 1998a; Rice and Ruina, 1983; Ruina, 1983). a is known as the direct effect and is related to the 'direct' frictional change caused by the change in sliding velocity (Dieterich and Kilgore, 1994). b is the evolution effect, which controls the magnitude of delayed frictional evolution caused by the change in sliding velocity (Faulkner et al., 2010; Marone, 1998a; Rice et al., 2001; Ruina, 1983). The state variable θ is assumed to represent the evolution of a fault's microstructural state and provides a memory of previous episodes of slip (Cocco and Bizzarri, 2002).

Several formulae have been proposed to model the evolution of the state variable, based on observations in laboratory experiments and modelling (Beeler et al., 1994; Bhattacharya et al., 2015; Dieterich, 1979b; Ruina, 1983). The two most common laws are the aging law (Dieterich, 1979b) and slip law (Ruina, 1983). The aging law is defined as:

$$\dot{\theta} = 1 - \frac{V\theta}{D_c}, \quad (1.6)$$

where $\dot{\theta}$ is the dimensionless derivative of state with respect to time. The dominant physical process involved in the aging law is time-dependent microstructural evolution (Dieterich, 1979b). In the static case, θ is equal to time t and can be interpreted as the average time elapsed since the frictional contacts existing at a given time were first formed (Scholz, 2019). Alternatively, the slip law can be defined as:

$$\dot{\theta} = -\frac{V\theta}{D_c} \log \frac{V\theta}{D_c}. \quad (1.7)$$

Slip law assumes that state evolution arises from slip-dependent microstructural evolution, rather than time (Ruina, 1983). With this law, any change in friction, including strengthening during quasi-stationary contact, requires slip (Marone, 1998a).

Figure 1.4 demonstrates the frictional response of a rate-and-state dependent system under the two end-member conditions – velocity weakening friction $(a - b) < 0$, which can result in unstable sliding, and velocity strengthening friction $(a - b) \geq 0$, which results in stable sliding.

Stick-slip instabilities occur when both: 1) $a < b$, and 2) system stiffness $k < k_c$, the critical stiffness. k_c can be defined as follows, considering a spring-slider model (Figure 1.2; Scholz, 2019, 1998):

$$k_c = \frac{\sigma_n(b-a)}{D_c}. \tag{1.8}$$

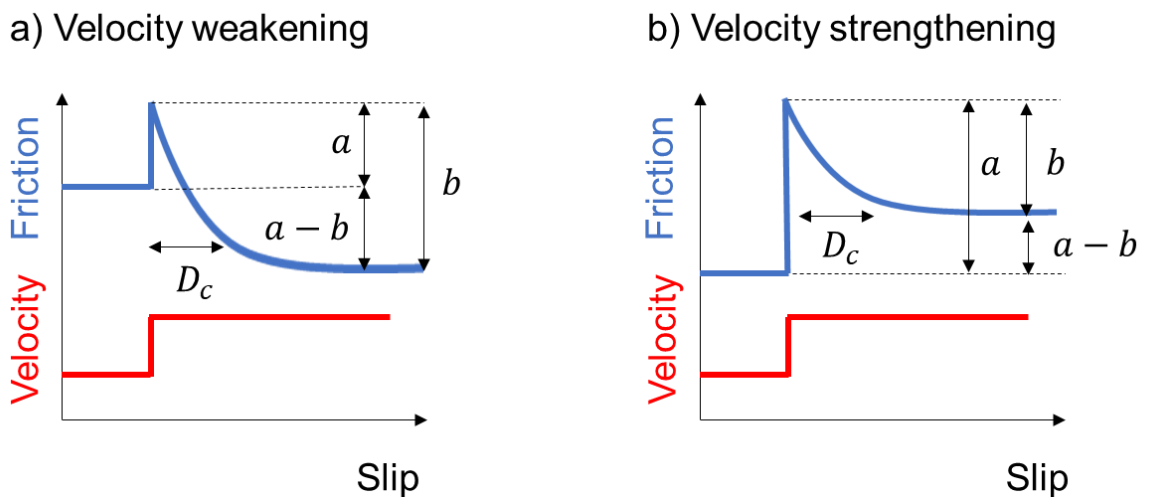

Figure 1.4: *Schematic diagram of how a step-wise increase in velocity (red lines) affects the frictional response (blue lines) of a) velocity weakening and b) velocity strengthening materials.*

The material property, $(a - b)$, is the primary control of whether slip slides unstably or stably. $(a - b)$ is generally negative at low temperatures. Stiffness k can be described by the relation $k = C\frac{G}{L}$, where C is a crack shape factor, G is the shear modulus and L is the linear fault dimension in m. The stiffness criterion (Equation 1.8) can be used to define a critical patch size L_C (Rice, 1993), above which instability can nucleate:

$$L_C = \frac{CGD_c}{\sigma_n(b-a)}. \tag{1.9}$$

This framework has been successfully used to explain the variety of frictional sliding behaviour observed during the earthquake cycle, from stable sliding, to slow and fast stick-slip events (Leeman et al., 2016; Scuderi et al., 2016). Constraining L_C would be ideal as it would allow the use of elastic dislocation models to make predictions of the ground surface movement. In practice, it is very difficult to determine L_C quantitively (Ampuero and Rubin, 2008; Rubin and Ampuero, 2005; Wu and McLaskey, 2019), but has been estimated to be larger than the sample size in previous studies (Harbord et al., 2017; McLaskey and Yamashita, 2017). L_C is difficult to derive as on one hand, Rice (1993) found that it is proportional to $(b - a)$ while on the other hand, Dieterich (1992) found that L_C is proportional to b through laboratory experiments with metre-

scale blocks of rock and analytical solutions, assuming that healing can be neglected throughout nucleation (i.e. $L_C = \frac{\mathrm{CGD_c}}{\sigma_\mathrm{n} \mathrm{b}}$). Because of this, nucleation length estimates can vary significantly. Disparities between L_C derived using the $(b - a)$ formulation and using the b formulation are particularly large near the transition from velocity weakening to velocity strengthening friction, e.g. at the base of the seismogenic zone where large earthquakes tend to occur (Rubin and Ampuero, 2005). Moreover, Lapusta and Rice (2002) found through 2D fault modelling governed by rate-and-state friction that L_C does not scale with either $(b - a)$ or b.

1.2.2 Earthquake nucleation and propagation

As earthquake nucleation and propagation phases are intrinsically linked, it is important to discuss how nucleation evolves into propagation. Earthquake propagation is defined as the dynamic shear resistance that propagates along fault interfaces. Crustal earthquake ruptures generally propagate at sub-Rayleigh wave speeds, between 0.75 and $0.95C_R$, where C_R is the Rayleigh wave speed (Rosakis et al., 2007). Laboratory observations and theoretical modelling suggest that earthquakes initiate slowly, growing and accelerating before seismic waves are radiated (McLaskey, 2019). Earthquake nucleation begins with quasi-static and aseismic slip in the nucleation zone (Figure 1.5). This localised zone starts to slip, decreasing shear stress within the nucleation zone while increasing stress near the edges. The edges form the tips of a quasi-static shear crack. Stress concentrations near the crack tip enable the nucleation zone to expand slowly through crack growth. Following slow rupture expansion, where rupture velocity $\mathrm{V_r}$ is less than the shear wave velocity, β, V_r rapidly accelerates, slip velocities approach m/s and seismic waves are radiated.

Monitoring earthquake nucleation in nature is extremely difficult due to ambient noise which masks its low amplitude signal (Ellsworth and Beroza, 1995). Therefore, observations of the nucleation phase of laboratory analogues for earthquakes (stick-slips) are useful in characterising this phase. Johnson and Scholz (1976) used a network of near-fault strain gauges to measure fault strength milliseconds before stick-slip. They found that faults rapidly (< 10 μs) weakened following the arrival of the rupture tip, with faults breaking down ahead of a dynamically propagating shear crack. Further experimental studies have found that the nucleation phase of stick-slip is characterised by distinct rupture phases (McLaskey and Kilgore, 2013; Ohnaka and Shen, 1999; Okubo and Dieterich, 1984). Andrews' (1976) theoretical finding of the possibility that rupture velocity V_r can exceed shear wave velocity, so-called 'super-shear ruptures', was experimentally verified by Xia, Rosakis and Kanamori (2004) in analogue experiments and Passelègue et al. (2013) in rock experiments. However, as of yet, borehole strain

gauges at kilometres in depth have yet to detect any similar nucleation processes (Johnston et al., 2006; Roeloffs, 2006).

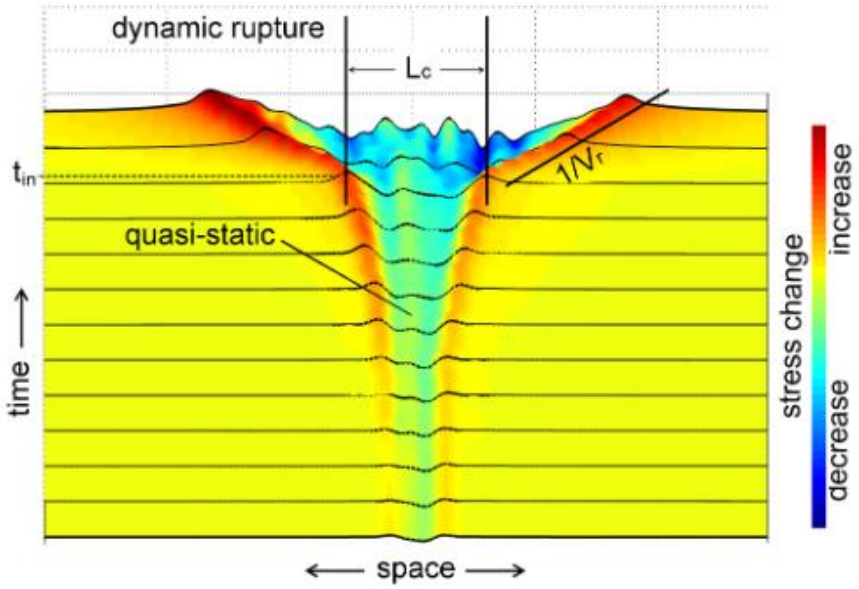

***Figure 1.5**: Schematic diagram of dynamic rupture initiation in a nucleation zone, assuming a smooth nucleation model. Slow, localised slip at the centre of the zone grows to a critical length L_C and then accelerates to seismic velocities with rupture velocity V_r. Black horizontal lines and colours represent local shear stress changes that result from fault slip (Ohnaka, 2000 and McLaskey et al., 2019).*

1.3 GROUND MOTION PREDICTION EQUATIONS (GMPES)

Empirical GMPEs estimate the magnitude of peak ground motion caused by an earthquake (Boore, 2003; Douglas and Edwards, 2016). GMPEs are used for a wide range of applications, including site-specific seismic characterisation for structural design, the development of region-wide seismic hazards maps for use in building codes, and social and financial loss estimation (Lam, 2023).

Simplified, ground motion is estimated by convolving the following terms in the time domain (multiplying in the frequency domain): the earthquake source; path response, which describes geometric spreading and attenuation effects from the source to the receiver; site response, which describes wave amplification due to local site soils and geology under the receiver; and instrument response, which describes how a seismometer or sensor modifies a recorded signal (Figure 1.6). The earthquake source is the term with the highest uncertainty because the majority of earthquakes are either too deep or too remote to be directly observed (Benioff, 1964). Limited seismic data due to poor data quality, quantity or limited frequency recording range are additional issues that seismologists face when analysing recorded seismic waves. Extracting the

earthquake source from recorded ground motions is difficult as separating the source radiation from the path and site response is challenging due to their frequency dependence (Abercrombie, 2021). Estimates often contain significant systematic and/or random uncertainties due to assumptions such as arrival time, velocity structure of the underlying geology and earthquake location. Moreover, interpretations of earthquake source properties from seismograms rely on source models, which are difficult to physically test. Nevertheless, much progress has been made in reducing the uncertainty in this term (Atkinson, 1993; Atkinson and Boore, 1998; Boore and Atkinson, 1992). Common methods used for estimating the earthquake source in practice include spectral modelling and inversion (Andrews, 1986; Scherbaum, 1990), using Empirical Green's Functions (Abercrombie, 2015; Mueller, 1985) and estimating radiated energy (Kanamori et al., 2020; Kaneko and Shearer, 2014). Questions remain as to how to better resolve earthquake source properties, particularly those of small to medium (below magnitude $M_w = 6$) earthquakes and complex sources in varied tectonic settings.

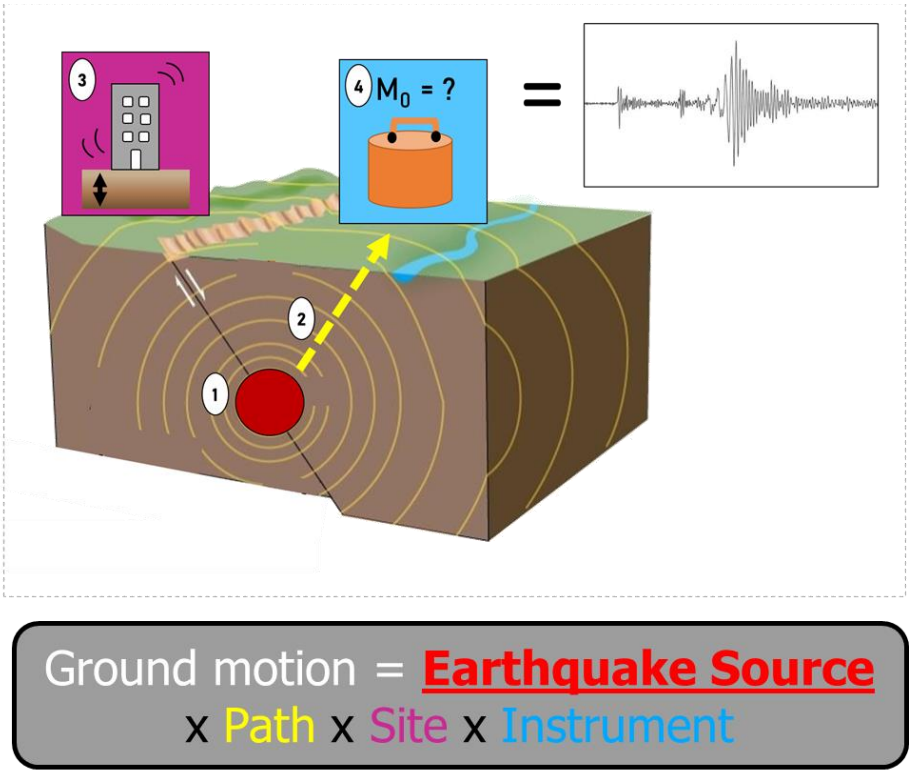

Figure 1.6: *Schematic illustration of the four terms used in GMPEs to estimate peak ground motion. After IRIS (no date).*

1.4 THE EARTHQUAKE SOURCE

The source of an earthquake is defined as the dynamic evolution of slip over the fault area during an earthquake. Accurate characterisation of the earthquake source is crucial as it controls the

magnitude and frequency content of the radiated wavefield of the earthquake (Udias et al., 2014a). Seismic waves radiated during an earthquake can be used to characterise the earthquake source by assuming a source model, which physically and mathematically describes how stress is applied across a fault area. Using continuum mechanics equations, properties that satisfy these models known as earthquake source properties can be derived, quantifying how stress deforms the earthquake source and generates slip.

1.4.1 Earthquake source models and the Brune model

The amplitude of seismic waves generated at the earthquake source is a function of the seismic moment M_0 of the earthquake (Equation 1.1), and crustal properties (i.e. density and shear wave velocity) of the earthquake source. The slip rate of fault slip during an earthquake is known as the source time function. The source time function represents the time dependence of seismic moment release M_0 (Udias et al., 2014b). Early studies of fracture dynamics were based on experimental work on fracturing in crystals and metals (Griffith, 1921; Irwin, 1957; Starr, 1928). This work was then applied to earthquake sources to solve several dynamic problems, with notable studies by Eshelby (1957), Kostrov (1964), Freund (1972), Madariaga (1976) and Keylis-Borok (1959).

Brune (1970) introduced a source time function as a seismic wave radiation model for small earthquakes that are completely contained in the lithosphere. Brune's model assumes that a fault has a circular shape. This simple, dynamic model is based on a shear stress pulse that is instantaneously applied to the entire area of a circular fault of a finite radius (Figure 1.7). The shear stress pulse decreases stress (also known as the stress drop), generating a plane SH wave that propagates perpendicularly to the fault plane with shear wave velocity β (Udias et al., 2014c). The Brune model neglects rupture velocity as it assumes that rupture occurs instantaneously across the fault, so rupture propagation is not modelled.

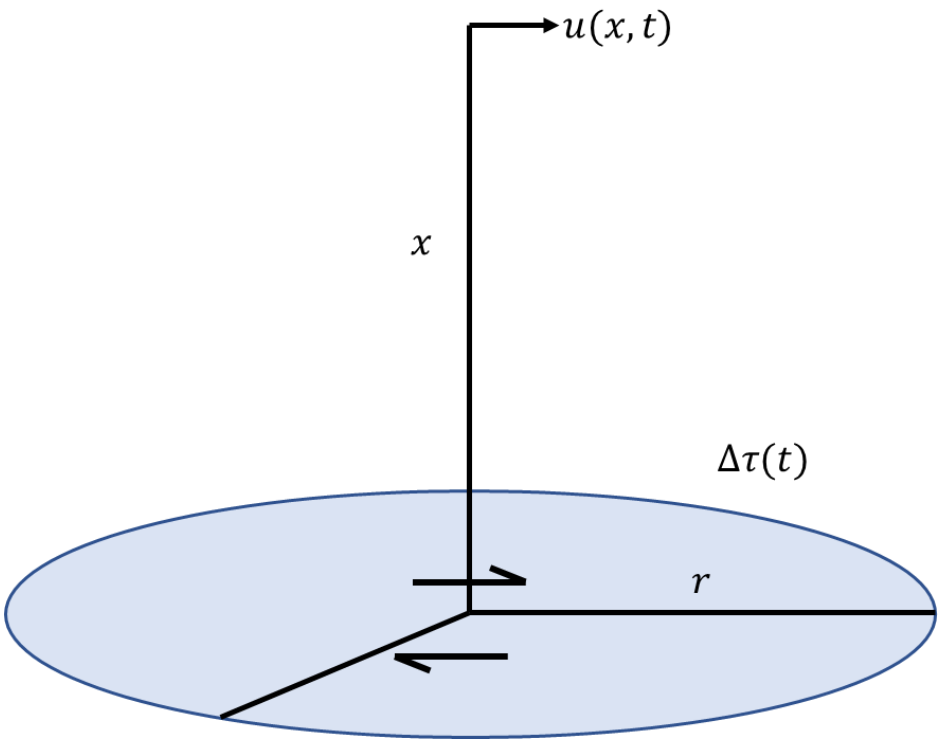

Figure 1.7*: The geometry and mechanics of a Brune model, which describes rupture on a circular fault with finite radius r as a function of displacement x and time t with slip $u(x,t)$ and stress drop $\Delta\tau(t)$. After Udias* et al. *(2014c).*

In the Brune model, the seismic moment is a continuous function of time t:

$$M_0(t) = M_0\left[1 - \left(1 + {}^{t}/_{t_r}\right) e^{{}^{-t}/_{t_{1/2}}}\right] H(t). \tag{1.10}$$

$H(t)$ is the Heaviside function (unit step function in time; Berg, 1936) and $t_{1/2}$ is the rise time, which is the time taken for fault slip to reach its maximum. The moment function can be converted to moment rate through differentiation:

$$\dot{M}_0(t) = M_0 \frac{t}{{t_{1/2}}^2} e^{{}^{-t}/_{t_{1/2}}} H(t). \tag{1.11}$$

To obtain useful and universal source properties from source time functions, functions are transformed from the time domain (in seconds, s) to the frequency domain (in Hertz, Hz) using the Fourier Transform (Bracewell, 2000). For the Brune model, assuming a finite rise time $t_{1/2}$, the spectrum of its moment-rate source time function $\dot{M}_0$ can be estimated by a constant plateau at low frequencies and a high frequency decay of $1/f^2 = 1/\gamma$ for frequencies greater than the corner frequency, f_0 (Figure 1.8; Aki, 1967; Brune, 1970; Madariaga, 2009):

$$\dot{M}_0(f) = \frac{M_0}{1 + \left(\frac{f}{f_0}\right)}. \tag{1.12}$$

Corner frequency f_0 is approximately inversely proportional to the rise time $t_{1/2}$ ($f_0 \approx 1/t_{1/2}$).

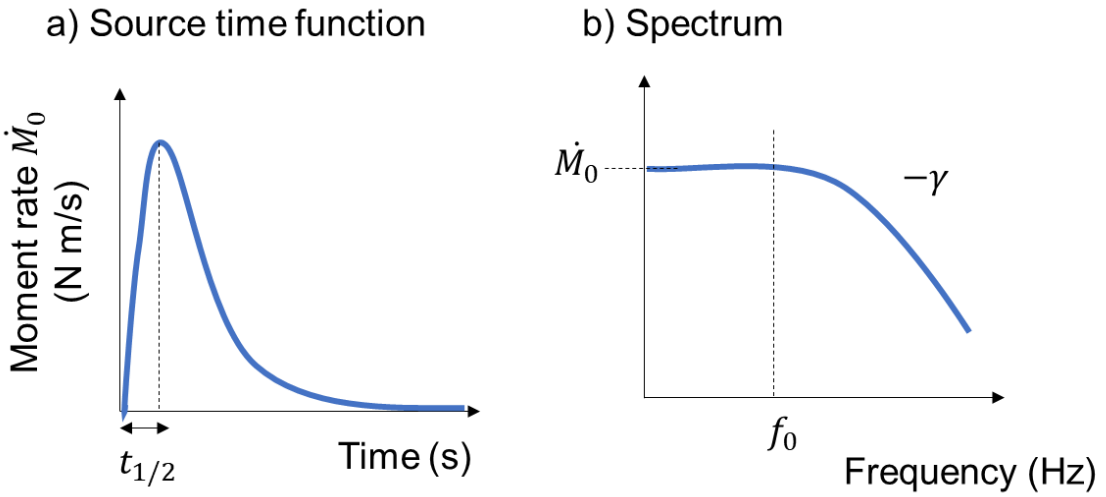

***Figure 1.8**: a) Moment-rate source time function $\dot{M}_0$ of a Brune signal, $t_{1/2}$ is the rise time. b) Fourier amplitude spectrum of a Brune signal, $-\gamma$ is the high frequency decay at frequencies greater than the corner frequency, f_0 (Brune, 1970).*

The Brune (1970) model is just one of several earthquake source models applied. Other source models such as those proposed by Sato and Hirasawa (1973) and Madariaga (1976) consider an expanding fault, describing both earthquake nucleation and propagation. Moreover, Haskell (1964, 1966, 1969) proposed a rectangular dislocation fault model. While a rectangular fault model could be considered ideal for modelling rectangular simulated faults such as the experimental configuration presented in this thesis, the model is difficult to use at high frequencies due to problematic features such as potential infinite energy release and the inter-penetration of matter (Madariaga, 2009). This is because slip across the fault is constant and therefore, there is an infinite displacement gradient at the fault tip.

1.4.2 Earthquake source properties

Earthquake stress drop $\Delta\tau$, seismic moment M_0, corner frequency f_0 and source radius r are all types of earthquake source properties. The Brune model relates corner frequency f_0 to source radius r (as well as rise time $t_{1/2}$), assuming the source geometry outlined in Figure 1.7:

$$r = \frac{2.34\beta}{f_0}. \tag{1.13}$$

β is the shear wave velocity of the source material. Earthquake source properties quantitatively describe source mechanics, making them fundamental for source characterisation in GMPEs. For example, corner frequency has been used to determine the source radius of crustal earthquakes from seismic wave spectra (e.g. Hanks and Wyss, 1972; Boatwright, Fletcher and Fumal, 1991). Following Eshelby (1957), Brune (1970) demonstrated that the stress drop can be approximated using the moment and source radius of a rupture, as stress is proportional to strain:

$$\Delta\tau = C\frac{M_0}{r^3}. \qquad (1.14)$$

The constant C depends on the rupture area's geometry and is equal to $7/16$ for a circular fault (Kanamori and Anderson, 1975). Recalling Equation 1.13, stress drop $\Delta\tau$ is therefore proportional to corner frequency.

Accurate estimation of seismic moment, stress drop and corner frequency (and therefore, rise time and source radius) from measured seismic waves is important as they control peak ground motion. Figure 1.9 highlights the impact of over- or underestimating a seismic source's stress drop for an event of the same magnitude. For two earthquakes with the same seismic moment, the earthquake with the higher stress drop (smaller source radius, or larger corner frequency) will generate higher ground velocities and ground accelerations. Attenuation affects smaller earthquakes even more (Figure 1.9c), making these source properties important to constrain across earthquake magnitudes.

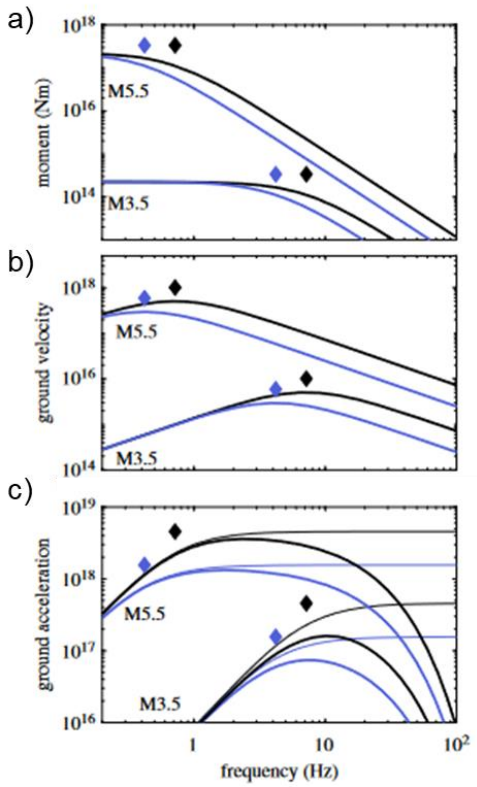

Figure 1.9*: Comparison of source spectra for model M_W 5.5 and 3.5 earthquakes with a 5 MPa (blue lines) stress drop and a 25 MPa (black lines) stress drop. Corner frequency is indicated by diamonds. a) Displacement spectra, b) relative ground velocity spectra and c) relative ground acceleration spectra. Thinner lines in c) represent ground acceleration spectra with the same initial sources (outlined in a) but with reduced attenuation (Abercrombie, 2021).*

Estimates of the earthquake energy budget can be derived by measuring the radiated energy and fracture energy. Radiated energy E_R is defined as the potential energy released during an earthquake that is radiated as seismic waves (Kostrov, 1974). Radiated energy can be estimated by using the following equation (Vassiliou and Kanamori, 1982):

$$E_R = \frac{1}{4\pi^2 \rho \beta^5} \int_0^{+\infty} \left| f \dot{M}_0(f) \right|^2 df. \qquad (1.15)$$

ρ is the density and β is the shear wave velocity of the material the waves propagate through. As discussed in Section 1.2.1.1, the seismological analogue for fracture energy is the breakdown work (Abercrombie and Rice, 2005), which is only analogous to fracture energy if fault weakening is concentrated near the propagating rupture tip. Radiated energy and fracture energy are the hardest properties to measure, as they are estimated from the high-frequency component of the seismic source: 80% of the energy in a simple circular source model (such as the Brune model) is

radiated above the corner frequency with a high-frequency fall-off. Moreover, these properties are the most affected by wave attenuation (Abercrombie, 2021).

Significant questions remain as to whether earthquake source properties vary with physical parameters such as earthquake depth and fault heterogeneity (e.g. fault material, roughness, branching and damage; Manighetti et al., 2007; Ben-Zion and Ampuero, 2009; Candela et al., 2011; Brodsky, Kirkpatrick and Candela, 2016; Abercrombie et al., 2021; Bedford, Faulkner and Lapusta, 2022). It is important to constrain how source properties vary with these physical parameters, as these parameters are known to play important roles in fault stability. For example, previous studies on fault complexity and roughness have shown that slip on immature, rougher faults generates a higher degree of source mechanism heterogeneity than mature, smoother faults (Bailey et al., 2010; Goebel et al., 2014; Powers and Jordan, 2010). Moreover, compilations of source properties from studies of laboratory events and earthquakes show that earthquake source properties are generally scale-invariant, with constant stress drop across different seismic moments (Aki, 1967; Selvadurai, 2019). Self-similar earthquake models, where earthquake source properties are scale-invariant, propose that small and large earthquakes rupture similarly, with similar physical mechanisms behind nucleation and propagation. The scale-invariance of earthquakes has been proposed in numerous studies (e.g. Abercrombie, 1995; Abercrombie and Rice, 2005; Aki, 1967; Hanks, 1977; Ide, 2003; Kanamori and Brodsky, 2004; Kanamori and Rivera, 2004; Shearer et al., 2006). Nevertheless, the concept of self-similarity across earthquake scales has been criticised, with Cocco, Tinti and Cirella (2016) arguing that the inference of self-similar behaviour of stress drop scaling is strongly model dependent.

1.4.3 Relating properties of laboratory-generated stick-slip to natural faults

Determining earthquake source properties remains a challenge, requiring an interdisciplinary approach to source characterisation that incorporates physical and geological observations with seismological models. Integrated fault studies (Tobin et al., 2007) that bridge the gap between field geology and seismology play an important role in understanding earthquake processes such as nucleation. Specifically, laboratory experiments are useful for simulating natural fault processes under controlled conditions, enabling parameters such as shear stress and displacement to be accurately and precisely measured. With additional sensors such as strain gauges and piezoelectric crystals, additional information can be obtained such as how the stress and strain field of a rock sample changes under different experimental conditions. Simultaneous measurements of seismic wave radiation and force (or strain) data during laboratory stick-slip have shown that stick-slips can reflect natural earthquake processes. For example, physical processes including supershear rupture (Passelègue et al., 2013), high-frequency radiation (S.

Marty et al., 2019) and slow slip events (Leeman et al., 2016) have been observed using laboratory experiments. By recording and analysing the resultant mechanical properties of slip along with the radiated wavefield, the gap between rock mechanical experiments and seismology can be bridged.

Comparing stick-slip properties and earthquake source properties requires removing additional wave effects from recorded seismic waves, i.e. path and instrument effects (Figure 1.6). While this is considerably difficult for natural earthquakes (Section 1.3.1), laboratory systems (sensors and recording equipment) can be calibrated to derive the absolute magnitude of seismic events (Figure 1.10; Goodfellow and Young, 2014).

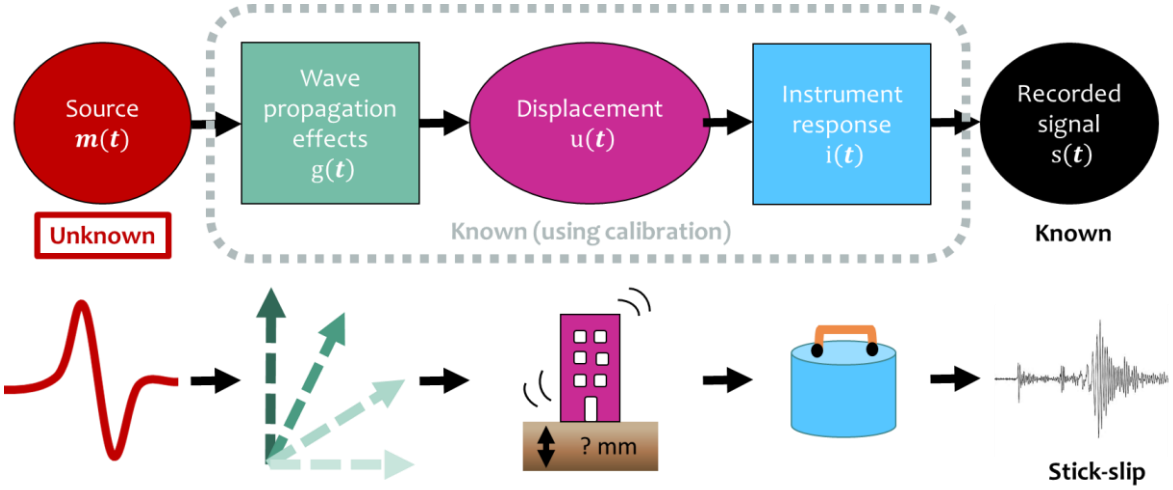

***Figure 1.10**: Flow diagram of sequential events that link the laboratory stick-slip source to the recorded signal and how calibration can be used to determine the source. After McLaskey and Glaser (2012).*

1.5 SEISMIC ACQUISITION SYSTEMS

Previous laboratory studies have shown that laboratory stick-slip and earthquake waveforms have extremely similar shapes. Additionally, stick-slip is routinely preceded and followed by smaller seismic events known as acoustic emissions (AEs). Lockner (1993) defines AEs as transient elastic waves within a material created by rapid energy release due to irreversible deformation. Stick-slip and AE waveforms visually resemble earthquake seismograms with P- and S-wave arrivals and codas (Figure 1.11; McLaskey et al., 2014). AE magnitudes also obey the Gutenberg-Richter relation for earthquakes, and foreshock and aftershock phenomena can also be observed within AE sequences (Lockner, 1993). Consequently, many inferences of stick-slip and AEs for larger-scale earthquake mechanics have been made. For example, Kaproth and Marone (2013) interpreted observations of slow stick-slip events in frictional sliding experiments using serpentinite as mechanical evidence for their origin in nature. Lei et al., (2004) and

Thompson, Young and Lockner (2009) both observed the time-space distribution of AEs during rock fracture and discussed implications for damage zone creation and dynamic rupture. Laboratory stick-slip and AE sources have the potential to reduce the uncertainty in natural earthquake source properties through geometrical constraints and accurate monitoring.

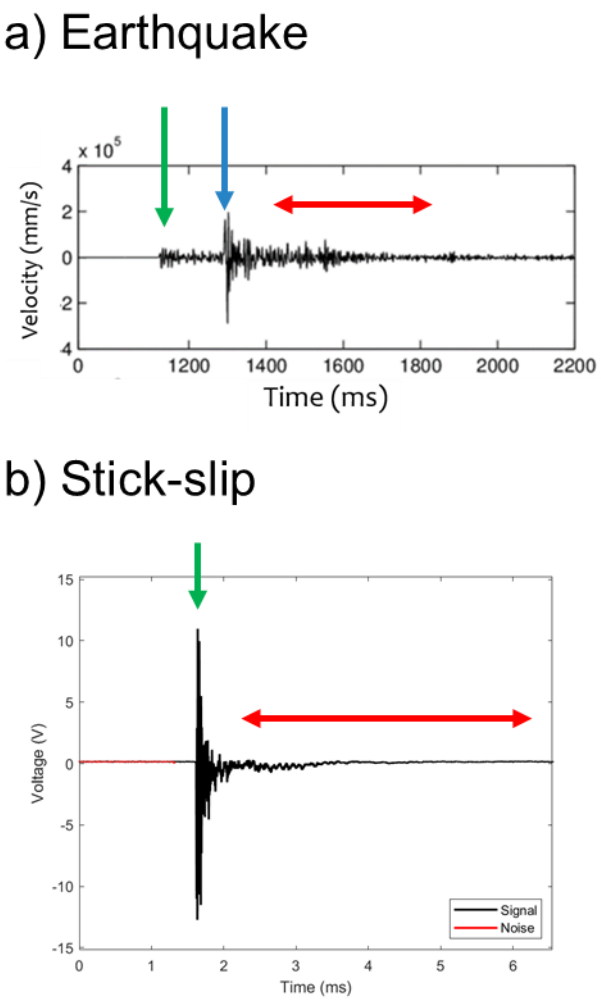

Figure 1.11*: Comparison of the form of an a) earthquake (2011 Tohoku earthquake measured in Sendai city; Mori, Tobita and Okimura, 2012) and b) laboratory stick-slip PMMA_30_001 at 30 MPa (Chapter 4). Green arrows indicate P-wave arrival, blue arrow indicates S-wave arrival and red arrows indicate the seismograms' codas.*

However, as in these cases, seismic acquisition systems are routinely uncalibrated and can only provide limited information, i.e. relative rather than absolute measurements of source properties. Calibrating seismic acquisition systems is advantageous as the absolute amplitude, time history and form of stick-slip and AEs can be determined. From this information, the physical mechanisms that generate stick-slips and AEs can be better constrained by analysing the time history and size of seismic moments and forces, which is crucial for the comparison of laboratory-generated events to natural earthquakes and faults (McLaskey et al., 2014). Moreover,

experimental results measured using different laboratory setups can be compared more reliably and accurately if recording systems are properly calibrated, allowing transparency across different instruments and laboratories.

Piezoelectric sensors (Berlincourt, 1971) are routinely used in seismic acquisition systems due to their simplicity in mounting to apparatus, optical properties and their sensitivity in comparison to capacitive transducers (McLaskey and Glaser, 2010). In the past, calibrating seismic acquisition systems has proven difficult as it is often unknown what piezoelectric sensors inherently measure: displacement, velocity or acceleration. Often, the recorded signal output is a complicated mixture of the three and is frequency-dependant meaning that, for example, one frequency band may measure velocity while another measures acceleration (McLaskey and Lockner, 2016). A second issue is that seismic wave propagation has added complications such as scattering, attenuation and apparatus boundary reflections which makes modelling more difficult. Other complexities include the limited bandwidth of AE amplifiers, sensor coupling and non-linear sensor response. For example, McLaskey and Glaser (2010) quantified sensor aperture effects and found that at high frequencies, recorded wave amplitudes are decreased due to multiple wavelengths being averaged over the sensors' areas of contact, or aperture.

1.6 THESIS AIMS AND STRUCTURE

It is clear from reviewing the literature that there is a gap that requires bridging between seismological models of earthquake sources and observations of the earthquake source. Faults exhibit structural complexity that is not yet encapsulated in source models, and problems remain in estimating the source properties of small-to-medium earthquakes. Therefore, this thesis aims to evaluate the source properties of laboratory-generated stick-slip to assess the validity of seismic source models for our laboratory system. This problem requires using a calibrated acoustic system where signals are able to give various source properties of laboratory events such as moment magnitude. Once this calibration is determined then 'laboratory seismology' is used to assess the changing properties of stick-slips generated under different laboratory conditions, namely normal stress and surface roughness.

The thesis is structured as follows. Chapter 2 describes the laboratory methods and experimental set-up used for data collection, including a detailed description of the triaxial deformation apparatus used to collect data in the Rock Deformation Laboratory, University of Liverpool. Chapters 3, 4 and 5 present the majority of the research conducted in this thesis. Chapter 3 describes how the seismic acquisition apparatus used in frictional sliding experiments is calibrated so that measured P- and S- waves can be used to estimate the source properties of

laboratory stick-slips, analogues for earthquakes. Chapter 4 presents a single frictional sliding experiment of poly(methyl methacrylate) (PMMA), a useful analogue material for crustal rocks, which generates spontaneous stick-slip that radiate seismic waves. Mechanical measurements are compared to seismic estimates of source properties using the Brune model and spectral fitting. Chapter 5 investigates the role of roughness and normal stress on source properties and their evolution with cumulative slip. Appendices are located at the end of each of these data chapters. The chapters were written to be stand-alone manuscripts, therefore, there may be some repetition of key concepts in these chapters. However, these chapters are intrinsically linked and have some references to previous chapters within them (i.e. Chapter 4 references the methods section of Chapter 3). Chapter 6 summarises the main conclusions of each of the previous chapters and discusses the implications of the work for the problems outlined in the introduction and potential avenues for further work. A complete reference list for the whole thesis is then presented, followed by a publication associated with this thesis. A digital appendix with all Matlab codes is available for access: https://github.com/lbrotherson/PhD.

2 EXPERIMENTAL DESIGN

2.1 INTRODUCTION

All experimental work in this thesis (Chapters 3, 4 and 5) was conducted on a high pressure, high temperature triaxial deformation apparatus in the Rock Deformation Laboratory, Department of Earth, Ocean and Ecological Sciences, University of Liverpool. This chapter gives a detailed outline of sample preparation, the triaxial deformation apparatus and an overview of the seismic acquisition apparatus used.

2.2 TRIAXIAL DEFORMATION APPARATUS

The basic design of the triaxial deformation apparatus is outlined below. This is followed by further descriptions of the pressure vessel, standard sample assembly, seismic sample assembly, confining pressure system, axial loading system, force measurement and servo-controlled system.

2.2.1 Basic design

The triaxial deformation apparatus (Figure 2.1) used in this thesis is a high pressure, high temperature deformation rig, able to apply up to 250 MPa confining pressure (equivalent to approximately 10 km lithospheric depth), 200 MPa pore fluid pressure and temperatures up to 200 °C. A differential load of up to 300 kN can be applied to a sample via a servo-controlled electro-mechanical loading system. Pore-fluid pressure can be applied using a servo-controlled pump, which controls pore fluid control at the top (upstream) and bottom (downstream) of 20 mm diameter cylindrical samples. As the pore fluid system was not used in this thesis, it will not be discussed further. For more information, see Mitchell and Faulkner (2008).

Most experiments conducted in this thesis are performed under axisymmetric compression conditions. This is where the largest principal stress (σ_1) is increased axially whilst the other principal stresses (σ_2 and σ_3) are held equal:

$$\sigma_1 \geq \sigma_2 = \sigma_3. \qquad (2.1)$$

While axisymmetric extension tests ($\sigma_1 = \sigma_2 \geq \sigma_3$) can be carried out by using an attachment to connect the loading piston to the sample assembly, these tests were not carried out in this study and so will not be described in detail. For more information, see Faulkner and Armitage (2013).

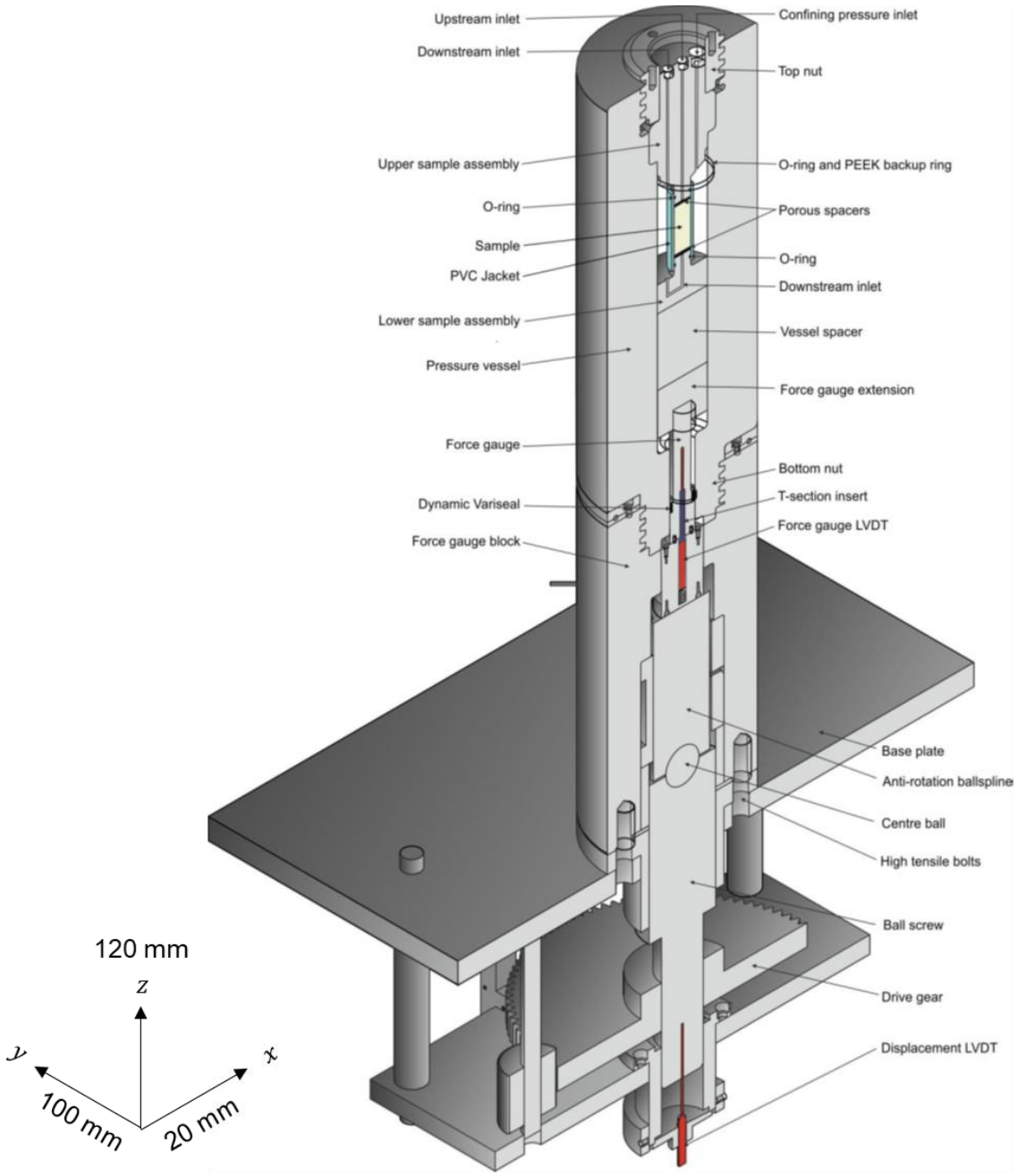

Figure 2.1*: Cross-section schematic of high pressure triaxial deformation apparatus used in this work (scale: 1:5.6. After Bedford (2017).*

2.2.2 Pressure vessel

The pressure vessel is made from hot work tool steel (Jessop Saville classification H.50 Sheffield steel manufacturers, or American Iron and Steel Institute classification AISI H.13) and is cylindrical, with an internal bore of 60 mm and an outer diameter of 180 mm (Figure. 2.1). While the maximum working pressure of the pressure vessel is 250 MPa, it has been tested up to 375 MPa, 1.5 times its working pressure for safety purposes (High Pressure Technology Association, 1975). The pressure vessel resides at the top of the apparatus, above the axial loading column,

with the sample assembly inserted via an opening at the top. Once the sample assembly is inserted, it is secured by a threaded top nut and sealed by an o-ring at the top of the sample assembly. To support this o-ring and prevent it from escaping between the sample assembly and the vessel, a high tensile strength Poly (oxy-1, 4-phenyleneoxy-1, 4-phenylenecarbonyl-1, 4-phenylene) (PEEK) backup ring is added (Faulkner and Armitage, 2013).

2.2.3 Seismic sample assembly

Ball impact and frictional sliding experiments are conducted using the seismic sample assembly (Figure 2.2). In contrast to other studies (such as Bedford, Faulkner and Lapusta, 2022) which use a standard sample assembly with no feedthrough electrical wiring, the seismic sample assembly allows electrical measurements to pass through the sample at high pressures. 120° and 180° piezoelectric crystals (PZT-5H, fundamental frequency = 1.5 MHz, Boston Piezo-Optics Inc.) are secured in the top and bottom platens respectively with silver loaded epoxy and copper backing. The piezoelectric crystals are made of lead-zirconate-titanate (PZT) and are overtone polished to limit the energy loss at higher harmonic frequencies (e.g. 9^{th} overtone, 11^{th} overtone; Berlincourt, 1971). The crystals are gold coated for electrical connectivity at the top and bottom surfaces of each crystal. The piezoelectric crystals, referred to as acoustic sensors when mounted to the top and bottom platens of the seismic sample assembly, detect P- and S-waves generated during experiments. Due to the high frequencies expected in these experiments, the electrical cabling used can attenuate the signal, causing internal reflections at component connections (Allen, 2017; Blake, 2011). Therefore, high frequency (attenuation at 100 MHz = 3.61 dB, capacitance per metre = 105 pF) coaxial cables are used to ensure that their resistances are equal to the output of the seismic acquisition components used.

Samples up to 60 mm in length and 20 mm in diameter can be held by the sample assembly. Further details on direct shear geometries used in this thesis are given in Chapters 4 and 5.

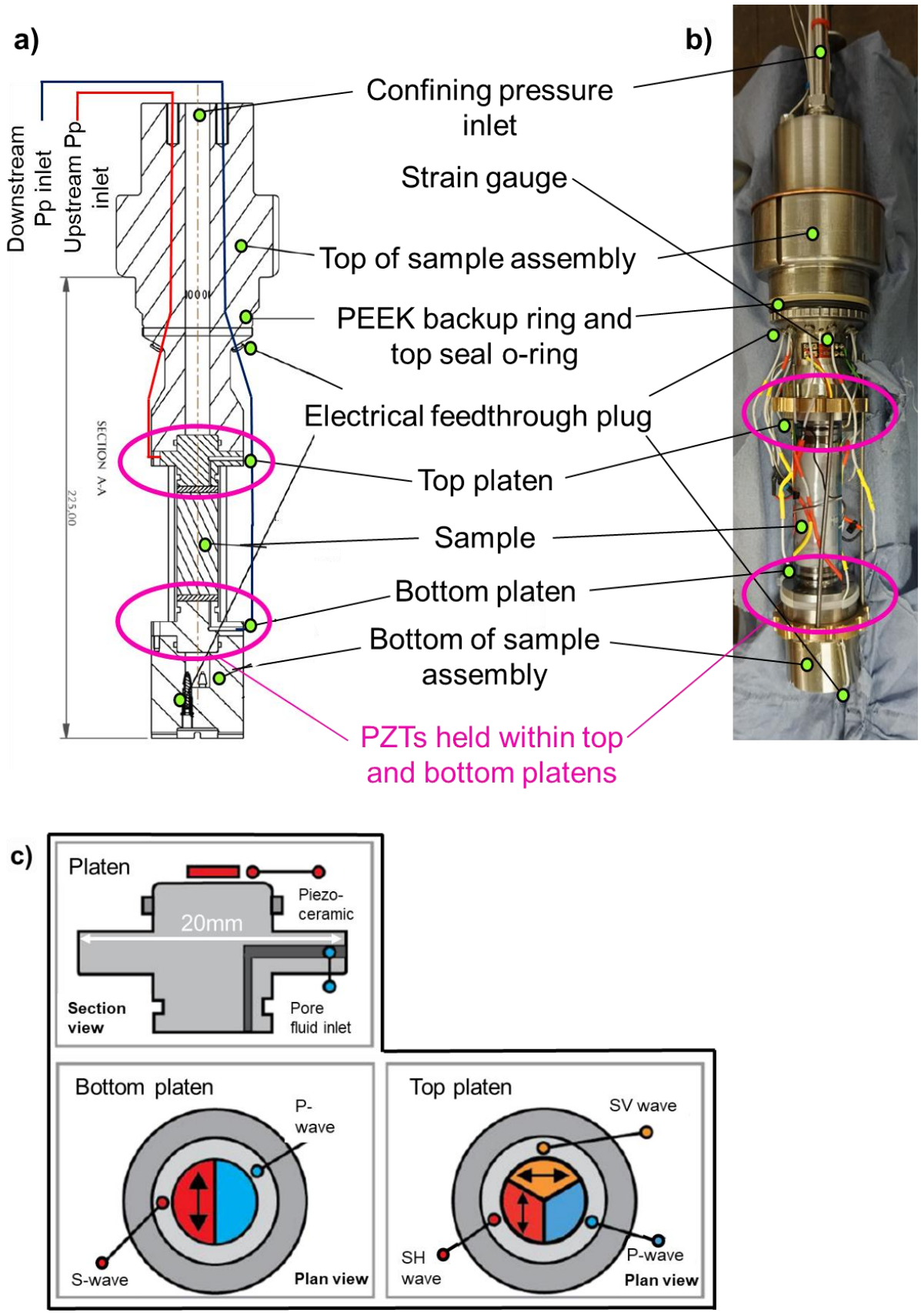

Figure 2.2: *a) Schematic illustration and b) photo of seismic sample assembly, showing sample position and platens with piezoelectric crystals (PZTs) mounted within. c) Schematic diagram of bottom and top platens, with the arrangement of PZTs shown for each platen. After Allen (2017).*

2.2.4 Direct shear geometries

For this work, steel slider geometries have been adapted to allow for the sliding of solid slabs of material, in contrast to past Rock Deformation Laboratory studies which have solely focused on rock cubes (e.g. Allen et al., 2017), cylinders (e.g. Rice-Birchall, Faulkner and Bedford, 2021) or gouge (e.g. Bedford and Faulkner, 2021). A single direct shear geometry using slabs of polymethyl methacrylate (PMMA, or Perspex), an engineering plastic from the polymerization of methyl methacrylate, is used (Figure 2.3). Direct shear geometries are advantageous over other geometries such as 30° saw cut geometries as displacement, shear and normal stresses are directly comparable to displacement, force measurements, and confining pressure. The geometry used consists of two L-shaped, 17-4 stainless steel sliders with a concave section removed are used to house the slabs, which are glued in place with Loctite Precision Super Glue. In general, PMMA samples are ordered to be ~0.4 mm thicker than the loading ledge (4 mm rather than 3.6 mm) to avoid plastic on metal sliding due to frictional wear (Figure 2.3a). PMMA samples with dimensions of 36 x 18 x 4 mm were laser cut by the University of Liverpool Core Services with an accuracy of ±10 μm.

Before insertion into the pressure vessel, a sample is placed adjacent to two soft silicon rubber spacers which accommodate sample displacement. Sample spacers of 17-4 stainless steel are positioned above and below the sample, as in previous studies (e.g. Harbord, 2018). This is to protect the sample assembly from long-term damage and to reduce the likelihood of the polyvinyl chloride (PVC) jacket holding the sample pinching away from the o-rings (C. Harbord, Pers. Comm.). Next, the sample is wrapped in low friction (μ = 0.05-0.10) polytetrafluoroethylene (PTFE) shim to limit the effect of jacket friction near the frictional interface. A circular piece of PTFE is placed at the top, circular end of the bottom slider to reduce radial friction so that only axial friction is measured. Before insertion into the seismic assembly, the sample is placed into a PVC jacket of 19 mm internal diameter, which seals on the o-rings of the upper and lower platens of the assembly when confining pressure is applied (Figures 2.2 and 2.3).

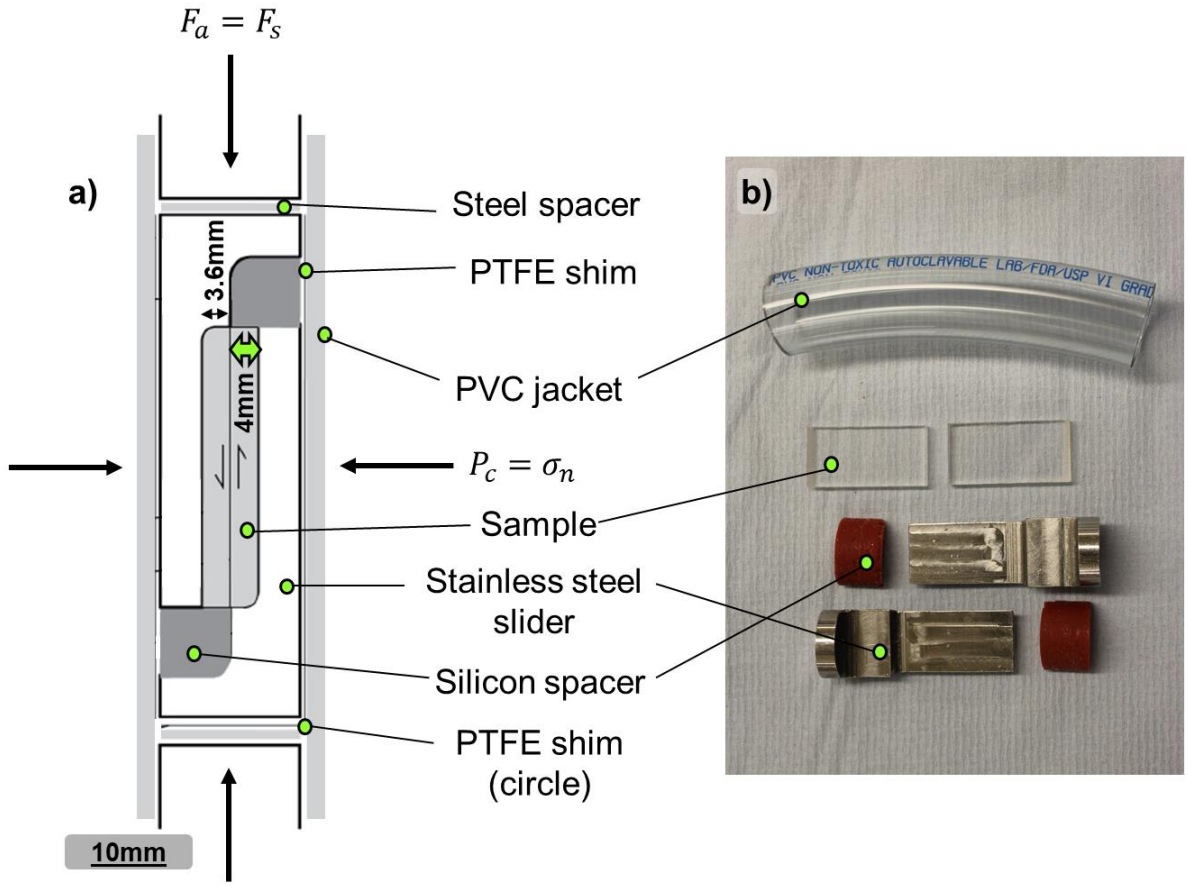

Figure 2.3: *a) Schematic of seismic sample assembly experimental configuration used to conduct slabbed, single direct shear experiments in this work. b) Photo of PMMA slabs, silicon spacers, stainless steel slider and PVC jacket. PMMA samples are 0.4 mm thicker (4 mm) than the loading ledge (3.6 mm) to avoid plastic on metal sliding due to frictional wear. Normal stress σ_n is equal to confining pressure P_c.*

2.2.5 Confining pressure system

Low viscosity (10 cST, around 0.01 PA s) silicone oil is used as the confining medium within the vessel to prolong the life of the pressure vessel as it is non-corrosive and does not become overly viscous at high pressure, alleviating the possibility of the confining fluid freezing in the pipes. The silicon oil enters via the confining fluid pipe at the top of the sample assembly (Figure 2.2). To increase pressure, an air-driven SC hydraulic pump is used (Figure 2.4). The pump can be isolated from the vessel via the valve system once the required confining pressure is reached (Figure 2.5). During an experiment, confining pressure is measured by both an analogue gauge and a Honeywell Pressure (RDP TJE-type) transducer with a resolution of 7 kPa. Pressure is controlled by a Nova Swiss 10cc control pump, adapted to be driven by a gearbox and servo-controlled motor (Figure 2.6). As the pump is servo-controlled, the pump can hold pressure at a constant value by responding and adapting to changes detected by the transducer. This is particularly

useful when the axial piston is used, as the servo-controlled pump can compensate for any pressure changes that the piston causes when it moves inside the vessel.

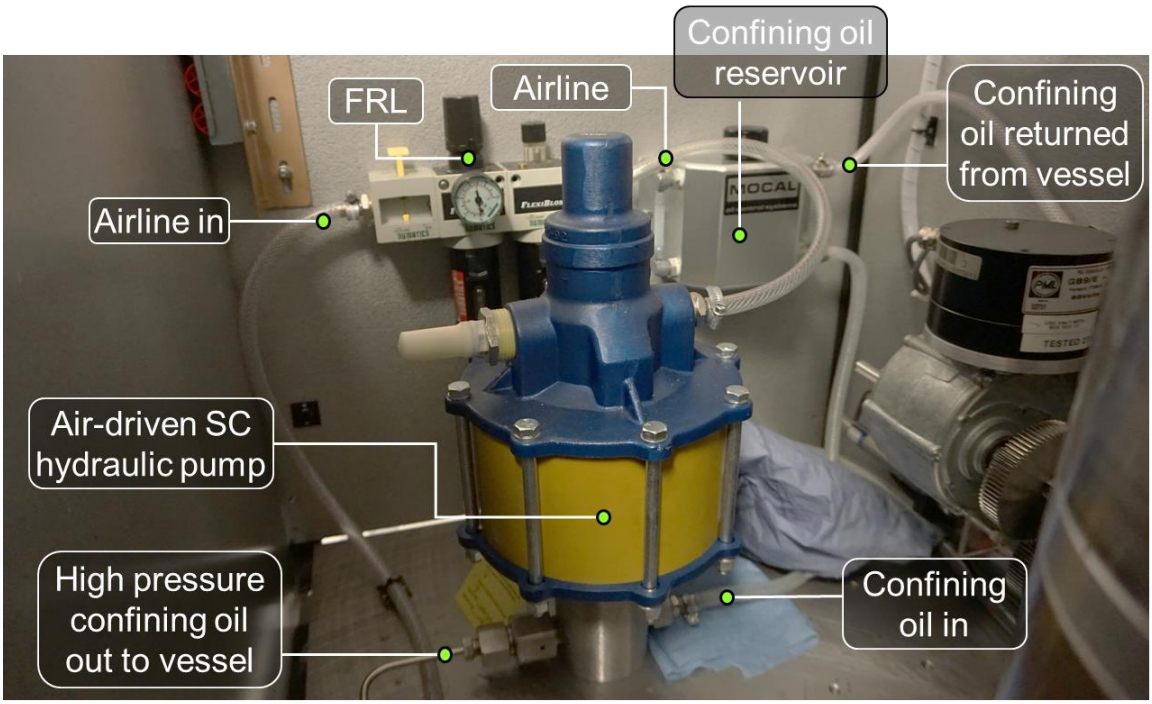

Figure 2.4: *Air-driven SC hydraulic pump, which increases the confining pressure within the vessel. Air flow into the pump is controlled by a manual pump at the front of the rig (Figure 2.12). Air flows through a Filter Regulator Lubricator (FRL) to remove compressor debris and lubricants from the air stream. Oil is stored in a reservoir which transfers the oil to the pump, where it is pressurised and delivered to the vessel.*

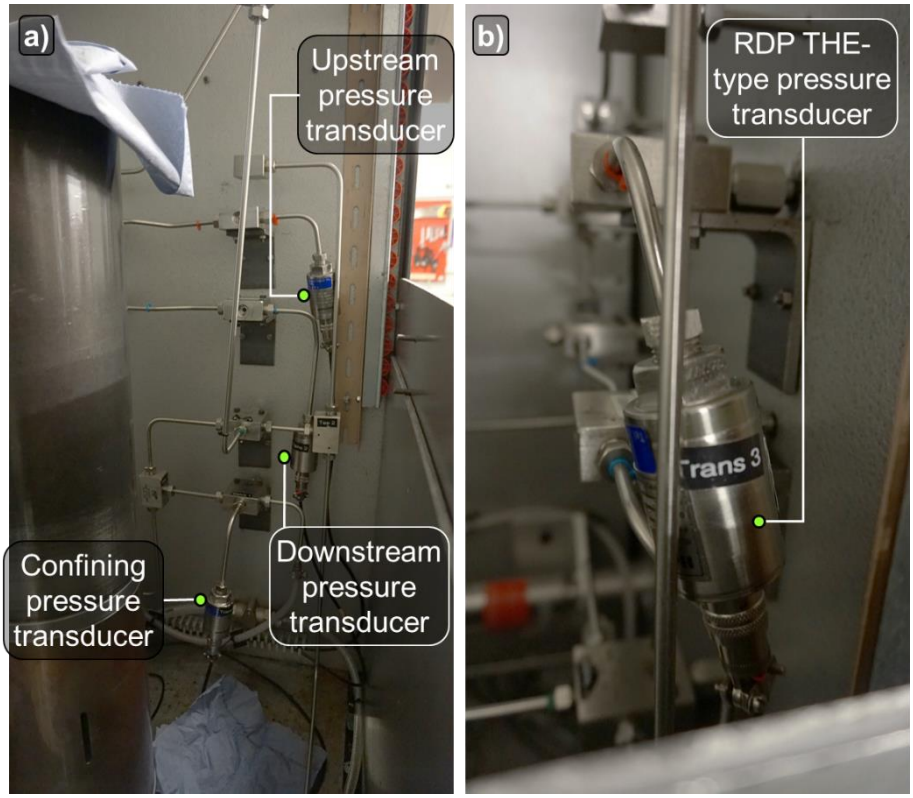

Figure 2.5: *a) Pressure transducers are connected to the upstream, downstream and confining pressure systems. b) During an experiment, an RDP TJE-type transducer is used to monitor the pressure.*

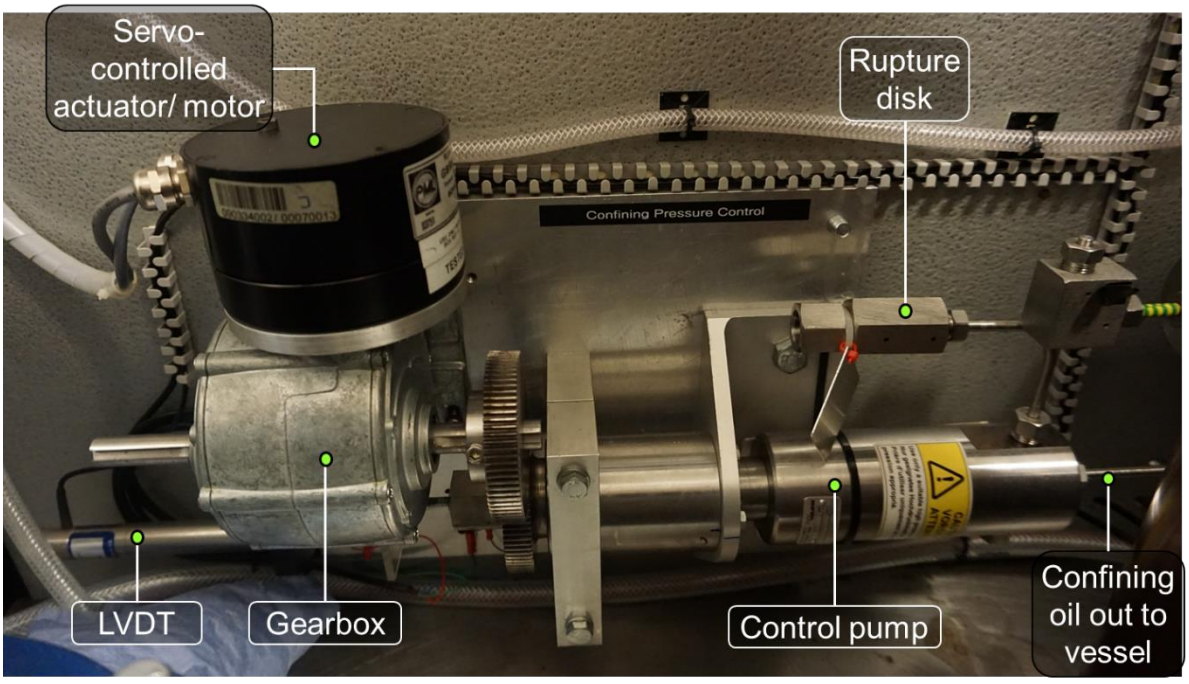

Figure 2.6: *Confining pressure control pump, which is connected to a servo-controlled actuator/motor and gearbox. Displacement of the control pump's piston is measured by an LVDT.*

2.2.6 Axial loading system and force gauge block

Axial loading is applied by an electromechanical, servo-controlled axial piston. The piston consists of a force gauge column that penetrates the base of the pressure vessel and is driven by a ball screw actuator below (Figures 2.1 and 2.7). The pressure vessel screws into the force gauge block, which is connected to the rig's base plate by eight M16 high-tensile bolts (Figures 2.1 and 2.8). A spacer is placed between the force gauge block and the pressure vessel. This can be replaced with a cooling plate for use in high temperature experiments to minimise the effect of temperature on force gauge measurements. The force gauge column is sealed into the base of the vessel by a dynamic Variseal, which is supported by two PEEK backup rings (Figure 2.7). This prevents silicon oil from leaking from the bottom of the pressure vessel. The force gauge extension is in contact with the force gauge column and applies a load to the bottom of the sample assembly (and the sample). This applied load is measured by the elastic deformation of the force gauge column (Figure 2.7a).

An internal linear variable displacement transducer (LVDT) is supported via insertion into a T-section within the column (Figure 2.7). The T-section pushes against an internal shoulder of the column, above the level of the Variseal. This ensures that the LVDT solely measures deformation above the internal shoulder of the column. Consequently, no correction for seal friction is required, as the deforming length of the force gauge is above the pressure seal (Paterson and Wong, 2005). The force gauge column is made of M300 maraging steel, which is preferable as it has a high yield strength (~2 GPa) whilst remaining ductile. Moreover, the Young's Modulus (~200 GPa) is equivalent to the steel pressure vessel, meaning that the cross-sectional area of the column can be reduced to produce more elastic deformation. This increases the force gauge's resolution while remaining below the material's yield stress. The ball screw can be subjected to up to 500 kN (300 kN under the maximum differential load and 200 kN while at the highest confining pressure of 250 MPa). Under maximum load, a 20 mm diameter sample subjected to 300 kN would experience a maximum differential stress of ~1 GPa. The design of the force gauge means that a factor of safety of 2 to the material yield strength is achieved at these maximum loading conditions. Overall, the force gauge resolution is better than 0.03 kN.

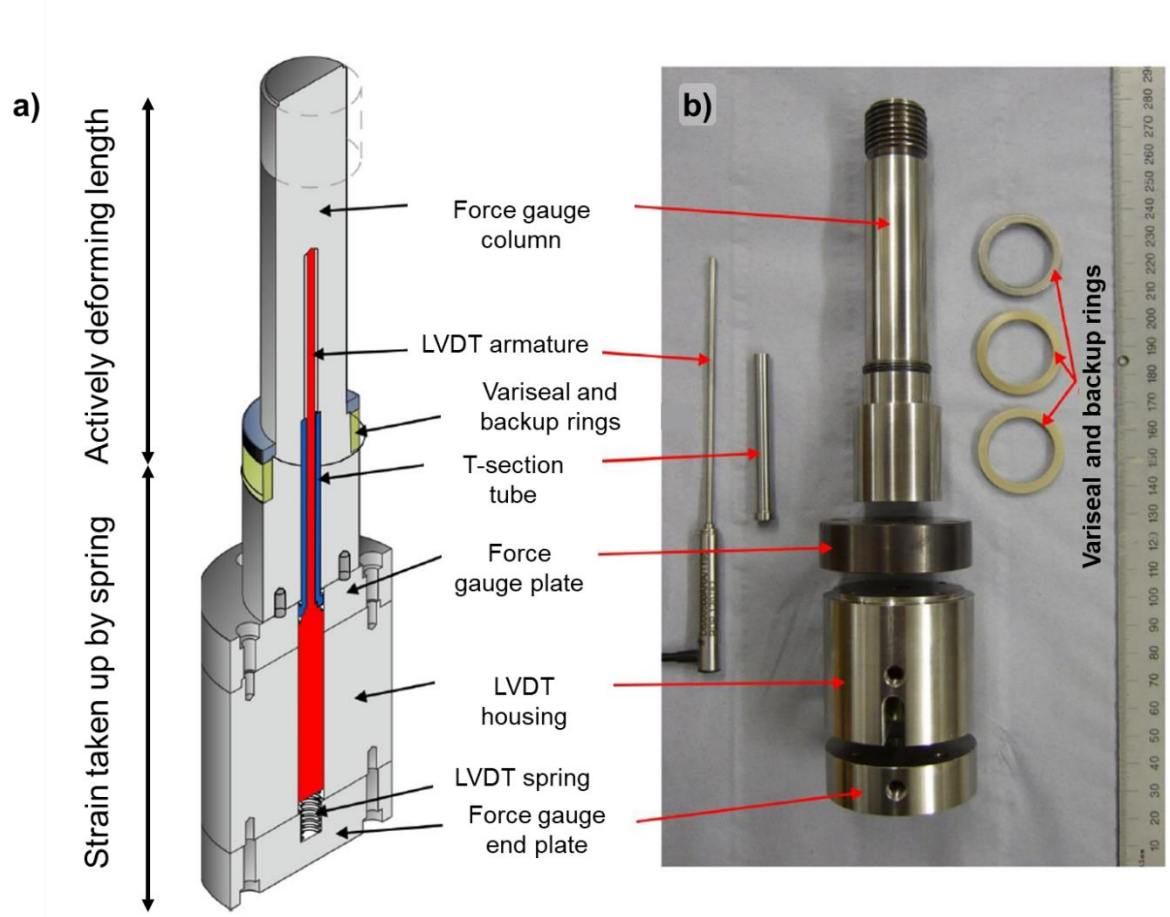

Figure 2.7: *a) Diagram and b) photo of the force gauge, including the dynamic Variseal and backup rings. After Bedford (2017).*

The force gauge column resides on top of a high torque, anti-rotation THK ball spline. The ball spline moves with very little friction along a vertical ball-bearing raceway. This converts the rotary motion of the ball screw load actuator to linear motion. The base of the spline has a hemispherical seat to ensure coupling with the ball screw (Figure 2.7), which ensures that the load applied from the ball screw stays concentric. In the ball screw, the ball-bearing raceway is helical, allowing the ball screw to rotate with minimal friction under high loads. The ball screw is powered by a Printed Motor Works GM12 pancake-type motor and gear train (Figure 2.8), which consists of a Parvalux gearbox (115:1 ratio) connected in series to a Hydro-mec worm gearbox (36:1 ratio). The screw is then connected to the pinion of the main driver gear (5:1 ratio). In total, the gear ratio from the drive motor to the ball screw is 20700:1. The motor has a maximum speed of 3000 rpm, resulting in the maximum rotation for the main drive gear of 0.14 rpm. As the lead of the ball screw is 10 mm, the maximum loading velocity is therefore 23 μm/s.

The motor can supply a maximum torque of 1.31 Nm, which equates to 27.1 kNm provided by the gear train (ignoring frictional effects). The torque needed to rotate the ball screw under a maximum load of 500 kN can be calculated:

$$Torque = \frac{Axial\ Force\ \times Lead}{2\pi\eta}, \tag{2.1}$$

where η is the efficiency factor, typically equal to 0.9 (THK, n.d.). Knowing axial force (500 kN), lead length (10 mm = 0.01 m) and η, the torque required to move the ball screw under maximum load is 885 Nm. This is well below the maximum torque provided by the gear train (27.1 kNm).

As displacement is measured by the displacement LVDT at a distance from the sample, a correction must be made to account for elastic deformation (or stiffness) of the loading column. Applying this correction enables the true displacement of a sample during loading to be calculated. An additional correction must be made for negating the effect of increased confining pressure on the force value measured by the force gauge. Both corrections are made by measuring the stiffness of the column at 50 MPa confining pressure, which is calculated from the gradient as force increases with displacement (Bedford, 2017). To account for different confining pressures, gradients of the force range where stick-slip behaviour typically takes place are calculated for each confining pressure (Figure 2.9).

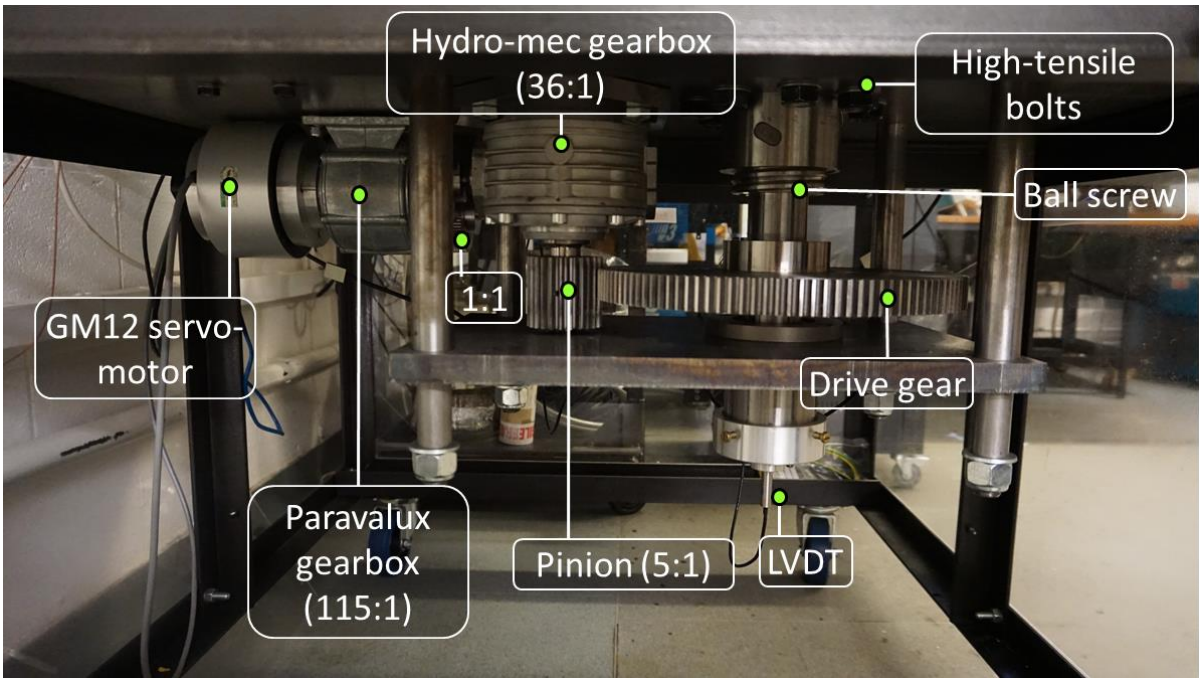

Figure 2.8: *Underside of the base of the rig, where the axial loading system is connected to the system. A GM12 servo-motor is attached to the gear train, which rotates the ball screw with a total ratio of 20700:1. Displacement of the axial loading column is measured by an LVDT at the bottom. The axial loading column is connected to the base plate of the rig below by high-tensile bolts.*

2.2.6.1 Loading column calibration

Force measurements made using the force gauge during frictional sliding experiments reflect both the stiffness of the loading column and the stiffness of the sample. By using Hooke's Law ($F = kx$), the amount of slip during stick-slip x_{fault} in m can be calculated by measuring the decrease in force from peak to residual force $\Delta F = F_p - F_r$ with associated stress drop and slip, and knowing the machine loading stiffness, i.e. the stiffness of the loading column, k:

$$x_{fault} = \frac{\Delta F}{k}. \qquad (2.2)$$

The machine loading stiffness k is derived through calibration of the loading column in the triaxial deformation apparatus. A 'blank' cylindrical 17-4 stainless steel sample with a 19 mm diameter and 50 mm length is jacketed with PVC and loaded at 50 MPa confining pressure. While frictional sliding experiments in this thesis are carried out between 30 – 50 MPa, calibration at 50 MPa is considered sufficient as the machine stiffness is similar. Using the axial loading system, the sample is compressed to a load point displacement of 0.41 mm to 28 kN. Then, the load point displacement is decreased back to 0 mm, extending the sample. This 'cyclic loading' process is repeated twice more (3 cycles in total) to observe any permanent plastic deformation. The data is recorded in LabView with a sample frequency of 1 Hz. The cyclic loading process returns 6 curves (3 loading and 3 unloading) describing how the loading column deforms with load point displacement at 50 MPa (Figure 2.9). The gradients of the loading curves give the machine loading stiffness k, which varies depending on load point displacement (and force).

Loading column calibration is carried out using the Matlab code *triaxial_calibration.m*. To find k for particular stick-slips, it is assumed that k is constant during slip and as force decreases from peak force F_p to residual force F_r. The force values between which stick-slip occurs during frictional sliding experiments are used to calculate k. For example, if an experiment has stick-slips that occur between 5 – 8 kN (i.e. $F_p = 8$ kN and $F_r = 5$ kN), the gradients of the 6 curves between 5 – 8 kN (0.125 – 0.168 mm) are calculated by dividing the force values by load point displacement. These three values are averaged to give the machine loading stiffness k for that experiment, i.e. 75 kN/mm for this example. From this, the amount of slip during stick-slip x_{fault} in frictional sliding experiments can be calculated. During slip, any unloading that is unaccounted for by the machine stiffness k is due to the experimental sample's stiffness and represents fault displacement, x_{fault}. Machine loading stiffness k varies with confining pressure and is accounted for by calculating k using the force values between which stick-slip occurs for each frictional sliding experiment.

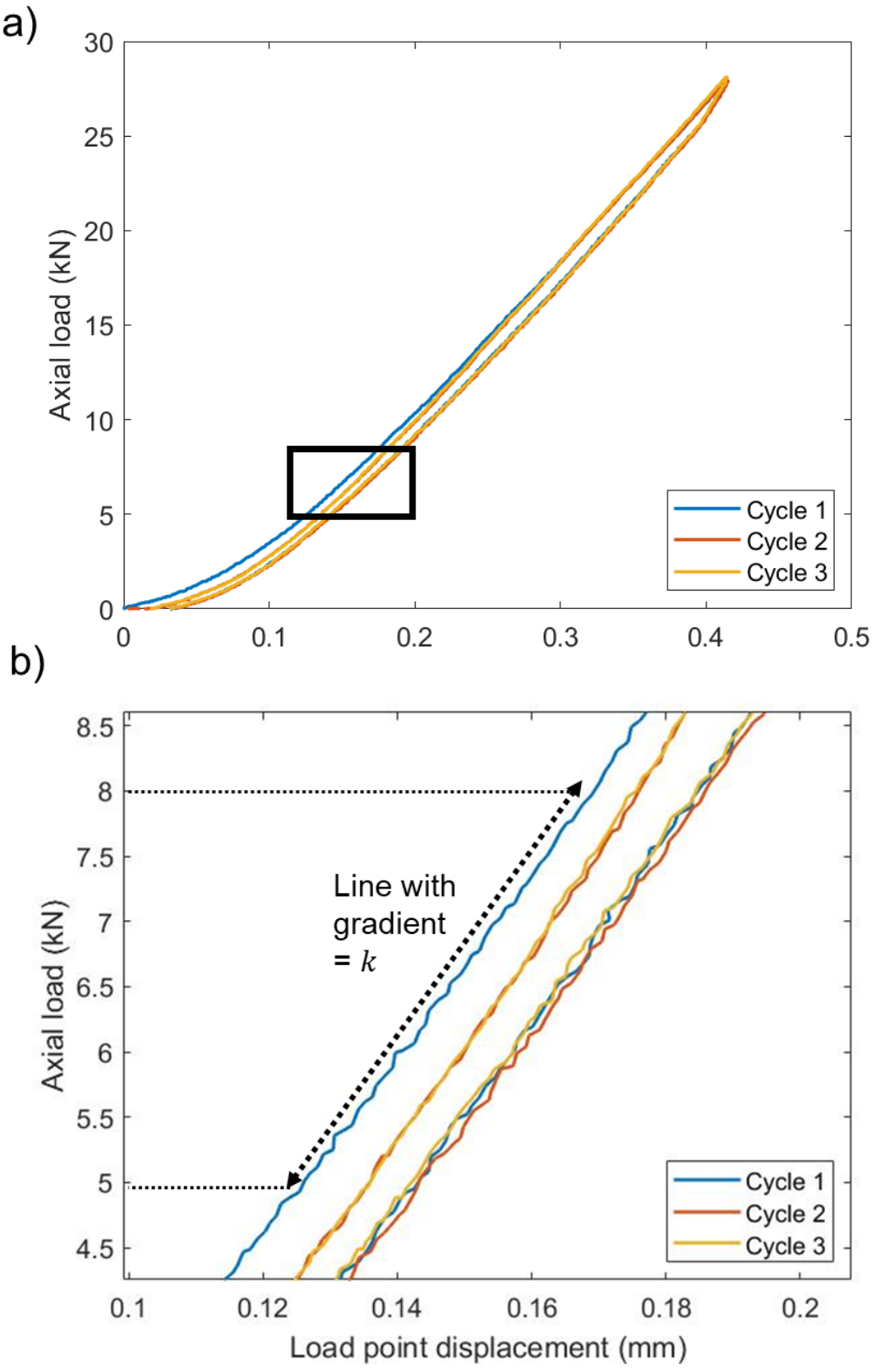

Figure 2.9: *a) Cyclic loading of 'blank' steel sample at 50 MPa confining pressure with the extent in the black box. b) Extent shows how machine loading stiffness k is calculated for an example experiment with stick-slips that occur between 5 – 8 kN.*

2.2.7 Strain gauge

An issue with the force gauge is that during stick-slip events, the zero offset (red cross, Figure 2.10) can be jolted due to the inertia of stick-slips, as they are energetic events. Stick-slip inertia can cause force jogs in force gauge data, where force during slip appears to increase (or decrease) more than it does during stress drop (Figure 2.10). To ensure that only deformation without zero offsetting (i.e. solely sample deformation) is measured, a Tokyo Sokki Kenkyujo Co., Ltd strain gauge is attached above the top platen of the seismic assembly (Figure 2.2). The strain gauge used is type FCB-2-11, which has a gauge resistance of 120 ± 0.5 Ω, gauge length of 2 mm and X and Y gauge factors of 2.13 ± 1%. The gauge is carefully oriented so that the axial and radial strain gauges were parallel and orthogonal to the shear direction, respectively. TF-2M connecting terminals (Tokyo Sokki Kenkyujo Co., Ltd) are attached to either side of the strain gauge to connect them with wiring to the 9-pin male D-sub connector. Once connected to the in-vessel 9-pin female connector, strain gauge signals are conditioned using a Modular 600 multichannel amplifier (Figure 2.11b) with a gain of 100,000. During axial loading in frictional sliding tests (i.e. the elastic loading preceding the first stick-slip) force measurements are accurate as there is no jolting. At this initial point, strain and force measurements are proportional. In this thesis, strain and force proportionality during loading are observed to correct force measurements' zero offsets to ensure that they are accurate and absolute, rather than relative. The force gauge correction using the strain gauge is described in Chapter 5.

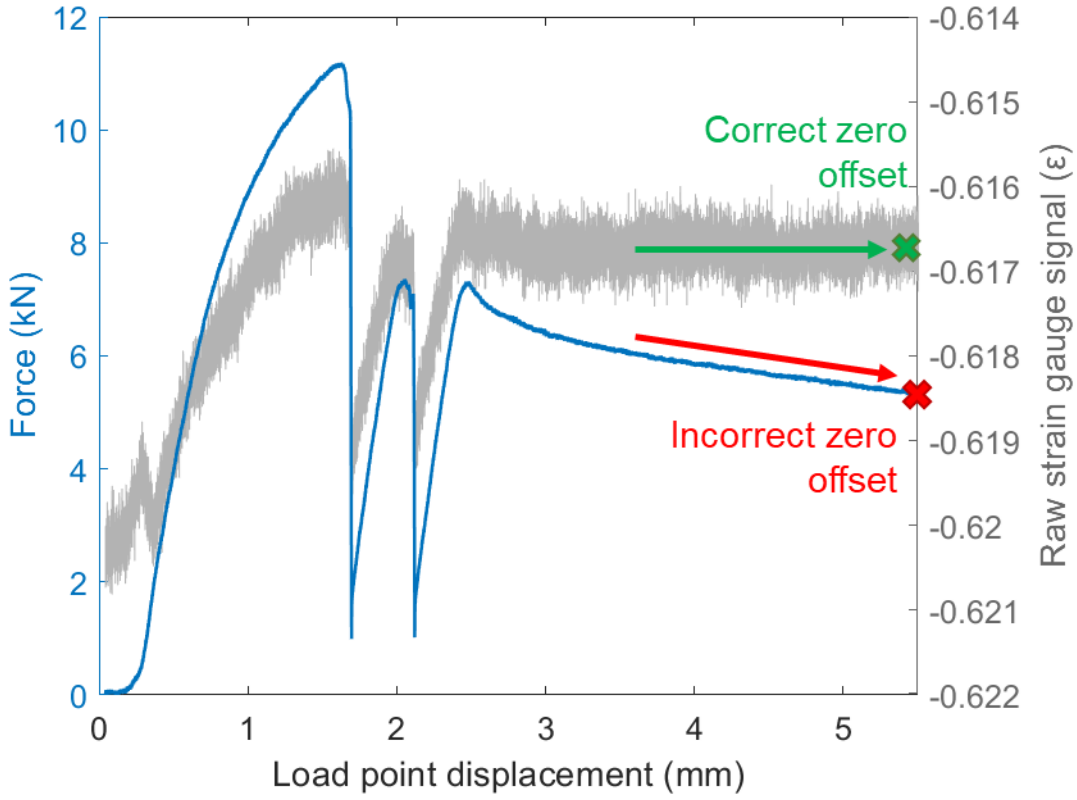

Figure 2.10: *Example of 2 stick-slips (build-up of elastic strain followed by sudden stress drop) from test PMMA_120_50. Strain gauge data (grey line) are not proportional to force gauge data (blue line) during the entire test, showing that the force gauge is affected by the inertia of the stick-slips. This can be seen at the end of the test by the force gauge's downward trend (red arrow) versus the strain gauge's flat trend (green arrow), leading to an incorrect zero offset (red cross versus correct offset, green cross).*

2.2.8 Data logging and servo-control system

All triaxial deformation apparatus experimental data (including pressure and displacement data) are logged using LabVIEW software on the rig computer. The software also allows interfacial control of experimental parameters via a series of servo-control boxes. Before logging, pressure measurements from the transducer are amplified from millivolt to volt DC or AC signals by the RDP amplifier (Figures 2.11 and 2.12). Next, signals are digitised by a 4-channel, 16-bit input analogue-to-digital module (NI 9215). Signals are conditioned by servo-loops within the Compact RIO, where they are compared to working set points (WSPs), which are set by a LabVIEW programme on the computer (Figure 2.11). If the WSPs and digital signals do not match, a signal is sent from the 4-channel, 16-bit digital-to-analogue voltage output module (NI 9263) to the servo-control box. The magnitude of this signal is dependent on user-selected PID (Proportional, Integral, and Derivative gain) open loop settings. PIDs reduce the error between the desired control parameter (e.g. confining pressure) and the WSP to produce reliable confining pressure

and load point displacement measurements (Tan et al., 2006). Finally, a servo-amplifier within the servo-control box amplifies the signal to voltages and currents that are high enough to drive the confining pressure, pore pressure and axial load actuators and motors (Allen, 2017; Bedford, 2017). The servo-control system's workings are outlined in Figure 2.11.

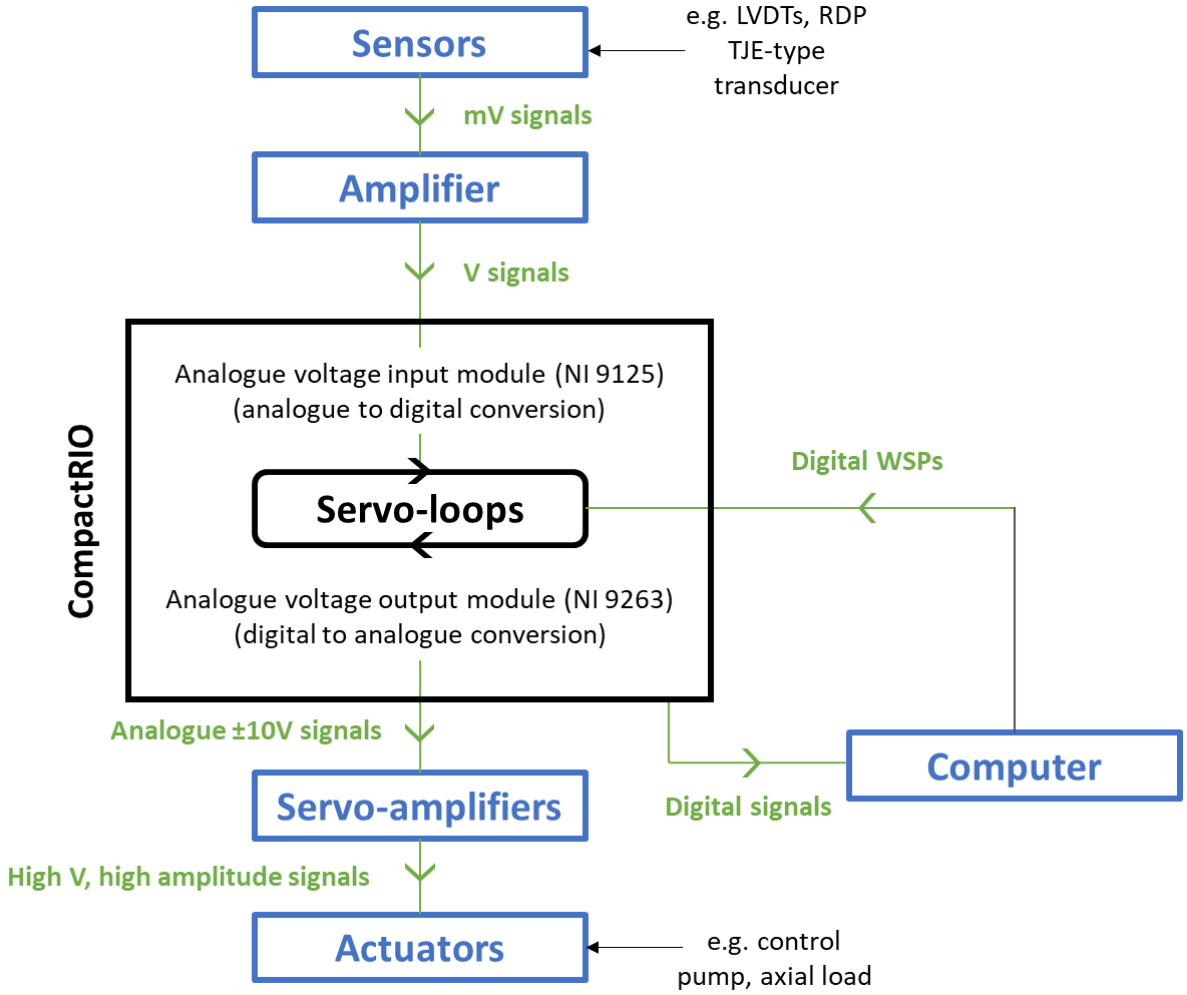

Figure 2.11: *Schematic of the servo-control system, including the CompactRIO module. After Allen (2017).*

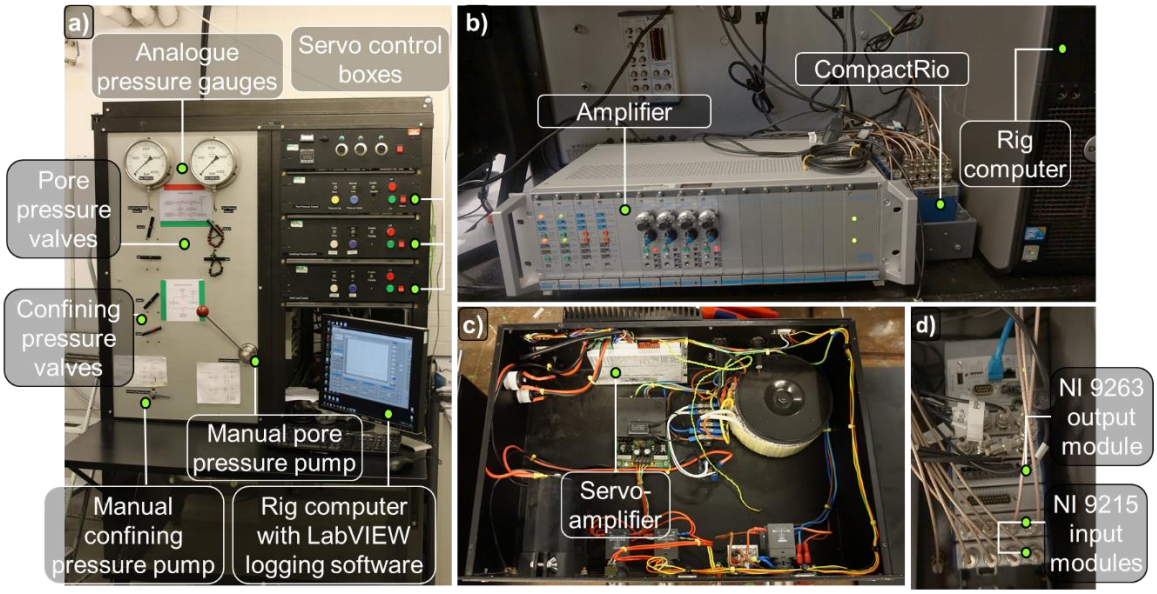

Figure 2.12: *a) Outside of the triaxial deformation apparatus (TR3) with external pressure gauges and manual valves and pumps. b) Modular 600 multi-channel amplifier, CompactRIO and rig computer. c) Servo-amplifier inside the control boxes that send high voltage, high current signals to the actuators and motors. d) NI 9215 input modules and NI9263 output module inserted into the chassis of the CompactRIO.*

2.3 SEISMIC ACQUISITION APPARATUS

The seismic acquisition apparatus consists of the following four components, the latter three of which are used in this thesis: the Trigger Hit Count (THC) unit, digital oscilloscopes, the Pulser Amplifier System (PAS) and a computer with CecchiLeach seismic processing software installed (Figure 2.13).

Two, four-channel Handyscope HS4 USB digital oscilloscopes (TiePie) with 50 MHz sampling rate, 12-bit resolution, 128 kilo-samples per channel and 200 mV to 80 V Full-Scale Volts (FSV) input range were used to collect and digitise seismic signals, including ball drops, stick-slips and AEs (Figure 2.13). The units are combined in a primary-secondary (Cimpanu, 2020) configuration to provide up to 8 channels for data acquisition. While up to 16 channels are available (four, four-channel oscilloscopes), only 6 channels are required to measure using all P-wave and S-wave piezoelectric acoustic sensors (Figure 2.14).

The THC (Itasca IMaGE/Applied Seismology Consulting) is a multi-channel system that applies trigger and hit count logic during the monitoring of seismic signals. The THC applies a user-selected Global Trigger Threshold (GTT) to ensure that only signals above the GTT voltage (e.g. 750 mV) are measured. Two other user-specified parameters, the number of channels needed to trigger and the timing window, can be controlled to reduce noise acquisition. In this thesis, the THC is not used due to an internal issue where voltage outputs were approximately 50% lower than expected. Triggering can also be controlled using the Trigger Level parameter, which sets a percentage of the FSV as the trigger threshold. For example, with Trigger Level = 1 at FSV = 20 V, signals will be recorded when above $0.01 \times 20 = 0.2$ V.

The PAS (Itasca IMaGE/Applied Seismology Consulting), consisting of Pulser Amplifier Desktop units (PADs) and a Pulser Interface Unit (PIU), are used for the pre-amplification of signals. with gains from 30 to 70 dB (Gain Levels 1 to 5), selectable by the user. Two PADs are used, PAD-006-1949 and PAD-006-1951, to amplify signals detected by P-bottom and S-bottom piezoelectric crystals (Figure 2.2). The frequency response of each PAD is broad, with plug-in filter circuits to adapt the unit to a desired frequency range. The impact of the PAS on measured signals is detailed in Chapter 3, Section 3.3.

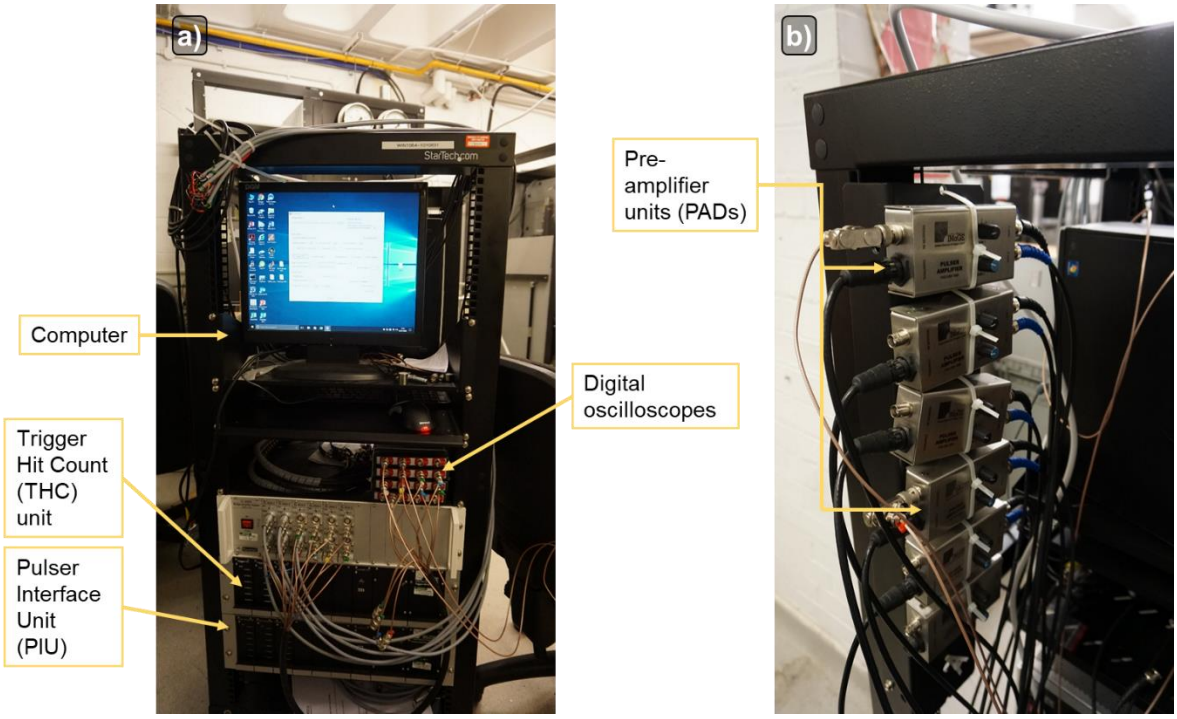

Figure 2.13: *Seismic acquisition apparatus used to record seismic signals from ball drop and frictional sliding experiments. a) Front of apparatus including a computer with CecchiLeach installed and Trigger Hit Count (THC) unit. Pulser Amplifier System (PAS) consist of the Pulser Interface Unit (PIU, a) and pre-amplifier units (PADs, b).*

For all frictional sliding experiments described in this thesis, the PAS and digital oscilloscopes are connected in a systematic fashion (Figure 2.14) and controlled via CecchiLeach software on the computer (USB com port interface). In this thesis, this software is used to acquire waveforms from ball drop impacts for acoustics sensor calibration and laboratory-generated stick-slips.

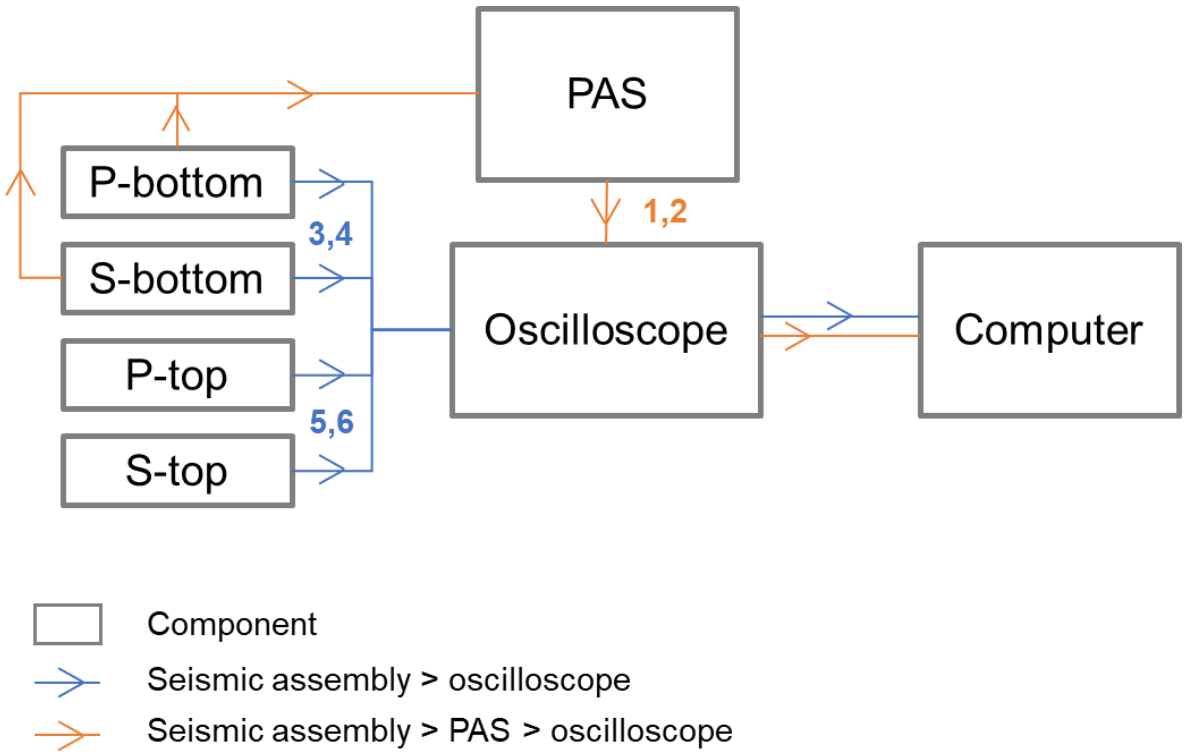

Figure 2.14: *Schematic diagram of seismic acquisition apparatus used to acquire seismic signals. Numbers indicate the channel number for each connection on the digital oscilloscope and CecchiLeach system (odd numbers = P-wave, even numbers = S-wave).*

2.4 Scanning Electron Microscopy (SEM)

SEM analyses were carried out in the SEM Shared Research Facility at the University of Liverpool using a Zeiss GeminiSEM 450 field-emission gun (FEG) SEM (Figure 2.15). The Zeiss GeminiSEM is optimised for high-speed, high-resolution data acquisition, making it ideal for detailed surface imaging. It is also a state-of-the-art variable pressure FEG SEM, meaning that non-conductive and vacuum-sensitive materials can be analysed. Electron backscatter diffraction (EBSD) images were captured using a high-speed Oxford Instruments Symmetry EBSD detector, based on complementary metal-oxide semiconductor (CMOS) technology. Combined with the Aztec Oxford Instrument acquisition software, EBSD images of selected pre- and post-experimental sample surfaces are captured to qualitatively understand how the topography of simulated fault surfaces evolves with slip during frictional sliding experiments.

Before SEM analyses, sample surfaces are carbon coated using an Emitech K950X vacuum evaporator. Two carbon rods with a sharpened contact point between them are used to pass current through, causing the evaporation of carbon from the surface. This ensures a high-quality coating of carbon on post-experimental sample surfaces, making them conductive and suitable for SEM analyses (Goldstein et al., 1992). Before placing into the SEM chamber, samples are taped to the sample stage using copper tape to reduce the effect of surface charge on image capture (Goldstein et al., 1981).

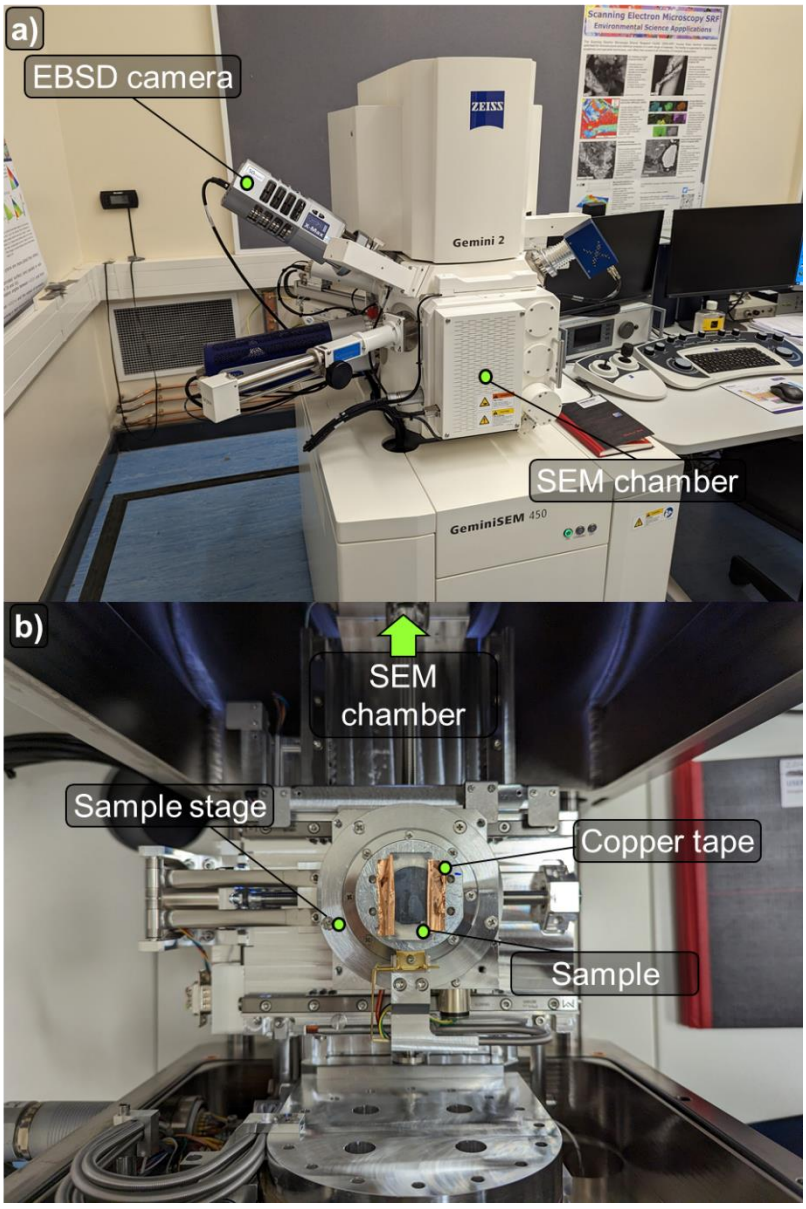

Figure 2.15: *a) The Zeiss GeminiSEM 450 field-emission gun (FEG) SEM based in the SEM Shared Research Facility at the University of Liverpool. b) Plan view of the sample before placing it into the SEM chamber.*

3 ABSOLUTE ACOUSTIC SENSOR CALIBRATION FOR ANALYSIS OF LABORATORY-GENERATED EARTHQUAKE SOURCE PROPERTIES

3.1 INTRODUCTION

Laboratory frictional sliding experiments have been used to investigate frictional properties of materials since Da Vinci who studied rotational resistance and sliding friction over 500 years ago (Hutchings, 2016). Classic frictional studies by Bowden et al. (1939) and Bowden and Tabor (1958) initiated modern studies of friction, finding that if two surfaces slide together, motion can sometimes be oscillatory rather than smooth. Surfaces 'stick', building up elastic strain energy, and then 'slip', releasing stress. This frictional process is known as stick-slip friction. Rabinowicz's (1958) study of stick-slip behaviour showed the impact of machine stiffness on whether surfaces slide stably (creep) or unstably (stick-slip). Brace and Byerlee (1966) linked frictional instability (stick-slips) to natural earthquakes, suggesting that laboratory stick-slip behaviour is analogous to shallow crustal earthquakes and thus, earthquake processes could be studied in the laboratory. By sliding two simulated fault blocks together, observed stick-slip instability at their interface has been used to simulate a variety of natural fault processes. Various authors have used the analogous behaviour of stick-slip instability to investigate topics ranging from earthquake nucleation (Harbord et al., 2017; Ostapchuk and Morozova, 2020; Shibazaki and Matsu'ura, 1998) to frictional properties (Dieterich and Kilgore, 1994; Kaproth and Marone, 2013) and earthquake source property estimation (Johnson et al., 1973; Kammer and McLaskey, 2019). Source properties estimated from laboratory experiments include seismic moment, corner frequency, stress drop and source radius (McLaskey et al., 2015).

Stick-slip is often preceded and followed by extremely small seismic events, known as acoustic emissions (AEs). AEs are acoustic wave radiation, emitted by phenomena such as frictional slip. When a material is irreversibly changed due to deformation, its structure undergoes inelastic strain which releases local stress concentrations. This emits energy in the form of AEs. AEs are associated with slip on frictional surfaces, fracturing and plastic deformation, making them useful in detecting microscale laboratory deformation (Lockner, 1993). For example, Lei et al. (2004) and Thompson, Young and Lockner (2009) observed the time-space distribution of AEs during rock fracture and discussed implications for damage creation and dynamic rupture. Moreover, AEs have been shown to follow statistical earthquake relations such as the inverse Omori law for foreshocks (S. Marty et al., 2019; Papazachos, 1973) and the Gutenberg-Richter frequency-magnitude relation (Ostapchuk and Morozova, 2020). AE waveforms visually resemble

earthquake seismograms with P- and S-wave arrivals and codas (Chapter 1, Figure 1.11; McLaskey et al., 2014).

AEs and seismic waveforms generated by stick-slip instability can be detected by piezoelectric acoustic sensors, which record events with high precision and high frequency. Piezoelectric sensors are routinely used in AE recording systems due to their simplicity in mounting to apparatus and their sensitivity in comparison to capacitive transducers (McLaskey and Glaser, 2010). Amplifiers can be incorporated into acoustic recording systems to amplify events with a low signal-to-noise ratio (SNR). Unfortunately, acoustic recording systems such as the equipment in the Rock Deformation Laboratory are commonly uncalibrated, as piezoelectric crystals are often used for more basic measurements such as simple counting of the number of AEs during experiments. The type of measurement that piezoelectric acoustic sensors record tends to also be poorly constrained, as they can behave differently depending on the frequency band e.g. as a velocimeter between 100 Hz and 10 kHz and as an accelerometer between 10 kHz and 1 MHz. This is because sensors are inertial, meaning that the natural frequency controls the transition between different measures. Below the natural frequency, displacement is measured. At around the natural frequency, velocity is measured. Above the natural frequency, acceleration is measured (Dunn et al., 2014; Hummady et al., 1997). Consequently, uncalibrated acoustic recording systems can only provide limited information, i.e. relative magnitude and frequency. This makes the physical interpretation of results difficult.

To solve this issue, absolute calibration has been carried out on the laboratory's acoustic recording system for the first time. The method of McLaskey et al. (2015) uses an external source (ball impact) to calibrate internal sources (stick-slips and AEs), relating momentum to moment. While the paper by McLaskey et al. (2015) gives a comprehensive explanation of the method, an explanation of how it was applied in Liverpool's Rock Deformation Laboratory and a modified workflow are outlined in the following sections. Experimental testing of the calibration method is presented to further demonstrate the method's advantages and limitations.

3.2 ABSOLUTE ACOUSTIC SENSOR CALIBRATION

3.2.1 Data processing workflow

Figure 3.1 outlines the workflow used to acquire and process ball drop data to calibrate the acoustic sensors, modified after McLaskey et al. (2015).

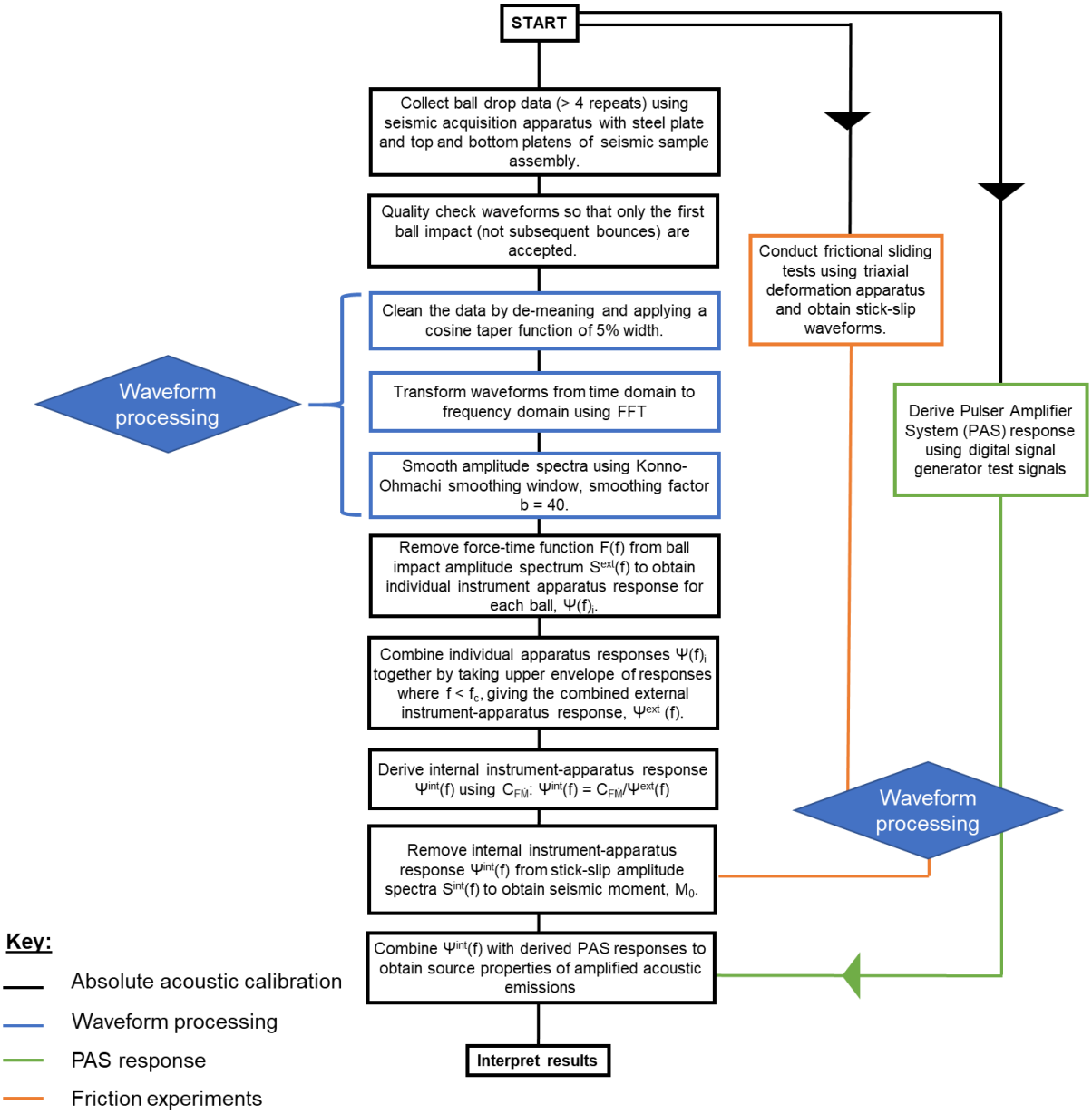

Figure 3.1: *Workflow used to acquire and process ball drop data to calibrate acoustic sensors following the method of McLaskey et al. (2015; black outline), with additional, modified steps for waveform processing (blue outline), friction experiments (orange line) and Pulser Amplifier System (PAS) response estimation (green line).*

3.2.2 Theoretical framework

Seismic wave propagation is an extremely complex phenomenon. Therefore, as previously used by McLaskey and Glaser (2012) and McLaskey et al. (2014) a simplified, idealised framework consisting of linear systems theory (which assumes a Green's function representation of wave propagation effects) is used. Several assumptions are made and are described in the sections below.

3.2.2.1 Linear system representation of seismic signals

Seismic signals can be represented as a set of linear, time-invariant systems (Hsu, 1985; Oppenheim et al., 1983). The formulation used here follows the nomenclature of McLaskey et al. (2015), where ⊗ denotes convolution in time, subscripts represent vector and tensor components, a comma between subscripts represents a spatial derivative and repeated subscripts are summed. Subscripts *int* and *ext* signify quantities relating to internal seismic sources (e.g. AEs, stick-slips and earthquakes) and external seismic sources (e.g. ball impact or meteorite impact), respectively. Internal and external seismic sources are constructed differently – internal sources act internally, enacting a moment rate on their surroundings within a body, while external sources are forces that act externally on a body. A Green's function $g_{ki}(t)$ is the impulse response of a medium or system and represents wave propagation effects such as scattering, attenuation and geometrical spreading (Aki and Richards, 1980; Stump and Johnson, 1977). Expanding this point-source about the point as a Taylor expansion (Pourahmadi, 1984), equivalent forces which compromise the seismic source are represented by force vector f_i and moment tensors of increasingly high order (e.g. $m_{ij}, m_{ijl}, m_{ijlm}$ etc.). Therefore, ground displacement as a function of time $u_k(t)$ can be described by the following formulation for both internal and external sources:

$$u_k(t) = g_{ki}(t)\otimes f_i(t) + g_{ki,j}(t)\otimes m_{ij}(t) + g_{ki,jl}(t)\otimes m_{ijl}(t) + g_{ki,jlm}(t)\otimes m_{ijlm}(t) + \cdots. \quad (3.1)$$

For internal sources, where linear momentum is conserved, $f_i = 0$. While higher order terms (greater than order 2) also contribute to $u_k(t)$, McLaskey et al. (2015) deem them as negligible due to their relatively small contribution to $u_k(t)$ in comparison to the second term, $g_{ki,j}(t)\otimes m_{ij}(t)$. Consequently, only the second term of the Taylor expansion applies:

$$\mathrm{u}_k^{int}(t) = g_{ki,j}^{int}(t)\otimes m_{ij}^{int}(t) = s^{int}(t)\otimes i_k^{int}(t)^{-1}, \quad (3.2)$$

where $g_{ki,j}^{int}(t)$ is the Green's function of the internal event, $m_{ij}^{int}(t)$ is the internal seismic source (also known as the moment tensor), $s^{int}(t)$ is a recorded internal signal (e.g. a stick-slip or AE) and $i_k^{int}(t)$ is the internal instrument response function.

As linear momentum is not conserved for externally acting sources such as ball impacts or meteor impacts, the formulation for ground displacement uses the first term of the Taylor series expansion:

$$\mathrm{u}_k^{ext}(t) = g_{ki}^{ext}(t) \otimes f_i(t) = s^{ext}(t) \otimes i_k^{ext}(t)^{-1}, \tag{3.3}$$

where the force time vector $f_i(t)$ represents the seismic source. $s^{ext}(t)$ is the recorded external signal (e.g. a ball impact) and $i_k^{ext}(t)$ is the external instrument response function.

3.2.2.2 Hertzian impact theory

The impulsive force with which a ball acts on a massive body can be described by Hertzian impact theory. The theory has previously been described in detail (Goldsmith, 2001; Love, 1927; McLaskey and Glaser, 2010) and so only a summary will be outlined in this thesis.

The impulsive force (force pulse, or force-time function) a ball imparts when dropped onto a massive body can be approximated by a 'half sine' pulse (Hunter, 1957):

$$f_H(t) = f_{H\,max} sin\left(\frac{\pi t}{t_c}\right), \qquad 0 \leq |t| \leq t_c \tag{3.4}$$

$$f_H(t) = 0, \qquad |t| \geq t_c, \tag{3.5}$$

where $f_{H\,max}$ is the maximum force a ball imparts, t is time and t_c is the contact time:

$$t_c = 4.53\left(\frac{4\rho_1\pi(\delta_i + \delta_j)}{3}\right)^{\frac{2}{5}} R_1 {v_0}^{\frac{-1}{5}}. \tag{3.6}$$

In Equation 3.6, the material parameter $\delta_{i,j} = \frac{1-\nu_{i,j}^2}{\pi E_{i,j}}$, where ν and E are the Poisson's ratio and Young's modulus respectively. Subscripts i and j refer to the two different bodies in contact: in this work, $i = 1$ refers to the material of the steel balls (S420 steel), $i = 2$ the material of the ceramic balls (aluminium oxide, Al_2O_3 ceramic), $j = 3$ the material of the seismic assembly (17-4PH, Rockwell C45, H900 steel) and $j = 4$ the material of the steel calibration plate (S275 steel). For example, for a steel ball impacting on the steel calibration plate, the equation is as follows:

$$t_c = 4.53\left(\frac{4\rho_1\pi(\delta_1 + \delta_3)}{3}\right)^{\frac{2}{5}} R_1 {v_0}^{\frac{-1}{5}}.$$

ρ_1, R_1 and v_0 are the radius, density and approach velocity of the ball respectively. At the initiation of contact between the ball and the material surface, $t = 0$.

While the calculations of Hunter (1957) use Newton's second law, in practice, when two bodies come into contact, energy dissipates due to elastic wave propagation. Reed (1985) presented a correction to Hunter's calculation by using force relation $f = k_1 \alpha^{3/2}$, where k_1 is a constant which depends on the material and geometrical properties of the two bodies and α is the distance of approach of the centres of the bodies when they are in contact. In this case, force can be defined by the following:

$$f(t) = f_{max} sin\left(\frac{\pi t}{t_c}\right)^{\frac{3}{2}}, \qquad 0 \leq |t| \leq t_c \tag{3.7}$$

$$f(t) = 0, \qquad |t| \geq t_c, \tag{3.8}$$

where the maximum force is defined by:

$$f_{max} = 1.917 \rho_1 \pi \left(\delta_i + \delta_j\right)^{\frac{-2}{5}} {R_1}^2 {v_0}^{\frac{6}{5}}. \tag{3.9}$$

Figure 3.2 details the two variations of force pulses using Hunter's and Reed's 'half sine' and '$\sin^{3/2}$' pulses respectively. Figure 3.2a shows an exemplar force-time function (17 mm steel ball) normalised by t_c and f_{max}, while Figure 3.2b shows a Fast Fourier transform (FFT) of the force-time function, normalised by t_c. The shape of the force-time function's Fourier spectra forms a series of lobes with the locations of zeroes highlighting frequencies with negligible or no spectral amplitude.

Appendix 3.5.1 outlines the material properties used to calculate theoretical Hertzian force-time functions for calibration using f_{max} and t_c.

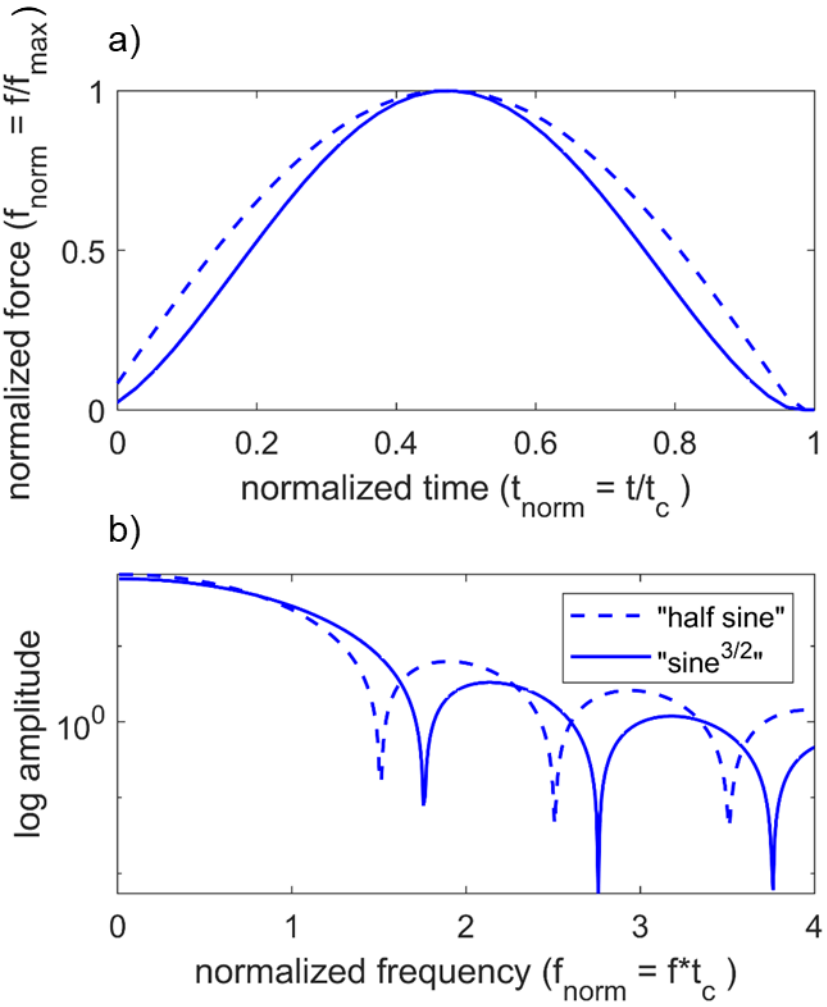

Figure 3.2: *Force pulses derived from 'half sine' (dashed line) and 'sin$^{3/2}$' (solid line) Hertzian impact laws. a) shows the force-time function while b) shows its Fourier transform. After McLaskey and Glaser (2010).*

3.2.2.3 Empirical Green's functions

The method of McLaskey et al. (2015) uses the theory that an empirical Green's function (EGF) can be removed from seismograms (Abercrombie, 1995; Mueller, 1985). In seismology, EGFs enable the calculation of spectral ratios and deconvolved source-time functions, allowing for both spectral and time-domain source modelling (Abercrombie, 2021). With this theory, the source properties of one seismic event are estimated using another, small, collocated event with an assumed or known source function as a reference. For McLaskey et al.'s calibration method, instrument effects are not separated from wave propagation effects or radiation geometry. Instead, these effects are combined into what is known as an internal instrument-apparatus response function $\psi^{int}(t)$ for a chosen internal source (e.g. a stick-slip) signal $s^{int}(t)$ and source moment-rate, $\dot{m}(t)$:

$$\psi^{int}(t) \equiv s^{int}(t) \otimes \dot{m}(t)^{-1} = \Lambda_{ij} \int g^{int}_{ki,j}(t)dt \otimes i^{int}_{k}(t), \quad (3.10)$$

where the time integral arises due to the time derivative associated with $\dot{m}(t)$. Λ_{ij} is a vector that defines the time history of the source, with the sum of the squares of its eigenvalues equal to 2 (Bowers and Hudson, 1999). $g^{int}_{ki,j}(t)$ is the Green's function of an internal source and $i^{int}_{k}(t)$ is the internal instrument response. For external sources, the external instrument-apparatus response $\psi^{ext}(t)$ can be described as follows:

$$\psi^{ext}(t) \equiv s^{ext}(t) \otimes f(t)^{-1} = \Xi_i g^{ext}_{ki}(t) \otimes i^{ext}_{k}. \quad (3.11)$$

$s^{ext}(t)$ is the external source signal (e.g. the recorded signal of a ball impact)and Ξ_i is a vector of unit length that defines the time history (Bowers and Hudson, 1999). $g^{ext}_{ki}(t)$ is the Green's function of an external source and i^{ext}_{k} is the external instrument response.

In the EGF theory, two collocated events are recorded by the same instrument and their focal mechanism are assumed identical. In this study, two events are compared: the EGF source $\psi^{EGF}$and the test source ψ^{test}. Consequently:

$$\psi^{EGF} = \psi^{test}. \quad (3.12)$$

To solve for moment tensor source $\dot{m}^{test}(t)$, the instrument-apparatus response function ψ^{EGF} is obtained from recorded signals $s^{EGF}(t)$ using Equation 3.10. The properties of this EGF source $\dot{m}^{EGF}(t)$ are known or assumed. Following this, Equation 3.12 is substituted into Equation 3.10 so that the source of a test event $\dot{m}^{test}(t)$ can be obtained from recorded signals $s^{test}(t)$.

For AEs and stick-slips, the absolute magnitude of potential EGF and test events are unknown. To solve this issue, in the method of McLaskey et al. (2015), the EGF method is adapted so that a ball impact acts as an EGF source, as the absolute magnitude and source spectrum of a ball impact is well known through using Hertzian Theory. However, while a ball impact source $f_i(t)$ acts externally to the body, the AE or stick-slip source $\dot{m}_{ij}(t)$ acts internally, requiring an expression to relate internal and external sources which is described in Section 3.2.2.4.

3.2.2.4 Ball impact and earthquake spectra: relating momentum to moment

Seismic sources can also be described by the characteristics of their frequency spectra. The Fourier transforms of an external force, $f(t)$, or an internal moment rate, $\dot{m}(t)$, can be used to estimate the source properties of seismic sources by averaging over the whole-time window. While the spectra amplitude is used, phase information is often ignored.

Figure 3.3 describes the key features of source spectra of internal (e.g. AEs, stick-slips and earthquakes) and external (e.g. ball drop impact) sources. For both types of sources, spectra have a characteristic corner frequency f_0 which is inversely proportional to the duration of the nonzero part of $f(t)$ or $\dot{m}(t)$, i.e. the rise time, $t_{1/2}$. For frequencies $f < f_0$, spectra have a long-period amplitude of Ω_0 and are flat. For frequencies $f > f_0$, spectra undergo a high-frequency decay of $\left(\frac{f}{f_0}\right)^{-\gamma}$ and fall below Ω_0.

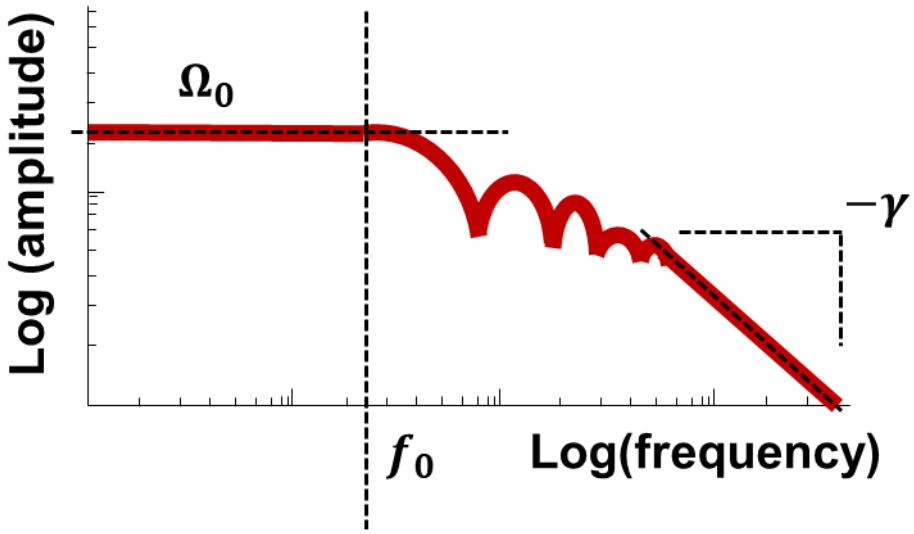

Figure 3.3: *Key features of internal and external seismic sources' frequency spectra. Long-period amplitude Ω_0 begins to fall off at corner frequency f_0 with a decay constant of $-\gamma$. After Brune (1970).*

For internal sources, Ω_0 is proportional to the scalar seismic moment M_0, which is the time integral of $\dot{m}(t)$. Likewise, for ball impact sources, Ω_0 is proportional to the change in momentum Δp the ball imparts on the impact surface, which is the time integral of $f(t)$, the force a ball imparts on the impact surface. At low frequencies, the frequency domain of both internal sources, $\dot{M}(f)$ and external sources, $F(f)$ can be described as such:

$$\dot{M}(f) = M_0 \qquad f \ll f_0 \tag{3.13}$$

and

$$F(f) = \Delta p \qquad f \ll f_0. \tag{3.14}$$

This description of internal and external sources in the frequency domain can be used to transform signals from the time domain to the frequency domain using the derivative theorem and Fourier transform (Bracewell, 2000). Following this, the internal instrument-apparatus response in the frequency domain, $\Psi^{int}(f)$, can be written using Equation 3.10:

$$\Psi^{int}(f) \equiv \frac{S^{int}(f)}{\dot{M}(f)} = \frac{\Lambda_{ij} G^{int}_{ki,j}(f) I^{int}_{k}(f)}{i2\pi f}. \quad (3.15)$$

The terms in this equation are as in Equation 3.10, with capitalisations representing each term in the frequency domain (Bracewell, 2000).

For an external source, the external instrument-apparatus response $\Psi^{ext}(f)$ can be defined as follows:

$$\Psi^{ext}(f) \equiv \frac{S^{ext}(f)}{F(f)} = \Xi_i G^{ext}_{ki}(f) I^{ext}_{k}(f), \quad (3.16)$$

The terms in this equation are as in Equation 3.11, with capitalisations representing each term in the frequency domain (Bracewell, 2000).

At low frequencies, the spectra of $F(f)$ and $\dot{M}(f)$ are flat: McLaskey et al. (2015) use this observation to relate them to a constant, under certain conditions. To relate the properties of internal seismic sources to external seismic sources, they assume that an unknown seismic moment M_0 of an internal source causes the same ground displacement $u_k(t)$ as an external source with a known change in momentum, Δp. In this case, where $u^{ext}_k(t) = u^{int}_k(t)$, the scale factor for force-moment-rate $C_{F\dot{M}}$ is defined:

$$C_{F\dot{M}} \equiv \frac{\dot{M}(f)}{F(f)} = \frac{\dot{m}(t)}{f(t)} = \frac{M_0}{\Delta p} \qquad f < f_0. \quad (3.17)$$

$C_{F\dot{M}}$ has the same units as velocity (m/s) and can be derived theoretically and empirically, with the former method being used in this thesis (Section 3.2.11). $C_{F\dot{M}}$ transforms the external instrument-apparatus response $\psi^{ext}(t)$ to the internal instrument-apparatus response $\psi^{int}(t)$ by converting momentum to moment. This scalar conversion is both time and frequency independent. $C_{F\dot{M}}$ relates the force-time function of an external seismic source (ball impact) to the moment-rate function of an internal seismic source (stick-slip or AE). To convert $\psi^{int}(t)$ to $\psi^{ext}(t)$, Equation 3.17 is substituted into Equation 3.10:

$$s^{int}(t) = C_{F\dot{M}} f(t) \otimes \psi^{int}(t). \quad (3.18)$$

In the case of this study and McLaskey et al. (2015), we assume the case of Equation 3.12. This assumes that internal and external sources have the same ground displacement ($u^{ext}_k(t) = u^{int}_k(t)$), are recorded on the same instrument ($i^{ext}_k(t) = i^{int}_k(t)$) and have the same recorded signal ($s^{ext}(t) = s^{int}(t)$). Consequently, Equations 3.11 and 3.18 can be equated:

$$\psi^{ext}(t) = C_{F\dot{M}}\psi^{int}(t). \tag{3.19}$$

In the frequency domain, this becomes:

$$\Psi^{ext}(f) = C_{F\dot{M}}\Psi^{int}(f) \qquad f < f_0 \tag{3.20}$$

Therefore, these equations can be used to relate the properties of internal to external seismic sources. For instance, the seismic moment of an earthquake can be used to calculate the seismic moment of a collocated meteorite impact which would create the same low-frequency ground motions.

3.2.2.5 Summary of method and limitations

To summarise, the technique uses an external impact (ball drop impact) to derive the internal instrument-apparatus response $\Psi^{int}(f)$ of the seismic sample assembly and acoustic sensors, a combination of instrument and path effects. Below the corner frequency f_0, the ball drop can be thought of as a reference source where its known source properties (i.e. force-time function) are used to estimate the source properties of a different, collocated event. Force (momentum) and moment can be related mathematically using a constant force-moment-rate scale factor, $C_{F\dot{M}}$. This method can be used to calibrate an entire acoustic recording system (i.e., seismic sample assembly, acoustic sensors and amplifiers).

While the method is robust and has been used to estimate seismic moments by various authors (e.g. McLaskey and Yamashita, 2017; Wu and McLaskey, 2019; Wu et al., 2019), the uncertainty in moment magnitude estimated by McLaskey et al. (2015) is around ± 0.2 magnitude units. This uncertainty is thought to be caused by various assumptions, such as $\Psi^{ext}(f) = C_{F\dot{M}}\Psi^{int}(f)$ and the corner frequency of an event considering the reliable frequency band of the acoustic sensor. These limitations will be considered when interpreting calibrated results (Chapter 4; Section 4.4.3).

3.2.3 Ball drop experimental design

Two different calibration setups (Figure 3.4) are used to compare geometric effects on measured waveforms: a simple, steel plate and a more geometrically complex seismic assembly, used within the vessel during frictional sliding experiments. Both calibration setups are connected through electrical cabling to the seismic acquisition apparatus (Chapter 2; Sections 2.2.3 and 2.3).

Figure 3.4: *Calibration setup (steel plate or seismic assembly) connected to seismic acquisition apparatus for ball drop experiments.*

A variety of ball sizes (1 – 20 mm diameter) and materials (S420 steel and aluminium oxide, Al_2O_3 ceramic) were used to obtain a suite of impact spectra, across a broad frequency range. Using an electromagnet (1.8 kg pull, 12V DC/1.4 W) held in place by a clamp stand, steel balls are held at a height of 95.5 mm above the surface of the steel plate and the top or bottom platen of the seismic assembly. By switching off the electromagnet, balls are automatically dropped onto the surface. Aluminium oxide balls are hand-held at a height of 95.5 mm, with much care taken to drop the ball directly above the sensor. Seismic waves radiated from the ball's impact point propagate throughout the sample and are recorded by piezoelectric crystals (Chapter 2; Figure 2.2). Switching the electromagnet on and off generates some electrical noise, which triggers the data acquisition software. However, the time between the electromagnet noise and the ball impact event is separated by enough time (> 200 ms) that the electromagnet does not contaminate the recorded signal of ground motion.

Approach velocity v_0 is calculated using one of the equations of motion based on Newton's Second Law, ${v_0}^2 = u^2 + 2as$. u is the initial velocity (0 m/s), a is the gravitational acceleration (9.81 m/s²) and s is the height that the ball drops, 95.5 mm. Therefore, $v_0 = 1.37$ m/s. Air resistance is not included in the calculation of approach velocity as the flight times of the balls are extremely short: 140 ms, calculated using $v = u + at$, rearranged to $t = \frac{v-u}{a}$ (Zayas, 1986). Material properties are derived online from material property pages (AZoM, n.d.).

Table 3.1 details all balls used in acoustic sensor calibration and calculated values of F_{max} and t_c for both the seismic assembly and the steel calibration plate. Each ball drop is repeated at least five times to ensure repeatability before stacking.

3.2.3.1 *Error propagation*

Errors are either derived from material property pages (e.g. AZoM, n.d.) or estimated using reasonable values considering absolute values. The following errors are propagated using standard propagation of uncertainty equations (e.g. Bevington and Robinson, 2003): ball density, ρ = ± 200 kg/m^3; ball diameter, R_1 = ± 0.1 mm; approach velocity, v_0 = ± 0.1 m/s; Poisson ratio, ν = ± 0.03; Youngs Modulus, E = ± 15 GPa.

Table 3.1*: Sizes, materials, maximum impact force and contact times of balls used within ball drop experiments.*

Ball diameter (mm)	Material	F_{max}, seismic assembly (N)	F_{max}, steel plate (N)	t_c, seismic assembly (µs)	t_c, steel plate (µs)
1.0 ± 0.1	Steel	6.16 ± 1.09	6.26 ±1.10	3.29 ± 0.108	3.24 ± 0.104
1.5 ± 0.1	Steel	13.8 ± 2.44	14.0 ±2.48	4.94 ± 0.163	4.84 ± 0.157
2.0 ± 0.1	Steel	24.5 ± 4.34	24.9 ±4.41	6.60 ± 0.217	6.48 ± 0.210
3.0 ± 0.1	Steel	54.7 ± 9.74	55.6 ±9.90	9.91 ± 0.327	9.74 ± 0.315
4.0 ± 0.1	Steel	96.7 ± 17.3	98.3±17.6	13.2 ± 0.438	13.0 ± 0.422
6.0 ± 0.1	Steel	215 ± 39.8	218 ± 39.5	19.9 ± 0.661	19.6 ± 0.638
8.0 ± 0.1	Steel	377 ± 68.9	383 ± 70.0	26.6 ± 0.889	26.1 ± 0.857
17.0 ± 0.1	Steel	1590 ± 308	1620 ± 313	57.0 ± 1.96	56.1 ± 1.89
19.0 ± 0.1	Steel	1960 ± 383	1990 ± 390	63.9 ± 2.21	62.9 ± 2.13
20.0 ± 0.1	Steel	2160 ± 424	2190 ± 431	67.3 ± 2.34	66.3 ± 2.26
10.0 ± 0.1	Ceramic	394 ± 73.8	401 ± 74.6	23.5 ± 0.959	23.0 ± 0.793
16.0 ± 0.1	Ceramic	966 ±187	984 ±189	37.8 ± 1.57	37.1 ± 1.30

3.2.3.2 *Data acquisition parameters*

CecchiLeach data acquisition software (Itasca Denver Inc.) is used to monitor seismic events. The CecchiLeach system can acquire data at high speed, with 10 MHz, 12-bit full-waveform acquisition at 128 kilo-samples per channel. When the ball impacts the surface of the steel plate, top or bottom platen of the seismic assembly, the system triggers when above the Trigger Level which is 1% of the Full-Scale Volts (FSV, Table 3.2 and Chapter 2, Section 2.3). The ball impact triggers the system to record, acquiring seismic waveforms. FSV is increased as ball mass increases, as higher ball masses generated larger signals, requiring FSV to be increased so that signals are not clipped. A Trigger Ratio of 0.25 is used to record a quarter of the waveform length as noise before the event. .atf files (Appendix 3.5.2) for each recording are obtained for processing. This process is repeated to obtain a minimum of five signals per ball with good SNR. Table 3.2 outlines the parameters used to obtain ball impact recordings.

Table 3.2: *Parameters of CecchiLeach seismic acquisition software used to record waveforms.*

Parameter (unit)	Value
Sampling Frequency (Hz)	10 MHz
Waveform Length	65536
Full-Scale Volts (V)	200 mV – 20 V
Trigger Source	Channels 1 and 2
Trigger Level	1
Receivers	Channels 1 and 2
Trigger Ratio	0.25

3.2.4 Steel plate

A 150 mm x 150 mm x 25 mm block of S275 steel was machined with curved corners to reduce high-frequency artefacts and finished with surface grinding to ensure minimal friction between the ball and the surface (Figure 3.5). A thickness of 25 mm is chosen to allow plate results to be comparable to seismic assembly results, as the seismic assembly platens have a similar thickness (24mm). The idea behind using the steel plate was that it would minimise internal reflections in comparison to the seismic assembly, which is geometrically more complex and much smaller. Using both allows a comparison of the signal to assess the effect of internal reflections on the analysis.

After marking the centre of the base of the plate, two 180° semi-circles of porous steel are glued on either side of the centre point with silver-loaded epoxy, acting as backing for the piezoelectric crystals to reduce wave attenuation. Next, this backing material is glued to the backs of the 180° P- and S-wave piezoelectric crystals (PZT-5H, fundamental frequency = 1.5 MHz, Boston Piezo-Optics Inc.), i.e. on the side opposite to where the signal arrives. It should be noted that the crystals are identical to those held within the platen of the seismic sample assembly (Chapter 2, Figure 2.2). The piezoelectric crystals are made of lead-zirconate-titanate (PZT) and are overtone polished to limit the energy loss at higher harmonic frequencies (e.g. 9th overtone, 11th overtone; Berlincourt, 1971). The crystals are gold coated for electrical connectivity at the top and bottom surfaces of each crystal. A copper backing is epoxied, using the silver-loaded epoxy resin, to each crystal and soldered to two coaxial cables, each with a BNC connector attached to connect the plate to the digital oscilloscope. A 4 mm-deep hole is drilled and tapped into one side of the plate, fitted with an M4 screw and connected via a grounding cable from the plate to both P- and S-wave BNC connectors to earth the crystals to the plate to complete the circuit.

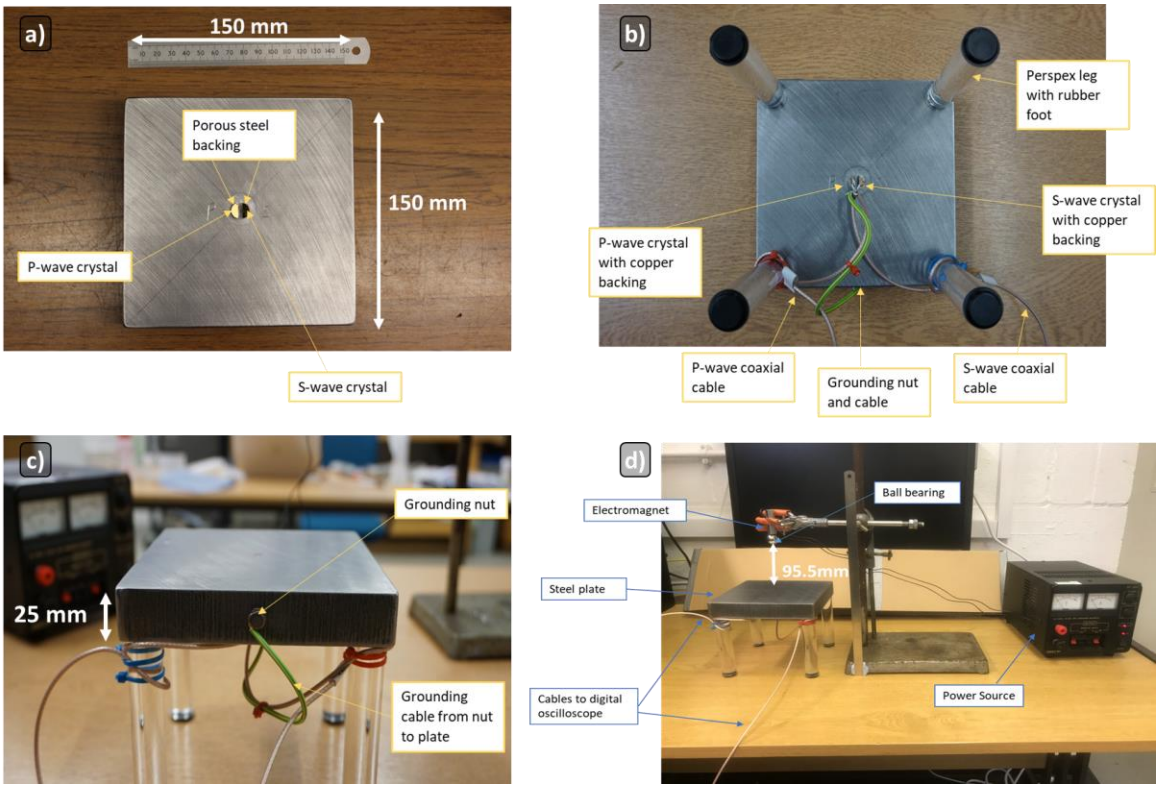

Figure 3.5: *Steel plate calibration setup. a) Semi-circular 180° P- and S-wave piezoelectric crystals are glued with silver-loaded epoxy onto 180° porous steel backing blocks, which are glued to the plate. b) Copper backing is glued onto each crystal and soldered to coaxial cables. c) Zoom of grounding nut which grounds the crystals to the plate via another coaxial cable. d) Steel plate calibration setup as referenced in Figure 3.4.*

3.2.5 Seismic sample assembly

To calibrate the piezoelectric crystals held within the seismic sample assembly (Chapter 2; Figure 2.2), the top and bottom platens of the seismic sample assembly are held by a vice (Figure 3.6). The vice is secured to the table-top with double-sided adhesive to reduce external changes in momentum, such as within the vice, or between the vice and the desk.

It should be noted that this calibration configuration reflects that of the second example of McLaskey et al. (2015), where the ball impacts and stick-slip/AE events are not precisely collocated. For accessibility, ball impacts occur on the top surface of the platens, whereas experimental stick-slip and AE events occur on the simulated fault between two plates of PMMA. Consequently, the signal may be modified slightly by the wavefield having to propagate through a small thickness of PMMA and also through the stainless steel of the direct shear slider assembly (Chapter 4, Figure 4.1). While this may decrease the method's accuracy, the technique has been validated as useful for estimating general features of source spectra (Kammer and McLaskey, 2019; McLaskey and Yamashita, 2017; Wu and McLaskey, 2019).

When assembled, the seismic assembly (and in particular, the PZT crystals and backing material) is under atmospheric pressure in laboratory conditions, rather than being contained within the high-pressure environment of the triaxial deformation apparatus. Therefore, the only difference between the measurements described in this chapter and those under experimental conditions in Chapters 4 and 5 is that the seismic assembly is under load. As we assume that the steel that the seismic assembly is composed of is linearly elastic, the application of confining pressure will not affect the elastic properties. Thus, waveform propagation should not be affected by confining pressure, meaning that absolute acoustic calibration in laboratory conditions should be a good approximation of the assembly under test conditions. This is advantageous in terms of pressure sensitivity in comparison to McLaskey et al.'s (2015) setup, which drops balls into a drilled cavity within a cylindrical sample of granite that is surrounded by PZTs, as granite is not linearly elastic. McLaskey et al. (2015) found that confining pressure has a negligible effect on acoustic sensor response, depending on resonant peaks at 5 – 500 kHz. They suggest that bench-top calibrations, such as in this study, are adequate for acoustic calibration, justifying the method's use.

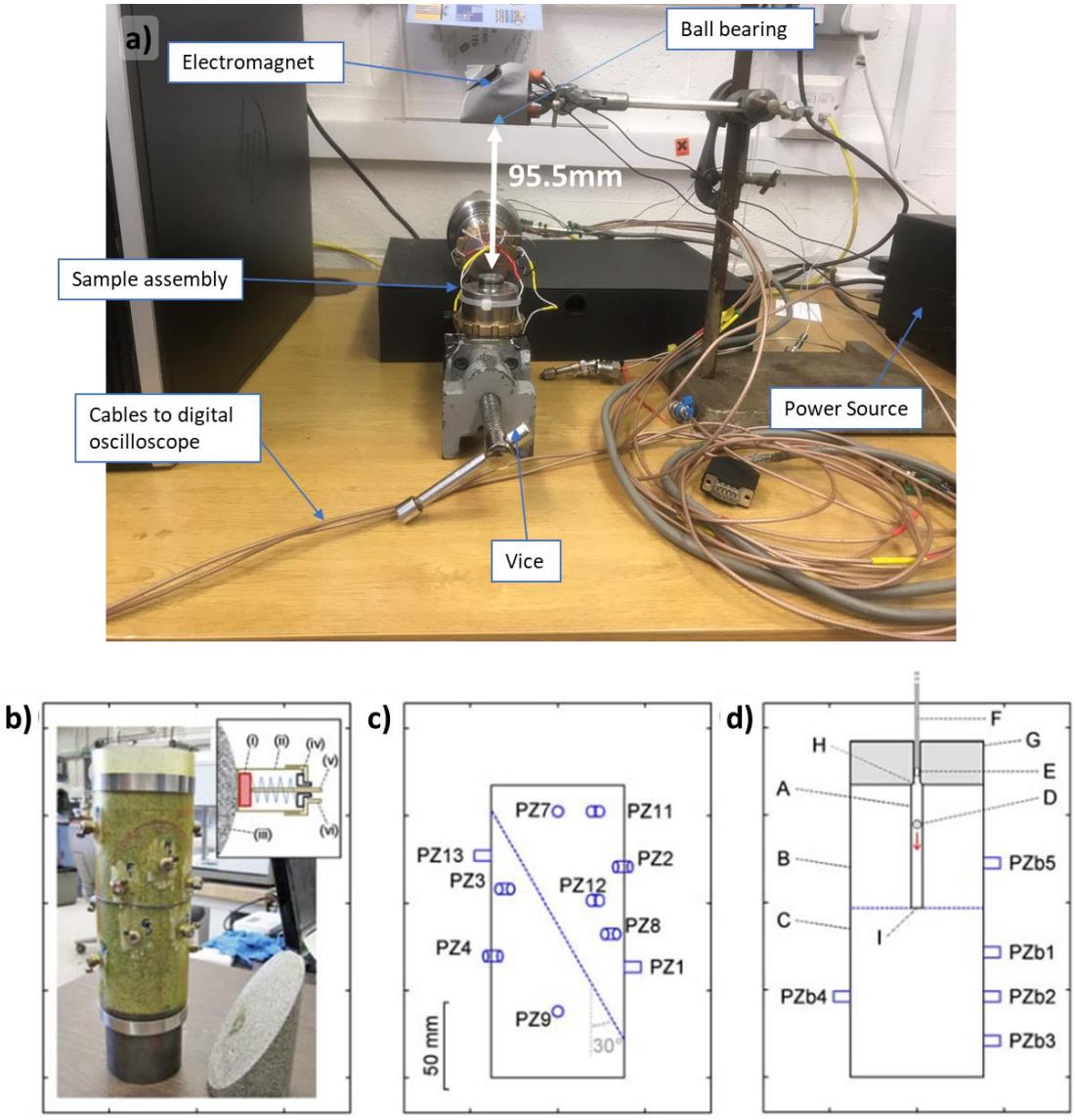

Figure 3.6: *a) Seismic assembly calibration setup for the bottom platen of the seismic sample assembly in Liverpool's Rock Deformation Laboratory. b-d) McLaskey et al.'s (2015) setup. b) Granite sample and sensors. c) Schematic of the test sample, showing a saw cut 30° simulated fault. d) Calibration sample where the ball is dropped. After McLaskey et al. (2015).*

3.2.6 Ball drop signals

Signals are recorded via CecchiLeach software as .atf data files (Appendix 3.5.2), which are processed using Matlab codes *balldrop_process.m*, *balldrop_spectra.m* and *main_v2.m*.

Seismic signals measured from repeated 17 mm steel and 16 mm ceramic diameter ball drop experiments on the steel plate and bottom platen of the seismic sample assembly are shown in Figures 3.7 and 3.8. Repeated ball impacts show that signals are highly consistent, allowing for the stacking of signals which averages the signal and reduces incoherent noise. Further waveform

detail can be observed in Figure 3.9, which shows the same repeated 17 mm ball impacts as Figure 3.8b overlain.

Comparing steel plate (Figure 3.7) and seismic assembly (Figure 3.8) signals, the seismic assembly appears to add more complexity through additional reflections. Moreover, seismic assembly signals have higher amplitudes (around a factor of 2) than steel plate signals. This could be due to constructive interference from internal reflections with shorter periods within the seismic assembly due to its complex geometry (Chapter 2; Figure 2.2). These results highlight the need to calibrate acoustic systems absolutely, as even with the thickness of the plate and seismic assembly platen being similar (~25 mm), there are significant differences between signals measured on the two different apparatuses.

It should be noted that all waveforms presented in this section are P-waves – examples of S-waves waveforms are presented in the digital appendix.

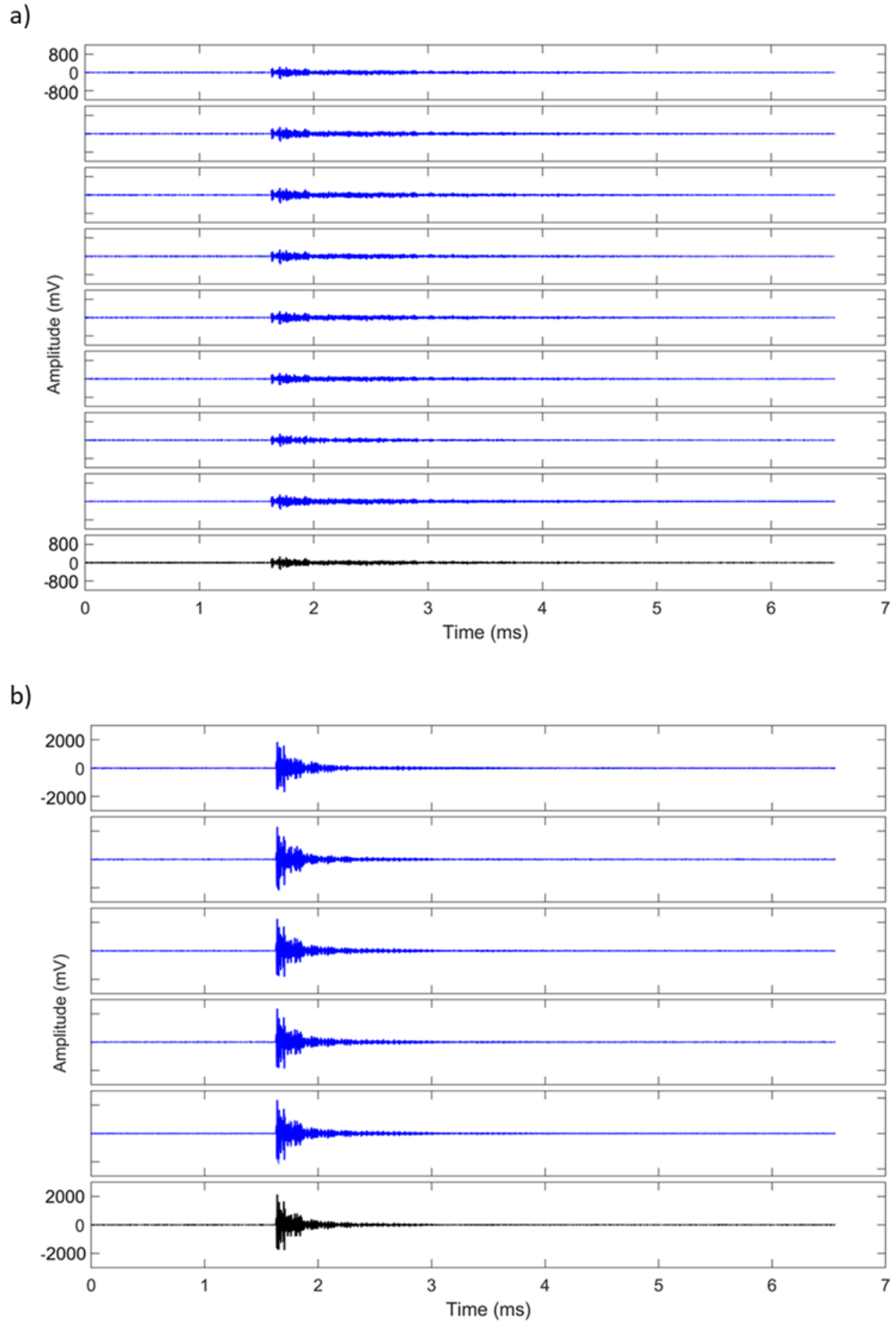

Figure 3.7: *Repeated (blue) and stacked (black) raw time series signals (before removal of linear trend and tapering) of a) 3mm steel and b) 16mm ceramic ball impacts on the steel plate.*

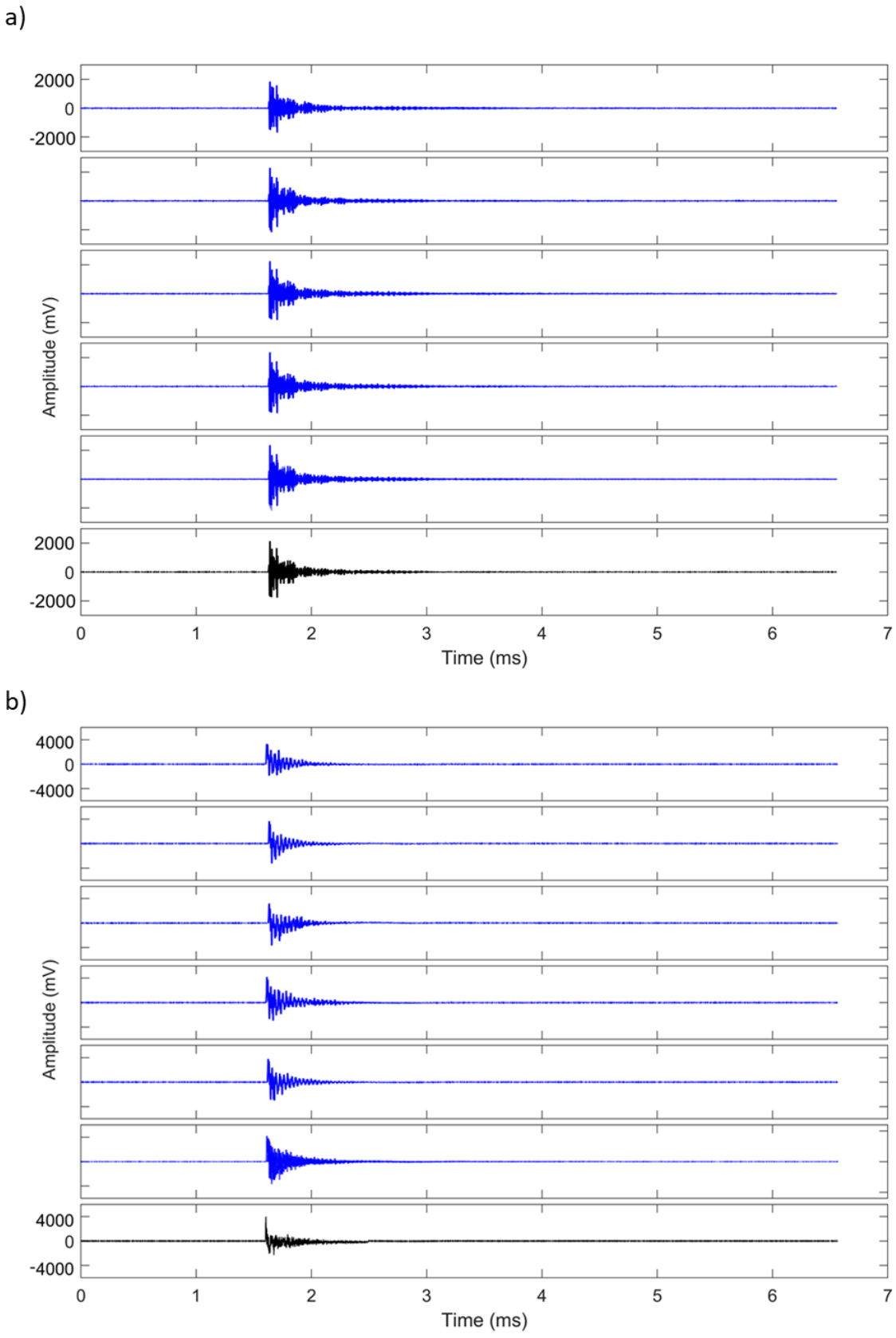

Figure 3.8: *Repeated (blue) and stacked (black) raw time-series signals of a) 3mm steel and b) 16mm ceramic ball impacts on the bottom platen of the seismic sample assembly.*

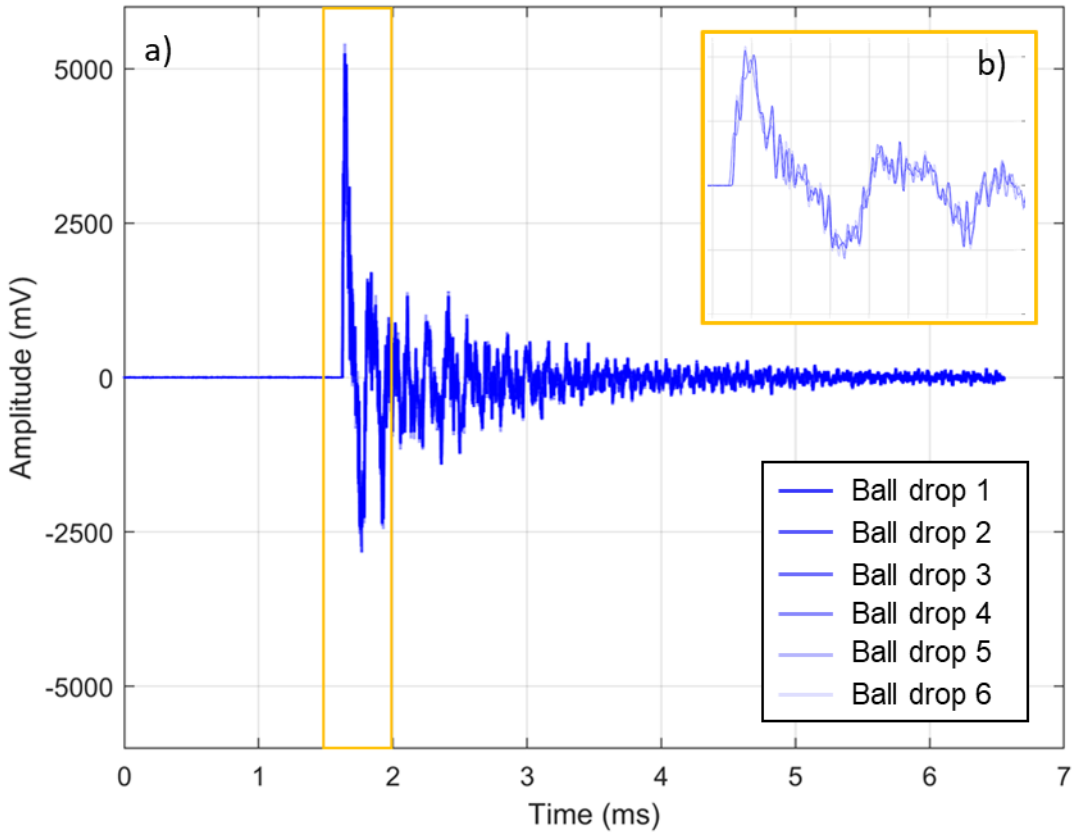

Figure 3.9: *a) 6 repeated raw time series of 17mm steel ball impact on the steel plate overlain with extent (yellow box). b) A more detailed plot of the 6 overlain signals, with darkness decreased with each repeat.*

3.2.7 Ball impact spectra, $S(f)$ and individual instrument-apparatus responses, $\Psi(f)_i$

Raw ball impact time series are de-meaned to remove any linear trends. Following this, a cosine taper of 5% width is applied so that Fast Fourier Transforms (FFTs) are not a function of the initial and final data points. Ball impact time series and subsequent stacks are transformed to the frequency domain using an FFT. The FFT routine applies a Konno-Ohmachi smoothing window (Konno and Ohmachi, 1998) to smooth amplitude spectra in the logarithmic scale, with a smoothing factor b = 40. For lower frequencies, the Konno-Ohmachi smoothing window is narrower with less smoothing, while at higher frequencies, the window is wider with more smoothing. This is desirable as spurious frequency peaks are smoothed, leaving only key fundamental frequencies (Konno and Ohmachi, 1998). The width of the smoothing window is determined by a weight function, $W(f)$, that depends on the signal's corner frequency, f_0, calculated using the following equation with smoothing factor b:

$$W(f) = \left[\frac{\sin\left(\left(\log_{10}{}^{f}/_{f_0}\right)\right)^{b}}{\left(\log_{10}{}^{f}/_{f_0}\right)^{b}}\right]^{4}. \qquad (3.21)$$

Following this, the weights are multiplied by the unsmoothed Fourier spectrum, ensuring that the ratios are normal distributions in the logarithmic space. The effect of Konno-Ohmachi smoothing on the Fourier Amplitude Spectrum (FAS) of the signal of the 17 mm ball drop on the steel plate is shown in Figure 3.10.

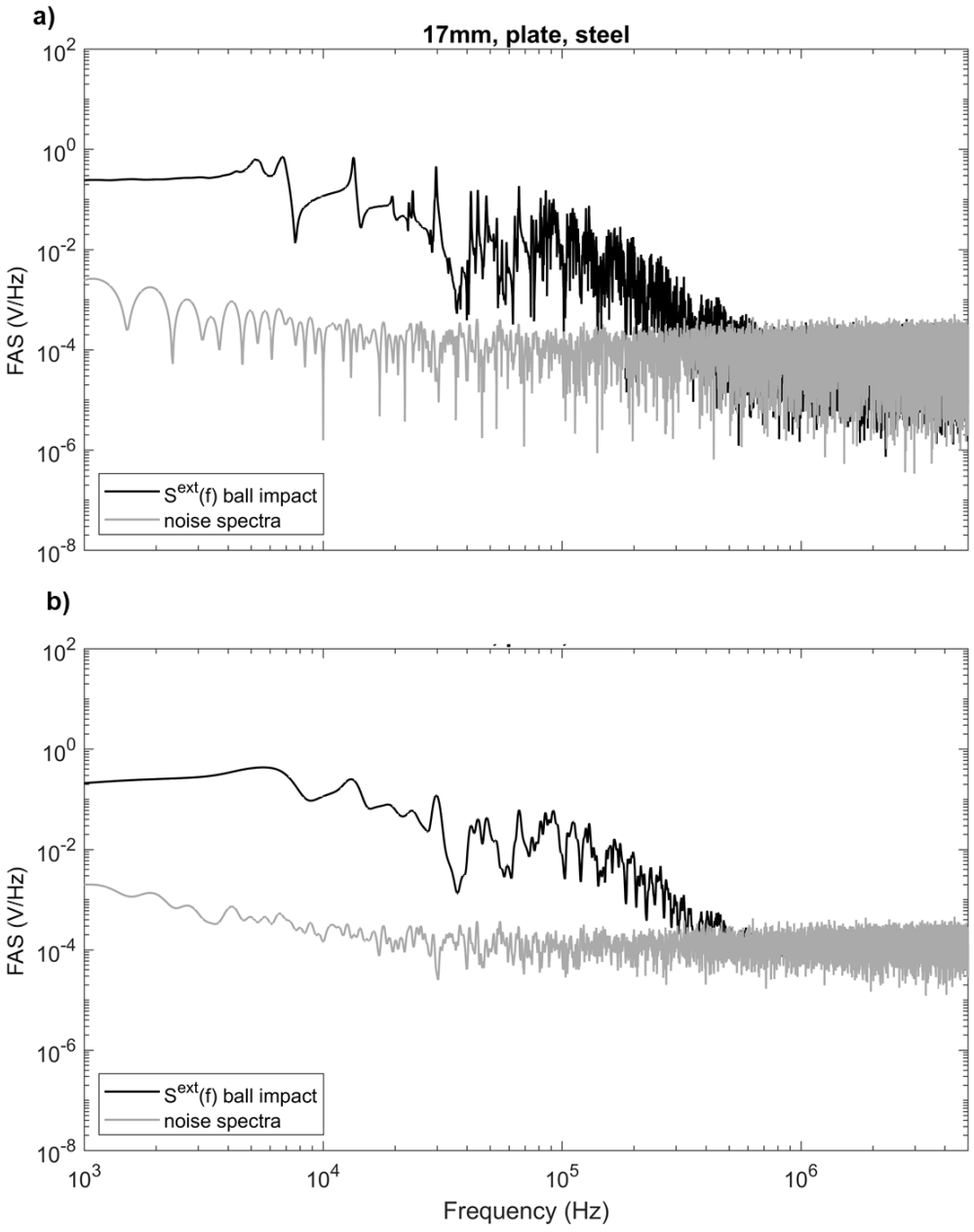

Figure 3.10: *Fourier Amplitude Spectrum of the 17 mm steel ball impact on the steel plate, a) unsmoothed and b) smoothed using the Konno-Ohmachi (1998) method, b = 40. Black lines are signal spectra and grey lines are noise spectra.*

The first 25% of the stacked time series is considered noise (Section 3.2.3.2) and therefore, only spectra with SNR > 3 are kept ('good' SNR, Figures 3.11 – 3.13). Spectra show good repeatability with repeated ball impacts. Following section 3.2.2.2, theoretical Hertzian force-time functions ($F(f)$, Figure 3.2, and blue dotted lines in Figure 3.11 – 3.13) are transformed via an FFT for each ball. Theoretical Hertzian force-time functions are normalised to the signal amplitude for plotting so that differences between the theoretical and measured frequency content can be observed. To reduce uncertainty, only frequencies below f_0 are accepted for deriving the external instrument-apparatus response, $\Psi^{ext}(f)$. This removes the influence of the finite nature of the source time function. Using the flat part of the spectrum (Figure 3.2) is equivalent to using a delta (impulse) signal.

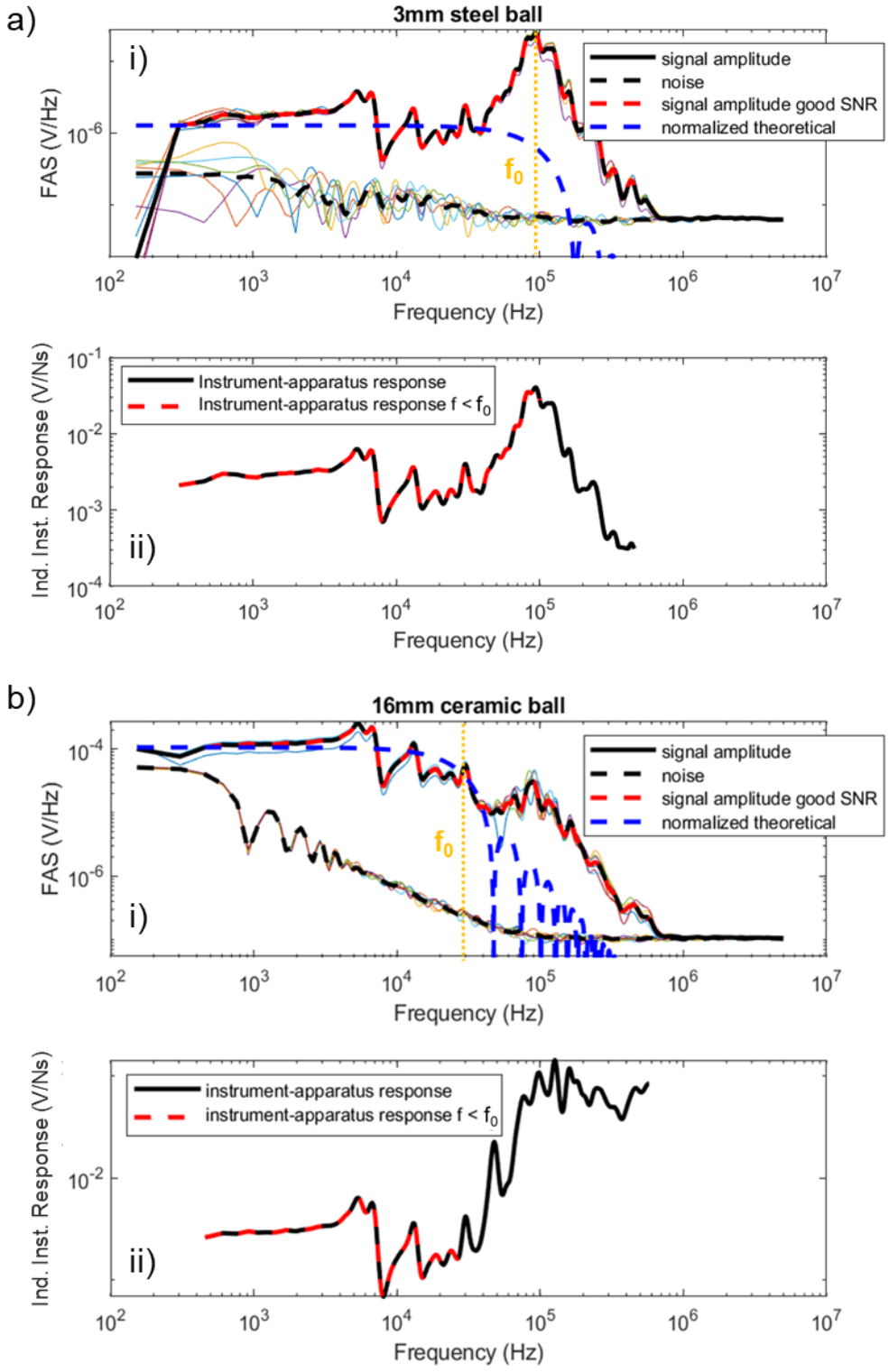

Figure 3.11: *For a) 3 mm and b) 16 mm ball steel plate impacts; i) repeated (multi-coloured solid lines) and stacked (solid black line) ball impact spectra $S(f)$, with noise spectra (multi-coloured and black dotted lines) and signal with SNR > 3 (red dotted line). The blue dotted line represents the transformed force-time function, $F(f)$, normalised by signal amplitude. Corner frequency f_0 of $F(f)$ is indicated by yellow dotted line. ii) Individual instrument-apparatus response $\Psi(f)_i$ (black solid line) with acceptable signal where the frequency is less than f_0 (red dotted line).*

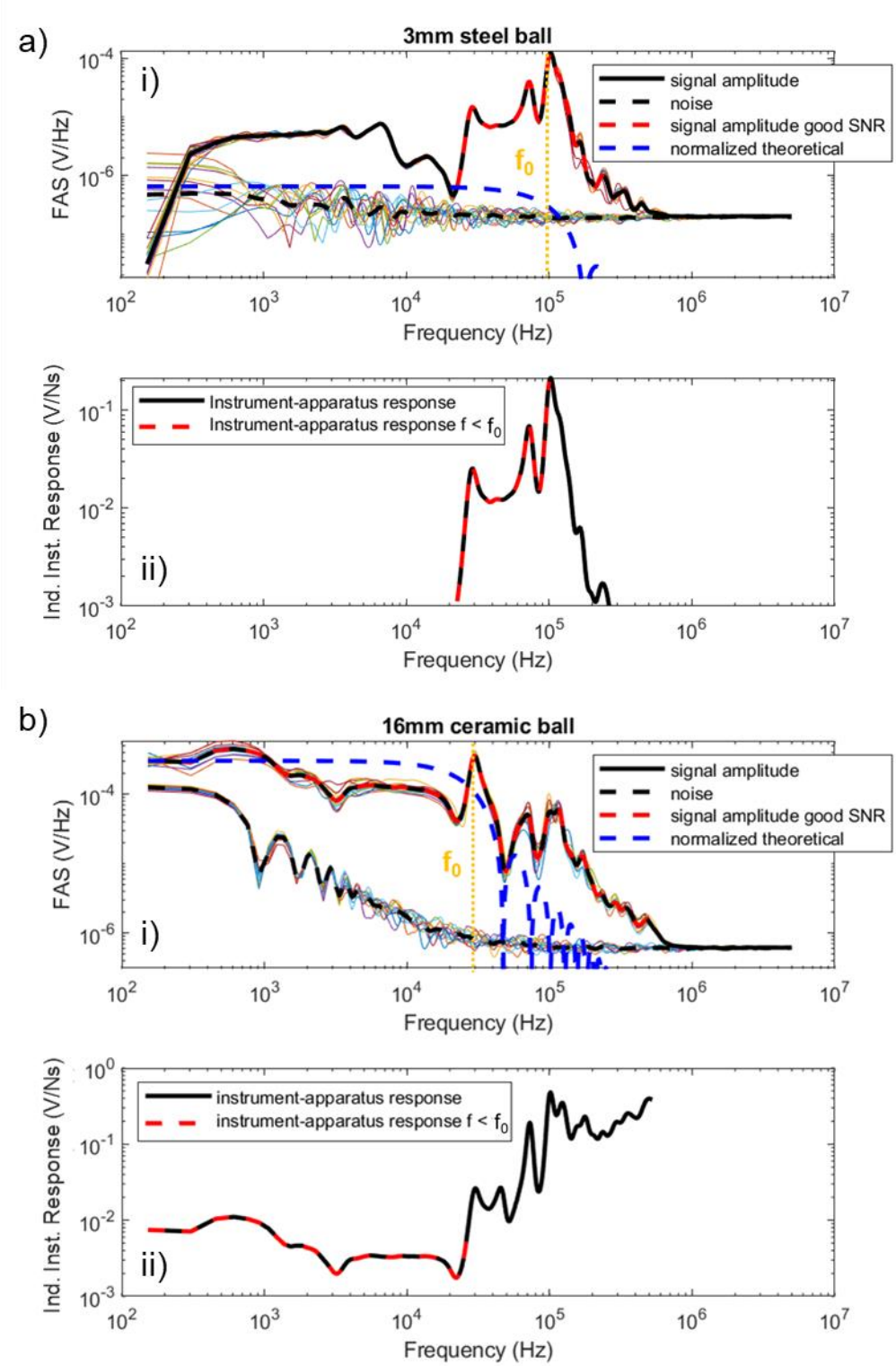

Figure 3.12: *For a) 3 mm and b) 16 mm ball top platen seismic assembly impacts; i) repeated (multi-coloured solid lines) and stacked (solid black line) ball impact spectra $S(f)$, with noise spectra (multi-coloured and black dotted lines) and signal with SNR > 3 (red dotted line). The blue dotted line represents the transformed force-time function, $F(f)$, normalised by signal amplitude. Corner frequency f_0 of $F(f)$ is indicated by yellow dotted line. ii) Individual instrument-apparatus response $\Psi(f)_i$ (black solid line) with acceptable signal where the frequency is less than f_0 (red dotted line).*

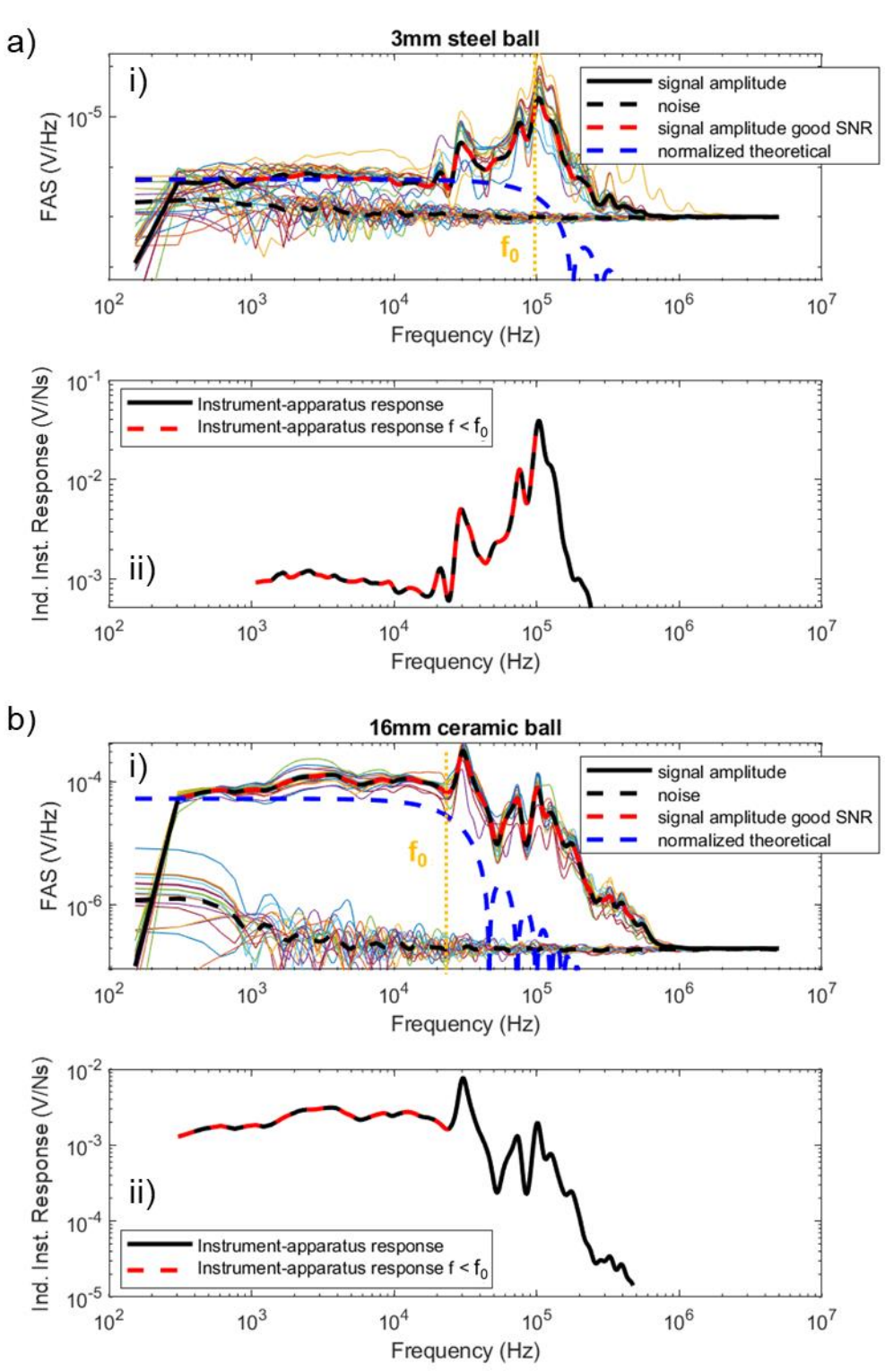

Figure 3.13: *For a) 3 mm and b) 16 mm ball bottom platen seismic assembly impacts; i) repeated (multi-coloured solid lines) and stacked (solid black line) ball impact spectra $S(f)$, with noise spectra (multi-coloured and black dotted lines) and signal with SNR > 3 (red dotted line). The blue dotted line represents the transformed force-time function, $F(f)$, normalised by signal amplitude. Corner frequency f_0 of $F(f)$ is indicated by yellow dotted line. ii) Individual instrument-apparatus response $\Psi(f)_i$ (black solid line) with acceptable signal where the frequency is less than f_0 (red dotted line).*

3.2.8 External instrument-apparatus response, $\Psi^{ext}(f)$

The external instrument-apparatus response can be constructed using spectra measured from a suite of different-sized balls. To combine individual ball drop responses (bottom panels, Figures 3.11 – 3.13), McLaskey et al. (2015) use a best-fit envelope to estimate the overall external instrument-apparatus response across all frequencies (Baltay et al., 2010). The envelope is constructed by using the ball drop spectrum with the maximum amplitude at each frequency. This assumes that each ball response represents a narrowband response that can be used to reconstruct a broadband response envelope, using the peak amplitudes at each frequency and combining them to get an external instrument-apparatus response across all frequencies. For example, at low frequencies (below 1 kHz), the largest 20 mm ball drop spectrum has the highest amplitude. At high frequencies (above 100 kHz), the smallest 1 mm ball drop spectrum has the highest amplitude. Consequently, the Matlab code *balldrop_spectra.m* loops over the whole frequency range, picking the highest amplitude out of all ball impact spectra as the enveloped external instrument-apparatus response. However, noting the similar form of individual responses with the alignment of all responses at common frequencies (e.g. 20 kHz, Figure 3.13), the median of all ball responses (the middle amplitude value across all frequencies) could also be considered an estimate of the overall instrument-apparatus response.

Individual instrument-apparatus responses $\Psi(f)_i$ for the steel plate and seismic assembly are shown in Figure 3.14 with the a), c) and e) envelope and b), d) and f) median response of all individual responses shown, giving the combined, external instrument-apparatus response, $\Psi^{ext}(f)$. By taking the upper envelope or median of all individual responses, the resulting instrument-apparatus response $\Psi^{ext}(f)$ describes how the steel plate, top and bottom platens of the seismic assembly, and seismic recording system modify the wavefield of external sources across a frequency range between 150 Hz – 300 kHz. While all three instrument-apparatus responses have a similar form (low amplitude below 10^4 Hz, high amplitude above 10^4 Hz), there are significant differences, particularly at lower frequencies for the bottom platen of the seismic assembly. Major differences between the steel plate and top and bottom platens of the seismic assembly are due to geometrical differences: the narrower, more complex platen shape will introduce more noise due to added reflections. Differences in response between the top and bottom platens are due to the different surface areas of the 180° and 120° PZT crystals, respectively.

Uncertainty in the instrument-apparatus responses is outlined by the dark and light grey shaded areas in Figure 3.14, which represent the data which lay between the 68% and 95% percentiles (approximately one and two standard deviations of the mean in a normal distribution, ± σ and ±

2σ). Uncertainty in the low-frequency plateau is particularly high for the top and bottom platens of the seismic assembly. A potential reason for this could include the smaller, more complex geometry of the platens in comparison to the simple steel plate, which may mask the true instrument-apparatus response with low-frequency noise. The low-frequency amplitudes (below 10^4 Hz) of the top platen and steel plate responses are similar and lower than the bottom platen. This is due to the identical crystal size of the piezoelectric crystals in the top platen and steel plate. However, the low-frequency amplitudes of the top platen and steel plate responses lay within ± 2σ of the bottom platen response. Further analysis in the following section will determine whether the envelope or median method of combining responses is best.

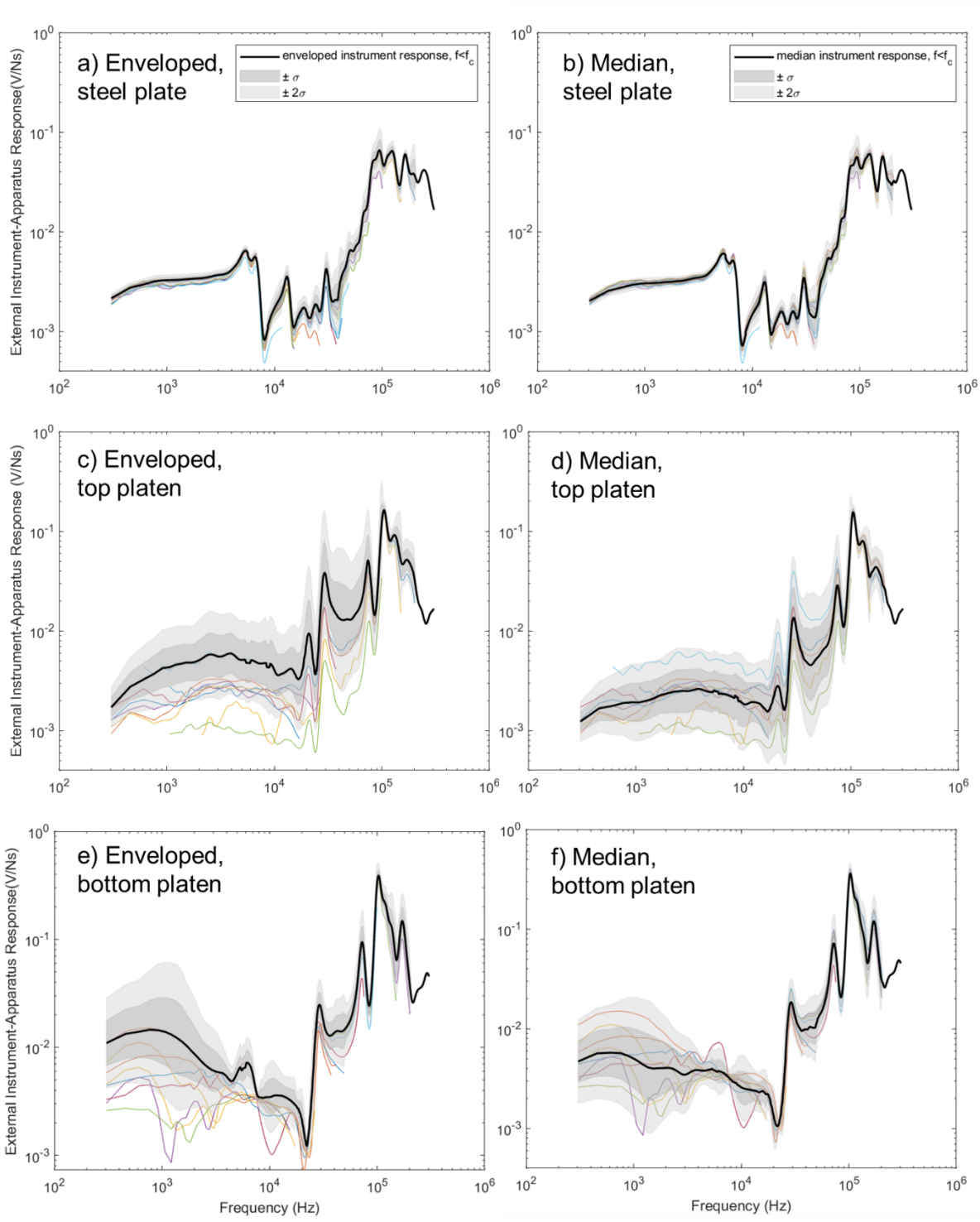

Figure 3.14: *a,d) Steel plate, b,e) top and c,f) bottom platen of seismic assembly enveloped (a, c and e) and median (b, d and f) instrument-apparatus responses $\Psi(f)$ (black line), constructed from individual instrument-apparatus responses $\Psi(f)_i$ (multicoloured lines). Dark and light grey shading indicates data where amplitudes are within ± σ and ± 2σ of the mean respectively.*

3.2.9 Bootstrapping: resampling dataset to create simulated samples

To test whether the envelope or median method is best for combining individual instrument-apparatus responses, it would be useful to compare the 68% and 95% percentiles of individual responses (shaded areas, Figure 3.14) to estimate confidence intervals for the combined instrument-apparatus responses. Standard errors and confidence intervals for the external instrument-apparatus responses can be derived by using bootstrapping. Converse to traditional hypothesis testing, which requires probability distributions and test statistics (e.g. t-values) to estimate sampling distributions, bootstrapping resamples datasets to create many simulated samples (Mooney and Duval, 1993). This is useful as it tests the variability of a certain statistic, e.g. the mean or median, without having to run an experiment a large number of times.

In this study, the external instrument-apparatus responses are the sampled datasets. Bootstrapping is conducted using Matlab's bootstrapping function, *bootci.m*. External instrument-apparatus response data are resampled 'with replacement', meaning that the same data point can be repeated and redrawn from the dataset. Data are resampled 2000 times to generate a distribution of the bootstrapped statistic, the median external instrument-apparatus response (Figures 3.14 b, d and f). Confidence intervals are calculated using the 'bias-corrected and accelerated' (BCa) method, which quantifies bias and skewness in the distribution of bootstrap estimates (Kulesa et al., 2015). Figure 3.15 shows the distribution of the median of the external instrument-apparatus response for the top platen of the seismic assembly as a histogram. 68% and 95% (approximately ± σ and ± 2σ of the mean) confidence intervals are also indicated. From this, a hypothesis test with a 95% confidence level can be run, with the null hypothesis expected to be rejected 5% of the time.

The medians of the individual instrument-apparatus responses for the 1 mm steel (0.0221), 1.5 mm steel (0.0222) and 16 mm ceramic (0.0291) ball responses, measured using the bottom platen of the seismic assembly (medians of coloured spectra, Figure 3.14f), lay outside the bootstrapped 95% confidence intervals (0.0223 and 0.0290). However, the majority of the medians of the individual instrument-apparatus responses lay within the 95% confidence intervals. This combined with the similar form of individual responses and the alignment of all responses at common frequencies suggests that the median instrument-apparatus response is suitable for acoustic calibration. The next section which describes how well the median and enveloped instrument-apparatus responses return 'true' ball drop spectra estimates in comparison to theoretical spectra further justifies the use of the median method.

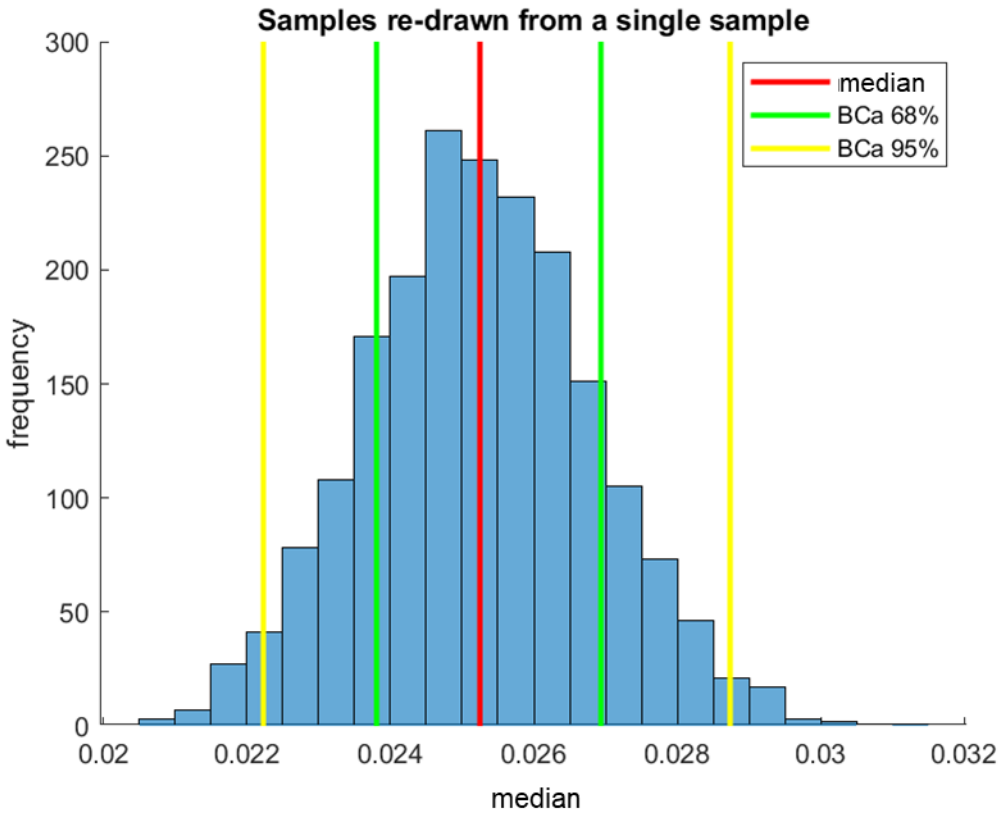

Figure 3.15: *Histogram showing the distribution of the bootstrapped statistic over all frequencies, the median (red line), for the external instrument-apparatus response of the bottom platen of the seismic assembly. 68% and 95% BCa confidence intervals (approximately ± σ and ± 2σ of the mean) are marked by green and yellow lines respectively.*

3.2.10 'True' ball drop source spectra estimation, $F(f)$

Following Equation 3.16, dividing recorded ball impact signals $S^{ext}(f)$ by the external instrument-apparatus responses $\Psi^{ext}(f)$ gives an estimation of the 'true' source spectrum of each ball impact, $F(f)$ (Figures 3.16 and 3.17). As shown by the wider shaded area of the top and bottom platens of the seismic assembly spectra in contrast to the steel plate spectra, amplitude uncertainty is higher for frequencies below 5 kHz. Moreover, the SNR of 3 mm ball impact signals measured using the bottom platen is higher than the top platen and steel plate, leading to spectra with narrower frequency bands. Nevertheless, the overall shape, including frequency nodes (zeros) for the true source spectra estimates generally fit the theoretical source spectra well, which validates the use of absolute acoustic calibration for source estimation.

The difference between true source spectra obtained using the enveloping and median methods of combining individual instrument-apparatus responses is most apparent at lower frequencies of the 16 mm ball impact (Figure 3.17). Neither the true ball drop source spectra derived using the enveloped nor median top platen instrument-apparatus response fit the 3 mm ball impact

very well at low frequencies. However, the 95% confidence interval of the median response fits slightly better.

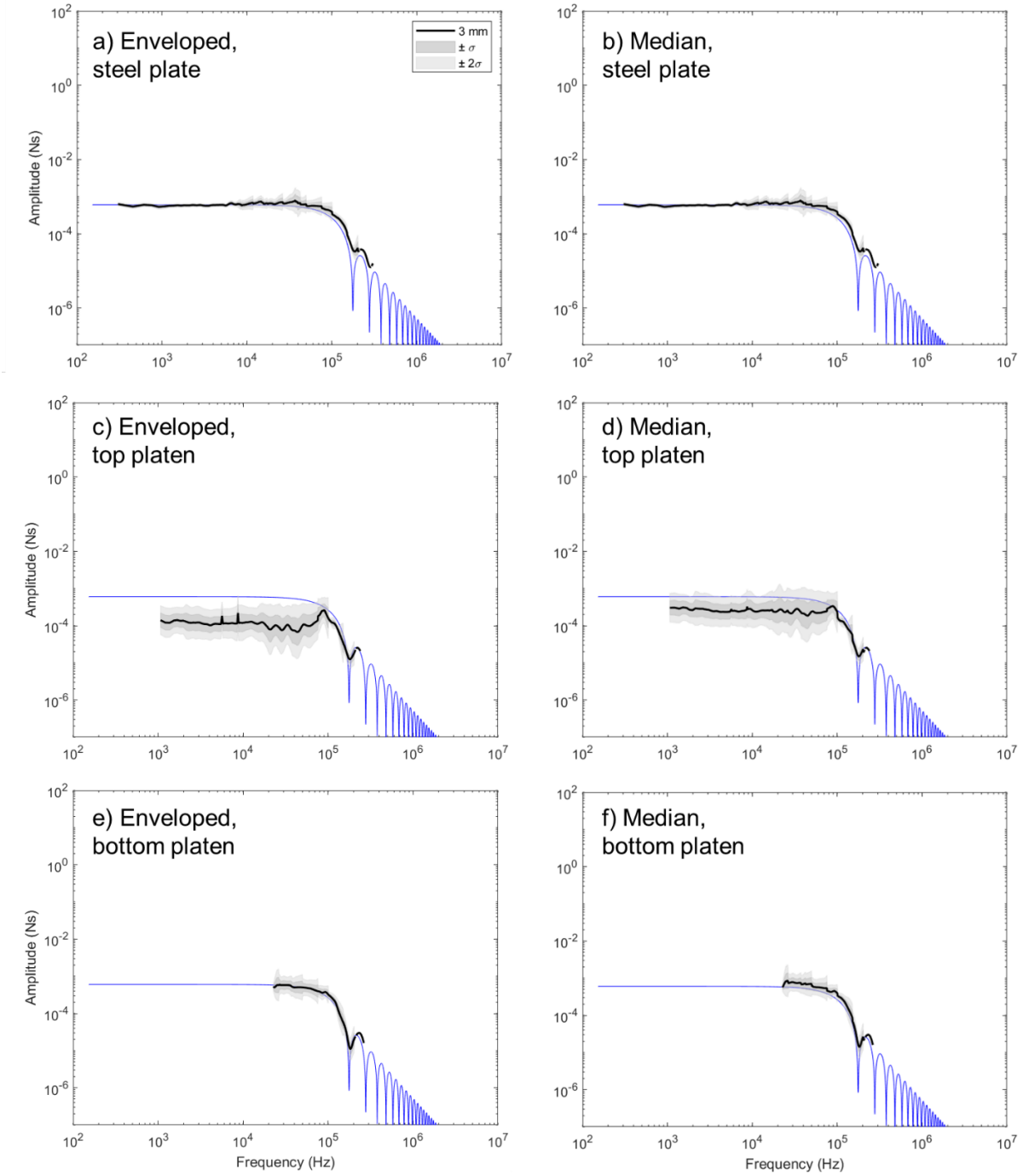

Figure 3.16: *a,d) Steel plate, b,e) top and c,f) bottom platen of seismic assembly enveloped (a, c and e) and median (b, d and f) estimate (black line) and theoretical evaluation (blue line) of 'true' source spectra, $F(f)$ for 3 mm ball impact.. Grey shading indicates data where amplitudes are within ± σ and ± 2σ of the mean.*

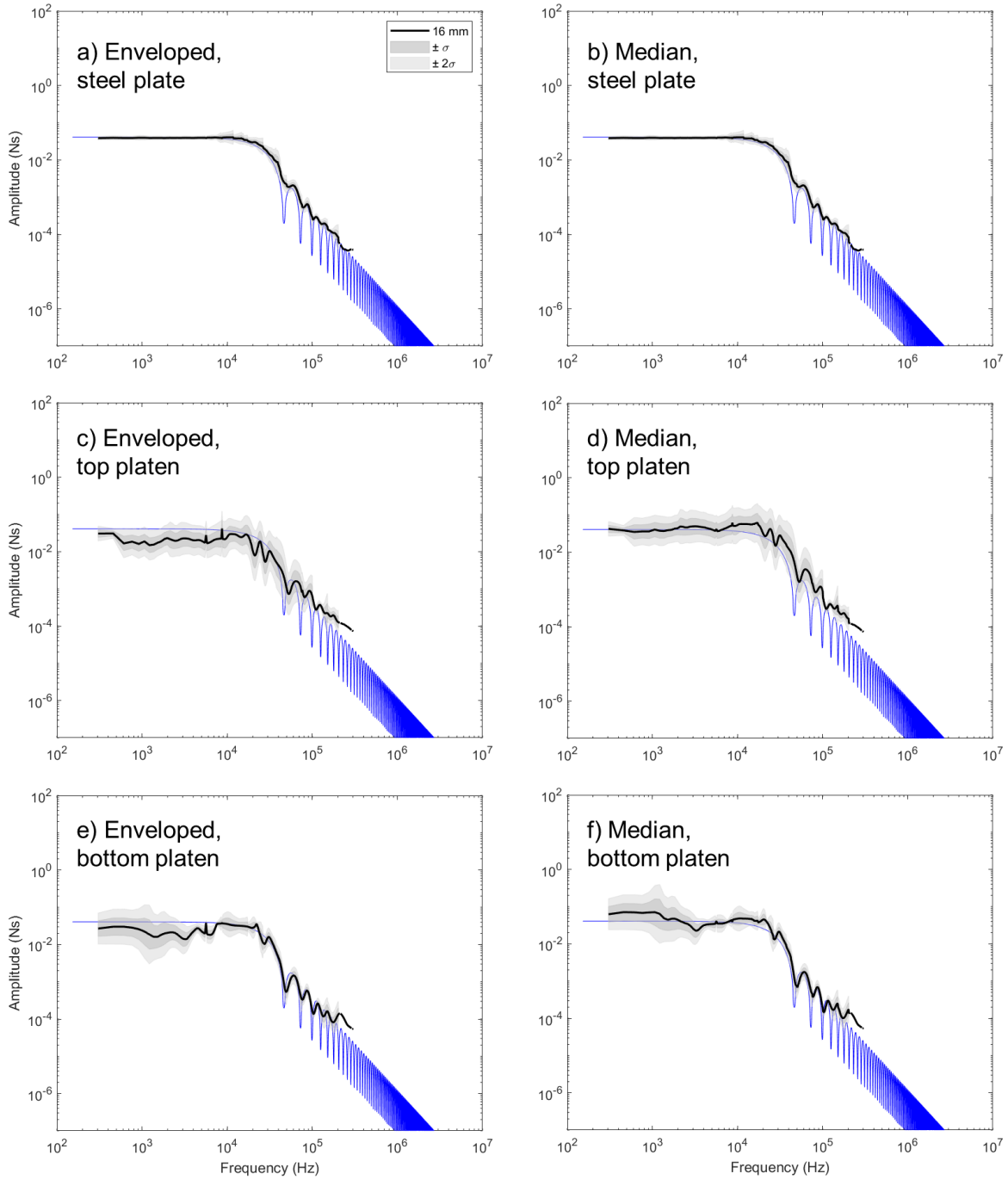

Figure 3.17: *a,d) Steel plate, b,e) top and c,f) bottom platen of seismic assembly enveloped (a, c and e) and median (b, d and f) estimate (black line) and theoretical evaluation (blue line) of true source spectra, $F(f)$ for 16 mm ball impact. Grey shading indicates data where amplitudes are within ± σ and ± 2σ of the mean.*

3.2.11 Internal instrument-apparatus response $\Psi^{int}(f)$: relating momentum to moment using $C_{F\dot{M}}$

McLaskey et al. (2015) estimate the force-moment relation $C_{F\dot{M}}$ empirically by deriving M_0 of stick-slip seismic signals using waveform modelling of their large, simple, square 1.5 m biaxial sample (McLaskey et al., 2014). A generalised ray theory code is used to calculate Green's

functions, which are used to generate synthetic seismograms for early parts of stick-slip signals (Hsu, 1985). The estimated change in momentum of stick-slip spectra, Δp_{equiv}, can be found by assuming that an internal source (in McLaskey et al.'s case, an AE) and therefore, $S^{int}(f) = S^{ext}(f)$. Rearranging Equation 3.16 gives the following equation:

$$\Delta p_{equiv} = F(f) = \frac{S^{int}(f)}{\Psi^{ext}(f)} \qquad f < f_0, \tag{3.22}$$

with Δp_{equiv} equal to the low-frequency level of the spectra, $F(f)$ below corner frequency f_0 (Figure 3.3). Knowing both M_0 and Δp_{equiv}, the force-moment relation $C_{F\dot{M}}$ can be calculated using Equation 3.17. Due to the small geometry of our setup, the wave modelling method is not suitable.

$C_{F\dot{M}}$ can also be derived theoretically, assuming that calibrated materials are isotropic and that path lengths and angles of incidence of internal (i.e. stick-slips and AEs) and external (i.e. ball impacts) sources are similar. In this case, $C_{F\dot{M}}$ is equal to the wave speed of the type of wave measured in the signal (i.e. P-wave or S-wave velocity, or an average of both as is the case for McLaskey et al. 2015). While the seismic assembly used in this study has a more complex geometry than McLaskey et al.'s 1.5 m square block of granite, testing has shown remarkable similarities in the general shape of spectra derived from the seismic assembly and the steel plate. Moreover, several authors (e.g. Yamashita et al., 2021; Fieseler et al., 2022; Li, Casanova and Einstein, 2022) have used the theoretical derivation of $C_{F\dot{M}}$ to find the internal instrument-apparatus response. Therefore, the theoretical assumption of $C_{F\dot{M}}$ is equal to either the P-wave velocity (5.65 km/s) or S-wave velocity (3.16 km/s) of 17-4 stainless steel. While friction experiments are carried out on PMMA, due to the geometry of the L-shaped steel sliders and the steel platens of the seismic assembly, steel is the dominant material that waves propagate through from their source to the piezoelectric sensors.

McLaskey et al. (2015) computed $C_{F\dot{M}}$ both empirically and theoretically. Their estimates varied widely: while empirical estimates of $C_{F\dot{M}}$ ranged between 3 – 26 km/s, their theoretical estimate based on the wave speed of Westerly granite was 7 km/s. Therefore, mechanical and seismic estimates of seismic moment M_0 will be compared in Chapter 4 to test the assumption of $C_{F\dot{M}}$ as equal to the P-wave velocity and determine whether the theoretical estimate is more accurate in our case. Figure 3.18 shows the internal instrument-apparatus response for both the top and bottom platens of the seismic assembly.

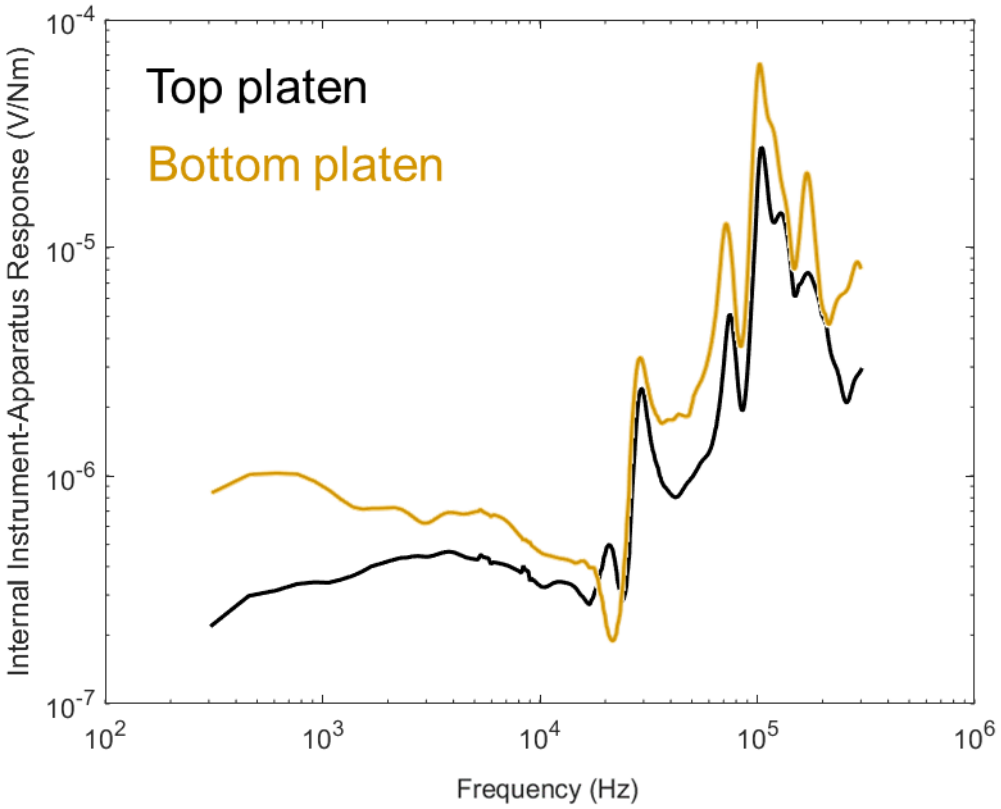

Figure 3.18: *Internal instrument-apparatus responses of a) top and b) bottom platens of the seismic assembly, derived by dividing external instrument-apparatus responses (Figure 3.14) by the force-moment relation* $C_{F\dot{M}}$.

3.3 EFFECT OF APPLYING THE PULSER AMPLIFIER SYSTEM (PAS)

3.3.1 Experimental set-up

The Pulser Amplifier System (PAS) is used in this work to limit noise acquisition via an amplitude trigger threshold and to amplify microseismicity related to acoustic emissions (AEs), respectively. The PAS unit has filters applied in its design, but the form of these filters is unknown. Very limited, qualitative data is provided by the manufacturer. Therefore, testing using a signal generator (RS Pro Arbitrary/Function Waveform Generator SDG800 Series, 125 MSa/s sample rate, 14-bit vertical resolution) is conducted to understand how the PAS amplifies waveforms.

Two types of test signals with different shapes (one pulse and several different sine waves) are applied to the PAS connection with properties outlined in Figure 3.19. Pulse wave properties are selected to create the narrowest time pulse possible to access the greatest range of frequencies while reducing the chance of signal clipping by using a small amplitude. A pulse wave with 500 kHz frequency (i.e. short, repeated pulses followed by zeros every 2μs; Figure 3.19a) is chosen as this lies within the frequency range with the highest amplification according to the equipment provider (Itasca Consulting Ltd, 2017). Pulse waves are constructed using the superposition of multiple sine waves of an increasing number of harmonics to make a wave as close to a delta (impulse) function as possible (Han and Nguyen, 2002; RS Pro, 2023). Sine wave frequencies are chosen to match respective peaks in the frequency spectra of the pulse waves. Amplification is negligible below 10 kHz. The seismic acquisition equipment connections are detailed in Figure 3.20. Multiple repeats (at least 8) of test signals are recorded and stacked to ensure reliability and observe how replicable the PAS response is.

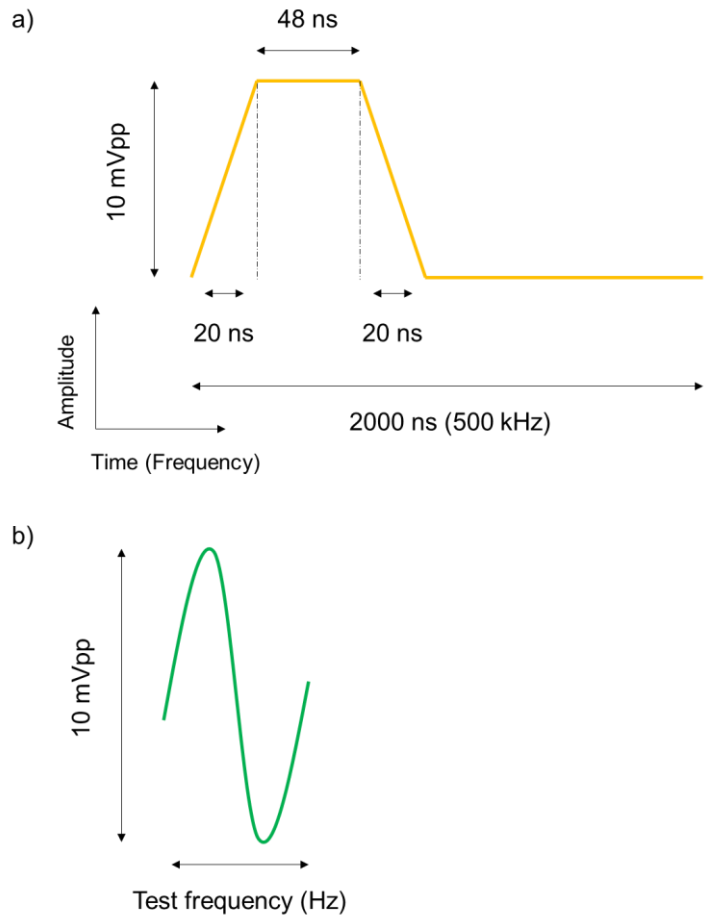

***Figure 3.19**: a) Pulse test wave generated by the digital signal generator: amplitude = 10 mV peak-to-peak (pp); rise time = 20 ns; fall time = 20 ns; width = 48 ns; time = 2000 ns (500,000 cycles per second, or 500 kHz). b) Sine test wave generated by the digital signal generator: amplitude = 10 mV peak-to-peak (pp); varying test frequency (Table 3.3).*

***Table 3.3:** Sine wave test frequencies used to derive PAS response.*

Frequency (kHz)
1
10
50
60
100
130
170
500
1000
1500
2000
2500
3000
3500

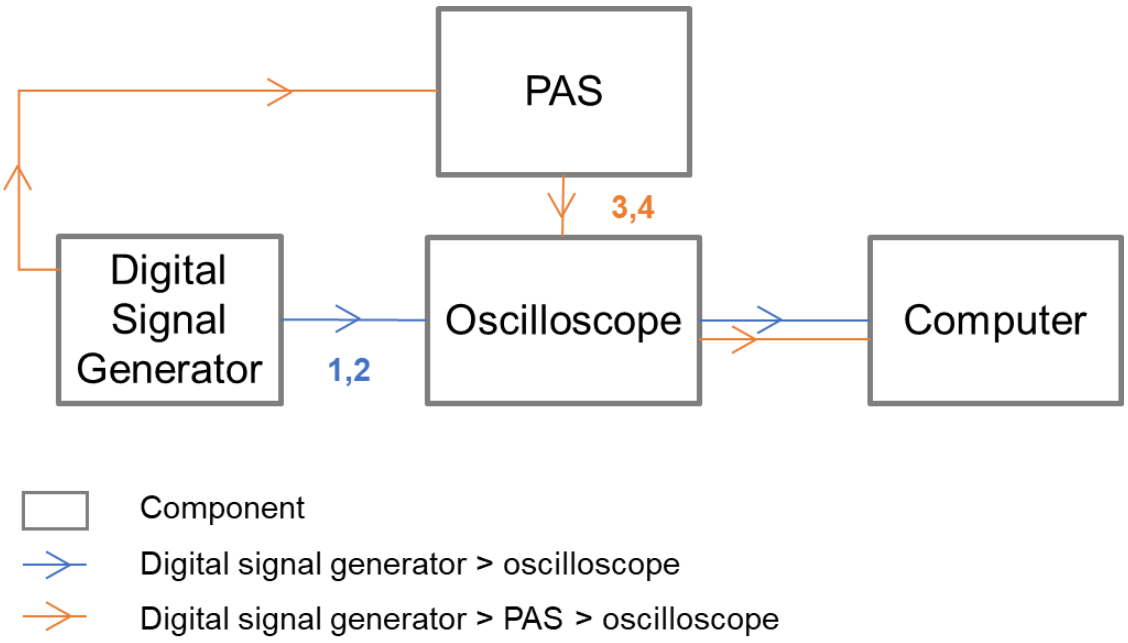

Figure 3.20: *Schematic of seismic acquisition apparatus connections used to amplify and measure signals. Numbers indicate the channel number for each connection on the digital oscilloscope and CecchiLeach system (odd numbers = PAD-006-1949, even numbers = PAD-006-1951).*

The PAS has five 'Gain Levels', from 1 to 5, from 30 dB (decibels) to 70 dB in 10 dB intervals (Itasca Consulting Ltd, 2017). dB can be converted to an amplitude gain by using the following equation:

$$A_{V(ratio)} = 10^{\frac{A_{V(dB)}}{20}}, \tag{3.23}$$

where $A_{V(ratio)}$ is the ratio of output to input voltage amplitude in volts ($A_{V(ratio)} = \frac{A_{V(output)}}{A_{V(input)}}$) and $A_{V(dB)}$ is the output voltage amplitude in dB.

Two Pulser Amplifier Desktop units (PADs) are used for amplification: PAD-006-1949 (odd numbers) and PAD-006-1951 (even numbers), but only the results for PAD-006-1949 are presented. Results are comparable. All processing is conducted using a Matlab code *THC_PAS_calibration.m*. Signals are processed in the same way as previously (waveform processing, Figure 3.1).

3.3.2 Transfer functions

To recover the unknown PAS response, signals are transformed from the time domain to the frequency domain. For linear time-invariant systems, such as these signals, a transfer function of a filter theoretically models the output of a system for each possible input (Laughton and Warne, 2004). The transfer function $H(s)$ of a filter is defined as the Laplace transform of the ratio of the

output signal, $Y(s)$ (i.e. the amplified and filtered PAS signals transformed to the spectral domain) and input signal $X(s)$ (i.e. the test signal transformed to the spectral domain):

$$H(s) = \frac{Y(s)}{X(s)}, \tag{3.24}$$

where $s = \sigma + j.\omega$, a complex variable with real (σ) and imaginary ($j.\omega$) parts. For our purposes, it is adequate to define $\sigma = 0$ as the system is stable, leaving $s = j.\omega$, which simplifies the Laplace transform to a Fourier transform (Widder, 2015). Therefore, the transfer function of the PAS (H_{PAS}) is simply the ratio of the Fast Fourier Transforms (FFTs) of the output signal (amplified by the PAS) and input signal (unamplified).

3.3.3 Results and discussion

Figure 3.21 shows the amplification of the pulse and sine test waveforms at Gain Level 4. Unamplified pulse spectra have several amplitude peaks at frequencies from 50 kHz to 4 MHz, which are amplified by the PAS. The PAS response peaks are present due to the imperfect pulse waveform (with rise and fall times of 20 ns), which is formed by the superposition of sine waves (RS Pro, 2023). Response peaks coincide with harmonic frequencies. Their amplitudes vary widely, reaching a maximum of 146 at 1 MHz. The amplitude of the 100 kHz pulse wave peak (Figure 3.21b) is 68.5. Conversely, the amplitude of the 100 kHz sine wave peak (Figure 3.21d) is 1130. Considering that Gain Level 4 represents a gain of 60 dB, the amplification should be $A_{V(ratio)} = 10^{\frac{60}{20}} = 1000$. This means that the pulse wave underestimates the PAS response, which could be because of the presence of other, more resonant harmonics that construct the pulse wave (Han and Nguyen, 2002; RS Pro, 2023).

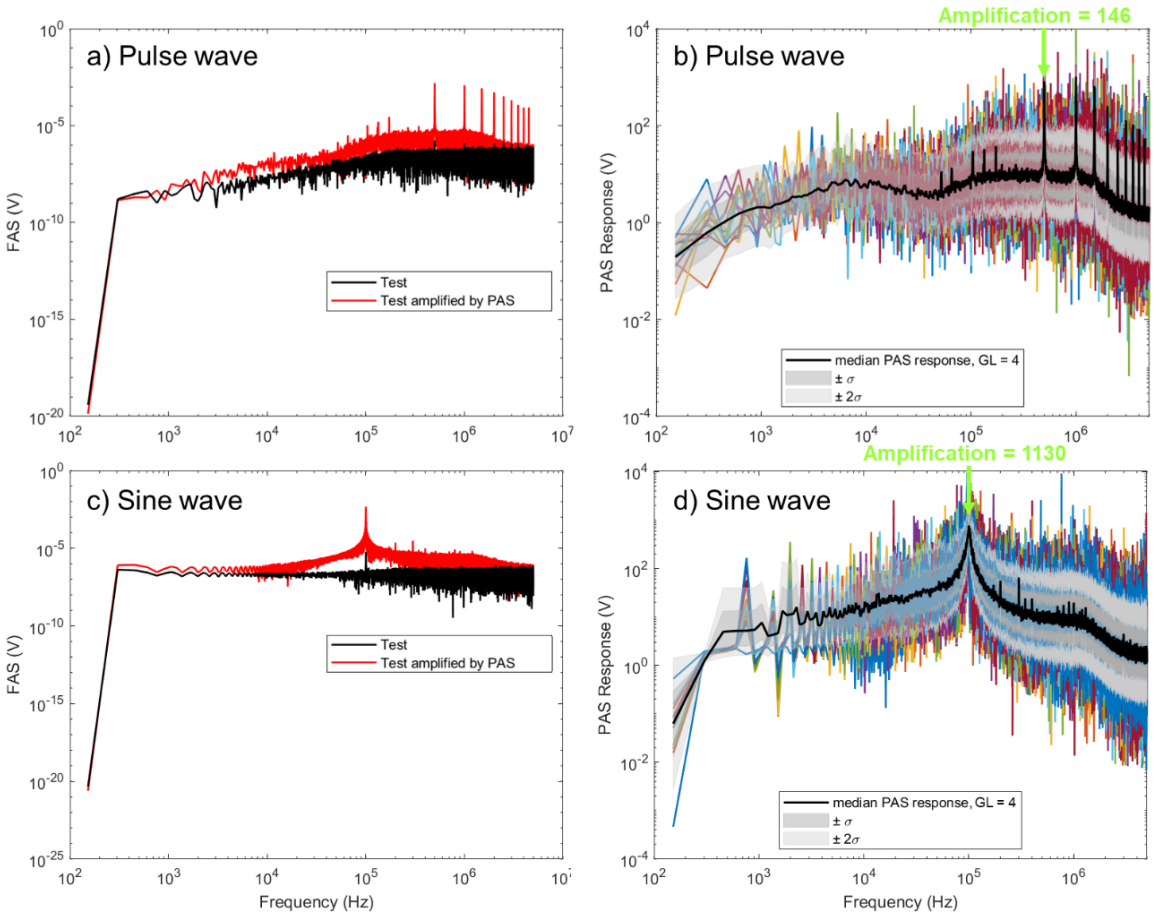

Figure 3.21: *a) FAS of pulse wave test signal (black line) and amplified by the PAS (red line) at Gain Level 4. b) PAS responses of pulse wave test signal (coloured lines) with averaged, median PAS response. c) FAS of 100 kHz sine wave test signal (black line) and amplified by the PAS (red line) at Gain Level 4. d) PAS responses of sine wave test signal (coloured lines) with averaged, median PAS response. Maximum amplification of b) pulse and d) sine waves highlighted by green arrows.*

Figure 3.22 shows the PAS response for Gain Levels 1 – 5 between 100 kHz and 2 MHz, where amplification is strongest, derived using both pulse and sine waves. Amplifier responses largely align with provided calibrations from Itasca Consulting Ltd, however, sine waves begin to overestimate the response above 500 kHz.

Pulse wave spectra are beneficial as they contain a wide range of frequencies and better represent the complex seismic waveforms that the system measures. However, sine waves are useful as there is a large gap in harmonic peaks between 200 kHz and 500 kHz for the pulse wave, and the pulse wave can underestimate the amplification. Therefore, results from both peak and sine test waves are interpolated to obtain a wide range of frequencies that accurately reflect the qualitative data provided by the manufacturer (Itasca Consulting Ltd, 2017).

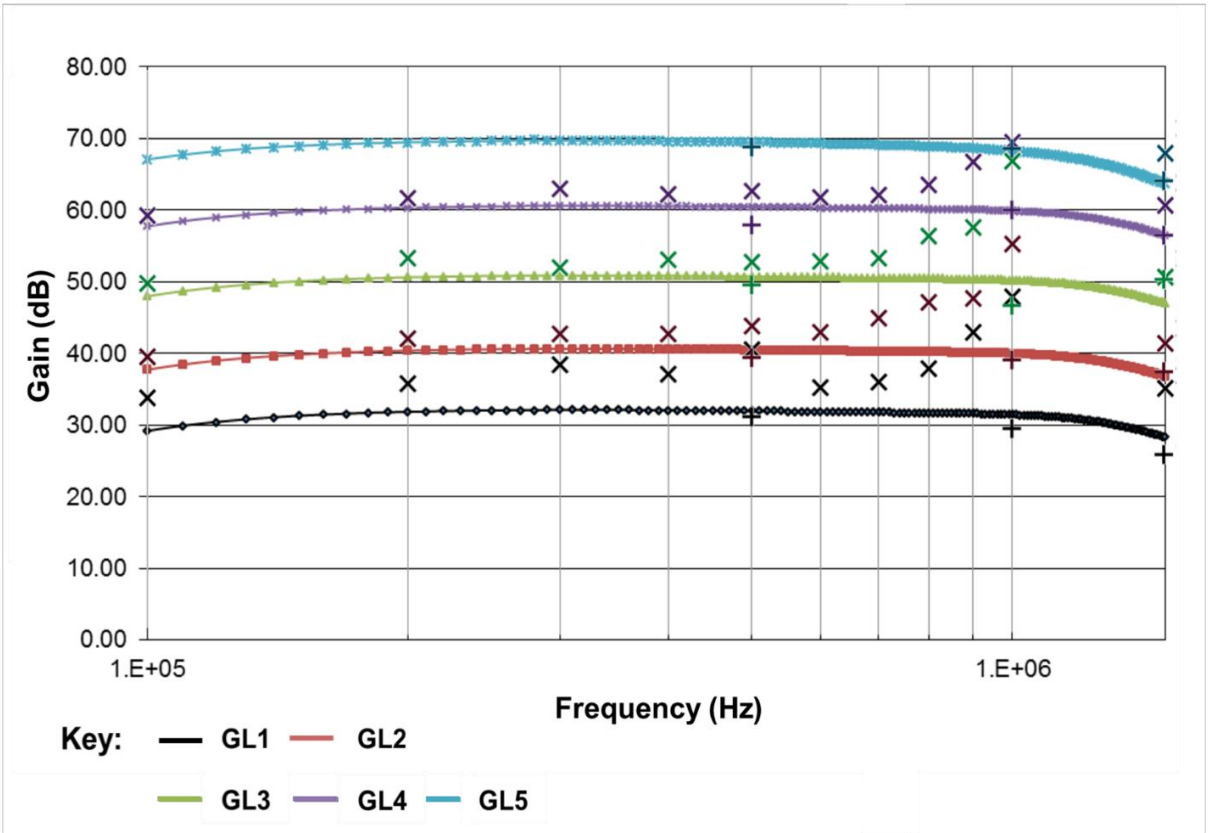

Figure 3.22: *PAS amplifier responses. Gain Level (GL) 1 – 5; pluses + are pulse signal responses; crosses X are sine signal responses. Results are overlaid on illustrative data (lines) given by the manufacturer (Itasca Consulting Ltd, 2017).*

To summarise, the PAS acts as a high-pass filter, making high frequencies clearer, particularly between 100 kHz and 1 MHz. While acoustic emissions (AEs) are expected to have high corner frequencies (above 10 kHz), the frequency dependence of the PAS responses is still significant as AEs will contain a range of frequencies within the signal. Past studies that have used amplifiers to measure acoustic emissions (e.g. Moradian, Einstein and Ballivy, 2016; Marty et al., 2019) have not captured the frequency dependence of amplification, instead assuming a flat response. The complexity in amplification across a range of frequencies is important to quantify as it allows the whole system to be fully calibrated (Dunn et al., 2014; Müller, 2018).

3.3.4 Internal instrument-apparatus response with PAS

Combining the PAS and internal instrument-apparatus responses allows the source properties of smaller AE events to be derived, in a similar fashion to Equation 3.24. As the internal instrument-apparatus and PAS response vectors are different lengths due to SNR criteria, the PAS response is interpolated so that frequencies are the same before multiplication. Figure 3.23 shows the amplified internal instrument-apparatus responses at Gain Level = 4.

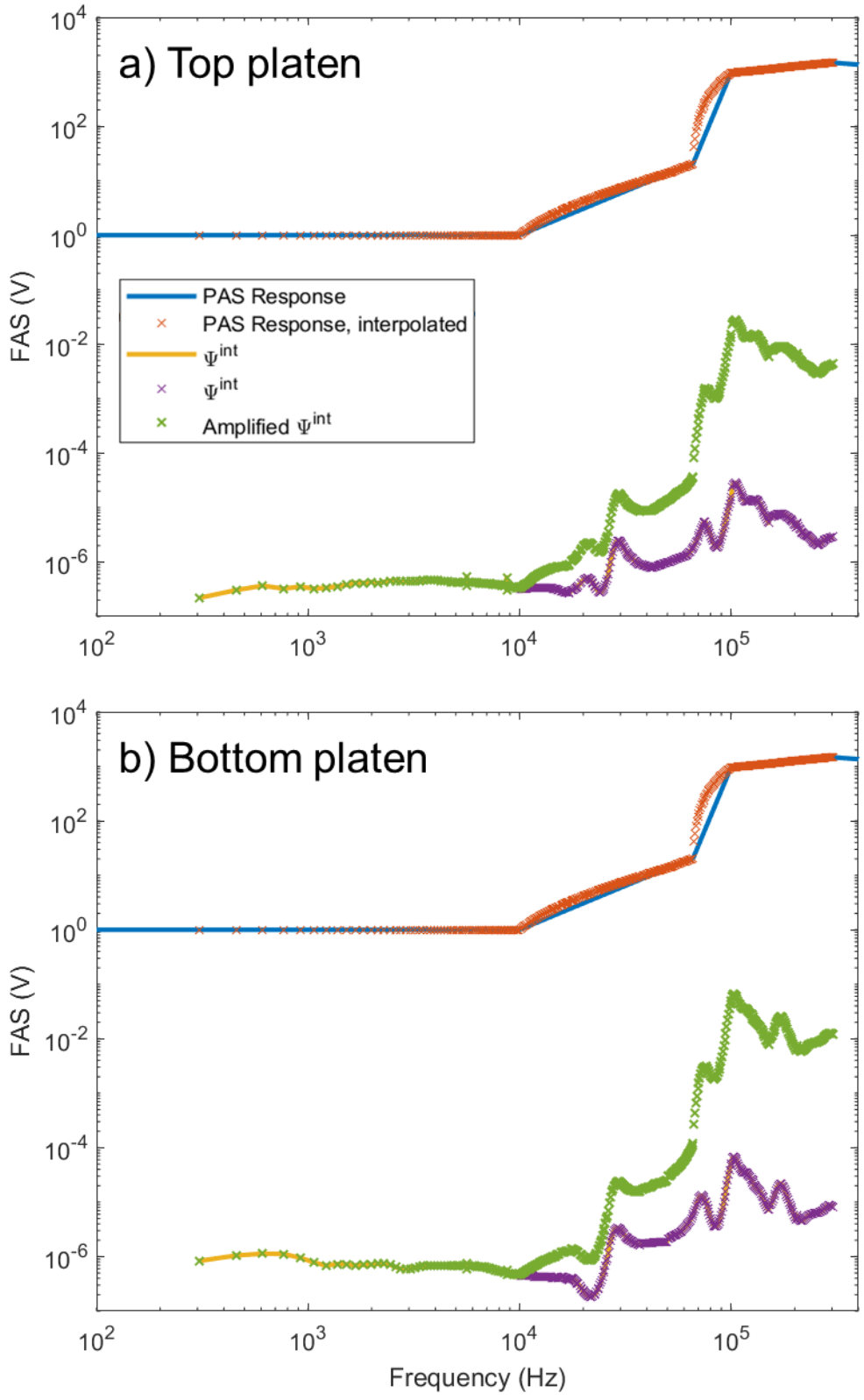

Figure 3.23: *Amplified internal instrument-apparatus responses of a) top and b) bottom platens of the seismic assembly, Gain Level = 4.*

3.4 MINIMUM EVENT MAGNITUDE

The smallest measurable event magnitude for the acoustic monitoring system can be estimated from the typical noise level recorded during a frictional sliding experiment in the triaxial deformation apparatus (Chapter 2; Figure 2.1). The servo-controlled motors, used to control confining pressure and load point displacement during experiments (Chapter 2; Sections 2.2.5 and 2.2.6; Figure 2.10), generate electrical noise. This electrical noise is amplified when amplifiers are applied. Figure 3.24 demonstrates the typical level of noise (unamplified) preceding frictional sliding experiment PMMA_400_30 (Chapter 5). The recording is taken after the seismic sample assembly is placed into the vessel and connected to the seismic acquisition apparatus and the servo-control motors for confining pressure and load point displacement are applied (Chapter 4, Section 4.2.2). The peak noise level is 0.07 V. A recorded signal must have an SNR > 3, i.e. an amplitude greater than $\pm$ 0.21 V to be accepted for Brune modelling and subsequent estimation of source properties.

To characterise the minimum event size, the unamplified seismic signal measured using the bottom platen of the seismic assembly during a representative stick-slip event (PMMA_400_30_001; Chapter 5, Figure 5.5) is scaled so that its amplitude is equal to the low noise level (0.07 V, where SNR < 3) and high noise level (0.21 V, above which SNR > 3). Following the data processing workflow outlined in Figure 3.1, the signals are divided by the amplified internal instrument-apparatus response (Gain Level = 4) for the bottom platen (Figure 3.23b). This exemplifies an event of equivalent magnitude when amplified, i.e. much smaller if it were unamplified. Additional examples using theoretical ball drop spectra (blue lines, Figure 3.16 – 3.17) divided by the internal instrument-apparatus response are added for context.

Source spectra are then fit using Brune models (Chapter 1, Section 1.4.1; Figure 3.3) with Matlab code *brune_fit.m*. The flat, low-frequency level is equivalent to the seismic moment. Results show that the minimum event size is 3×10^{-3} Nm, or moment magnitude $M_w = -7.75$ (Chapter 1, Section 1.1). This is comparable to other studies (McLaskey et al., 2014; McLaskey and Lockner, 2016), with the minimum event size in McLaskey et al. (2015) being $M_w = -7$.

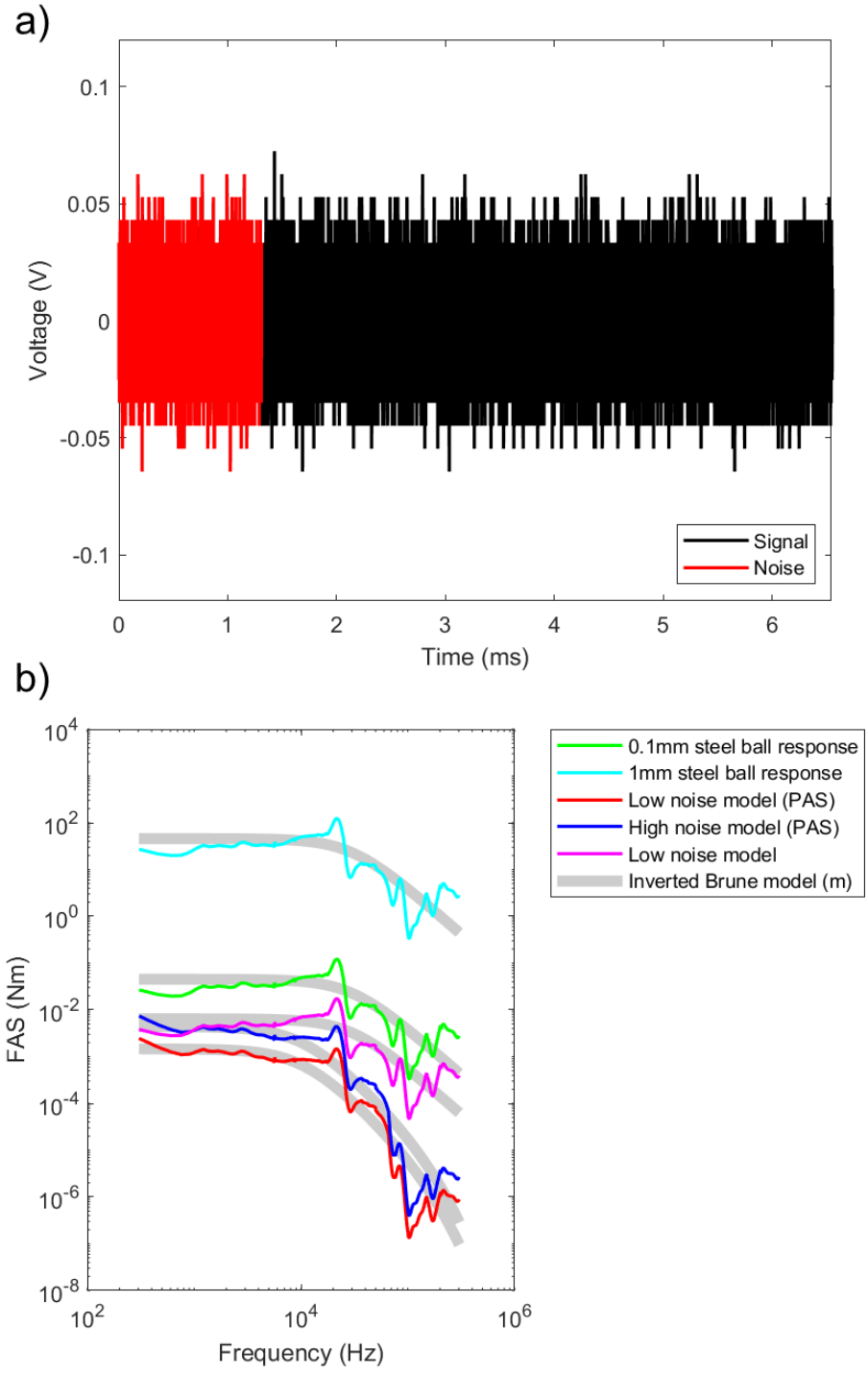

Figure 3.24: *a) Typical level of noise (unamplified, low noise level where SNR < 3) preceding frictional sliding experiment PMMA_400_30, measured using the bottom platen of the seismic assembly connected straight into the digital oscilloscope (Chapters 4 and 5). b) Model source spectra of a representative unamplified stick-slip waveform, scaled to the low noise level of 0.07 V (magenta line). Red (low noise level) and blue (high noise level; above which SNR > 3) lines represent the spectra of events of equivalent magnitude when amplified at Gain Level = 4. Green and cyan lines represent theoretical ball impact spectra. Grey lines show Brune model fits for each spectrum.*

3.5 APPENDIX

3.5.1 Material properties used to calculate theoretical Hertzian force-time functions for calibration using f_{max} and t_c.

Property	Symbol	Value (units)
Density, steel ball	ρ_1	7700 $\pm$ 200 kg/m^3
Density, ceramic ball	ρ_2	3690 $\pm$ 200 kg/m^3
Poisson ratio, steel ball	υ_2	0.28$\pm$ 0.03
Poisson ratio, ceramic ball	υ_2	0.21$\pm$ 0.03
Poisson ratio, seismic assembly	υ_3	0.27$\pm$ 0.03
Poisson ratio, steel plate	υ_4	0.3$\pm$ 0.03
Young's modulus, steel ball	E_1	205 $\pm$ 15 GPa
Young's modulus, ceramic ball	E_2	287 $\pm$ 15 GPa
Young's modulus, seismic assembly	E_3	197 $\pm$ 15 GPa
Young's modulus, steel plate	E_4	210 $\pm$ 15 GPa

3.5.2 Screenshot of example (20 mm ball impact on seismic assembly) .atf file.

.atf files record seismic waveforms that radiate from ball impact and laboratory-generated earthquake (AE and stick-slip) events. AmpToVolts varies with Full-Scale Volts and converts digital count amplitudes to volts.

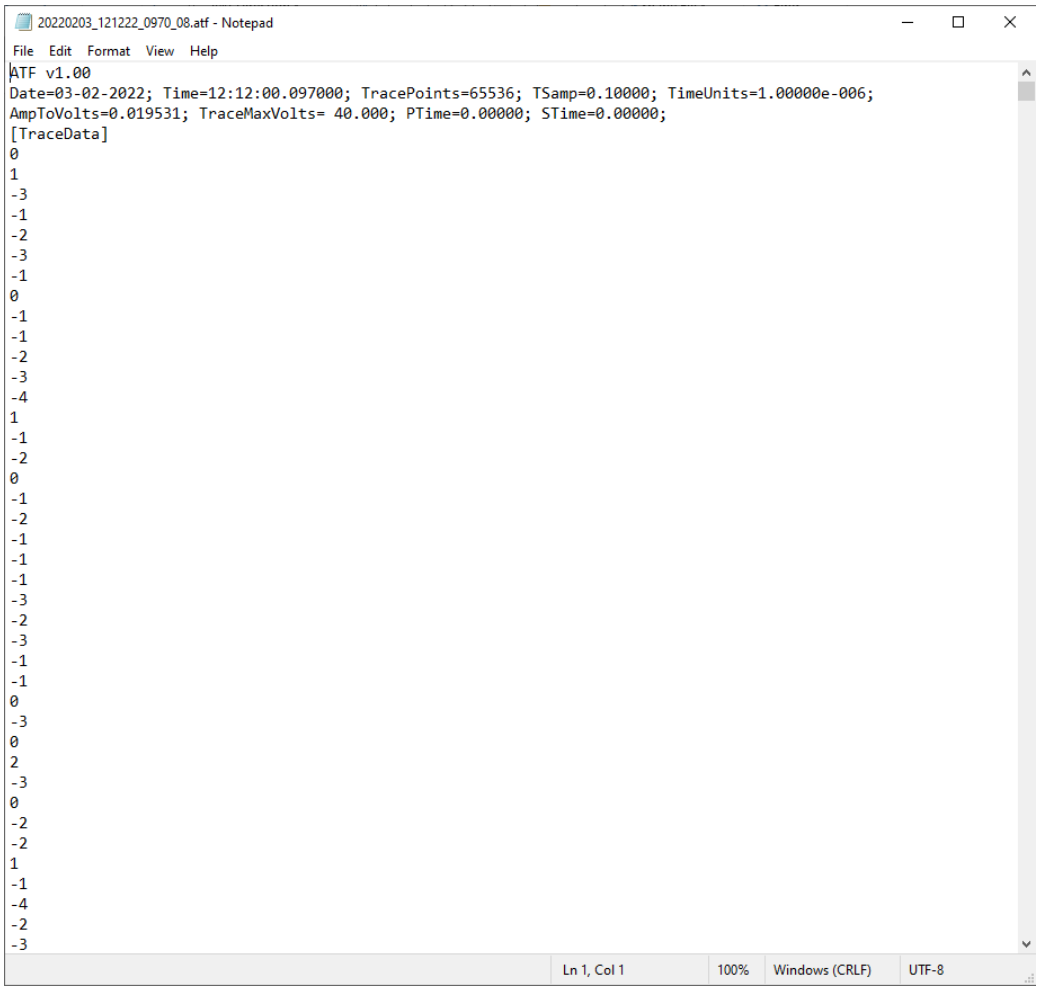

3.5.3 Data acquisition parameters used in this chapter in the CecchiLeach software.

Ball diameter (mm)	Material	Full-Scale Volts, seismic assembly (V)	Full-Scale Volts, steel plate (V)
1.0 ± 0.1	Steel	4	0.8
1.5 ± 0.1	Steel	8	0.8
2.0 ± 0.1	Steel	8	2
3.0 ± 0.1	Steel	8	2
4.0 ± 0.1	Steel	8	2
6.0 ± 0.1	Steel	8	2
8.0 ± 0.1	Steel	8	2
17.0 ± 0.1	Steel	8	8
19.0 ± 0.1	Steel	20	8
20.0 ± 0.1	Steel	40	20
10.0 ± 0.1	Ceramic	8	4
16.0 ± 0.1	Ceramic	20	4

4 MECHANICAL AND SEISMIC ANALYSIS OF LABORATORY-GENERATED EARTHQUAKE SOURCE PROPERTIES

4.1 INTRODUCTION

Earthquakes are dynamic frictional instabilities which form along tectonic faults, generating seismic radiation that can sometimes lead to catastrophic damage. Understanding the processes that control fault strength evolution during the seismic cycle is a key problem in the relation of earthquake source properties, including stress drop, seismic moment and source-time function, to geologic fault slip rates. There is great debate on whether earthquake source and rupture processes are self-similar or are scale-dependent across magnitude scales (Abercrombie and Rice, 2005; Baltay et al., 2011; Blanke et al., 2021; Cocco et al., 2016; Ide, 2003; Kanamori, 2004). The static stress drop can be defined as the difference between the shear stress averaged over a fault before an earthquake and after the earthquake (Brune, 1970; Candela et al., 2012; Cao and Aki, 1986). While a constant stress drop implies a self-similar source process across magnitude scales, variation in stress drop suggests that it is scale-dependent. Reducing the uncertainty in stress drop is crucial as it controls the seismic energy budget (Singh and Ordaz, 1994) and near-field ground motion, hence its wide use in ground motion prediction equations (e.g. Douglas and Edwards, 2016; Baltay et al., 2017; Abercrombie, 2021). Earthquake source property estimation continues to be difficult due to uncertainty in source properties including seismic moment and corner frequency, and source model dependence (Strasser et al., 2009).

Moreover, in nature, a range of slip behaviour from aseismic creep to earthquake slip is observed, but relating this to fault properties is difficult (Dieterich, 1992; Ide et al., 2007; Madariaga, 1979; Tinti et al., 2016). The geological evolution and the effect of the structural properties of faults on seismic sources have been discussed in various studies (e.g. Scholz, 2019). Progressive strain localisation has been shown to form slip zones in less deformed damage zones, with local stress heterogeneities associated with complex stress failure sequences (Ben-Zion et al., 2003; Ben-Zion and Sammis, 2003). Fault heterogeneity (e.g. varied geometry, frictional properties and composition) has been shown to control rupture dynamics (Romanet et al., 2018), resulting in varying slip and stress drop distributions (Abercrombie et al., 2017; Cocco et al., 2016). Other structural properties of faults such as fault segmentation, roughness and damage that are expected to evolve with increased deformation may lead to differences in observed stress drop (Allmann and Shearer, 2007; Dresen et al., 2020; Manighetti et al., 2007; Morad et al., 2022). Moreover, lateral heterogeneity in fault materials (e.g. clay and quartz) has been shown to produce fault weakness and reduce fault stability (Bedford et al., 2022). Experimental and

modelling studies are largely in agreement with field observations, which suggest that fault heterogeneity strongly influences rupture propagation (Blanke et al., 2021; Dresen et al., 2020; Goebel et al., 2017). In particular, coseismic off-fault damage has been shown to enhance high-frequency radiation (Okubo et al., 2019). During rupture propagation, high-frequency waves (greater than 1 Hz) are likely to be the most damaging and cause strong ground motion (S. Marty et al., 2019; Passelègue et al., 2013).

Historically, earthquake nucleation and rupture models have focussed on individual seismic events on a relatively large, pre-existing fault. Models predict stable sliding before dynamic rupture over a critical nucleation patch (Dieterich, 1992, 1979a, 1979b, 1978; Ohnaka, 1992). This quasi-stable, pre-seismic slip may only involve slow, aseismic slip or produce precursory events with lower slip rates and accelerations than during the coseismic 'slip' phase (Bolotskaya and Hager, 2022; Cattania and Segall, 2021; Ide et al., 2007; McLaskey and Lockner, 2014; Scholz et al., 1972; Selvadurai and Glaser, 2017; Shreedharan et al., 2020). While foreshock activity before large seismic events have been widely observed (Papadopoulos et al., 2010; Reasenberg, 1999; Trugman and Ross, 2019; Zhang et al., 2021), in other cases such as the M_w 6 2004 Parkfield California earthquake, little to no foreshock activity has been detected (Bakun et al., 2005; Langbein et al., 2005). Cascade and pre-slip models have been considered as possible explanations for the nucleation of larger events (Ellsworth and Beroza, 1995; McLaskey and Lockner, 2014). However, it is still unclear which of the two processes is culpable and how to distinguish this nucleation phase from the preceding, late-interseismic preparation phase (Bolotskaya and Hager, 2022).

Since the 1960s, laboratory frictional sliding experiments have generated stick-slip events which have been regarded as analogues for shallow, natural earthquakes (Bedford et al., 2022; Brace and Byerlee, 1966; Dieterich, 1992; Goebel et al., 2015; Johnson et al., 2013; McLaskey et al., 2015; Rivière et al., 2018; Ruina, 1983; Scholz et al., 1972; Xia et al., 2004). Laboratory stick-slip events (Chapter 1, Section 1.2.1) are spontaneous jerks caused by sliding at a simulated fault interface. During the initial 'stick' phase, elastic strain builds up and then stress is suddenly released during the 'slip' phase. Microscale observations in the laboratory have demonstrated some of the underlying physical processes that govern earthquakes, from frictional healing (Scuderi et al., 2014) to supershear rupture (Passelègue et al., 2013). Specifically, measuring radiated wavefields can give additional insight into seismic sources such as stick-slips, enabling source properties to be estimated under carefully controlled experimental conditions. Calibrating acoustic monitoring equipment can isolate the seismic source from other waveform components (such as path and instrument effects), reducing waveform complexities due to the geometry of measurement systems (McLaskey et al., 2015).

Nevertheless, several issues remain. Discrepancies between waveform modelling and spectral estimates of earthquake source properties following absolute acoustic calibration are prevalent, with stress drop estimates showing little or no correlation between both types of estimates and differences of a factor of 10 (McLaskey et al., 2015). Moreover, the origin of high-frequency radiation over the continuum from slower to fast earthquakes continues to be poorly understood (Das, 2007; Wirth et al., 2022). While some authors have considered transitions from slow to fast earthquakes and the effect on the frequency of radiated waveforms (e.g. McLaskey and Yamashita, 2017; Wu and McLaskey, 2019; Bolton et al., 2022), often experimental conditions are systematically changed to generate heterogeneous fault evolution.

In this chapter, a direct shear experiment on poly(methyl methacrylate) (PMMA) plastic is carried out to understand how fault property evolution with slip results in systematic changes to seismic source properties, with no additional experimental input (i.e. no change to strain rate or confining pressure). PMMA is a useful analogue material for frictional sliding experiments as it is around 20 times more compliant than Westerly granite, generating events with a smaller nucleation length (~ mm vs cm). Seismic wavefields radiated during stick-slip are measured using calibrated piezoelectric acoustic sensors. To validate the calibration of our setup using the ball drop method (Chapter 3), mechanical and seismic estimates of the seismic moment are compared and show a good correlation between them. Then, the evolution of seismic source properties including stress drop, seismic moment and average rupture velocity with cumulative slip is investigated. Finally, method limitations, implications for fault stability criteria, fault healing and earthquake source property estimation for seismic hazard analysis are discussed.

4.2 METHODS

4.2.1 Experimental configuration and preparation

Dry (zero pore fluid pressure, ambient laboratory conditions) direct shear tests are carried out on rectangular PMMA slabs using a triaxial oil-medium deformation apparatus ($\sigma_1 > \sigma_2 = \sigma_3$) in the University of Liverpool's Rock Deformation Laboratory. PMMA's mechanical properties are well known and its elastoplastic behaviour is favourable to stick-slip nucleation. PMMA has been used in previous studies which have highlighted the similarity between radiation patterns emitted in PMMA-PMMA sliding experiments and natural earthquakes, with double couple sources observed (McLaskey and Glaser, 2011). As the slabs are thin relative to their length and width (36 x 18 x 4 mm), the effects of the block thickness can largely be ignored and the configuration resembles a crack-like model (Figure 4.1; Zhou et al., 2020). The configuration is an adaptation of previous configurations that have already been used to perform frictional sliding experiments (Figure 4.1; Ashman and Faulkner, 2023; Bedford et al., 2022). PMMA is used as it

generates stick-slip events with much smaller nucleation length L_c than other materials such as Westerly granite:

$$L_c \approx C \frac{G\delta_c}{\sigma_n(\mu_p - \mu_r)}. \quad (4.1)$$

C is the crack shape factor (typically $7\pi/24$ for a circular crack), G is the shear modulus, δ_c is a characteristic slip distance in m, σ_n is the normal stress, μ_p is the peak friction level and μ_r is the residual friction level (Andrews, 1976; Dieterich, 1992; Eshelby, 1957). As the shear modulus G of PMMA (1.7 GPa) is around 20 times smaller than Westerly granite (30 MPa), a more complex sequence of events can be expected to develop during frictional siding experiments due to the significantly (around 20 times) smaller nucleation length.

Slabs of PMMA are cut to shape using a laser by the University of Liverpool Core Services with an accuracy of ±10 μm. One narrow edge of each slab is ground and polished to create a curved edge (4mm radius) to fit the stainless-steel slider (Figure 4.1). The slabs protrude by 0.4 mm above the stainless-steel slider to ensure solely slab-slab contact and avoid slab-steel holder contact (Figure 4.1).

Surfaces are wet ground using Z_{rms} = 18.3 μm grit silicon carbide to create homogenous roughness and to reduce cohesion (S. Marty et al., 2019). Gouge produced by polishing is removed by compressed air and samples are cleaned using an ultrasonic bath and left to dry completely to ensure a clean surface before frictional sliding. During experiments, sample slabs are offset using rubber spacers to create a nominal contact area A of 468 – 567 mm^2. Thus, shear stress τ in Pa can be calculated:

$$\tau = \frac{F_a}{W(L_i + u_c)}, \quad (4.2)$$

where F_a is the axial load in kN, W is the width of the slab surface in m, L_i is the initial length of contact in m (2.6 x 10^{-2} m) and u_c is the displacement, corrected for stiffness, in m. Adding the stiffness-corrected displacement to the initial length of contact accounts for the increase in nominal contact area during experiments (Harbord, 2018).

The stiffness corrected displacement, u_c, accounts for the stiffness k of the loading column (Chapter 2, Section 2.2.6.1) and can be calculated via triaxial calibration by loading a 'blank' cylindrical steel sample in the triaxial deformation apparatus at constant normal stress (constant confining pressure). The stiffness can be found by taking the gradient of the curve at the target axial load in kN (Chapter 2; Figure 2.9).

Consequently, the stiffness-corrected displacement u_c can be calculated as follows:

$$u_c = \frac{F_p - F_r}{k}, \tag{4.3}$$

where F_p and F_r are the peak and residual axial force of a stick-slip in N, respectively. F_p is reached after elastic loading, where elastic strain builds up. After F_p is reached, shear stress is suddenly released and slip accelerates, with force decreasing to F_r.

Once prepared and glued with Loctite® Super Glue to stainless steel L-shaped sliders, the PMMA sample is placed into polytetrafluoroethylene (PTFE) and polyvinyl chloride (PVC) jackets to isolate the sample from the confining medium. An additional thin disk of PTFE is placed at the bottom of the sample to minimise friction between the sample and loading platen so that only any shortening perpendicular to the sliding surface can be accommodated. Then, the jacketed sample is placed into a sample assembly with two P- and two S-wave piezoelectric sensors (seismic sample assembly; Chapter 2, Figure 2.2) at either end of the sample. Sensors are mounted perpendicular (90°) to the fault interface (Figure 4.1c).

The direct shear configuration results in normal stress σ_n equating to confining pressure P_c. This sample configuration is advantageous over more traditional 30° saw cut configuration experiments. This is because the nominal contact area decreases linearly with displacement: thus, the fault normal stress is not altered by the application of load and the load point velocity v_{LP} is equivalent to fault velocity.

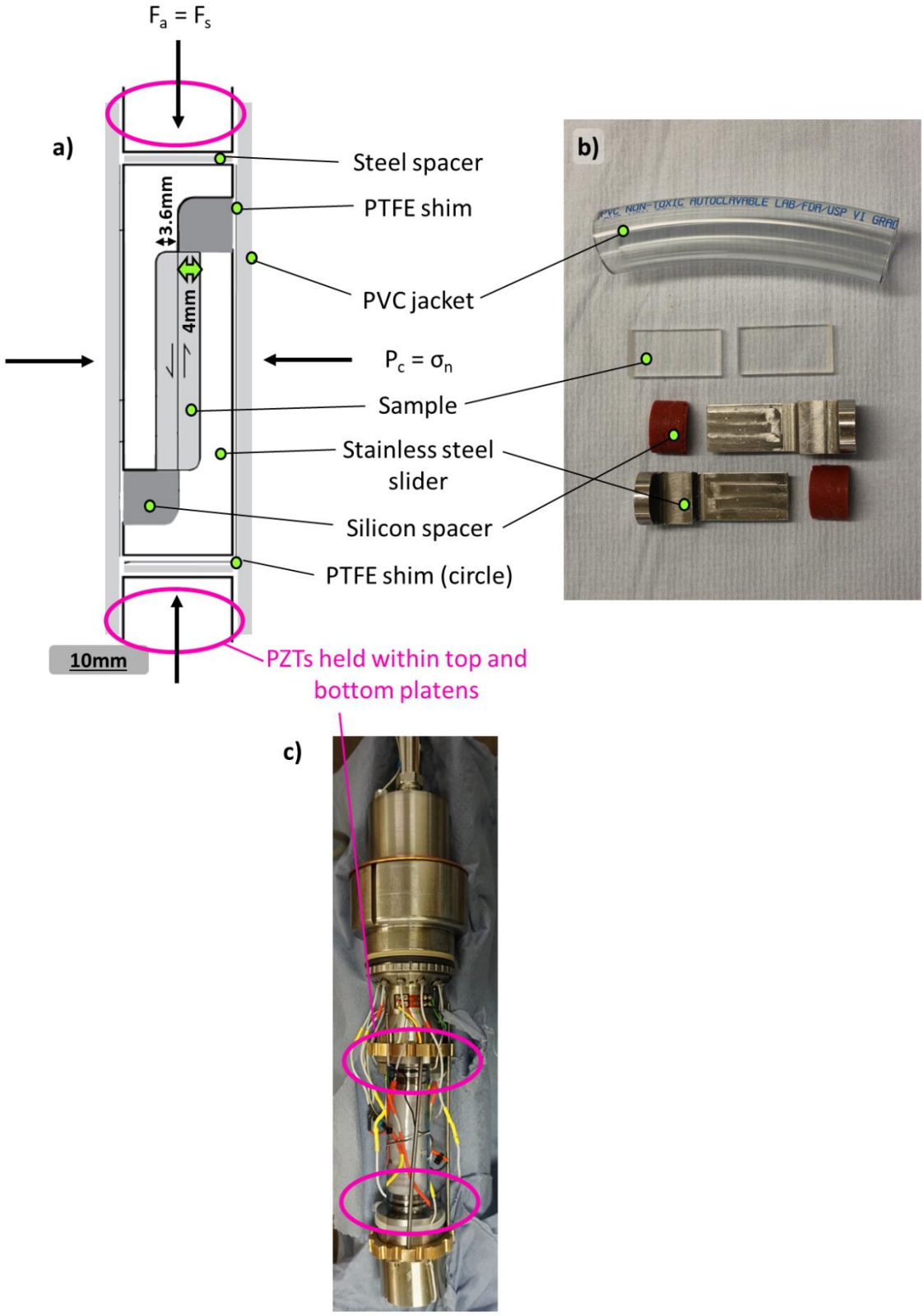

Figure 4.1: *a) Schematic of seismic sample assembly experimental configuration used to conduct single direct shear experiments. b) Photo of PMMA slabs, silicon spacers, stainless steel slider and PVC jacket. c) Photo of seismic sample assembly, showing sample position and platens with piezoelectric crystals (PZTs) glued within (pink ovals).*

4.2.2 Mechanical loading

All experiments are performed using a triaxial deformation apparatus designed and built by D. Faulkner (Chapter 2). The apparatus can reach a confining pressure of 250 MPa with a resolution of 0.01 MPa, and an axial load of 300 kN with a resolution of ~10 N (Faulkner and Armitage, 2013; Mitchell and Faulkner, 2008).

Experiments are conducted by initially increasing the confining pressure in the vessel to the target normal stress (30 MPa) using a compressed air driven pump. The apparatus is left for 30 minutes to allow the pressure to equilibrate from any adiabatic changes. After a stable target normal stress is reached, the confining pressure servo-control system is applied to maintain a constant normal stress. Then, the axial piston is driven upwards using the loading servo-control system until a small force is detected, which is when the axial piston contacts the seismic assembly (Figure 4.2). This point of contact is the 'hit-point' displacement, which is used to correct all force and displacement data. After the hit-point is reached, mechanical data are observed and recorded via a LabView script and the frictional sliding experiment begins. Mechanical data are recorded at a sampling frequency of 10 Hz.

To generate spontaneous stick-slip behaviour, a constant load point velocity of 1 μm/s is maintained by the axial loading servo system. The mechanical properties of stick-slips are measured after the interface has sheared 1.5 mm, well above the displacement that the peak shear stress is observed (around 10 MPa at 0.9 mm). Samples are sheared up to a maximum displacement of 5 mm.

Stick-slip instabilities are associated with a build-up of shear stress and a sudden stress drop with measurable fault slip, which radiates seismic waves. Monitoring the evolution of shear stress while applying a constant load point velocity allows the experiment to quantify fault slip and the frequency and magnitude of stress drops.

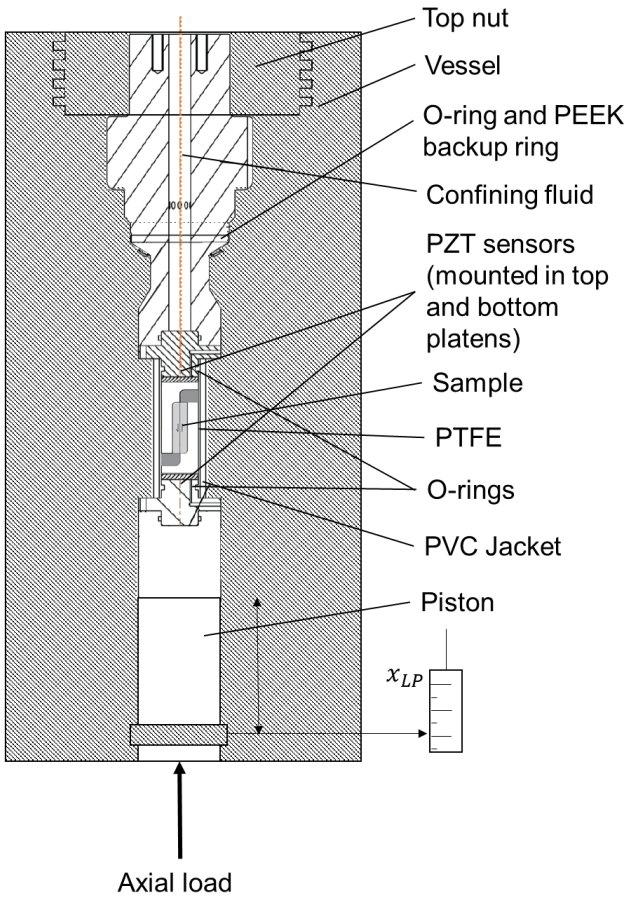

Figure 4.2: *Schematic diagram of the PMMA sample inside the seismic sample assembly, placed within the pressure vessel of the triaxial deformation apparatus. The sample 'fault' interface is oriented in the loading axis direction, allowing for simple calculation of mechanical observations such as fault slip.*

4.2.3 Seismic data acquisition

Two P- and two S-wave piezoelectric sensors (Boston Piezo-Optics Inc., 10 mm diameter) mounted within both platens (top and bottom) of the seismic sample assembly are used to detect seismic waves radiated from large stick-slip events. The magnitude and frequency of stick-slip events are quantified by using McLaskey et al.'s (2015) absolute acoustic calibration method (Chapter 3), which assumes small ball drop impacts on the platens of the seismic sample assembly as empirical Green's functions. The method links momentum to moment, allowing path and instrument effects to be deconvolved from recorded seismic signals, leaving solely the source of the events.

Events are recorded during the experiment using a high-frequency acoustic monitoring system with a sampling rate of 10 MHz. A multi-channel, 12-bit oscilloscope with 8 channels is used to record voltage signals. A trigger voltage threshold is set (1% of maximum voltage 20 V, i.e. 0.2 V) to minimise noise detection. Further description of the triaxial apparatus and the high-frequency acoustic monitoring system is given in Chapters 2 and 3 of this thesis.

4.2.4 Mechanical data processing

Following data acquisition in LabView, mechanical data are post-processed in Matlab 2020a. Shear stress τ is calculated using Equation 4.2 with code *friction_process.m*. Stiffness-corrected displacement u_c is calculated using Equation 4.3 with code *triaxial_calibration.m*.

4.2.4.1 Automatic stick-slip detection: find_stickslip_v4.m

Peak and residual shear stresses (τ_p and τ_r respectively) of large stick-slip stress drops are detected automatically using a short-term average and long-term average (STA-LTA) routine, executed using code *find_stickslip_v4.m*. Using Matlab function *mov_mean*, the centred moving average of shear stress values are calculated over three window lengths (a short, medium and long-term average window, dependent on the user-selected value of the window length, i.e. the number of points in a window, of a stick-slip, *slength*). The minimum displacement and maximum duration of a stick-slip, *smin,* and *tmin* respectively, are estimated and used to reduce the likelihood of false picks due to instrument noise. Lower and upper displacement bounds, *llimit* and *ulimit,* are used to limit the displacement range of detection to when large stick-slips occur. An additional tolerance value, *stol*, is used to account for noise emanating from the servo-control system, with noisier experiments requiring a higher tolerance to detect stress drops.

Results were initially verified manually to observe the routine's accuracy, with stress drops in MPa and load point displacement in mm detected to ± 1% accuracy when verified manually. Occasionally, small precursor events were also detected, but these were more difficult to pick due to their lower amplitude and noise level. Precursor events are generally picked manually by selecting τ_p at the local maximum and τ_r at the local minimum. Table 4.1 outlines the parameters used in this chapter and Figure 4.3 outlines an example of automatic stick-slip picks.

Table 4.1: *Parameters used in code find_stickslip_v4.m to automatically detect stick-slip events.*

Parameter	Value (units, if applicable)
slength	5
smin	0.75 (mm)
tmin	0.01 (s)
llimit	1.5 (mm)
ulimit	5.5 (mm)
stol	0.97

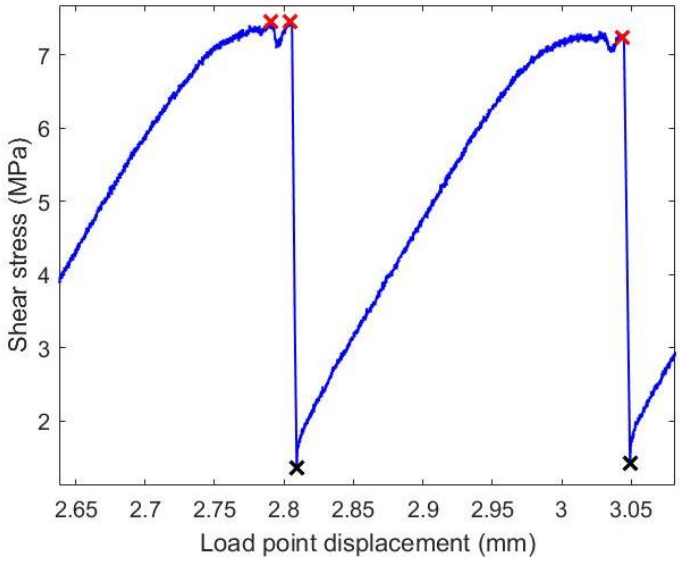

Figure 4.3: *Start (red crosses) and end (black crosses) of large stick-slip events, automatically detected by find_stickslip_v4.m code. While the start of a precursor event (first red cross) is detected, the end is not, highlighting the difficulty in picking smaller precursors.*

Once τ_p and τ_r are derived, the mechanical stress drop $\Delta\tau_m$ in Pa can be found (Figure 4.4a):

$$\Delta\tau_m = \tau_p - \tau_r. \tag{4.4}$$

4.2.4.2 Calculation of fault properties and 'mechanical' seismic moment

The machine loading stiffness k (around 83 kN/mm at 30 MPa) is derived through prior calibration of the loading column with a 'blank' sample at pressure with stick-slips occurring between 1–7 kN (Equation 2.1; Chapter 2, Section 2.2.6.1). Due to the experimental system setup, direct measurements of force F and load point displacement x_{LPD} can be used to calculate peak and residual shear stress, τ_p and τ_r using Equation 4.2. Following this, the mechanical static stress drop $\Delta\tau_m$ is calculated using Equation 4.4. Stick-slip occurs when the fault weakening rate with slip is greater than the maximum rate of elastic unloading, which results in a force imbalance and slip acceleration. The average fault slip during stick-slip, x_{fault} in m, can be calculated by assuming slip occurs when the fault weakening rate with slip is greater than the maximum rate of elastic unloading, which results in a force drop ($\Delta F = F_p - F_r$) and acceleration (Section 4.2.1):

$$x_{fault} = \frac{F_p - F_r}{k}. \tag{4.5}$$

Pre-seismic slip is defined as the small amount of fault slip (~1 μm) that precedes large stick-slips (~10s of μm slip), stress drop and rupture. Pre-seismic fault slip is much slower than dynamic

earthquake (and stick-slip) slip and has been detected before large earthquakes in nature, such as along the Nankai trough in the 1944 (Tonankai) and 1946 (Nankaido) earthquakes (Linde and Sacks, 2002; Sato, 1977). Pre-seismic slip has been proposed as the underlying process that drives earthquake nucleation (Kaproth and Marone, 2013). Therefore, pre-seismic slip is calculated in this study using mechanical measurements (force and load point displacement). An idealised laboratory stick-slip with zero pre-seismic slip (Figure 4.4a) will load completely elastically with a combined machine and sample stiffness $k_{m+sample}$ (Chapter 2, Section 2.2.6.1) until it reaches the peak force, F_p. If a laboratory stick-slip has significant pre-seismic slip, the fault will load elastically until it starts to slowly deform and slip (Figure 4.4b). In this case, the peak force F_p is smaller than expected in the idealised case where loading is completely elastic. To calculate the amount of pre-seismic slip in m, the expected peak force of each stick-slip, F_p' (i.e. in the idealised case of zero pre-seismic slip) is forecasted using linear extrapolation (Figure 4.4). F_p' is calculated by assuming that loading is completely elastic at the start of loading (following the previous stick-slip stress drop) with the combined sample-machine loading stiffness $k_{m+sample}$. F_p' is then used to calculate the pre-seismic slip, $x_{preseismic}$ using trigonometry and Equation 4.5.

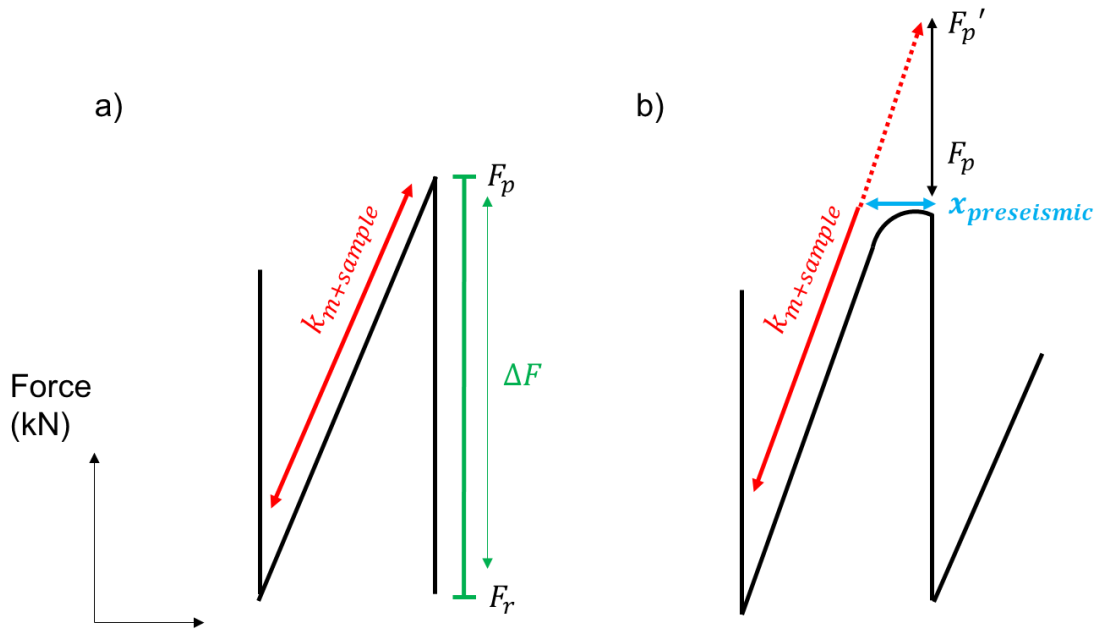

Figure 4.4: *a) Schematic diagram of idealised stick-slip with zero pre-seismic slip: elastic strain increases force until it reaches peak force F_p, where force (and therefore, shear stress) is released causing a decrease of ΔF in force to residual force, F_r. b) Schematic diagram of a stick-slip with significant pre-seismic slip. Pre-seismic slip, $x_{preseismic}$ is calculated using the expected peak force of each stick-slip, F_p'.*

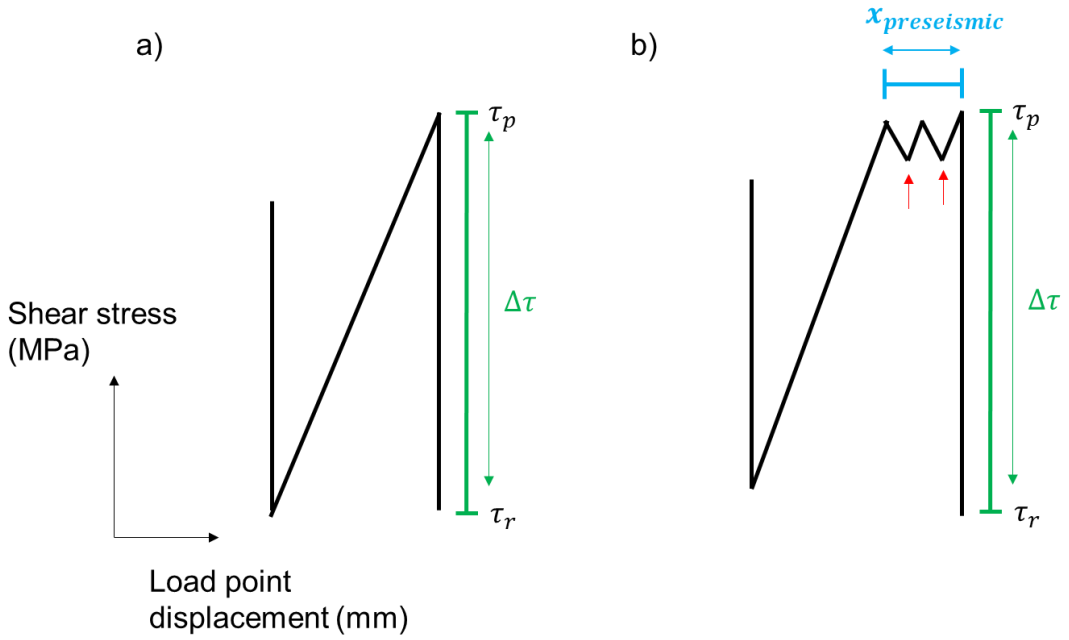

Figure 4.5: *a) Schematic diagram of idealised large stick-slip with zero pre-seismic slip: elastic strain increases shear stress until it reaches peak shear stress τ_p, where shear stress is released causing a decrease (stress drop) of $\Delta\tau$ in shear stress to residual shear stress, τ_r. Shear stress is proportional to force (Equation 4.2). b) Schematic diagram of a stick-slip with significant pre-seismic slip $x_{preseismic}$ (blue line). Green arrows indicate large stick-slip, red arrows indicate small precursory events.*

The average slip velocity $\bar{v}$ in m/s of both large stick-slip and precursory events is calculated by dividing fault displacement x_{fault} by the event duration, Δt in s:

$$\bar{v} = \frac{x_{fault}}{\Delta t}. \qquad (4.6)$$

While $\bar{v}$ of precursory events can be calculated accurately at 10 Hz sampling frequency due to their long durations (up to 8 s), as large stick-slip events have a very short duration (<1 s), $\bar{v}$ is generally underestimated for large stick-slip, representing the lower limit of slip velocities.

The seismic moment (Chapter 1, Section 1.1) derived from mechanical data $M_{0,m}$ in Nm can be expressed by the formula:

$$M_{0,m} = GAD, \qquad (4.7)$$

where G is the shear modulus of the experimental apparatus in Pa, A is the rupture area in m^2 and $D = x_{fault}$, the average fault slip in m.

4.2.4.3 Estimation of shear modulus, G

While rupture area A (468 – 567 mm^2; Section 4.2.1) and average fault slip D (measured during the experiment) are known values, shear modulus G is difficult to calculate directly, as it is equal to the ratio of shear stress to shear strain. Shear stress is easily derived, but shear strain (the ratio of an object's original dimensions and displacement due to applied stress) is difficult to quantify due to the complex geometry of the apparatus.

To relate laboratory stick-slip to earthquakes, McGarr (2012) used data from rupture propagation experiments (Johnson and Scholz, 1976; Lockner and Okubo, 1983) to constrain a crack propagation and arrest model. The study found that while fault stiffness $k_{m+sample}$ and event duration Δt for stick-slip and earthquakes differ, even with laboratory and natural faults of the same dimension, the product $k_{m+sample} \times \Delta t$ is scale independent for laboratory stick-slip and earthquakes. $k\Delta t$ is the same order of magnitude (~10 MPa s/m) for stick-slip and earthquakes. The scale independence for earthquakes is consistent with earthquake source properties such as stress drop and average slip velocity (Kilgore et al., 2017). Combining this scale-independent product $k_{m+sample} \times \Delta t$ with Walsh's (1971) dimensional relation for stiffness (that stiffness is proportional to the ratio of shear modulus of the loading system G and the dimension of the slipping region) leads to the following equation:

$$k_{m+sample} \times \Delta t \approx 1.1 \frac{G}{\beta}. \qquad (4.8)$$

β is the shear (S-) wave velocity in m/s. Equation 4.8 can be rearranged to estimate the shear modulus of the loading system G. $k_{m+sample}$ is calculated by finding the mean gradient of all stick-slips (all 12 are outlined in Table 4.2), which is found to be 33.9 kN/mm using measured force and load point displacement (Figure 4.4a). The mean event duration Δt can also be calculated using mechanical data (although this is probably overestimated – see Section 4.2.4.2) and is found to be 0.342 s (Table 4.2). The shear wave velocity β is assumed to be 1.20 km/s, as the sample configuration is predominately made of PMMA. Using these values, $G \approx 33.3$ GPa.

To capture uncertainty in the approximation (Equation 4.8), in this study, G is estimated to be between 23.3 – 43.3 GPa, which is in line with previous studies with similar setups (Jia et al., 2020; Kilgore et al., 2017; McGarr, 2012). Moreover, the shear moduli of the three main materials involved in loading, PMMA, 17-4 stainless steel and H.50/AISI H.13 hot work tool steel, are 1.7 GPa, 80.7 GPa and 81 GPa respectively. Considering this study's interest in near-fault moment release, the shear modulus of PMMA should dominate, making the estimate of $G \approx 33.3$ GPa reasonable.

All calculations of fault properties and mechanical estimates of source properties are carried out using Matlab code *stickslip_process.m*.

4.2.5 Seismic data processing

Seismic data are processed using Matlab code *acoustic_process_v3.m* using the data processing workflow outlined in Chapter 3, Section 3.2.1 (McLaskey et al., 2015). The algorithm quality controls seismic data by ensuring that the signal-to-noise ratio (SNR) is greater than 3 (Chapter 3, Section 3.3.4). Consequently, internal instrument-apparatus response and stick-slip spectra vectors can be different lengths due to SNR criteria. To solve this issue, stick-slip responses are linearly (in log-log space) interpolated so that frequencies are the same before division. As P-wave data are used, McLaskey et al.'s (2015) theoretical estimation of the force-moment relation $C_{F\dot{M}}$ is equal to the seismic assembly's P-wave velocity, 5.65 km/s.

The internal instrument-apparatus response is divided from the stick-slip signals, leaving solely the source spectrum. The amplitude of the flat, low-frequency part of the spectrum is equal to the seismic moment $M_{0,s}$ in Nm. Event source spectra are fit with a Brune (1970) model curve using a non-linear least squares (Teunissen, 1990) function in script *brune_fit.m*. Brune's (1970) model is based on the instantaneous application of a shear stress pulse to a circular fault of finite radius, which causes stress evolution to instantaneously drop from pre-event shear stress to post-event shear stress (Chapter 1, Section 1.4.1). Beyond the finite radius r of the source, the velocity of shear displacement u goes to zero for times larger than r/β. Thus, Brune's model assumes that rupture is contained in the crust – this assumption is discussed in Section 4.4.3. Brune's model assumes a simple, circular earthquake source with the moment rate function given by:

$$\dot{M}(\mathrm{f}) = \frac{M_{0,s}}{\left[1 + \left(\frac{f}{f_0}\right)^{n\gamma}\right]^{1/\gamma}}, \tag{4.9}$$

where $M_{0,s}$ is the seismic moment in Nm, f is frequency, f_0 is corner frequency (both in Hz) and n and γ describe the high-frequency spectral decay (Abercrombie, 2021; Brune, 1970). In this work, n is assumed to equal 2 in line with previous studies (Udias et al., 2014c). After setting initial values and upper and lower bounds for solvable parameters, the script solves for $M_{0,s}$, f_0 and, if desired (unfixed), a proxy parameter for γ, κ, in s:

$$\kappa = -\frac{\ln 1/\gamma}{\pi f}. \tag{4.10}$$

In previous studies, γ has been estimated to be approximately 1 or 2 for earthquake models (e.g. Aki et al., 1969; Hanks, 1979). To reduce the effect of the trade-off between corner frequency f_0 and spectral decay $e^{-\pi\kappa f}$, which governs the shape of the spectrum around f_0, the spectral decay parameter κ is held constant at 2.6 μs (Anderson and Hough, 1984). κ is calculated before the final amplitude spectra fit by running model *brune_fit.m* with κ unfixed, allowing κ to change iteratively alongside $M_{0,s}$ and f_0. The average value of κ, 2.6 μs, is then used.

To compare seismic results to mechanical results and other seismological studies, the seismic static stress drop $\Delta\tau_s$ in Pa is generally estimated using a circular fault model with the following equation:

$$\Delta\tau_s = \frac{7}{16}\frac{M_{0,s}}{r^3}. \tag{4.11}$$

However, due to the geometry of the experimental setup (Figure 4.1), it may be more suitable to use a rectangular fault model:

$$\Delta\tau_s = \frac{2}{\pi}\frac{M_{0,s}}{W^2 L}. \tag{4.12}$$

W and L are the width (18 mm) and length ($L = L_i + u_c$; Equations 4.2 and 4.3) of the slab, respectively (Stein and Wysession, 1991). Estimates of $\Delta\tau_s$ using both a circular and rectangular fault model are compared to demonstrate the impact of rupture model geometry on stress drop estimates.

The source radius r in m is estimated using corner frequency measurements:

$$r = 2.34\frac{\beta}{2\pi f_0}. \tag{4.13}$$

The shear wave velocity β is assumed to be 1.20 km/s, as the sample configuration is predominately made of PMMA.

The observed rise time in s of the displacement pulse of each stick-slip waveform $t_{1/2} \sim 1/f_0$, can be used to estimate the average rupture velocity $\bar{v}_s$ in m/s of large stick-slip events on rectangular faults (adapted from Equation 19, Deichmann, 1997):

$$\bar{v}_s = \frac{1}{\sqrt[3]{\frac{\pi}{2}\frac{{t_{1/2}}^3}{M_{0,s}}\Delta\tau_s} + \frac{1}{\alpha}\sin\theta}. \tag{4.14}$$

α is the sample P-wave velocity (assumed to be 1.54 km/s) and θ is the initial take-off angle of the ray from the perpendicular, equal to 90° in this case (Boatwright, 1980).

4.2.6 Comparing mechanical to seismic estimates of source properties

As a result of a shear displacement u, the available stress across the fault decreases to the dynamic shear resistance during rupture, τ_f. τ_f acts to resist fault slippage, which causes the fault to lock and slip to cease (Orowan, 1960). The dynamic stress drop ($\tau_0 - \tau_f$, where τ_0 is the tectonic stress, i.e. the shear stress before rupture; equivalent to τ_p; Figure 4.5a) controls how much energy is lost as frictional heating and how much goes into seismic wave generation. Several studies have highlighted that static seismic stress drop $\Delta\tau_s$ appears to be a small fraction of dynamic stress drop $\tau_0 - \tau_f$ (Abercrombie, 2021; Aki, 1967; Brune and Allen, 1967; Wyss and Molnar, 1972).

While there is no way to determine dynamic shear resistance τ_f, it is widely accepted that it is very small during seismic slip. Experimental studies have shown that $\tau_f \sim 0.1$ due to co-seismic weakening mechanisms such as flash heating, dehydration reactions and thermal pressurisation (Di Toro et al., 2011). It is probable that τ_f is small in PMMA experiments, as PMMA asperities have been shown to thermally weaken during shear, which reduces friction (Ben-David et al., 2010).

The static mechanical stress drop $\Delta\tau_m$ from mechanical measurements provides a direct estimate of the stress released during slip (the difference between peak and residual shear stress, $\tau_p - \tau_r$; Figure 4.5a). It should be noted that dynamic shear resistance and residual shear stress are not equal i.e. $\tau_f \neq \tau_r$ (Orowan, 1960). Consequently, $\Delta\tau_m$ and $\Delta\tau_s$ are not directly comparable.

Blanke et al. (2021) found a relationship between mechanical stress drop and seismic stress drop. By observing acoustic emissions during stick-slip, they found that mechanical stress drops $\Delta\tau_m$ scale with seismic stress drop-moment magnitude dependence (gradients of M_W-$\Delta\tau_{AE}$ slopes). This is of particular interest as the dependence of stress drop on seismic moment and rupture dimension are key areas of uncertainty, with many contrary findings (Aki, 1967; Allmann and Shearer, 2007; Cocco et al., 2016; Huang et al., 2016; Ide, 2003; Kanamori and Brodsky, 2004). While it is not possible to calculate multiple M_W-$\Delta\tau_s$ slopes and compare to $\Delta\tau_m$ due to limited data, it would still be interesting to see if static stress drops $\Delta\tau_s$ (calculated using seismic data; Equations 4.11 and 4.12) and $\Delta\tau_m$ (calculated using mechanical data; Equation 4.4) scale and whether stress drop is dependent on seismic moment.

Seismic moment calculated from mechanical and seismic data ($M_{0,m}$ and $M_{0,s}$ respectively) are easier to directly compare, as they are both measures of rupture size.

4.3 RESULTS

4.3.1 Mechanical observations

In this test, a sequence of 12 spontaneous large stick-slip events (static mechanical stress drop $\Delta\tau_m > 0.5$ MPa; Figure 4.5a) were observed (Figure 4.6). The experimental results show a wide range of mechanical and seismological behaviour and slip dynamics, including stable sliding, quasi-stable pre-seismic slip with small precursory events (static mechanical stress drop $\Delta\tau_m <$ 0.5 MPa; Figure 4.5b) and large stick-slip (Table 4.2 and Figure 4.5a). Large stick-slip events occur regularly, on average, once every 250 s. The amplitude of large stick-slip events slowly decreases as cumulative displacement increases.

Detailed plots of shear stress vs. load point displacement for the first (PMMA_30_001) and last (PMMA_30_012) large stick-slip events are shown in Figures 4.6b and 4.6c respectively. Stress drop $\Delta\tau_m$ (and fault slip x_{fault}, as they are proportional; Equation 4.5) decreases with cumulative displacement, by up to 23% comparing the largest event PMMA_30_001 to the smallest event PMMA_30_008. Large stick-slip events are often preceded by smaller precursory events (Figure 4.5c). These events exhibit period-doubling, alternating between small, slow and large, fast stick-slips, which has been seen in numerical models (Gu et al., 1984) and in friction experiments where the loading stiffness approaches the critical weakening rate (Leeman et al., 2016; Scuderi et al., 2016; Shreedharan et al., 2020). This period-doubling has also been observed in nature along the San Andreas fault at Parkfield (Veedu and Barbot, 2016) and is likely to be caused by interactions between the roughened frictional interface of PMMA and potentially gouge created during sliding.

Table 4.2: *Properties of laboratory-generated stick-slip events from PMMA direct shear experiment.*

Event Name	Starting load point displacement (mm)	Max. duration (s)	No. precursors	$M_{w,s}$	$M_{w,m}$, G = 23.3 GPa
PMMA_30_001	1.67	0.3 ± 0.1	0	-4.30	-4.08
PMMA_30_002	1.90	0.3 ± 0.1	1	-4.30	-4.09
PMMA_30_003	2.12	0.2 ± 0.1	1	-4.32	-4.10
PMMA_30_004	2.34	0.2 ± 0.1	1	-4.33	-4.10
PMMA_30_005	2.57	0.3 ± 0.1	1	-4.33	-4.11
PMMA_30_006	2.80	0.4 ± 0.1	1	-4.34	-4.11
PMMA_30_007	3.04	0.5 ± 0.1	1	-4.35	-4.11
PMMA_30_008	3.28	0.4 ± 0.1	2	-4.36	-4.12
PMMA_30_009	3.77	0.4 ± 0.1	3	-4.37	-4.14
PMMA_30_010	4.02	0.4 ± 0.1	4	-4.39	-4.13
PMMA_30_011	4.30	0.4 ± 0.1	4	-4.39	-4.13
PMMA_30_012	4.57	0.3 ± 0.1	5	-4.39	-4.15

Mechanical static stress drop measurements τ_m show a decrease in stress drop with load point displacement (Figure 4.7a). Static stress drops of small precursory events generally increase as a large stick-slip event approaches. For precursors to event PMMA_30_012, $\Delta\tau_m$ increases from ~0.1 MPa to ~0.4 MPa, with a large stick-slip stress drop of ~6 MPa (Figure 4.7a). Slower, smaller precursor events (occurring over durations of ~ 5 s with ~1 μm slip, versus 0.1 s with ~ 50 μm slip; Table 4.2 and Figure 4.6) have mechanical stress drop magnitudes between 2 – 8% of large stick-slip stress drops, consistent with previous studies (Ide et al., 2007; Leeman et al., 2016; Scuderi et al., 2016; Shreedharan et al., 2020). Large stick-slip stress drop magnitude decreases with slip (Figure 4.6a). Notably, audible large stick-slip events became quieter as static mechanical stress drop τ_m decreased with experiment progression, which has been observed in other studies (McLaskey and Yamashita, 2017; Tinti et al., 2016). The duration of large stick-slips increases slightly towards the middle of the experiment as the amount of small precursor events increases (Table 4.2).

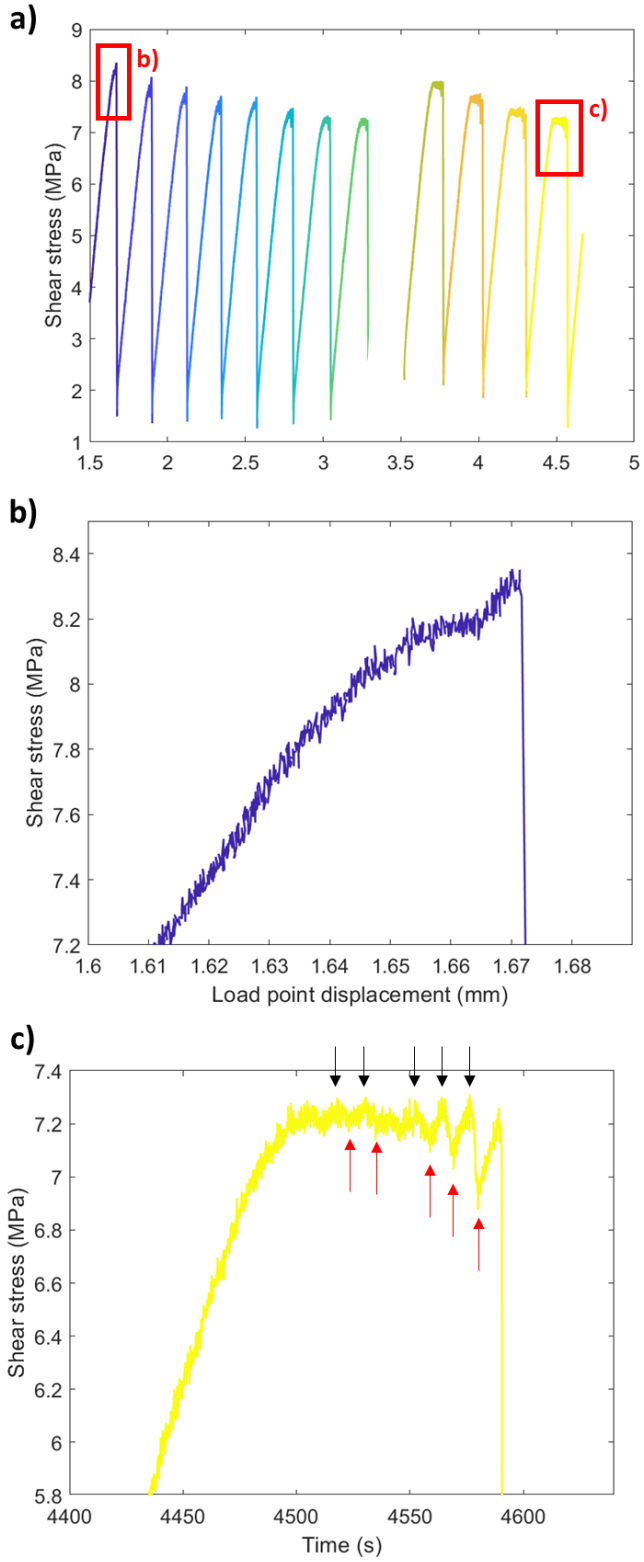

Figure 4.6: *a) Shear stress as a function of load point displacement (a-b) and time (c) for 12 stick-slip events, PMMA_30_001 to PMMA_30_012 (same colour code and map 'parula' used throughout the chapter for each event). Smaller precursory events preceding large stick-slip events can be observed in more detailed plots of the first (b) and last (c) large stick-slip. c) Manual picks of the start (black arrows) and end (red arrows) of precursory events preceding event PMMA_30_012.*

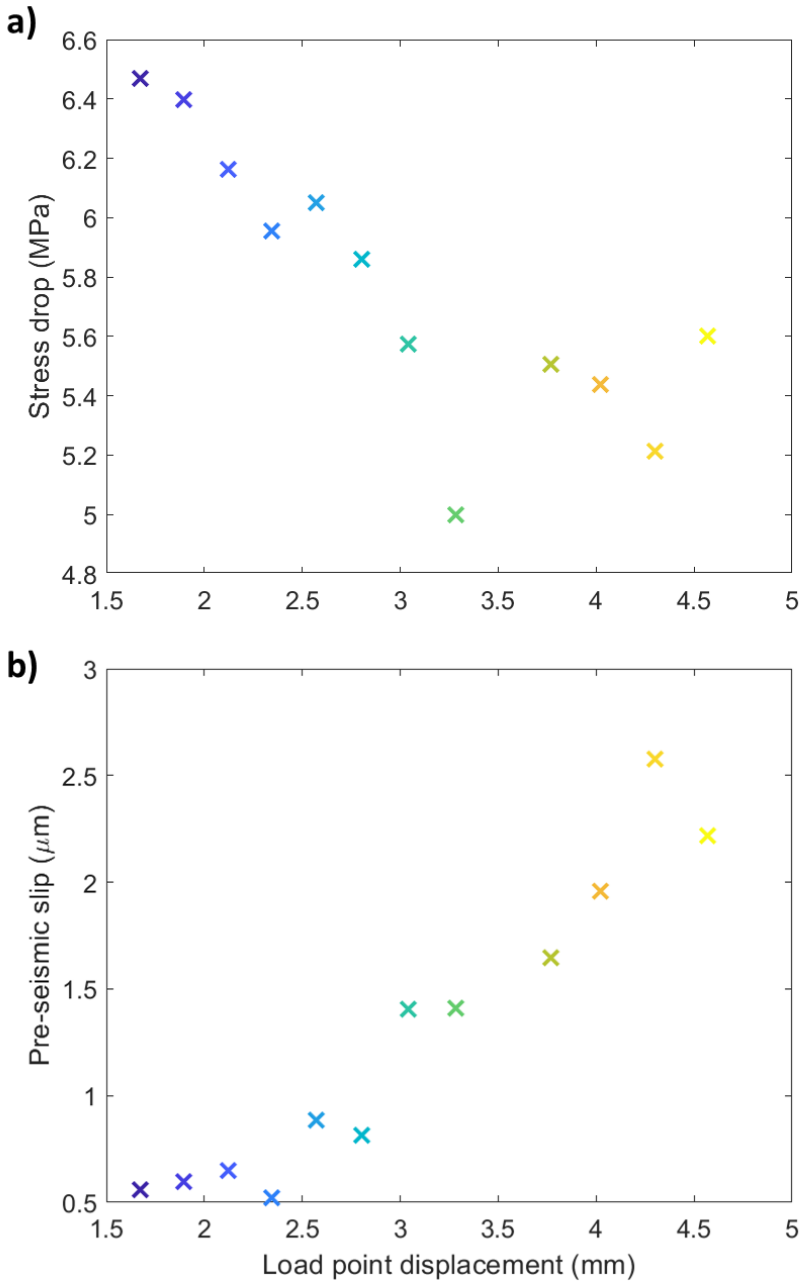

Figure 4.7: *a) Static mechanical stress drop $\Delta\tau_m$ and b) pre-seismic slip preceding each large stick-slip, coloured crosses represent each stick-slip with colour code outlined in Figure 4.6 in this and future figures in this chapter.*

4.3.2 Acceleration of slip velocity of precursory events before large stick-slip events

As slip increases, the combined sample-machine loading stiffness (i.e. the slope of the shear stress-load point displacement plot in Figure 4.5a) decreases as τ_p is approached. Pre-seismic slip (and slip duration) generally increases with displacement, with more precursory events in the latter stages of the experiment (Figure 4.6b). This highlights a clear transition in frictional behaviour with displacement, from more pronounced stick-slips with little pre-seismic slip at the

start, to stick-slips with significant pre-seismic slip and precursory events that appear to accelerate towards the stick-slip.

As loading is controlled by a constant load point velocity, the pre-seismic slip must cause the average stressing rate on the sample to decrease (McLaskey and Lockner, 2014). Pre-seismic slip increases with cumulative displacement, from ~0.5 μm to 2.5 μm (Figure 4.7b). Moreover, precursory events during pre-seismic slip (red arrows; Figure 4.6b) have durations up to ~8s and have lower slip rates (mean of ~0.5 μm/s) than main stick-slip events (mean of ~0.2 mm/s, a minimum estimate due to low resolution in fault slip). These events appear to transition from oscillatory slip to more pronounced, large stick-slips with much larger stress drops. These slow, precursory events were not detected by seismic acquisition apparatus – this could either be because they are aseismic or that the signals had smaller amplitudes than the noise level.

4.3.3 Seismic observations

Figures 4.8a and 4.8b present recorded P-wave motion and spectra (before absolute acoustic calibration) from the top sensor for 12 large stick-slip events. Waveforms for slower precursor events were unable to be recorded. The largest discrepancy between P-wave spectra (Figure 4.8b) is around 60 – 70 kHz, with later stick-slips exhibiting high frequency energy depletion. This may be linked to the mechanical observation of stick-slips becoming less impulsive with more pre-seismic slip later in the experiment. Removing the internal instrument-apparatus response (Figure 4.8c) from uncalibrated spectra gives displacement spectra, with the flat, low-frequency part representing the seismic moment in Nm (Figure 4.8d; Chapter 1, Section 1.4.1). Spectra are then fit with Brune (1970) models to find the low-frequency amplitude (equivalent to seismic moment, $M_{0,s}$) and corner frequency f_0. The low-frequency part of the source spectra (the seismic moment) ranges from around 300 – 1500 Nm (Figure 4.8d), which may result in higher uncertainty and difficulty using the Brune model.

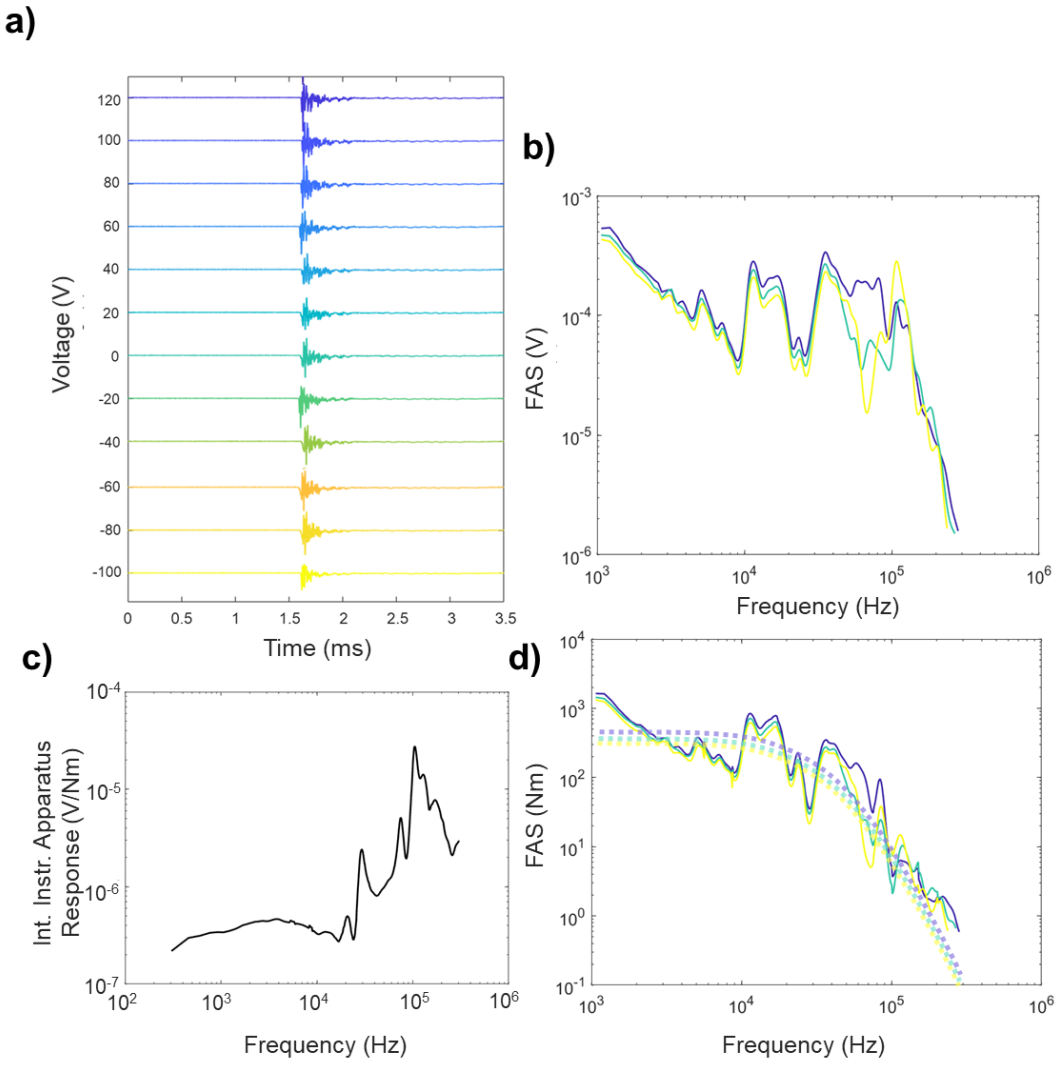

Figure 4.8: *a) P-wave seismograms for 12 large stick-slip events measured using the top platen of seismic assembly. b) Fast Fourier Transform of seismograms in a) give signal spectra, $S^{int}(f)$; events PMMA_30_001, PMMA_30_008 and PMM_30_012 are shown as examples. c) Internal instrument-apparatus response $\Psi^{int}(f)$ for the top platen, derived using Equation 3.14, Chapter 3. d) Displacement spectra for example events, calculated by dividing signal spectra $S^{int}(f)$ in b) by $\Psi^{int}(f)$, black line in c). Translucent coloured lines show Brune models for each event, fitted using brune_fit.m.*

Figure 4.9 shows the evolution of seismic moment $M_{0,s}$ and static stress drop $\Delta\tau_s$ (derived using a rectangular fault model; Equation 4.12) with displacement, derived from spectral fitting. Both seismic moment and stress drop decrease with load point displacement. Seismic stress drop estimates are much higher than mechanical stress drop estimates (Figure 4.7) – this is discussed in the following section.

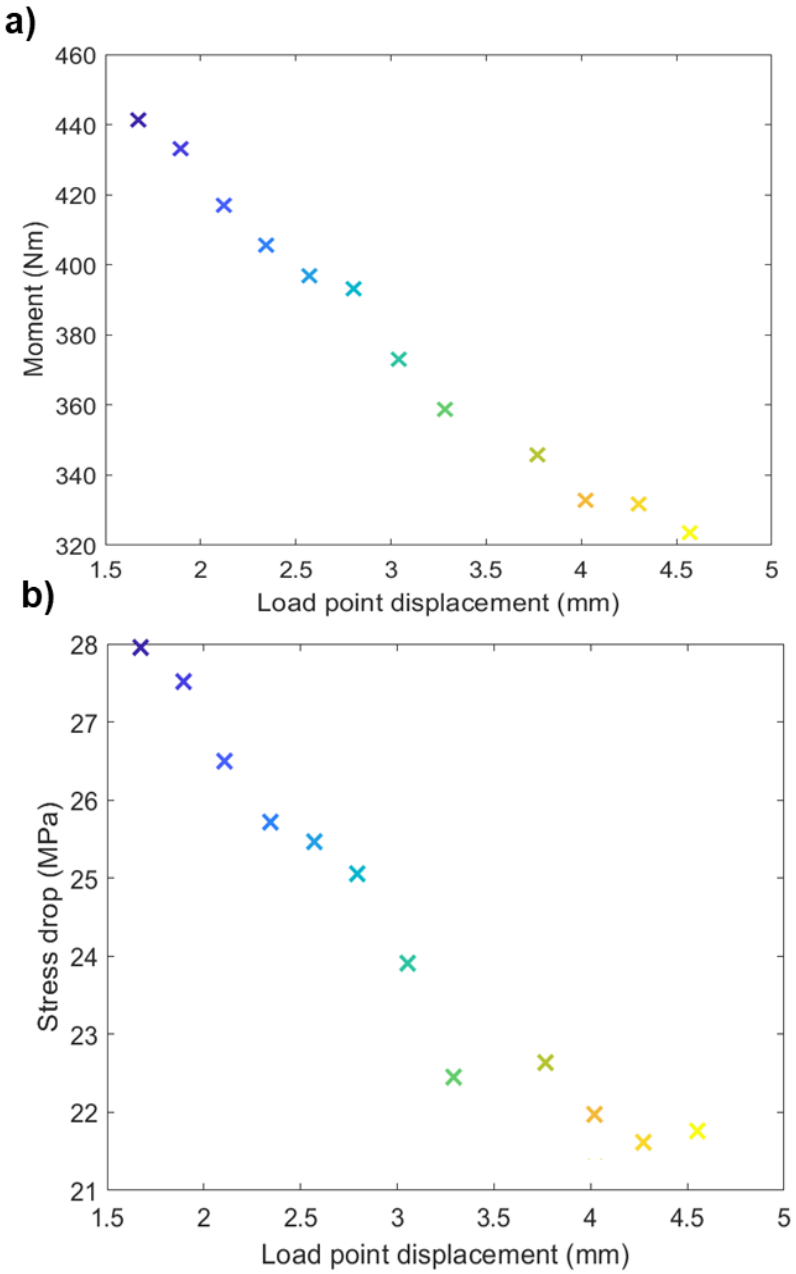

Figure 4.9: *a) Seismic moment $M_{0,s}$ and b) seismic static stress drop $\Delta\tau_s$ as a function of load point displacement.*

4.3.4 Comparison of mechanical to seismic moment and stress drop

Figure 4.10 shows how mechanical estimates of the seismic moment ('mechanical' seismic moment, $M_{0,m}$; Equation 4.7) with shear modulus G = 23.3, 33.3 and 43.3 GPa compare to those derived using spectral fitting ($M_{0,s}$). While estimates are well constrained, with R^2 = 0.8 for all three linear least squares fit lines and particularly using G = 23.3 GPa (gradient m = 1.19), there are significant differences between the two values. This could be related to errors involved in acoustic calibration (Chapter 3, Section 3.2.8) or the Brune model could be invalid for fitting stick-

slip source spectra. Using the relation $M_w = 2/3 \times \log_{10}(M_0) - 6.033$ (Hanks and Kanamori, 1979) to find the moment magnitude, moment estimates are accurate to $\pm$ 0.2 to $\pm$ 0.3 magnitude units for G = 23.3 and 33.3 GPa, and 43.3 GPa respectively. These results are similar to previous studies, which also found systematic differences between estimates using Brune modelling (McLaskey et al., 2015; McLaskey and Lockner, 2016).

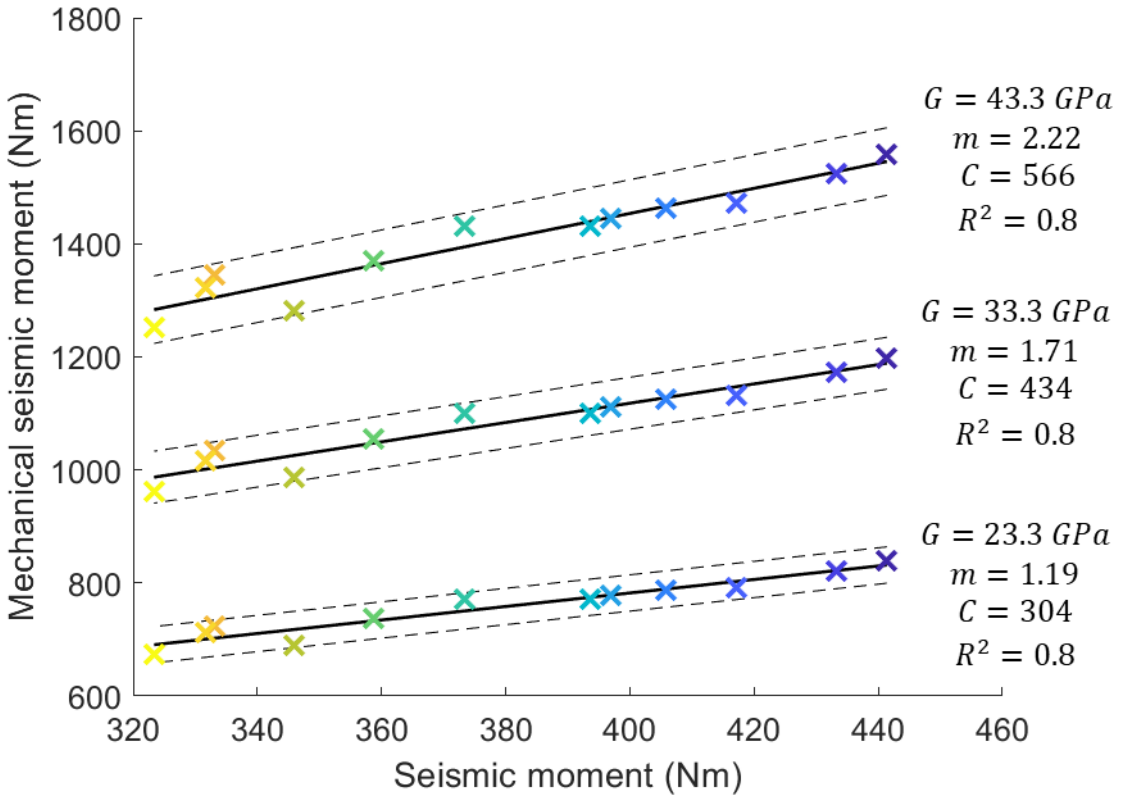

Figure 4.10: *Seismic ($M_{0,s}$) vs 'mechanical' ($M_{0,m}$) seismic moment of large stick-slip events (coloured crosses), with shear modulus G = 23.3, 33.3 and 43.3 GPa. Black solid lines with gradient m and intercept C are linear fits for each value of G, while black dotted lines represent 95% standard error prediction intervals.*

Comparing mechanical measurements ($\Delta\tau_m$) to seismic estimates ($\Delta\tau_s$) of stress drop (Figure 4.11) with both a circular fault model (Equation 4.11) and rectangular fault model (Equation 4.12), values scale with a good fit (gradient = 1.87, 5.40 R^2 = 0.812, 0.943, respectively). This suggests that there is some relation between the independently derived source properties, although it is unclear how to relate them, with the average frictional resistance during rupture τ_f unknown, albeit it should be low (Section 4.2.6). However, estimates using a rectangular fault model result in much larger seismic stress drops than mechanical stress drop measurements.

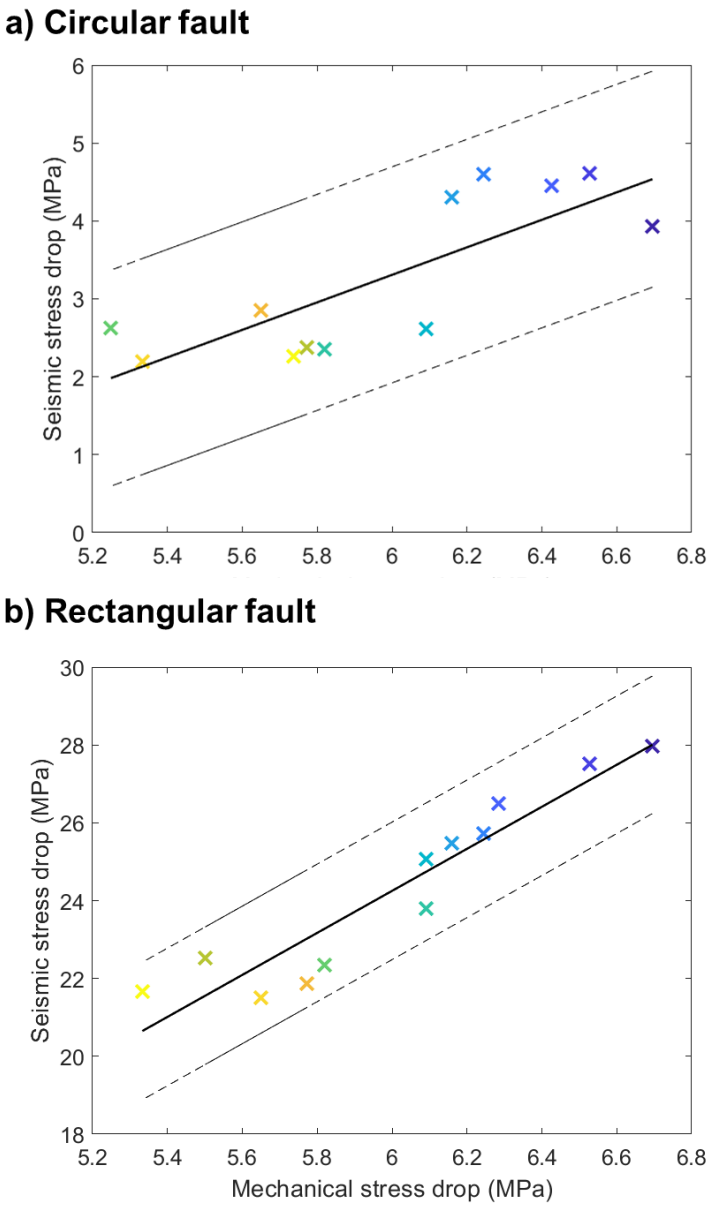

***Figure 4.11**: Mechanical ($\Delta\tau_m$) vs seismic ($\Delta\tau_s$) stress drop of large stick-slip events (coloured crosses), with $\Delta\tau_s$ calculated using a) a circular rupture model and b) a rectangular rupture model. The black solid line is a linear fit while black dotted lines represent 95% standard error prediction intervals.*

4.3.5 Seismic moment estimates compared using the top vs bottom platen of the seismic assembly

Figure 4.12 presents the seismic moment $M_{0,s}$ estimated using the top and bottom platens of the seismic assembly's (Figure 4.1) internal instrument-apparatus responses (Chapter 3, Figure 3.18). While there is some scatter ($R^2 = 0.624$), there is a strong correlation between both values, with a linear regression trendline gradient of 1.05. Scatter could be related to the unsuitability of Brune modelling or errors present in both instrument-apparatus responses (Chapter 3, Figure

3.14). However, results show that the absolute acoustic calibration method is robust across sensors.

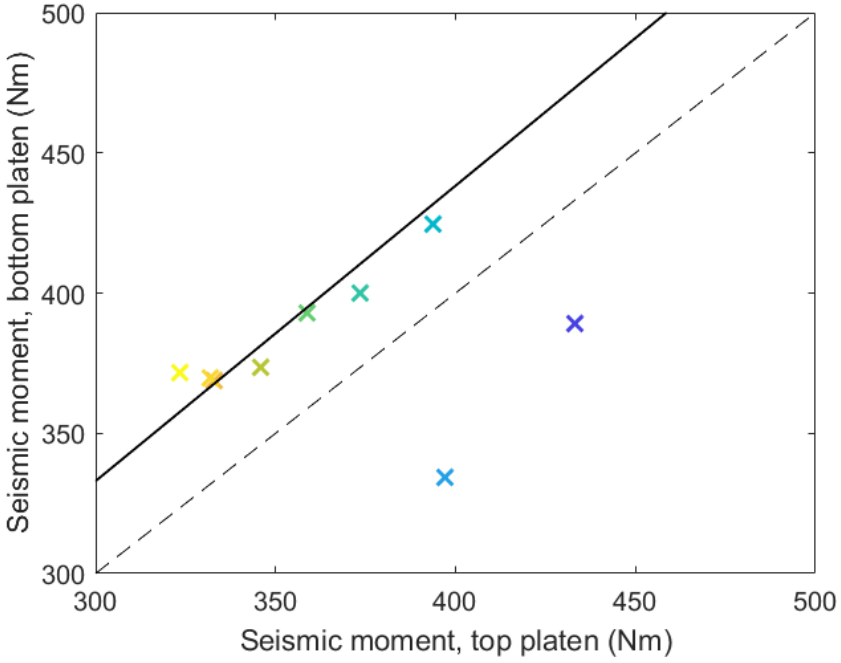

Figure 4.12: *Seismic moment $M_{0,s}$ estimated using the top and bottom platens of the seismic assembly's internal instrument-apparatus responses. The black solid line is a linear regression line ($y = 1.05x + 17.0$), black dotted line is 1:1 line ($y = x$).*

4.3.6 Rupture velocity and high-frequency energy depletion

Figure 4.13a shows average velocity $\bar{v}_s$ estimates as a function of load point displacement. Estimates are in line with expected values, considering that rupture velocity should be 0.5 – 0.9β, where β is the shear wave velocity (Stein and Wysession, 1991). There is a sudden reduction in the rupture velocity of events following the 5th large stick-slip, PMMA_30_005. This decrease in rupture velocity coincides with a systematic reduction of high-frequency content in the 20 – 100 kHz range as slip increases (Figure 4.13b). To estimate this energy depletion, the radiated energy E_R in J is obtained by multiplying displacement spectra by $i2\pi f$ to convert them to velocity spectra and integrating over f: $E_R = \frac{1}{4\pi^2 \rho \beta^5} \int_0^{+\infty} \left| f\dot{M}(f) \right|^2 df$ (Vassiliou and Kanamori, 1982). ρ is the material density of PMMA, 1180 kg/m^3. While this equation is generally used for S-wave spectra, it is still a useful method of P-wave energy estimation, especially in the very-near field where P-wave and S-wave spectra are both significant energy components. Figure 4.13c shows a systematic decrease in radiated energy with displacement.

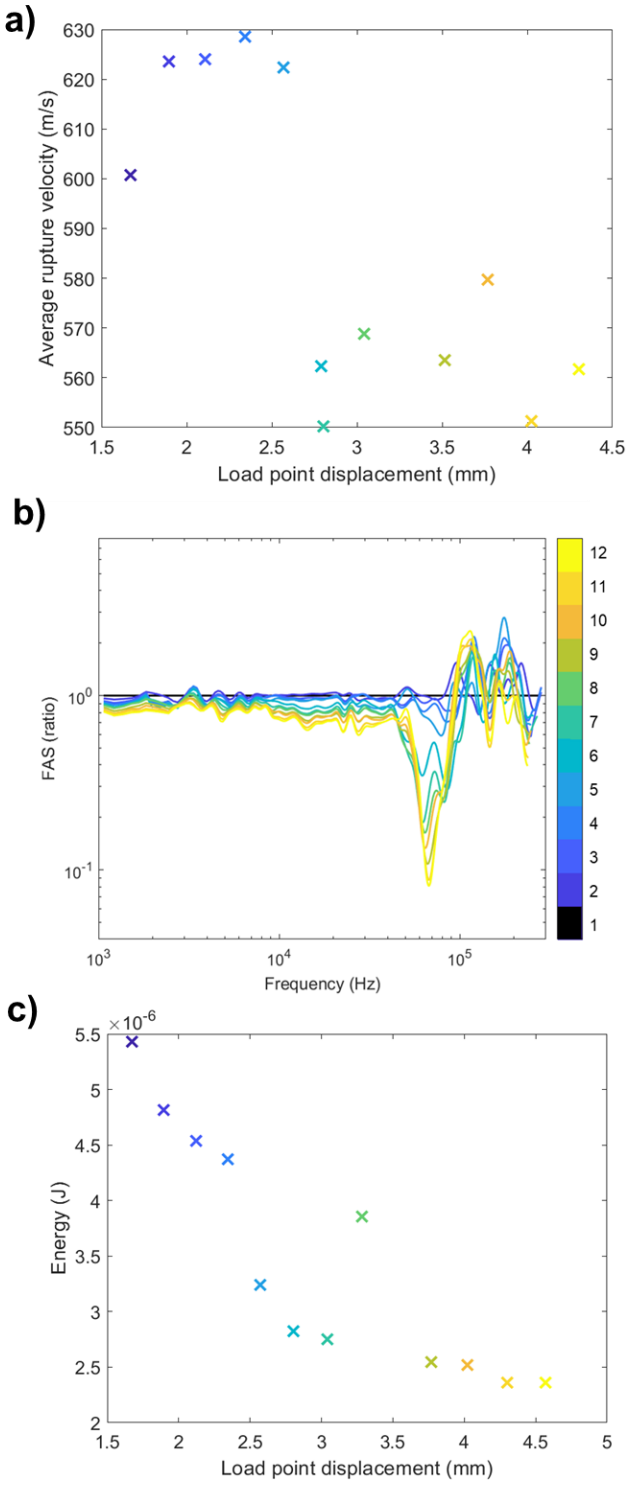

Figure 4.13: *a) Average rupture velocity calculated using seismic* property *estimates (Equation 4.14) with rectangular fault model. b) Spectral ratio of each large stick-slip with 1st event PMMA_30_001, highlighting systematic depletion of high-frequency radiation. c) Radiated energy calculated from velocity spectra.*

4.4 DISCUSSION

4.4.1 Stick-slip instability

Combining mechanical and seismological observations, source property variation during laboratory-generated earthquakes indicates that evolution in fault behaviour in a single experiment can be quantitatively monitored. Stick-slip behaviour progressively diminishes during sliding, evolving into stick-slip with preceding, quasi-stable pre-seismic slip. As discussed in Chapter 1, Section 1.2.1, stick-slip instability occurs due to fault weakening through either slip or velocity weakening (Ida, 1972; Marone, 1998a; Palmer and Rice, 1973; Rice and Ruina, 1983; Ruina, 1983). In this experiment, there is a transition from instability to quasi-stability. Assuming a rate-and-state framework (Chapter 1; Section 1.2.1.2), this decrease in stability could reflect an evolution of rate-and-state parameters with slip to take the system closer towards the stability boundary. Voisin, Renard and Grasso (2007) found that in a similar experiment with salt, contact asperities increased in length and width with accumulating slip, potentially increasing the critical slip distance D_c. At constant load point velocity, frictional behaviour depends on the stiffness k of the loading system (Scholz, 2019, 1998). Stick-slip oscillations occur when both: 1) $a < b$, where a is the direct effect and b is the evolution effect and 2) $k < k_c$, the critical stiffness. k_c can be defined as follows:

$$k_c = \frac{\sigma_n(b-a)}{D_c}, \tag{4.15}$$

where σ_n is the normal stress exerted on the stainless steel slider (Rice and Ruina, 1983). The development of gouge also affects stick-slip occurrence by potentially decreasing the $(a-b)$ value, though it is difficult to infer how in this study due to the experimental setup, i.e., no velocity steps (Beeler et al., 1996; Voisin et al., 2007). This experiment was conducted under constant load point velocity, normal stress and temperature. If D_c increases as slip accumulates in our experiment, k_c may decrease, leading towards stability where $k \sim k_c$. Topographical analysis of the PMMA surface interfaces pre- and post-experiment could be carried out in a future study to support this argument.

4.4.2 Pre-seismic slip and fault healing

Figures 4.5 – 4.7 show the relationship between pre-seismic slip (the total slip between the minimum interseismic shear stress and peak shear stress, τ_p), large stick-slip stress drop and slip velocity. Previous studies have shown pre-seismic slip to vary with loading stiffness (Shreedharan et al., 2020), effective normal stress (Acosta et al., 2019), loading rate (Leeman et al., 2018) and fault zone thickness (Anthony and Marone, 2005). However, the effect of fault

evolution and roughness on pre-seismic slip is not well documented. Our observations demonstrate an inverse relationship between stress drop magnitude and pre-seismic slip. As in previous studies, this suggests that faults that experience more pre-seismic slip partially release accumulated strain energy by sliding, resulting in a lower coseismic stress drop (Cattania and Segall, 2019). The theory of time-dependent fault healing, based on rate-and-state friction, outlines that increased healing results in an increase in the real area of contact at asperities, resulting in increased seismic magnitudes (Dieterich, 1978; Marone, 1998b; Shreedharan et al., 2020). As the experiment progresses, a transition from unstable stick-slip to stick-slip preceded by quasi-stable slip is observed. The degree of time-dependent healing may be increased by the evolution of rate-and-state parameters, e.g. an increase in D_c and/or a decrease in $(a-b)$. If the experiment were able to be lengthened, perhaps this quasi-stable slip would transition to stable slip, which would represent infinite pre-seismic slip (Shreedharan et al., 2020).

Proposing that earthquake nucleation on rough faults is driven by mutual stress transfer and feedback between creep and foreshocks, Cattania and Segall (2021) predicted through modelling that slip velocities increase with $1/t$, where t is the time to the large stick-slip. Figure 4.14 shows the relationship between the time t of each precursory event to the large stick-slip and average slip velocity $\bar{v}$, calculated using Equation 4.6. Results follow the prediction of $1/t$ acceleration in creep rates, which has also been predicted by nucleation springer-slider models on rate-and-state faults (Dieterich, 1992; Rubin and Ampuero, 2005). It should be noted that in this experiment, there is an increase in fault slip velocity, then periods of quiescence as a function of $1/t$ – this is also observed by Cattania and Segall (2021), who found that foreshocks occur in sub-clusters at multiple temporal scales. In their model, weaker sub-clusters were bounded by stronger patches with wider asperities, which typically failed in later bursts. Earthquakes occurring on stronger patches increased the shear stress on surrounding weaker patches, leading to a sudden acceleration in creep, loading asperities until failure.

This study's results also support the work of Bedford et al. (2022) in laboratory frictional experiments with geologically heterogeneous simulated faults (strong, rate-weakening quartz gouge and weak, rate-strengthening clay gouge). The study found that geological heterogeneity can lead to a pronounced reduction of strength and frictional stability. Similarly to this study, Bedford et al. (2022) demonstrated that geological heterogeneity and its evolution can have significant effects on fault strength and stability, and thus, on the occurrence of fast earthquake ruptures versus slow-slip transients.

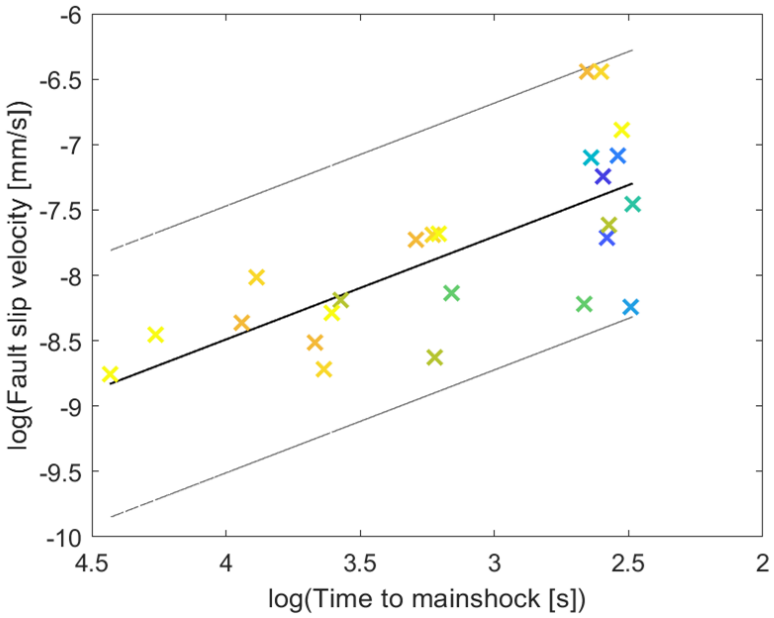

Figure 4.14: *Average slip velocity (natural logarithm, base e) during foreshock sequences in 11 of the 12 large stick-slip events (coloured crosses). Colours represent which stick-slip event precursor precedes, colour code as in Figure 4.5. The black solid line is proportional to 1/t while black dotted lines represent 95% standard error prediction intervals.*

4.4.3 Discrepancies between mechanical and seismic estimates of source properties

There are significant differences between mechanically derived ($M_{0,m}$ and $\Delta\tau_m$) and seismically derived ($M_{0,s}$ and $\Delta\tau_s$) seismic moment and static stress drop for large stick-slips (Figure 4.10 and 4.11). While both types of data show a gradual decrease in seismic moment and stress drop with cumulative slip with good correlation, discrepancies between mechanical measurements and seismic estimates remain following acoustic calibration. The likely reason for this is that the Brune source model may not be applicable to the data: a Brune model assumes a fault with a circular shape that is completely contained. The average source radius of large stick-slip events is 14.3 mm, which is smaller than the smallest sample dimension (18 mm; Figure 4.1 and Appendix 4.6.1). Nevertheless, events are not fully contained, nucleating within the sample but not accelerating fully to seismic speeds before the rupture reaches the ends of the sample (Wu and McLaskey, 2019).

While the Brune model may not be applicable to large stick-slip events, all data show decreases in seismic moment and stress drop with cumulative displacement. Decreases in seismic moment measured using seismic waves coincide with a decrease in corner frequency (Appendix 4.6.1). Figure 4.15 demonstrates three possible hypotheses for source property discrepancy, considering Equations 4.7, 4.9, 4.11, 4.12, 4.13 and 4.14.

A. **Limited variation in corner frequency f_0**; changes in seismic moment M_0 are dependent on average fault slip $D = x_{fault}$

   Observed variations in corner frequency f_0 are relatively small and represent fluctuations due to model fitting. The decrease in f_0 is an 'apparent' decrease due to model bias, which reduces f_0 with M_0.

B. **Moderate variation in corner frequency f_0**; changes in seismic moment M_0 and corner frequency f_0 are dependent on source radius r.

   Observed variations in f_0 are significant and due to changes in fault properties. The decrease in M_0 and f_0 is related to increasing source radius r with constant average shear wave velocity, $\bar{v}_s$. Source radius r is not necessarily just the slip area (i.e. r is not necessarily proportional to fault rupture area A in Equation 4.7). While the fault rupture A remains the same, the source radius is related to asperities on the fault. An increase in source radius r implies that asperities increase in length and that critical slip distance D_c increases (Mei and Wu, 2021).

C. **Moderate variation in corner frequency f_0**; changes in seismic moment M_0 and corner frequency f_0 are dependent on average rupture velocity $\bar{v}_s$.

   Observed variations in f_0 are significant and due to changes in fault properties. The decrease in M_0 and f_0 is related to decreasing average rupture velocity, $\bar{v}_s$ with constant source radius, r. The average rupture velocity is related to slip stability, which is controlled by rate-and-state parameters.

Hypothesis A is possible, but it is difficult to interpret whether observed variations in f_0 are significant due to the narrow range of corner frequencies (28 – 35 kHz) observed. Figure 4.8d shows that source spectra are very similar, with negligible differences in form. Chapter 5 will explore a wider range of magnitudes of large stick-slip events, which should provide a wider range of corner frequencies due to higher normal stresses (40 and 50 MPa) being applied. This way, Hypotheses A, B and C can be tested.

Recalling Equation 4.7 and knowing that fault rupture A remains constant due to the same simulated fault geometry being used, a decrease in seismic moment M_0 implies a decrease in average fault slip $D = x_{fault}$. Therefore, if there is variation in seismic moment with average fault slip, average fault slip could scale with source radius and rupture velocity.

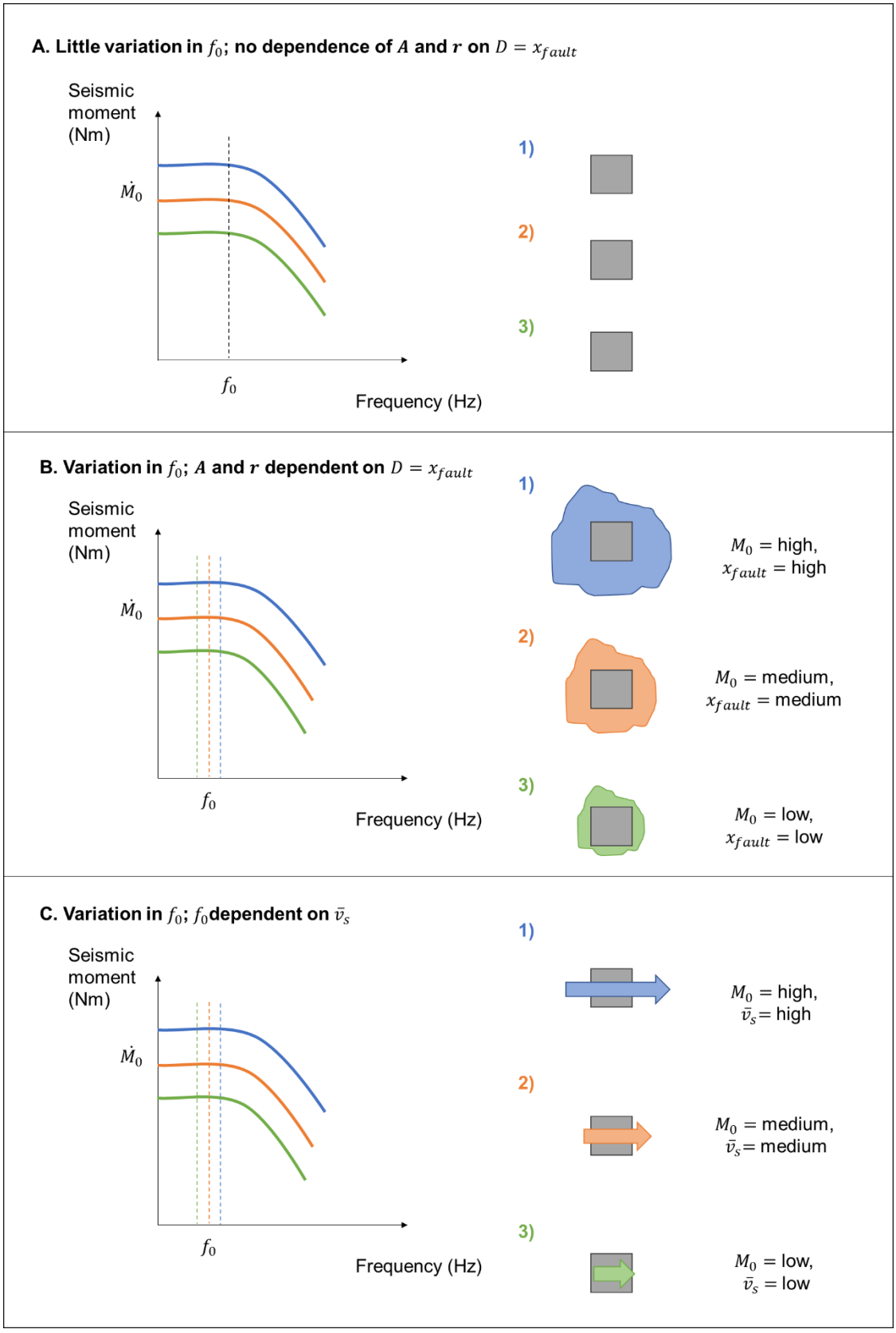

***Figure 4.15**: Concept diagram outlining three hypotheses for source property discrepancy. Symbols are defined as follows: f_0 = corner frequency; M_0= seismic moment; $D = x_{fault}$= average fault slip; $\dot{M}_0$= moment rate, r= source radius, $\bar{v}_s$= average rupture velocity.*

4.4.4 Earthquake source property evolution

P-wave seismic signals radiated during coseismic slip support the idea of evolving fault behaviour with accumulated slip. Stress drops of large stick-slip events were found to decrease with cumulative slip, with both mechanical and seismic estimates in agreement. Stress drop has a strong influence on peak ground acceleration, making it a key source property to constrain in seismic hazard analysis (Abercrombie, 2021; Baltay et al., 2011). Stress drops for natural earthquakes typically range from 0.5 to 50 MPa, with the variation thought to represent some variation in the earthquake source itself (Baltay et al., 2011). Self-similarity between small and large earthquakes has been shown through the lack of systematic dependence of stress drop on the seismic moment for events ranging from M_W -7 to 8 (Aki, 1967; Allmann and Shearer, 2009; Goodfellow and Young, 2014; Hanks, 1977; McLaskey et al., 2014). The results from this study support this theory of self-similarity and scaling (Figure 4.16). However, the disparity between mechanical and seismic estimates of stress drop highlights a key issue with the self-similarity theory: events are considered as self-similar across 4 orders of magnitude (Cocco et al., 2016).

Stress drops of slow precursors to stick-slips in this study are a magnitude lower than stick-slip events. Ide et al. (2007) suggested that slow and fast earthquakes may have different physical mechanisms: a future study should focus on constraining the source properties of these slower events to test this theory.

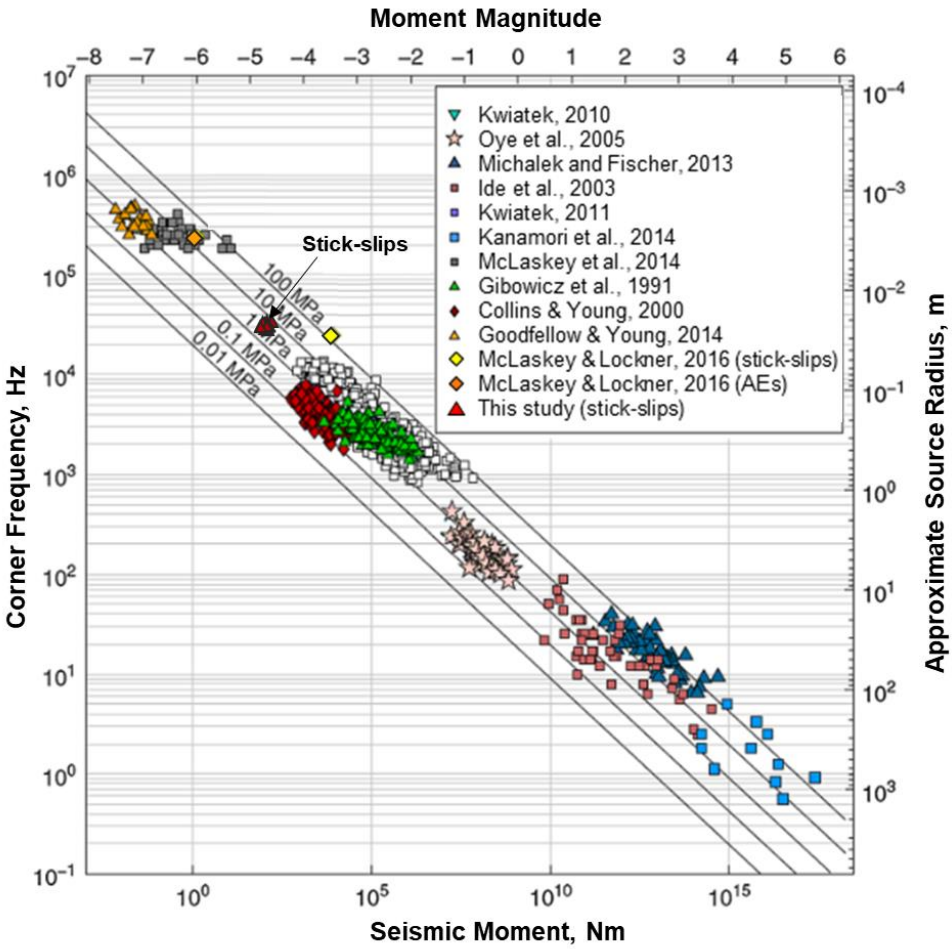

Figure 4.16: *Stick–slip source properties in this study (red triangles) calculated using circular fault model compared to other laboratory-generated, mining and natural earthquakes, and acoustic emissions (AEs). Adapted from McLaskey and Lockner (2016).*

Corner frequency and average rupture velocity of large stick-slip signals decrease over cumulative displacement, which has been observed in other studies (Voisin et al., 2008). There is a clear transition from stronger, impulsive signals early in the stick-slip cycle, to smaller, longer signals later on in the experiment. This is also reflected in the depletion of high frequencies in spectral ratios with accumulated slip. The decrease in radiated energy with slip is supported by a lower coseismic stress drop, which also implies that accumulated strain energy is released through increased pre-seismic sliding. The results support previous laboratory, modelling and natural studies on the role of transitional frictional behaviour in driving complex fault behaviour and slip (Bilek and Lay, 1999; Gu et al., 1984; Leeman et al., 2016; Liu and Rice, 2007). Structural maturity is a composite term that describes various aspects of a fault, including fault geometry, degree of wear and cumulative displacement (Perrin et al., 2021). While there is some debate in the literature, mature faults are generally thought to have large cumulative displacements (from hundreds to thousands of kilometres) and low apparent stresses. The evolution of fault

properties in this study may be comparable to increased structural maturity in natural faults, which have lower stress drops than immature faults (Manighetti et al., 2007). The results presented in this chapter are novel as they support Manighetti et al.'s (2007) model findings based on field observations, which could lead to improved incorporation of fault maturity into ground motion models. If the maturity of a given fault is known, the stress drop of an earthquake on that fault could be more accurately estimated using relations from laboratory experiments, field observations and modelling. This could lead to incorporating a fault maturity index into ground motion for seismic hazard assessment (Douglas and Edwards, 2016; Kotha et al., 2020; Radiguet et al., 2009).

Table 4.3 summarises the key relationships between measured variables and source parameters in this chapter, including where they agree and differ with other studies.

Table 4.3: *Summary of key relationships between measured source properties with comparison to other studies (+ = agrees with study, - = disagrees with study).*

Property	Observations	Comparison to other studies
Stress drop	Decreases with cumulative displacement	+ Manighetti et al. (2007)
	Decreases as pre-seismic slip increases	+ Cattania and Segall (2019)
	Stress drop and seismic moment scaling support self-similarity	+ Aki (1967), Allmann and Shearer (2009)… - Cocco et al. (2016)
Seismic moment	Decreases with cumulative displacement	+ Manighetti et al. (2007)
	Decreases as pre-seismic slip increases	+ Cattania and Segall (2019)
	Stress drop and seismic moment support self-similarity	+ Aki (1967), Allmann and Shearer (2009)… - Cocco et al. (2016)
Pre-seismic slip	Increases with cumulative displacement	+ Shreedharan et al. (2020)
	Fault slip velocities increase with $1/t$	+ Cattania and Segall (2021)
Corner frequency	Decreases with cumulative displacement	+ Voisin et al. (2008)
	Decreases as pre-seismic slip increases	+ Bilek and Lay (1999), Gu et al. (1984), Leeman et al. (2016) and Liu and Rice (2007)
Source radius	Increases with cumulative displacement	+ Voisin et al. (2008)
	Increases as pre-seismic slip increases	+ Bilek and Lay (1999), Gu et al. (1984), Leeman et al. (2016) and Liu and Rice (2007)
Average rupture velocity	Decreases with cumulative displacement	+ Voisin et al. (2008)
	Decreases as pre-seismic slip increases	+ Bilek and Lay (1999), Gu et al. (1984), Leeman et al. (2016) and Liu and Rice (2007)

4.5 CONCLUSION

The findings of this chapter have implications for seismic measurement of the large-scale behaviour of natural fault zones. Mechanical and seismic estimates of laboratory-generated earthquake (stick-slip) source properties agree: stress drop and seismic moment both decrease with cumulative displacement. This coincides with increased pre-seismic slip and an increase in the number of smaller, slower precursory events. High-frequency radiation and radiated energy are systematically depleted with displacement. The acceleration of the slip velocity of precursors to stick-slip follow the $1/t$ relationship predicted by Cattania and Segall (2021), supporting their hypothesis of positive feedback between creep and foreshocks. Estimates of seismic moment derived mechanically and by correcting radiated waveforms using absolute acoustic calibration (McLaskey et al., 2015) are accurate to ± 0.2 magnitude units. However, there is disparity in seismic and mechanical estimates of seismic moment and stress drop, which is likely due to the Brune model being unsuitable characterising the source properties of for large stick-slips.

The results presented highlight the key role of fault evolution in earthquake nucleation. On larger scales, the structural properties of faults such as maturity, segmentation, roughness and damage evolve with increased deformation. This may lead to differences in observed compared to predicted stress drop, which has important implications for seismic hazard assessment.

4.6 APPENDIX

4.6.1 a) Corner frequency, b) source radius and c) rise time as a function of load point displacement.

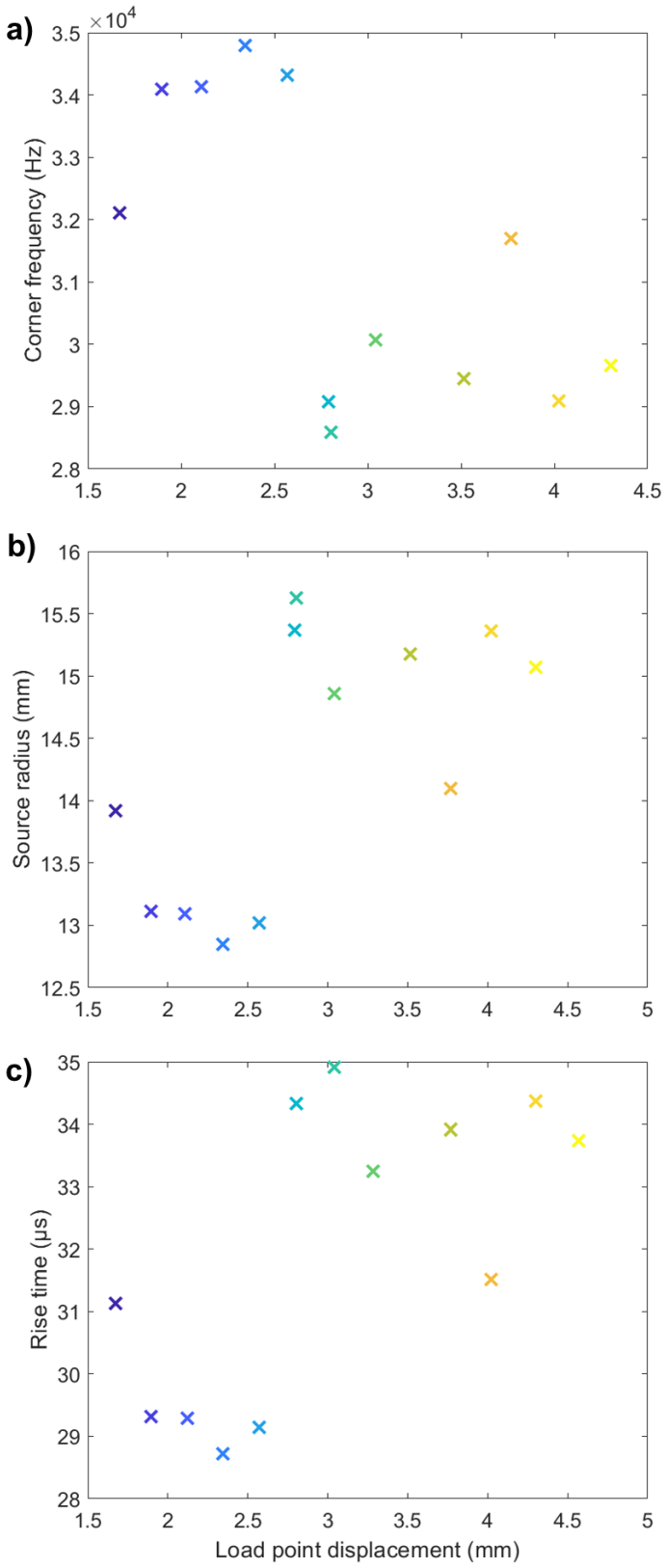

5 RADIATED WAVEFIELDS EMITTED FROM LABORATORY-GENERATED EARTHQUAKES IN FAULT ANALOGUES WITH VARYING ROUGHNESSES

5.1 INTRODUCTION

Fault interfaces are natural occurrences of shear that show topographical irregularity at various scales, from microscopic flaws in minerals to kilometre-scale faults along tectonic plate boundaries (Brown and Scholz, 1985). The irregularity, known as fault roughness, controls the nature of frictional contact in fault zones (Dieterich and Kilgore, 1994; Scholz, 1998). Many studies have suggested that roughness should have a large influence on earthquake and fault mechanics (Brodsky et al., 2016; Candela et al., 2012; Morad et al., 2022). Numerical models have shown the effect of roughness on both the static (Brodsky et al., 2016) and dynamic strength of faults (Fang and Dunham, 2013). Experimentally, roughness has been shown to affect both nucleation length (Okubo and Dieterich, 1986) and rate-and-state parameters (Harbord et al., 2017; Marone and Cox, 1994). In natural faults, the topography of fault rock surfaces can vary from smooth and polished (Siman-Tov et al., 2013) to rough and highly undulating (Candela et al., 2012; Power et al., 1988). Moreover, fault-surface roughness has been shown to evolve with cumulative slip, implying that earthquake nucleation, growth and termination on evolved, mature faults is fundamentally different than on newer, immature faults (Manighetti et al., 2007; Sagy et al., 2007).

A central question about earthquake rupture is how it modifies with observed fault variability, including fault roughness. Self-similar earthquake models, where earthquake source properties are scale-invariant, imply that small and large earthquakes rupture similarly, with similar physical mechanisms. In particular, this suggests that static stress drop should be independent of the seismic moment and earthquake source radius. The scale-invariance of earthquakes has been proposed in several studies (e.g. Abercrombie, 1995; Abercrombie and Rice, 2005; Aki, 1967; Hanks, 1977; Ide, 2003; Kanamori and Brodsky, 2004; Kanamori and Rivera, 2004; Shearer et al., 2006). Observed variations in stress drop (of over four orders of magnitude – Abercrombie, 2021) have been attributed to unmodelled sources of error such as near-surface attenuation or the directivity effect (Anderson and Hough, 1984; Imanishi and Ellsworth, 2006; Strasser et al., 2009). However, some studies have argued that observed source variations are not accounted for by these error sources and attribute them to fault heterogeneity. For example, in their study of the apparent stress for normal-fault earthquakes at subduction zones, Choy and Kirby (2004) suggested that earthquakes in rougher, immature faults with low cumulative displacement

radiate more energy per unit of moment than smoother, more mature faults. Singh and Suárez (1988) suggested that variations in the smoothness of seafloor topography could be a reason for the smaller number of aftershocks and lower stress drops in Central America compared to a global average. Moreover, Allmann and Shearer (2007) proposed that patterns of high and low stress-drop regions on the San Andreas fault in California during the M_w 6.0 Parkfield earthquake are mainly controlled by rock properties and stress field heterogeneities caused by fault roughness.

Through laboratory sliding friction tests, Patton (1966) found that under low normal stresses below 20 MPa, the roughness of rock discontinuities is a dominant factor that controls the maximum shear strength observed. Later experimental studies have shown that frictional behaviour and the transition from stable to unstable slip can vary for different initial surface roughnesses (Goebel et al., 2017; Morad et al., 2022; Ohnaka, 1973; Okubo and Dieterich, 1984). While Byerlee (1978) found that the maximum shear strength of faults at seismogenic depths is not affected by roughness, more recent observations have demonstrated that fault surface roughness is crucial for slip nucleation and dynamics at seismogenic depth as it modifies and influences asperity contact characteristics (Goebel et al., 2017; Harbord et al., 2017). Rate-and-state friction predicts that as normal stress increases, there is a transition from stable to marginally stable and unstable slip (Marone, 1998a; Rice and Ruina, 1983). However, above a critical normal stress (e.g. 200 MPa for saw-cut Westerly granite) instability can be suppressed (Harbord et al., 2017). At higher normal stresses, more asperities interlock due to the increase in the actual area of asperity contacts (Dieterich, 1979a, 1978).

As previously discussed in Chapter 4, Section 4.2.1, poly(methyl methacrylate) (PMMA) is a useful analogue for crustal rocks in laboratory frictional sliding experiments as its mechanical properties are well known and its elastoplastic behaviour is favourable to stick-slip nucleation. Specifically for PMMA-PMMA sliding interfaces, Bouissou et al. (1999) found that the residual strength following the 'slip' phase of stick-slip decreases with increasing normal stress. Moreover, they observed that at higher normal stresses, the time taken to reach regular stick-slip (converse to irregular stick-slip, where shear stress and recurrence time are highly variable) is longer than at lower normal stresses. Bouissou et al. (1999) interpreted both of these findings as evidence of asperities deforming plastically before stick-slip cycle regularisation. When stick-slip cycles are regular, asperity heights are smaller causing asperities to interlock more easily. Consequently, at higher normal stresses, interlocking occurs later and with lower residual strength.

While the aforementioned studies have analysed the effect of roughness and normal stress on fault instability, little is known about their effect on laboratory-generated earthquake source

properties. In this chapter, 12 direct shear experiments on poly(methyl methacrylate) (PMMA) are carried out using the acoustically calibrated seismic assembly to measure radiated waves during stick-slip. They show how the combination of fault roughness and normal stress influences seismic source properties of stick-slip, including stress drop, seismic moment and local magnitude. Post-experimental images of PMMA samples are captured using scanning electron microscopy (SEM)-based electron backscatter diffraction (EBSD), qualifying fault roughness evolution and damage creation during experiments. Finally, implications for source property estimation for seismic hazard assessment are discussed.

5.2 METHODS

5.2.1 Experimental configuration and roughness creation

Dry (zero pore fluid pressure, ambient laboratory conditions) direct shear tests are carried out on rectangular PMMA slabs using a triaxial oil-medium deformation apparatus ($\sigma_1 > \sigma_2 = \sigma_3$) in the University of Liverpool's Rock Deformation Laboratory. PMMA is a useful analogue material for frictional sliding experiments as it is around 20 times more compliant than Westerly granite, generating events with a smaller nucleation length (~ mm vs cm – Chapter 4, Section 4.2.1). The rectangular slabs are cut to shape using a laser by the University of Liverpool Core Services and have dimensions of 36 x 18 x 4 mm (± 10 μm).

Once cut, slab surfaces are wet ground with silicon carbide with the following root mean square roughness Z_{rms} (from roughest to smoothest; Duparré et al., 2002): Z_{rms} = 125, 18.3, 7.7 and 3.8 μm. Gouge produced by grinding is removed by an air blaster and samples are cleaned using an ultrasonic bath and left to dry completely to ensure a clean surface before frictional sliding. Samples are air blasted a second time after air drying to reduce the chance of dust particles contaminating the sample surface. During experiments, sample slabs are offset using rubber spacers to create a nominal contact area A of 468 – 567 mm^2.

The sample configuration is the same as described in Chapter 4, with roughened PMMA slabs glued to L-shaped 17-4 stainless steel sliders with Loctite® Super Glue (Figure 5.1). Then, the PMMA sample is placed into polytetrafluoroethylene (PTFE) and polyvinyl chloride (PVC) jackets to isolate the sample from the confining medium. An additional thin disk of PTFE is placed at the bottom of the sample to minimise friction between the sample and loading platen so that only any shortening perpendicular to the sliding surface can be accommodated. Then, the jacketed sample is placed into a sample assembly with two P- and two S-wave piezoelectric sensors (seismic sample assembly; Chapter 2, Figure 2.2) at either end of the sample. Sensors are mounted perpendicular (90°) to the fault interface (Chapter 4, Figure 4.1).

5.2.1.1 Sample preparation before SEM analyses

To enable SEM surface roughness analyses of PMMA slabs following frictional sliding experiments, slabs are carefully detached from the L-shaped stainless-steel sliders using a steel vice and copper hammer by gently tapping the slider (Figure 5.1c). To ensure that the surface remains untouched and well-preserved post-experiment, much care is taken to grip the slab as far away from the surface (i.e. as close to the long dimension of the L-shaped slider) as possible (Figure 5.1d). Broken or cracked samples are not used to ensure that solely roughness and damage created experimentally are analysed. Post-experimental PMMA slab samples are then air blasted to ensure a clean surface. It should be noted that a significant amount of gouge was removed from post-experimental samples, particularly at 30 MPa normal stress.

Before SEM analyses, sample surfaces are carbon coated using an Emitech K950X vacuum evaporator. Two carbon rods with a sharpened contact point between them are used to pass current through, causing the evaporation of carbon from the surface. This ensures a high-quality coating of carbon on post-experimental sample surfaces, making them conductive and suitable for SEM analyses (Goldstein et al., 1992).

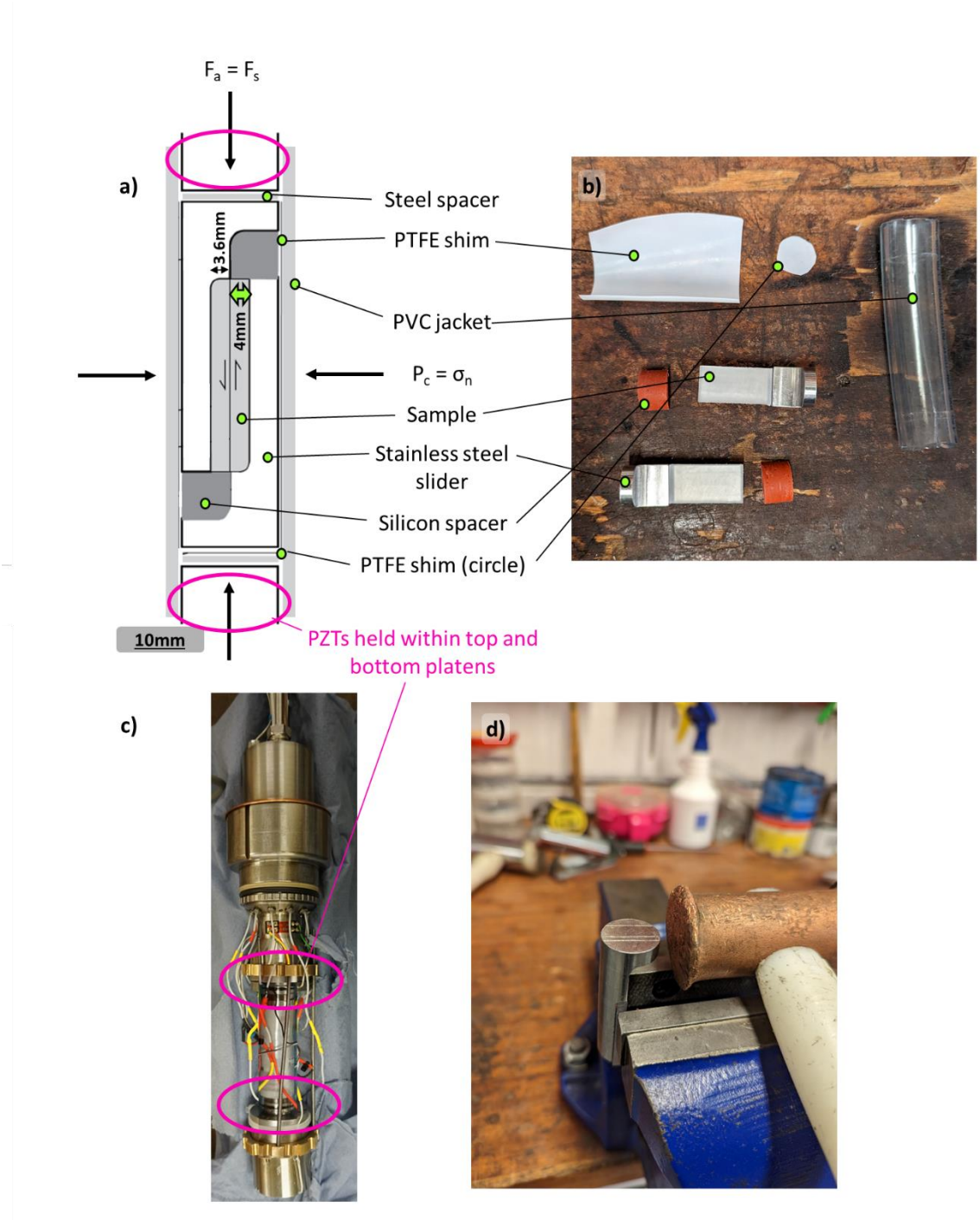

Figure 5.1*: a) Schematic of seismic sample assembly experimental configuration used to conduct single direct shear experiments. b) Photo of roughened (Z_{rms} = 18.3 µm) PMMA slabs, silicon spacers, PTFE shims, stainless steel sliders and PVC jacket. c) Photo of seismic sample assembly, showing sample position and platens with piezoelectric crystals (PZTs) mounted within (pink ovals). The strain gauge is glued above the top platen of the seismic sample assembly. d) After experiments, PMMA slabs are carefully removed from stainless steel sliders using a copper hammer to preserve the sliding surface for SEM imaging.*

5.2.2 Mechanical loading

All experiments are performed using a triaxial deformation apparatus designed and built by D. Faulkner (Chapter 2; Chapter 4, Figure 4.2). Experiments are conducted by initially increasing the confining pressure in the vessel to the target normal stress (30, 40 or 50 MPa) using a compressed air-driven pump. The apparatus is left for 30 minutes to allow the pressure to equilibrate from any adiabatic changes. Once a stable target normal stress is reached, the confining pressure servo-control system is applied to sustain constant normal stress. Next, the axial piston is driven upwards using the loading servo-control system until the hit-point is reached (Chapter 4, Section 4.2.2).

A constant load point velocity of 1 μm/s is maintained by the axial loading servo system to generate spontaneous stick-slip behaviour. The properties of stick-slips are analysed after the interface has sheared 1 mm, above the displacement that the peak shear stress is observed. Samples are sheared up to a maximum displacement of 5.5 mm. Mechanical data are observed and recorded via a LabView script at a sampling frequency of 10 Hz.

5.2.3 Seismic data acquisition

Two 10 mm diameter P- and two S-wave piezoelectric sensors (Boston Piezo-Optics Inc.) within both platens of the seismic sample assembly are used to detect seismic waves radiated from large stick-slip events (Chapter 2, Section 2.2.3). Source spectra of stick-slip events are derived by using McLaskey et al.'s (2015) absolute acoustic calibration method, which assumes ball impacts as empirical Green's functions (Chapter 3). The method links momentum to moment, removing path and instrument response spectra from measured signals, leaving solely the source spectra of stick-slip events.

Events are recorded during the experiment using a high-frequency acoustic monitoring system (Itasca IMaGE/Applied Seismology Consulting) with a sampling rate of 10 MHz. A multi-channel, 12-bit oscilloscope with 8 channels is used to record voltage signals. A trigger voltage threshold is set (1% of Full-Scale Voltage 40 V, i.e. 0.4 V) to minimise noise detection (Chapter 2, Section 2.3).

In some experiments, the Pulser Amplifier System (PAS) was used to amplify microseismicity related to acoustic emissions (AEs). However, it was difficult to measure AEs due to the large amplitude of low-frequency noise produced by the servo-controlled motors that control the confining pressure and axial loading systems (~0.8 V at Gain Level 3, comparable to AE events which were typically around 1 V amplitude at Gain Level 3 – Chapter 2, Section 2.2.5 and 2.2.6). Therefore, where the PAS was used, the limited number of AEs recorded (< 20) are not reported.

Further description of the high-frequency acoustic monitoring system is given in Chapters 2 and 3 of this thesis.

5.2.4 Strain gauge measurements and calibration

As stick-slip events are highly energetic, they impose a force on the loading system and sometimes this causes the zero offset to be jolted due to the inertia of the stick-slips (Chapter 2, Figure 2.10). Moreover, during a series of stick-slip experiments, the force gauge can drift due to the inertia of previous stick-slips. In these cases, force measurements can be inaccurate, leading to mechanical measurements of properties such as fault stress to be relative (to a reference that may change during the experiment), rather than absolute. To combat this, a 2 mm high-frequency strain gauge with a resistance of 120 ± 0.5 Ω and gauge factor X = Y = 2.13 ± 1 % (Tokyo Sokki Kenkyujo Co., Ltd) strain gauge is attached above the top platen of the seismic assembly (Figure 5.1c; Chapter 2, Figure 2.2). TF-2M connecting terminals (Tokyo Sokki Kenkyujo Co., Ltd) are attached to either side of the strain gauge to connect them with wiring to the 9-pin male D-sub connector. Once connected to the in-vessel 9-pin female connector, strain gauge signals are conditioned using a Modular 600 multichannel amplifier (Chapter 2, Figure 2.12b) with a gain of 100,000. Using the strain gauge ensures that only sample deformation is measured.

The strain gauge data are used to correct the zero-offset caused by stick-slip inertia (Chapter 2, Figure 2.10). Assuming that force (measured by the force gauge) and strain (measured by the strain gauge) are proportional during elastic loading preceding the first stick-slip, strain ε can be converted to strain-calibrated force F_{strain} using a force-strain conversion factor $C_{F\varepsilon}$:

$$F_{strain} = C_{F\varepsilon}\varepsilon. \tag{5.1}$$

F_{strain} and $C_{F\varepsilon}$ have units of N, while ε is the raw strain gauge signal, which is unitless. Figure 5.2 outlines the process of converting strain to force. $C_{F\varepsilon}$ is calculated by fitting force gauge and strain gauge data (Figure 5.2a) with a straight line using a regression that minimises the sum of square deviations (Figure 5.2b). Strain-calibrated force F_{strain} is then derived using Equation 5.1. It should be noted the strain gauge data has more high-frequency noise than the force gauge data. Moreover, sometimes there are strain jogs where the strain drifts during loading, potentially due to electrical noise interference (Figure 5.2a). However, the strain gauge data clearly show that the force gauge is affected by the inertia of the stick-slips. $C_{F\varepsilon}$ is calculated during elastic loading, disregarding strain jogs (Figure 5.2b).

To reduce the noise level and to smooth the strain gauge data, a 1D-centred moving-average filter with a window length of 100 samples is applied. A length of 100 is used as this is longer than the

length of a large stick-slip (maximum ~10 points) to capture longer-term trends but is short enough so that stick-slips are still detected by the *find_stickslip_v4.m* algorithm and stress drops remain accurate. The moving-average filter slides along the data with a window length of 100 (i.e. each window contains 100 data points centred on the middle value), computing averages of the data contained in each window. The load point displacement at which the large stick-slip occurs is assumed to be equal to the load point displacement detected by *find_stickslip_v4.m* before filtering, i.e. detected using force gauge data, F.

Applying a centred moving-average filter with these parameters gives a filtered strain-calibrated force estimate, $F_{strain,f}$. When using the moving average, the noise level is significantly reduced while capturing the force drop (and therefore, stress drop) calculated using strain accurately (Figure 5.2). For example, the stress drop of the first large stick-slip during test PMMA_120_50 is overestimated when using force gauge data (10.4 MPa) versus strain-calibrated force (9.7 MPa – Figure 5.2c) when using automatic stick-slip detection code *find_stickslip_v4.m*. Therefore, strain-calibrated force measurements are used to calculate the stress drop and recurrence interval of large stick-slips.

Nevertheless, filtering can mask short-term trends, particularly smaller precursory events that precede large stick-slips (Figure 5.2d). This is an issue as these small events characterise how much pre-seismic slip precedes each large stick-slip (Chapter 4, Section 4.2.4.2). Manually offsetting force gauge data to fit the strain gauge data could lead to incorrect calculation of stress drop measurements. Therefore, to calculate the stress drop of small stick-slip precursors, force gauge data F is used. Although there are issues with the zero-offset due to energetic large sick-slips, as precursors are much smaller (stress drops are no more than 15% of the stress drop of large stick-slips) and less energetic, inertia is much reduced.

To summarise, to calculate the stress drop and recurrence interval of large stress drops, the filtered strain-calibrated force estimate, $F_{strain,f}$ is used. To calculate the pre-seismic slip, stress drop and recurrence interval of small precursory stick-slip events that precede large stress drops, F, based on direct measurement, is used. In both cases, force is converted to shear stress using Equation 4.1 (Chapter 4). Further examples of the conversion from force to shear stress are presented in Appendix 5.6.1.

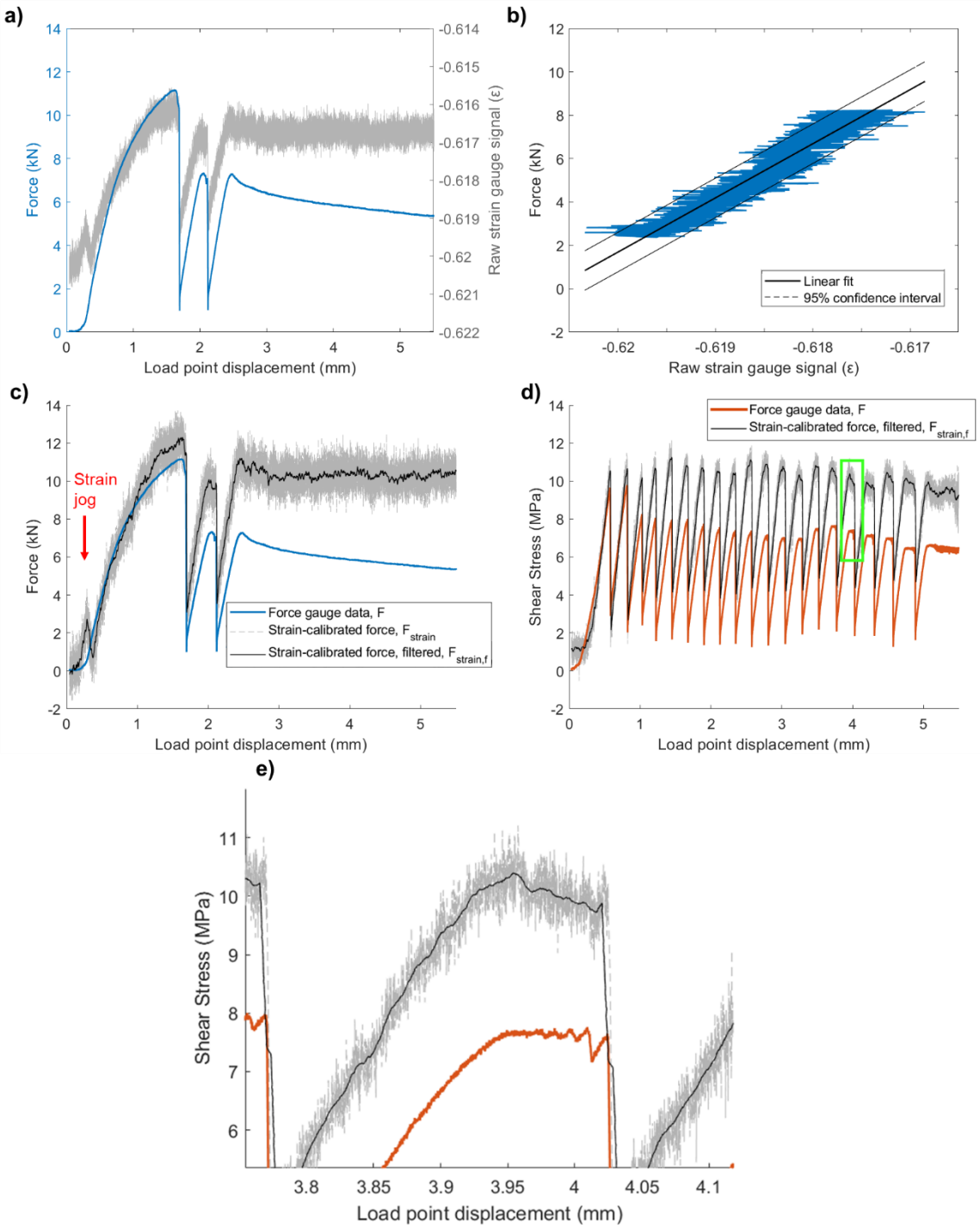

Figure 5.2: *a) Example of 2 stick-slips from test PMMA_120_50. Strain gauge data (grey line) is not proportional to force gauge data (blue line) during the entire test, showing that the force gauge is affected by the inertia of the stick-slips. b) Strain gauge data are plotted against force gauge data (blue line) during elastic loading and fit with a linear trendline of gradient* $C_{F\varepsilon}$*. c) Using Equation 5.2, strain-calibrated force* F_{strain} *is calculated (grey line) and filtered to give* $F_{strain,f}$ *(black line). d) For test PMMA_400_30 which has significant pre-seismic slip and precursory events, force gauge data* F *is used. Green extent box is zoomed in for e) where lack of detail for filtered data* $F_{strain,f}$ *can clearly be seen.*

5.2.5 Data processing

Following strain gauge calibration and obtaining demeaned force gauge data $F_{strain,f}$, mechanical data (force, load point displacement and time) are processed as described in Chapter 4, Section 4.2.4 using Matlab codes *friction_process.m, triaxial_calibration.m* and *find_stickslip_v4.m*, and Equations 4.2 – 4.8 (Chapter 4). Shear modulus G = 33.3 GPa is used to calculate seismic moment. Values used for stick-slip picking for each experiment using code *find_stickslip_v4.m* are presented in Appendix 5.6.2. Mechanical data are used to calculate static mechanical stress drop, average fault slip, recurrence interval, slip duration and pre-seismic slip (Figure 5.3).

P- wave seismic data measured using the top platen of the seismic assembly are processed as described in Chapter 4, Section 4.2.5 using Matlab codes *acoustic_process_v3.m* and *brune_fit.m*, Equations 4.9 – 4.14 and the data processing workflow outlined in Chapter 3, Section 3.2.1 (McLaskey et al., 2015) are used to process .atf files. Source (displacement) spectra are found by dividing the internal instrument-apparatus response (top platen; Chapter 3, Figure 3.18) from stick-slip spectra (Chapter 4, Figure 4.8). Displacement spectra are then fit using a Brune model with a non-linear least squares routine to find the seismic moment M_0, corner frequency f_0, source radius r and average rupture velocity $\bar{v}_s$ of each large stick-slip event. Seismic moment is converted to moment magnitude M_w using the relation $M_w = 2/3 \times \log_{10}(M_0) - 6.033$ (Hanks and Kanamori, 1979).

The limitations of spectral modelling using the Brune model for determining the seismic moment of large stick-slips are discussed in detail in Chapter 4. However, it remains useful for monitoring significant changes in the frequency content of seismic events. A circular rupture model is used to determine whether source radius or rupture velocity is more likely to vary with slip, as discussed in Chapter 4, Section 4.4.3. While little fault dimension variation is expected in a rectangular rupture model (Chapter 4, Equations 4.2 and 4.11 – related to the width and length of the fault, which change minimally), a circular rupture model assumes that the source radius is proportional to corner frequency (Chapter 4, Equation 4.12). If corner frequency changes significantly, this will either be due to changes in source radius or changes in rupture velocity.

5.2.5.1 Local magnitude M_L

Noting the limitations in spectral modelling for large stick-slip events outlined in Chapter 4, the local moment magnitude M_L (Richter, 1935) of each event is used in addition to seismic moment to characterise event size using seismic data. M_L was developed by Richter as the first earthquake scale that describes the size of an earthquake quantitatively. M_L can be defined:

$$M_L = \log_{10} A - \log_{10} A_0, \quad (5.2)$$

where A is the amplitude of displacement due to an earthquake and A_0 is the amplitude of a reference event, as measured on a Wood-Anderson seismograph (Gutenberg and Richter, 1941; Richter, 1935). The scale was calibrated such that an event of magnitude 0 has a displacement of 1 μm at a distance of 100 km. In this study, amplitude A is the amplitude of each large stick-slip P-wave measured using seismic acquisition apparatus, in V. Given the distances in the experimental setup are constant, A_0 is simply defined by the amplitude of a reference event, PMMA_120_50_001, the large stick-slip event with the largest amplitude across all experiments (54.0 V). As such, all magnitudes are relative to this reference event, rather than absolute. As M_L is, in this case, characterised using Volts and M_W is characterised using Nm, a 1:1 correlation between values is not expected, unlike other studies which have compared M_L to M_W using displacement seismograms. However, M_L and M_W should scale as they are both measurements of seismic event size. Significant differences in M_L and M_W scaling could relate to differences in physical source properties such as low or high stress drop or corner frequency, meaning that breaks in scaling are a potential proxy for source property variation across experiments.

While there are limitations to using M_L in areas with large regional variations in properties such as crustal velocity or across subduction zones, M_L is suitable for estimating the magnitude of near-source (< 100 km source-to-receiver distance) seismic events in simpler geological settings (Ristau, 2009). Due to the extremely short, and constant, source-to-receiver distances (< 100 mm) in frictional sliding experiments conducted in this study, M_L is a viable alternative for characterising the magnitude of large stick-slips.

Code *stickslip_process_rough.m* is used to make figures for source property comparison across different roughnesses and normal stresses.

5.2.6 Electron backscatter diffraction (EBSD) imaging

Scanning electron microscope (SEM) imaging was carried out in the SEM Shared Research Facility at the University of Liverpool using a Zeiss Gemini 450 field-emission gun (FEG) SEM (Chapter 2, Figure 2.15). Electron backscatter diffraction (EBSD) images were collected using a high-speed Oxford Instruments Symmetry EBSD detector. EBSD images of the 3.8 μm grit sample surface pre- and post-experiment are captured using the AZtec Oxford Instrument acquisition software. A variable pressure (VP) of 24 Pa and collector bias of 249 V are used to improve image quality and reduce the effect of surface charging on image capture (Goldstein et al., 1981). A low probe current of 2 nA is used, as solely surface topography and damage (rather than for instance, geochemical analyses of sub-sample grains in rock samples) are of interest in this study.

Using a magnification of 300x, areas of up to 37.5 mm^2 are imaged using EBSD imaging. Images are collected sequentially and then stitched together in AZtec to form image montages so that a representative area of each surface can be imaged. AZtec is used to convert .dat data files to .tif image files with automated brightness and contrast settings to enhance image quality. Dimensions of observed features (such as troughs) are measured using the ImageJ analyse menu.

5.3 RESULTS

5.3.1 Mechanical data

12 experiments are presented in this chapter (Table 5.1), with the experimental results showing a wide range of mechanical and seismological behaviour and slip dynamics. As load point displacement increases, three different modes of slip emerge: 1) a continuation of unstable stick-slip; 2) stable sliding and 3) quasi-stable sliding. Figure 5.3 highlights how each of the three modes is defined in this study using frictional stability criteria (Dieterich, 1978).

All experiments show initial elastic loading, characterised by an initially linear portion of each curve in the data (Figures 5.4 – 5.7). Following elastic loading, the fault interface yields as surfaces begin to slide on initiation of the first large-stick-slip, typically around 10 – 20 MPa which is within the expected range of shear stress for PMMA (Appendix 5.6.1; Bouissou et al., 1999). Following yielding and the first large stick-slip, stick-slips begin to occur regularly. Following this, the three different slip modes emerge, depending on experimental conditions. These three modes of slip can be defined using a slip-weakening friction framework with the following parameters: $k =$ system stiffness; $\sigma =$ normal stress; $\frac{\partial f}{\partial \delta} =$ the rate of change in frictional resistance, where ∂f is a small friction perturbation and $\partial \delta$ is a small displacement perturbation. While unstable stick-slip (Figure 5.3a) occurs when frictional resistance decreases faster than the driving force (Chapter 1, Section 1.2.1), stable sliding (creep; Figure 5.3b) occurs when frictional resistance decreases more slowly than the elastic system unloading (Segall, 2010). During quasi-stable sliding (intermediate stability; more stable than stick-slip, less stable than stable sliding), small oscillations in shear stress can be observed (Figure 5.3c). This is due to the frictional resistance decreasing at approximately the same speed as elastic unloading.

Table 5.1: *Summary of experimental conditions and stick-slip observations presented in this chapter.*

Experiment Name	Roughness Z_{rms} (μm)	Normal Stress (MPa)	No. large stick-slip events	No. small precursor events	Stable sliding ?	Quasi-stable sliding?
PMMA_120_30	125	30	15	9	Y	Y
PMMA_120_40	125	40	17	5	N	N
PMMA_120_50	125	50	2	1	Y	N
PMMA_400_30	18.3	30	18	24	N	Y
PMMA_400_40	18.3	40	21	2	N	N
PMMA_400_50	18.3	50	4	3	Y	Y
PMMA_800_30	7.7	30	8	3	Y	Y
PMMA_800_40	7.7	40	25	0	N	N
PMMA_800_50	7.7	50	22	47	N	Y
PMMA_1200_30	3.8	30	19	78	N	Y
PMMA_1200_40	3.8	40	21	1	N	N
PMMA_1200_50	3.8	50	19	12	N	N

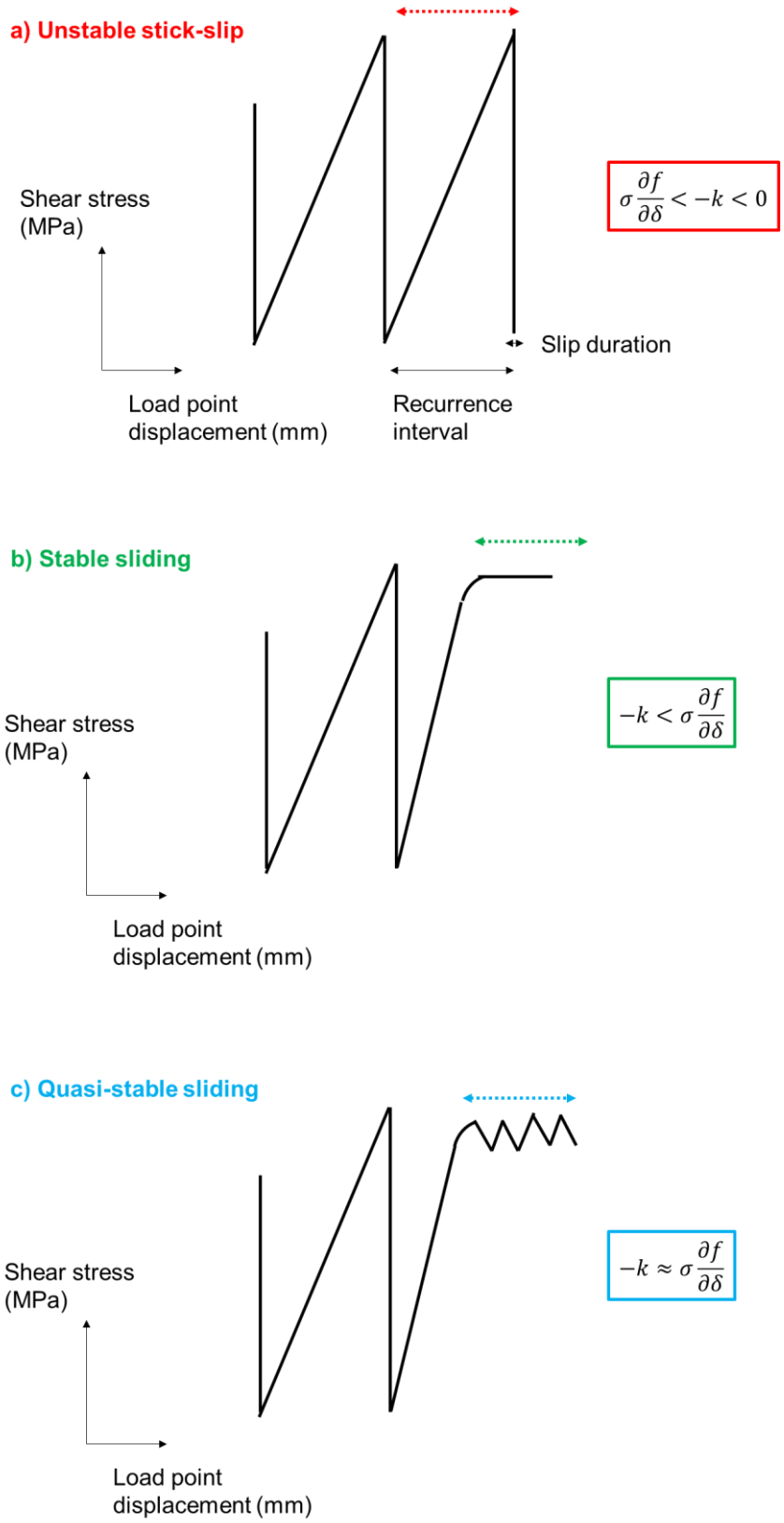

Figure 5.3: *Schematic diagram of how recurrence and slip duration are defined and three different modes of slip (indicated by colours arrows) which emerge following the initial large stick-slip: a) unstable stick-slip, b) stable sliding and c) quasi-stable sliding. Frictional criteria for each slip mode are in the right-hand text boxes.*

Mechanical results are first discussed as a function of roughness and normal stress and then analysed together for comparison. The results presented are shear stress derived from force gauge data, τ, to show detailed frictional sliding behaviour: examples of shear-calibrated force measurements used to calculate stress drops of large stick-slips are given in Appendix 5.6.1. Appendix 5.6.3 presents a table with statistical measurements (mean and range) of stress drop, slip duration and recurrence interval of large stick-slips.

5.3.1.1 125 µm data

A wide range of frictional behaviour is observed in the roughest surfaces (Figure 5.4a). At 30 MPa, large stick-slip begins with two large stick-slips with a much larger recurrence interval (541 s) than on average (154 s). No precursory events are observed until the sixth large stick-slip (2.33 mm displacement), after which precursory activity increases until the final stick-slip. Precursory events have a mean stress drop of 0.274 MPa with a mean slip duration of 6.87 s. Following the final stick-slip, there is a transition from quasi-stable sliding to stable sliding (Figure 5.4b). At 40 MPa, large stick-slips are more regular with a smaller range of recurrence interval. Fewer precursory events are observed, with a smaller mean stress drop (0.174 MPa) than at 30 MPa. At 50 MPa, only two large stick-slips are observed before a transition to stable sliding.

The roughest surfaces produced large stick-slips with the longest slip durations (Appendix 5.6.3). Moreover, on average they take the longest to yield and initiate the first large stick-slip.

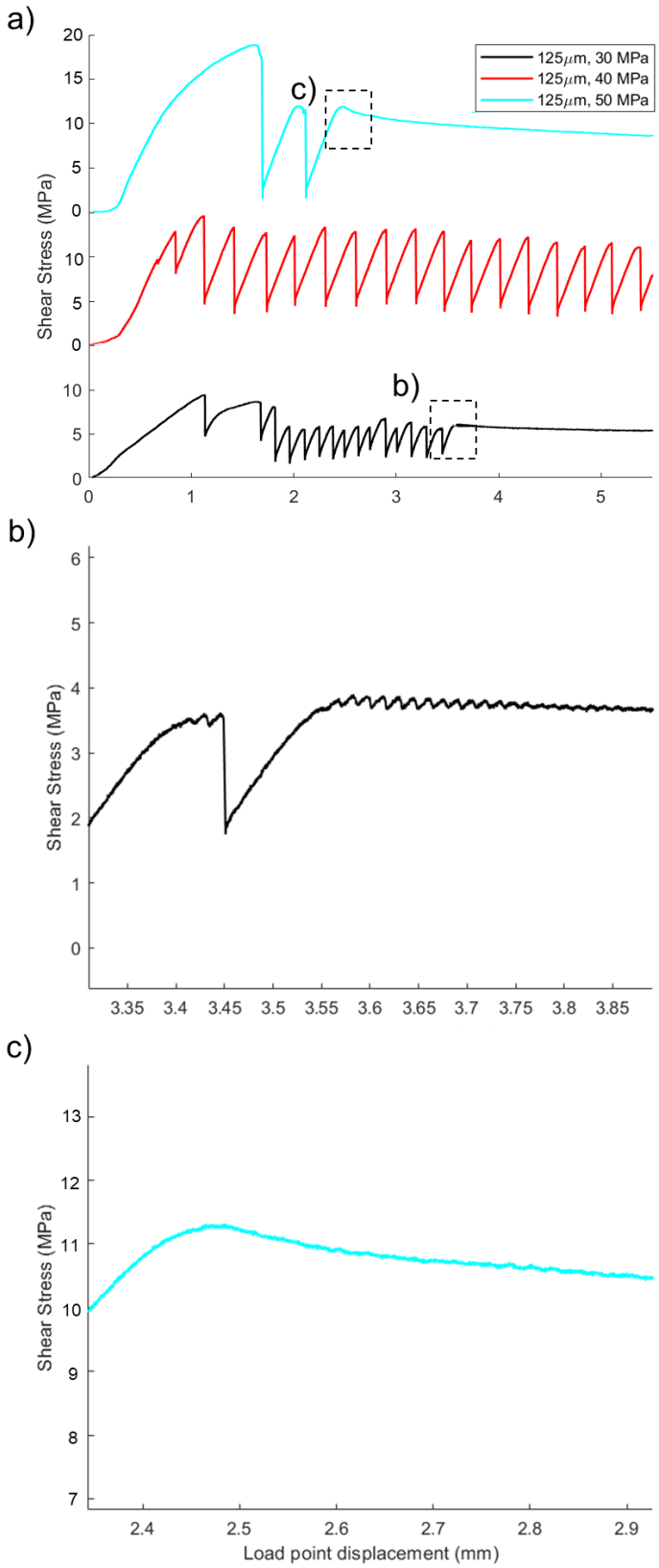

Figure 5.4: *a) Shear stress plotted as a function of load point displacement for experiments PMMA_120_30, PMMA_120_40 and PMMA_120_50, conducted using 125 μm grit roughened PMMA at 30, 40, and 50 MPa respectively. Extent plots b) and c) show more detail of b) a transition from stick-slip to quasi-stable sliding to stable sliding at 30 MPa and c) stable sliding at 50 MPa.*

5.3.1.2 18.3 μm data

For surfaces with 18.3 μm grit applied, large stick-slips are shorter in duration with a much smaller duration range (Figure 5.5a) than the 125 μm grit surfaces. At 30 MPa, the recurrence interval of large stick-slips increases as load point displacement increases. Precursory events are observed after 1.68 mm and the number of precursory events before each large stick-slip increases with load point displacement. Precursory events have a mean stress drop of 0.359 MPa with a mean slip duration of 7.32 s. after the final large stick-slip, there is a transition to quasi-stable sliding (Figure 5.5b). Very few precursory events are observed at 40 MPa, with a transition from quasi-stable sliding to stable sliding at 2.1 mm for the 50 MPa test.

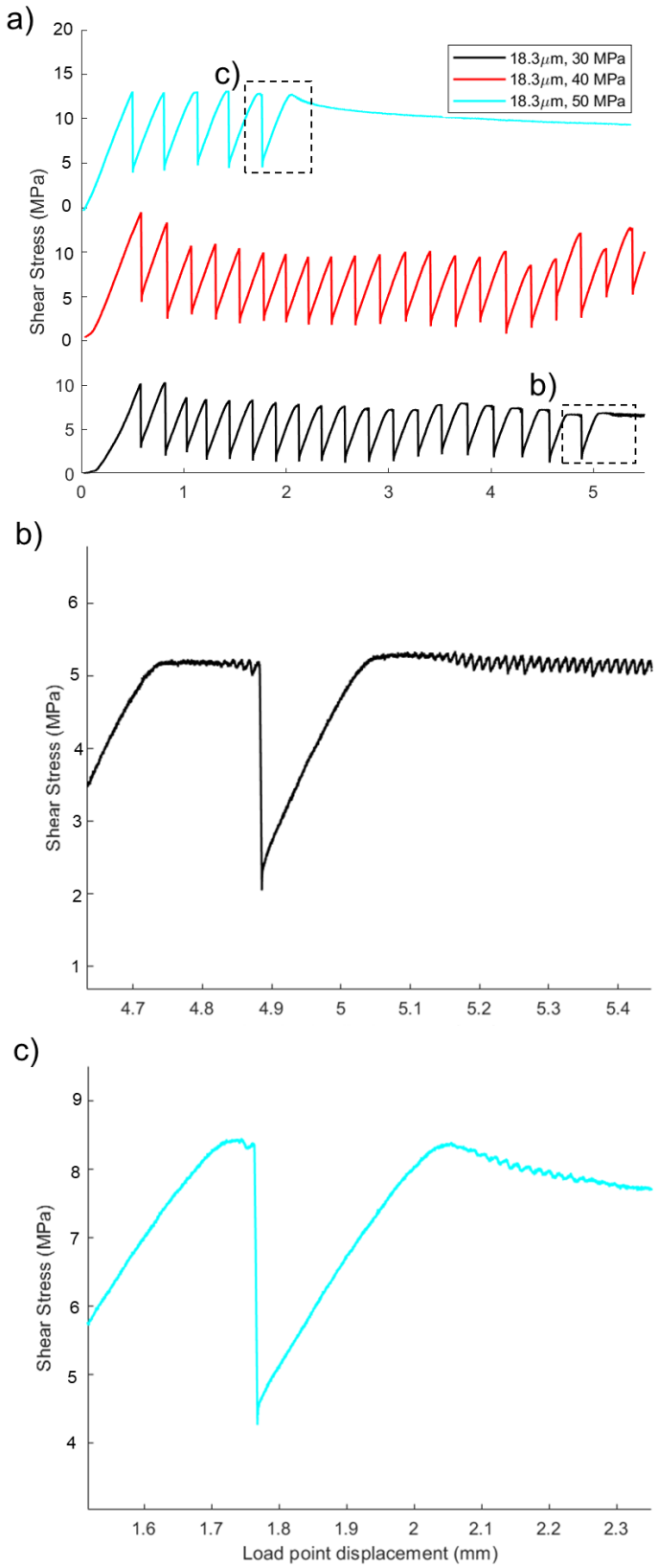

Figure 5.5: *a) Shear stress plotted as a function of load point displacement for experiments PMMA_400_30, PMMA_400_40 and PMMA_400_50, conducted using 18.3 μm grit roughened PMMA at 30, 40, and 50 MPa respectively. Extent plots b) and c) show more detail of b) a transition from stick-slip to quasi-stable sliding at 30 MPa and c) a transition from quasi-stable sliding to stable sliding at 50 MPa.*

5.3.1.3 7.7 µm data

For surfaces created using 7.7 µm grit, large stick-slips are shorter in duration with a much smaller duration range (Figure 5.6a). At 30 MPa, the recurrence interval of large stick-slips is regular throughout the test, with a range of 12.4 s. A transition from quasi-stable sliding to stable sliding can be observed following the final large stick-slip at 1.9 mm (Figure 5.6b). This stable sliding evolves into quasi-stable sliding at 2.5 mm and continues until the end of the test (Figure 5.6c). At 40 MPa, the stress drop range of large stick-slips is the largest of all tests (6.44 MPa), with stress drop decreasing to 4.52 MPa until 3.3 mm, where stress drop suddenly increases to 10.5 MPa. Stress drops at 50 MPa are significantly smaller (mean of 4 MPa) than other roughnesses at 50 MPa (means of 12.1, 8.62 and 5.56 MPa for 125, 18.3 and 3.8 µm grit respectively). There is also significantly more precursory activity in comparison to the 30 and 40 MPa tests, with period-doubling (alternating between small and large stick-slips) observed (Figure 5.6d). The mean stress drop of precursory events is 0.351 MPa, with a mean duration of 5.2 s.

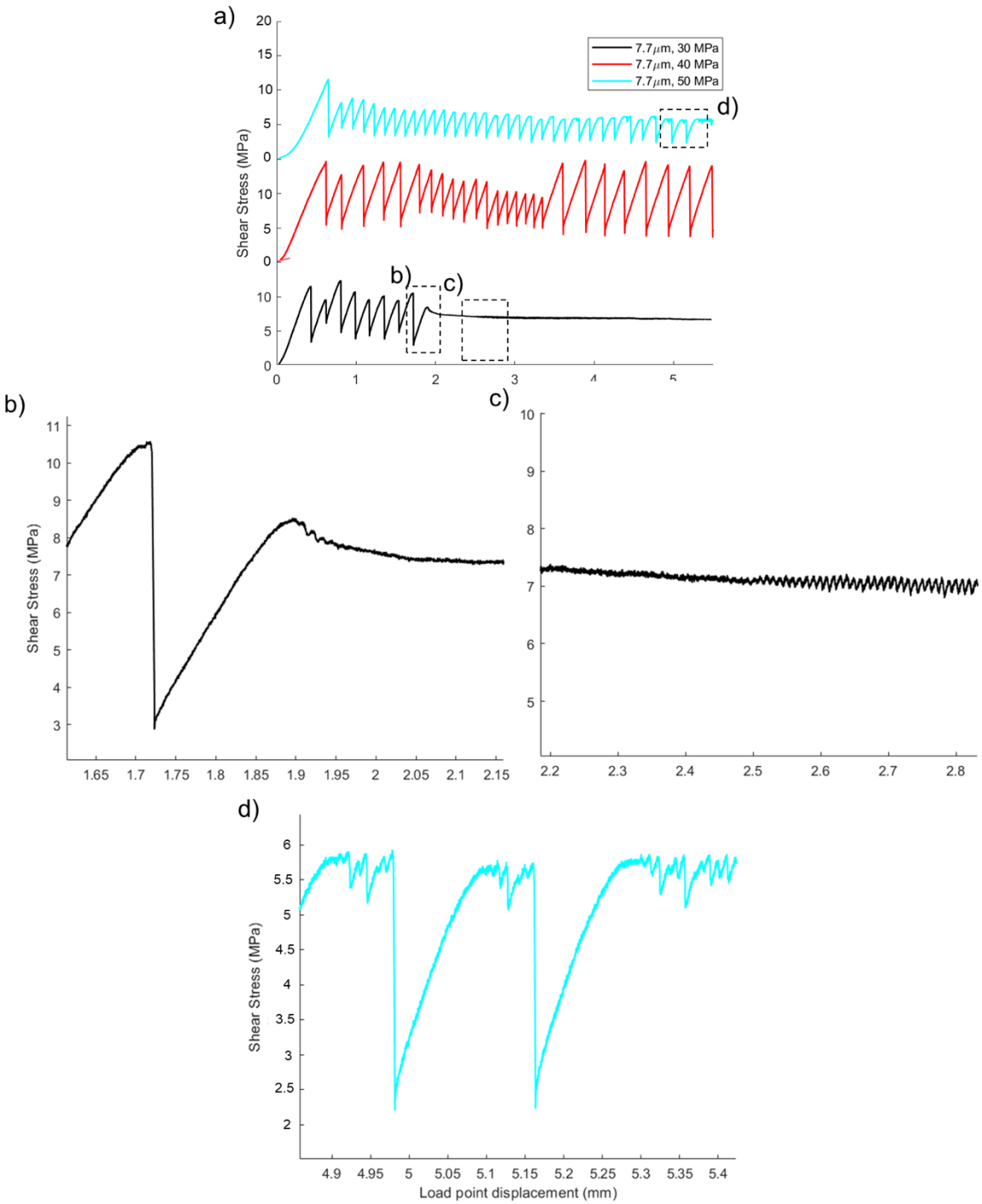

Figure 5.6: *Shear stress plotted as a function of load point displacement for experiments PMMA_800_30, PMMA_800_40 and PMMA_800_50, conducted using 7.7 μm grit roughened PMMA at 30, 40, and 50 MPa respectively. Extent plots b), c) and d) show more detail of b) a transition from quasi-stable sliding to stable sliding at 30 MPa, c) a transition from stable sliding to quasi-stable sliding at 30 MPa and d) quasi-stable sliding at 50 MPa.*

5.3.1.4 3.8 µm data

The smoothest surfaces exhibit continued stick-slip throughout the tests (Figure 5.7a). At 30 MPa, large stick-slips continue until 0.9 mm displacement, where there is a transition from stick-slip to quasi-stable sliding (Figure 5.7b). Interestingly, the stress drops of the quasi-stable slip increase with load point displacement, starting regularly and then evolving into more chaotic stress drops with period doubling (Figure 5.7c). After 1.8 mm, unstable stick-slip behaviour restarts, with significant precursory behaviour. The mean stress drop of precursory events is 0.422 MPa, with a mean duration of 4.9 s.

The smoothest surfaces produced large stick-slips with small stress drops and the shortest slip durations (Appendix 5.6.1). No stable sliding is observed at all normal stresses.

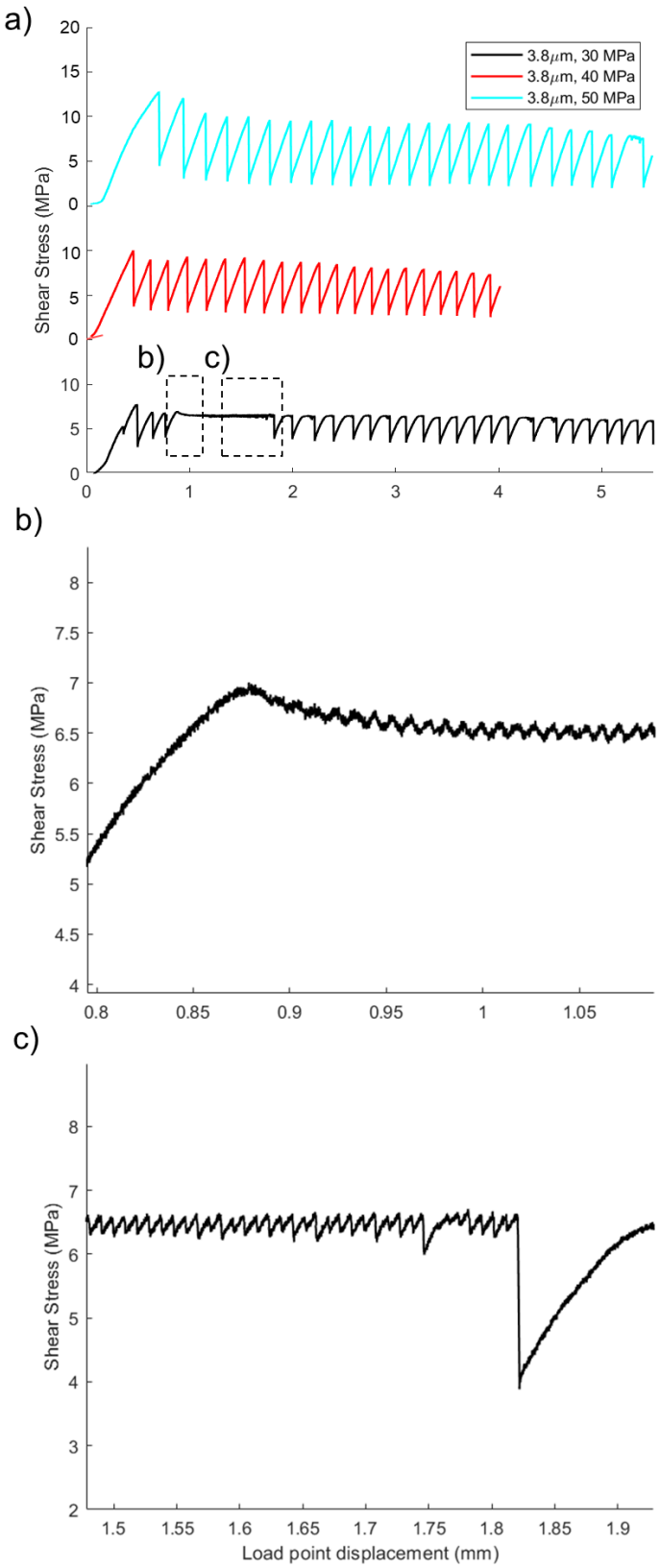

Figure 5.7: *Shear stress plotted as a function of load point displacement for experiments PMMA_1200_30, PMMA_1200_40 and PMMA_1200_50, conducted using 3.8 μm grit roughened PMMA at 30, 40, and 50 MPa respectively. Extent plots b) and c) show more detail of b) a transition from stable sliding to quasi-stable sliding at 30 MPa and c) a transition from quasi-stable sliding to stick-slip at 30 MPa.*

5.3.1.5 Mechanical data comparison

Figure 5.8 shows the mechanically measured static stress drop of large stick-slips as a function of load point displacement for all 12 experiments. In the majority of experiments, stress drop decreases with load point displacement. While the rougher surfaces (125 and 18.3 μm grit) tended to produce large stick-slips with higher stress drops, this was less pronounced at 30 MPa. Aside from test PMMA_800_50 (yellow pluses; Figure 5.8c), the static stress drop of large stick-slips generally increases with normal stress, although this increase is smaller between 40 – 50 MPa than between 30 – 40 MPa. Test PMMA_800_50 had lower stress drops than expected – this is potentially due to the large level of precursory events and pre-seismic slip observed.

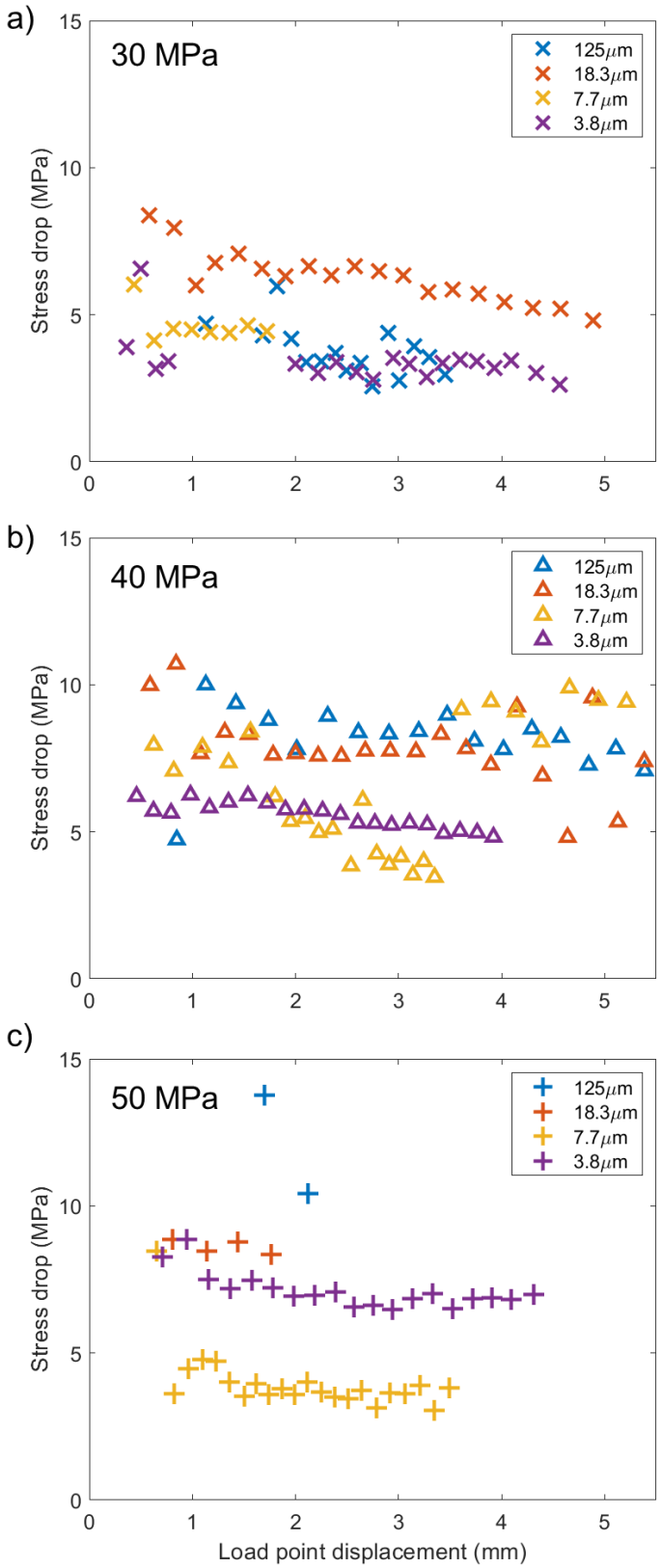

Figure 5.8: *Mechanical static stress drop as a function of load point displacement for experiments with all four roughnesses at a) 30 MPa (crosses), b) 40 MPa (triangles) and c) 50 MPa (pluses). Marker colours indicate the initial surface roughness and are outlined in the legend.*

Figure 5.9 outlines how pre-seismic slip changes with surface roughness, normal stress and load point displacement for large stick-slip events. Many events at 30 MPa have a significant amount of pre-seismic slip, with the smoothest surface (3.8 μm) having persistent pre-seismic slip through most of the test. At both 30 and 50 MPa, the 125 μm tests started with a large amount of pre-seismic slip, which decreases suddenly as slip transitions to either unstable stick-slip or stable sliding. Very little pre-seismic slip (under 1 μm) is measured at 40 MPa, which coincides with a lack of precursory events and relatively high stress drops of large stick-slips (Figure 5.8). Pre-seismic slip generally increases with load point displacement, which is consistent with the results of Chapter 4 and previous studies (Cattania and Segall, 2019; Shreedharan et al., 2020). Figure 5.7f) confirms that lower stress drops observed in test PMMA_800_30 are due to increased pre-seismic slip.

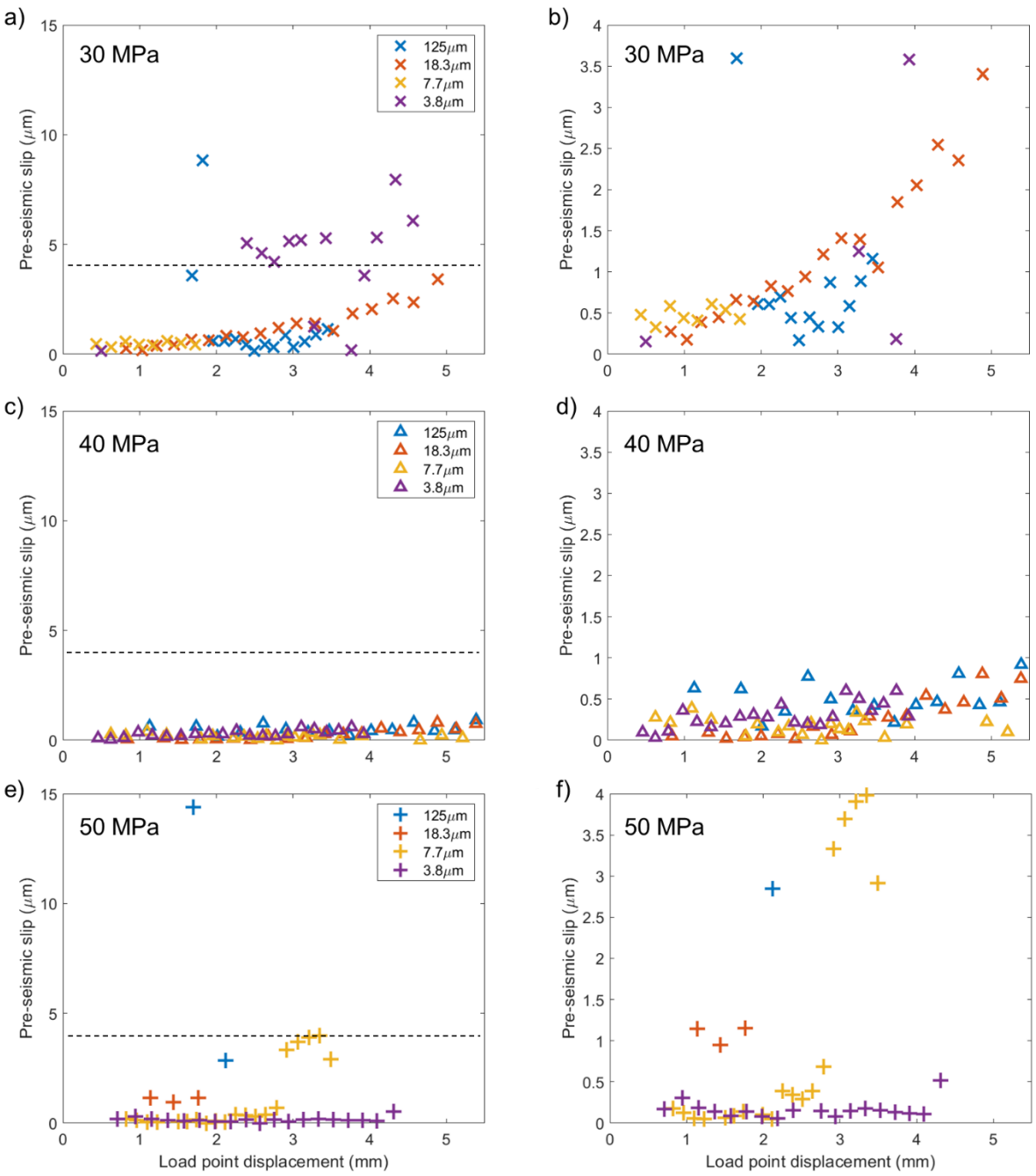

Figure 5.9: *Pre-seismic slip as a function of load point displacement for experiments with all four roughnesses at a) 30 MPa (crosses), c) 40 MPa (triangles) and e) 50 MPa (pluses). Black dotted line represents zoomed-in area presented in Figures b), d) and f).*

Figure 5.10 shows how the mechanically derived seismic moment (Chapter 4; Equation 4.7) with shear modulus $G = 33.3$ GPa varies with load point displacement for large stick-slip events. As static stress drop is proportional to average fault displacement (Chapter 4; Equations 4.5 and 4.6), mechanical stress drop (Figure 5.8) and seismic moment are proportional, showing similar trends. Rougher surfaces (125 and 18.3 μm grit) tended to produce large stick-slips with higher seismic moments and in general, the seismic moment of large stick-slips generally increases with

normal stress. This implies that the rupture patch is dependent on normal stress, which could be due to the fault interface having greater coupling for higher normal stress.

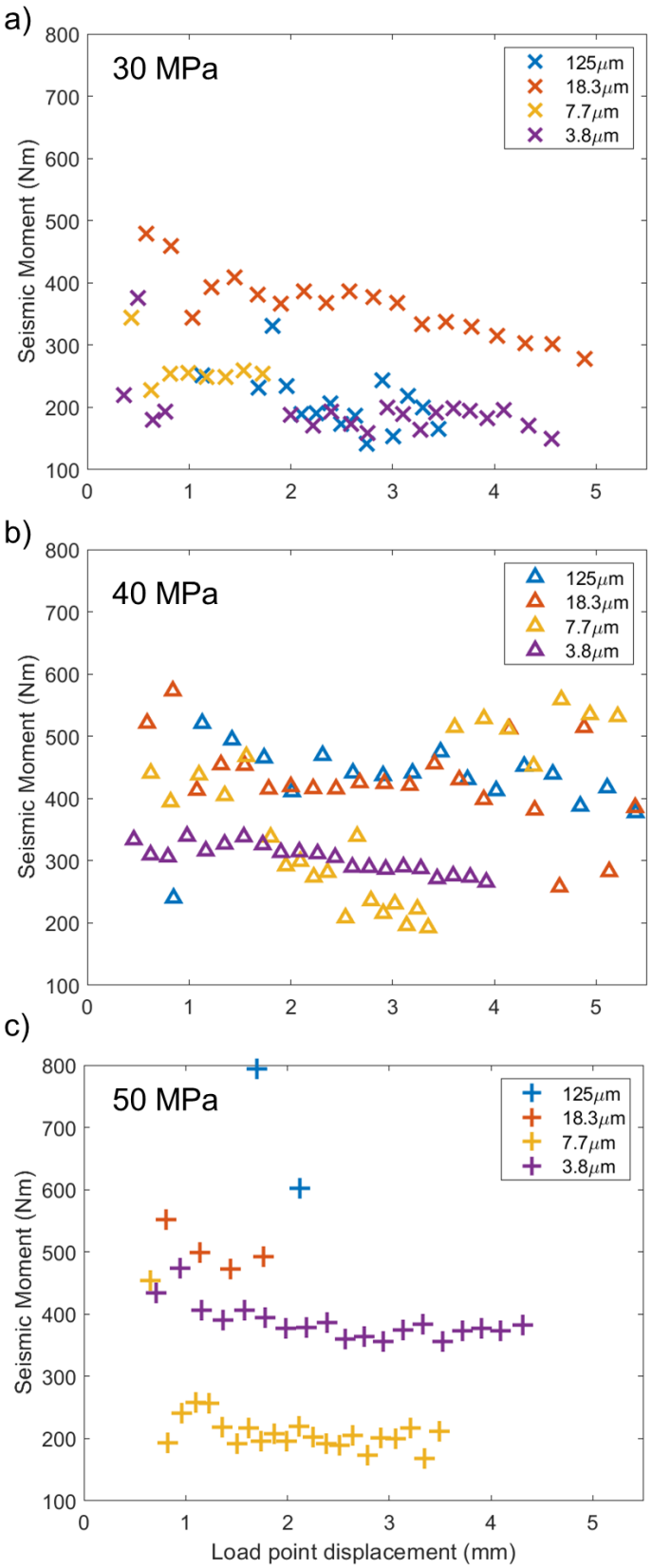

Figure 5.10: *Mechanical seismic moment as a function of load point displacement for experiments with all four roughnesses at a) 30 MPa (crosses), b) 40 MPa (triangles) and c) 50 MPa (pluses). Marker colours indicate the initial surface roughness and are outlined in the legend.*

5.3.2 Seismic data

Figure 5.11a shows the seismograms of the large stick-slip event with the highest amplitude, (reference event PMMA_120_50_001) and one of a much smaller amplitude, PMMA_1200_30_006. Seismic data are processed, with the internal instrument-apparatus response of the top platen divided from the spectra of measured signals to give displacement spectra (Figure 5.11b). While there is a significant difference (approximately 16 times) between the seismograms' amplitudes, there does not appear to be a large difference in the seismic moment (approximately 2 times), as indicated by the low-frequency spectral plateau. However, the corner frequency of event PMMA_1200_30_006 visually appears to be lower than event PMMA_120_50_001, which is also reflected in the fitted Brune model curves. The higher corner frequency, which reflects a higher proportion of high-frequency motion radiated, therefore contributes to the higher time-domain amplitudes.

To observe differences in frequency content and relate this to mechanical observations, event PMMA_120_300_006 is compared to an event of a similar seismic moment, PMMA_120_30_003. The corner frequency of event PMMA_120_30_003 visually appears to be higher than that of PMMA_120_300_006, which is again reflected in the fitted Brune models.

As corner frequency is inversely proportional to source duration (rise time), which is itself proportional to source radius and rupture velocity (Chapter 4; Equation 4.11), the low corner frequency of event PMMA_1200_30_006 could indicate either that it has a larger source radius (for constant rupture velocity, the shear wave velocity of PMMA, $\beta = 1.20$ km/s), or lower rupture velocity than events PMMA_120_50_001 and PMMA_120_30_003. Noting the findings of the previous chapter where corner frequency (and therefore source radius) remained around 30 kHz ($\sim$ 35 mm), these new results suggest that the source may not remain self-similar throughout the tests. The source radius of event PMMA_1200_30_006 is larger than the inferred rupture area, the sample dimensions (36 x 18 mm), meaning that corner frequency and source radius may not be related to the sample size. Source radius could instead be related to fault displacement during the 'slip' of stick-slip. Alternatively, rupture velocity could be related to fault slip as corner frequency is inversely proportional to rise time $t_{1/2}$ ($f_0 \approx \frac{1}{t_{1/2}}$; Chapter 1, Section 1.4.2), meaning that changes in corner frequency indicate changes to the duration of rupture.

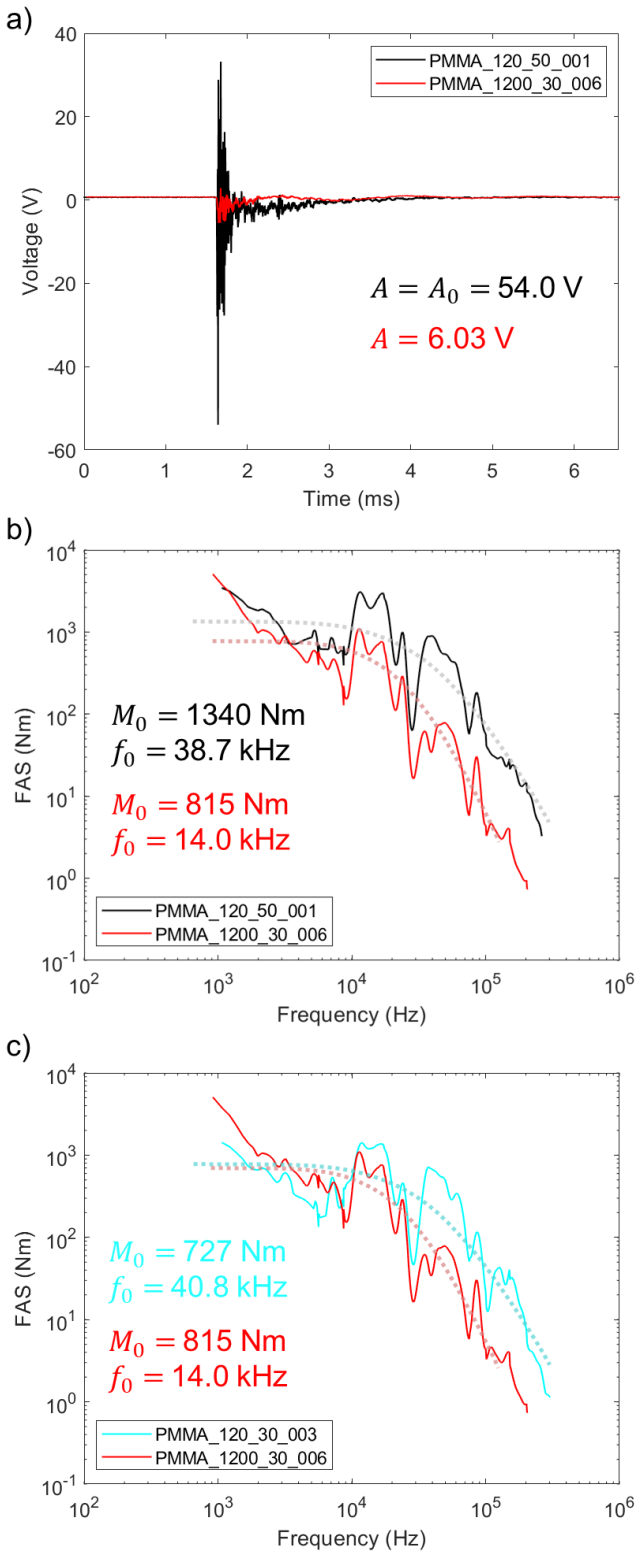

Figure 5.11: *a) Seismograms of large stick-slip events with vastly different amplitudes, PMMA_120_50_001 (black line) and PMMA_1200_30_006 (red line) measured using the top platen of the seismic assembly. b) Displacement spectra of large stick-slip events PMMA_120_50_001 (black line) and PMMA_1200_30_006 (red line) with respective Brune model fits (dotted lines). c) Displacement spectra of large stick-slip events with similar seismic moment M_0 but different corner frequencies f_0, PMMA_120_30_003 (cyan line) and PMMA_1200_30_006 (red line) with respective Brune model fits (dotted lines).*

Figure 5.12 shows source radius (measured using seismic waves and Brune modelling) as a function of average fault slip (measured mechanically) for all large stick-slip events (Hypothesis B, Chapter 4, Section 4.4.3). While there is no clear correlation between both parameters, events in tests PMMA_1200_30 (purple crosses; Figure 5.12a), PMMA_800_50 (yellow pluses; Figure 5.12c) and PMMA_1200_50 (purple pluses; Figure 5.12c) tend to have above average source radii when compared to other events. Moreover, smoother surfaces generally produce events with larger source radii than rougher surfaces.

Figure 5.13 shows the average rupture velocity (measured using seismic waves and Brune modelling) as a function of average fault slip for all large stick-slip events (Hypothesis C, Chapter 4, Section 4.4.3). Again, there is no clear correlation between both parameters, but events in tests PMMA_1200_30 (purple crosses; Figure 5.13a), PMMA_800_50 (yellow pluses; Figure 5.13c) and PMMA_1200_50 (purple pluses; Figure 5.13c) tend to have below average rupture velocity when compared to other events. Moreover, smoother surfaces generally produce events with lower rupture velocity than rougher surfaces.

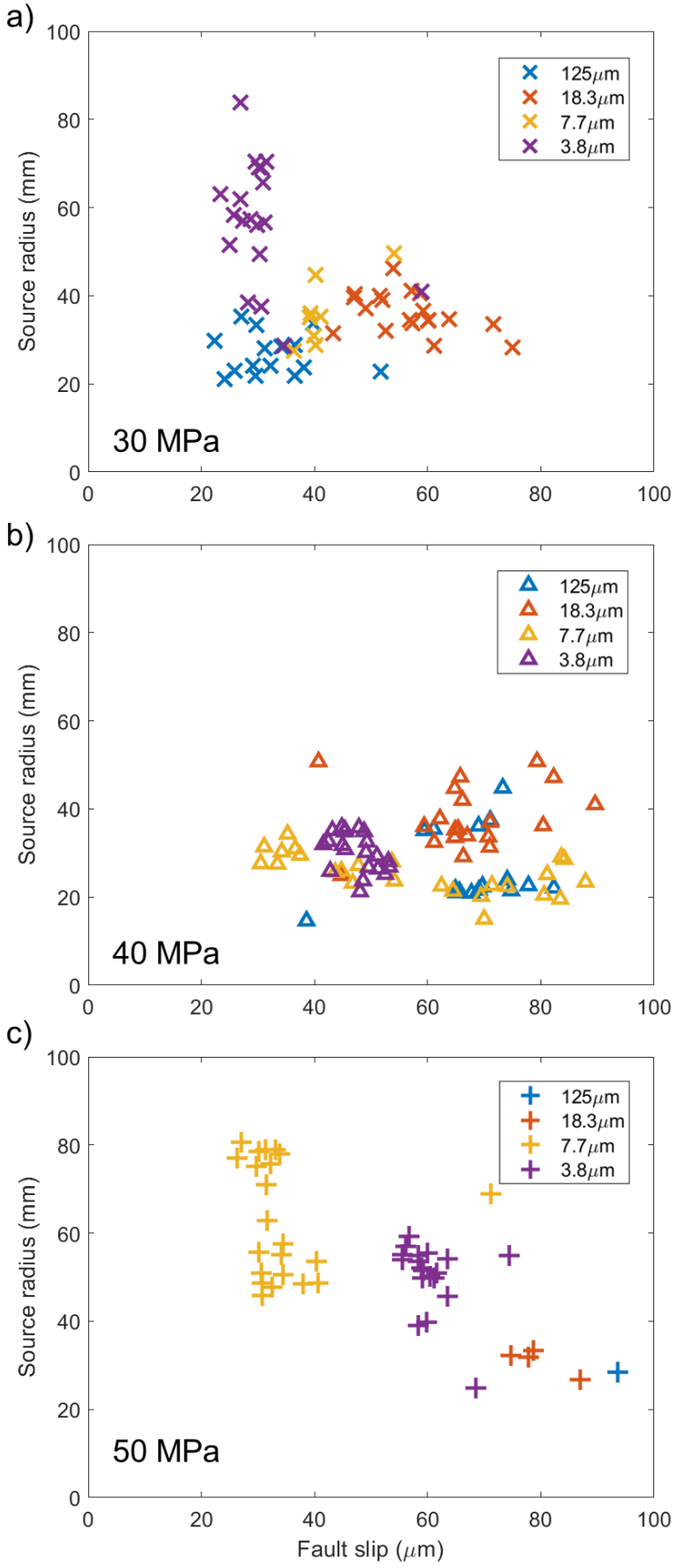

Figure 5.12: *Comparison of average fault slip and source radius, assuming a constant rupture velocity, for large stick-slip events at a) 30 MPa, b) 40 MPa and c) 50 MPa.*

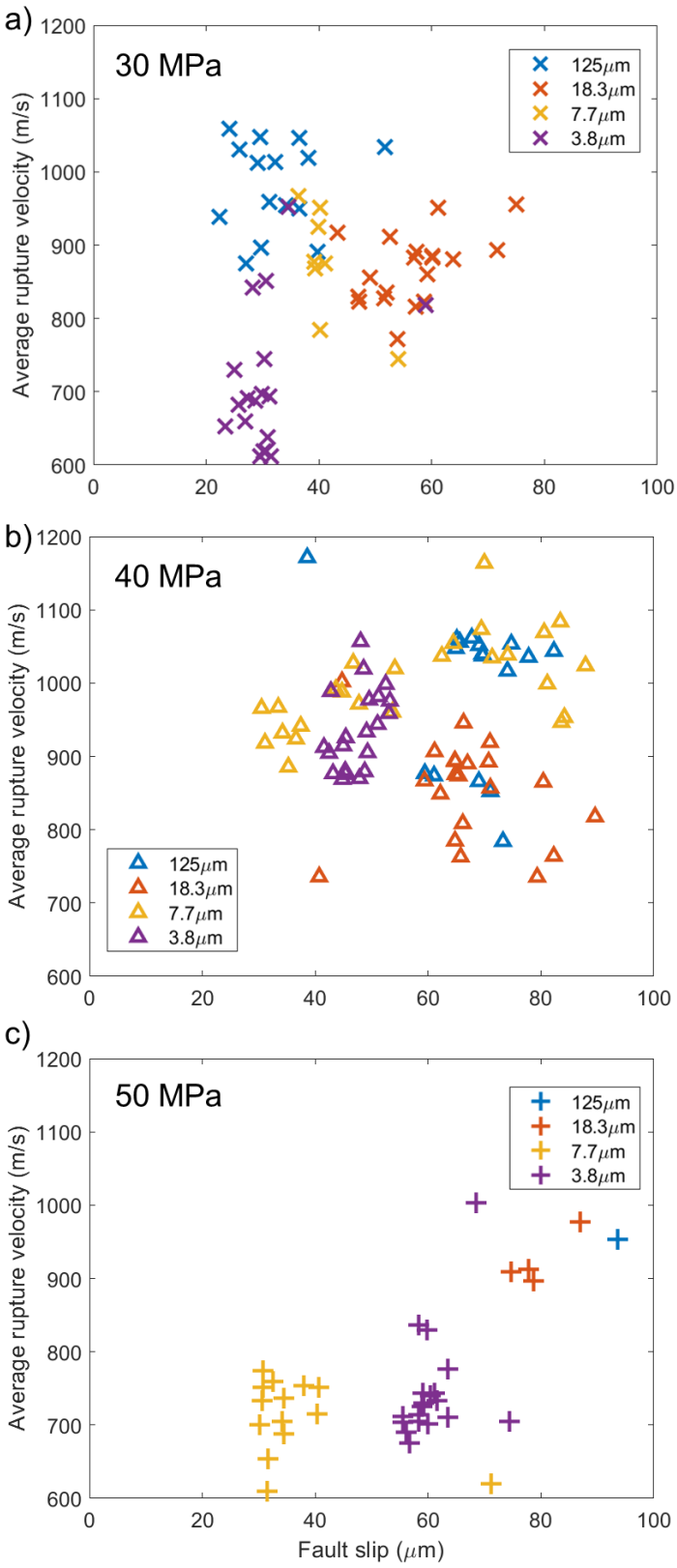

Figure 5.13: *Comparison of average fault slip and average rupture velocity, assuming a constant source radius* $r = 35$ *mm for large stick-slip events at a) 30 MPa, b) 40 MPa and c) 50 MPa.*

5.3.2.1 *Local magnitude vs moment magnitude*

Reference event PMMA_120_50_001 (Figure 5.11) is used in Equation 5.3 to determine an apparent local magnitude. M_L values are normalised so that M_L and M_W for the largest event, PMMA_120_50_001, are equal. The relationship between M_L and moment magnitude M_W at each normal stress can be observed in Figure 5.13. There is a moderate positive correlation between M_L and M_W (R^2= 0.587). The scatter observed could be due to the limitations of Brune modelling for quantifying seismic moment M_0 for large stick-slips or due to varying source properties. For example, large stick-slip PMMA_1200_30_006 (purple cross; Figure 5.14) resides outside of the upper 95% standard error prediction interval. Figure 5.11b and 5.11c outlined that this event has a lower corner frequency and larger source radius (or lower rupture velocity) than other events. Therefore, the breakdown in the relationship between M_L and M_W could be due to a larger source radius or lower rupture velocity. The 95% standard error prediction interval shows the error in M_W to be $\pm$ 0.2 magnitude units, which is equivalent to a factor of $\pm$ 200% (two times larger or smaller) in M_0. This is another possibility for the scatter, considering the range of low-frequency moments in Figure 5.11.

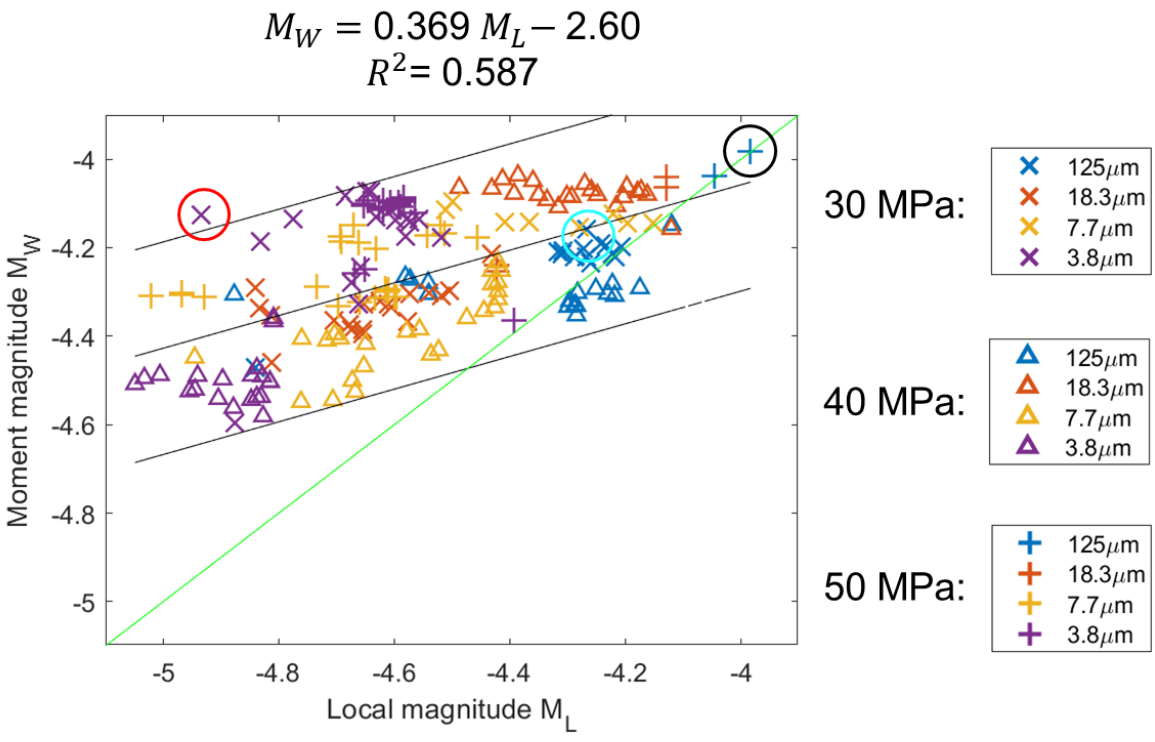

Figure 5.14: *Comparison of normalised local magnitude M_L with moment magnitude M_W for large stick-slip events at 30 MPa, 40 MPa and 50 MPa. Equation of linear regression line (black line; black dotted lines are 95% standard error prediction intervals) and R^2 value displayed on top of the graph. Black, red and cyan circles indicate events PMMA_120_50_001 (blue plus), PMMA_1200_30_006 (purple cross) and PMMA_120_30_003 (blue cross) respectively. The green line indicates where $M_L = M_W$.*

5.3.3 Electron backscatter diffraction (EBSD) images of pre- and post-experimental fault

SEM images (Figures 5.15 and 5.16) demonstrate how typical surface microstructures on 3.8 μm grit faults change following frictional sliding experiment PMMA_1200_30 at 30 MPa. Before the test is conducted, the initial surface roughness can be seen, with grooves (dark lines) in multiple directions, ranging from 0.5 – 10 μm in width (Figure 5.15a and 5.15c). Following frictional sliding, these grooves (light lines, Figure 5.15b and 5.15d) become more difficult to identify, are generally smaller, thinner and are infilled with gouge with a maximum diameter of 4 μm. Some gouge particles appear to be nanometric. Infilled grooves range from 0.5 – 10 μm in width. The grooves that were apparent in the pre-experiment sample (Figure 5.15c) appear to have been smoothed in the post-experiment sample (Figure 5.15d). Light patches indicate fault damage, of which there is a broad area in the post-experiment sample (top right; Figure 5.15b). Moreover, light and dark lines sub-parallel to the slip direction can be observed, highlighting striations created during frictional sliding (Figure 5.16).

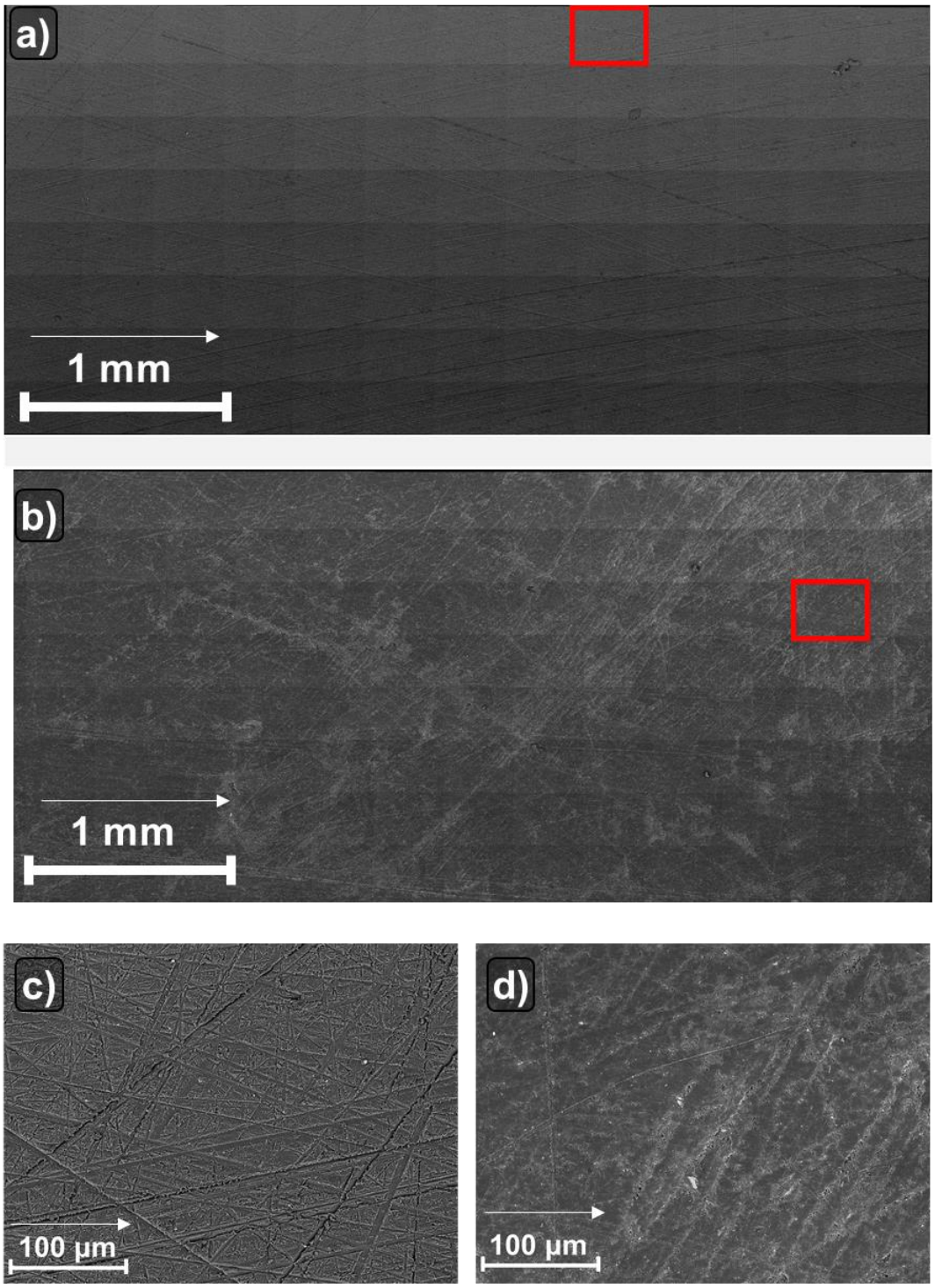

Figure 5.15: *Montage EBSD images of sample surface created using 3.8 µm grit (PMMA_1200_30) a) pre- and b) post-experiment. Further surface detail before and after the experiment can be observed in individual EBSD images c) and d) (red boxes in a) and b), respectively. Arrows indicate the direction of slip.*

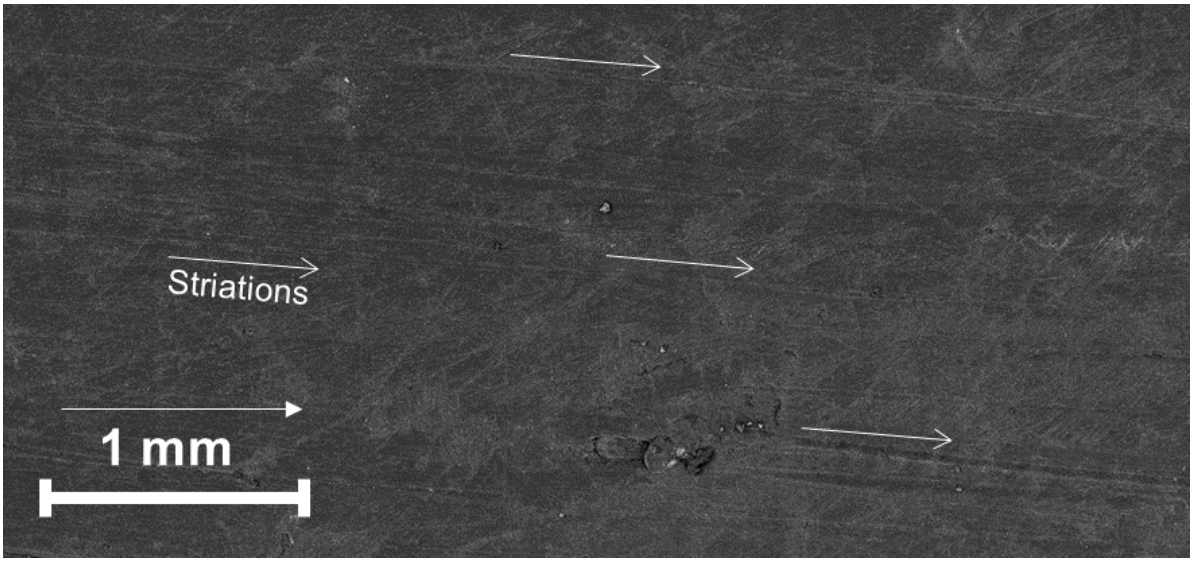

Figure 5.16: *Montage EBSD images of sample surface created using 3.8 μm grit (PMMA_1200_30), post-experiment with the direction of surface striations outlined. Arrow above the scale indicates the direction of slip; arrows across the image indicate the direction of striations.*

5.4 DISCUSSION

5.4.1 The role of roughness and normal stress on frictional behaviour

5.4.1.1 Asperity interactions

The initiation of stick-slip instability can be understood by considering asperity interactions, which will be affected by roughness, normal stress and the interplay between both factors. Asperities (locked areas, produced by uneven, sharp and rough surfaces) exist across multiple length scales and are often self-affine features, with 2D profiling of surface roughness amplitude remaining unchanged at different length and area scales (Candela et al., 2012, 2009). Two fundamental mechanisms based on asperity interactions have been presented to explain stick-slip generation and frictional strength variations: adhesion and interlocking (Figure 5.17).

Firstly, adhesion (Bowden et al., 1939; Bowden and Tabor, 1958; Dieterich, 1979a, 1978, 1972; Dieterich and Kilgore, 1994) assumes that contact asperities are welded together by van der Waals forces (attraction and repulsion between atoms; Margenau, 1939) due to high, local compressive stresses. During slip (relative to a reference plane), adhered junctions are sheared through to accommodate shear, increasing frictional strength. When relative slip ceases, asperity creep occurs between adhered junctions, increasing the real contact area with hold time, or stationary contact time (Dieterich and Kilgore, 1994). This mechanism implies that frictional healing during stationary contact time (or interseismic stick) contributes to fault strengthening. Several studies have shown that static frictional strength increases with stationary contact time

(Dieterich, 1979a, 1972; Karner and Marone, 2001; Linker and Dieterich, 1992; Marone, 1998a). However, on the initiation of slip, frictional resistance reduces to a smaller, dynamic frictional force (i.e. slip weakening friction) which may or may not evolve into slip instability depending on the system stiffness (Rice and Ruina, 1983).

Secondly, asperity interlocking (Boitnott et al., 1992; Scholz, 1998; Wang and Scholz, 1995, 1994) assumes that when two blocks make contact, the asperities with the highest amplitudes will penetrate each other and prevent sliding, increasing frictional resistance. This is particularly relevant at higher normal stresses, where due to high local compressive stresses, contacted asperities cannot slip over one another until the tips of the interlock asperities are sheared off. When contacts are sheared off and break, frictional resistance decreases. Stick-slip sliding has been suggested as the cyclic repetition of this process of interlocking and shearing of asperities, which causes surfaces to slide in an unstable way. In their micro indentation study, Scholz and Engelder (1976) found 'carrot' shaped wear grooves, with the sharp end of the grooves pointing in the direction of shear, as evidence for asperity interlocking. In this study, it is difficult to see the shape of post-experiment grooves in EBSD images due to infilled wear material and damage (Figures 5.15 and 5.16). However, the significant amount of gouge material air-blasted from post-experimental samples, particularly at 30 MPa normal stress, is evidence of this mechanism.

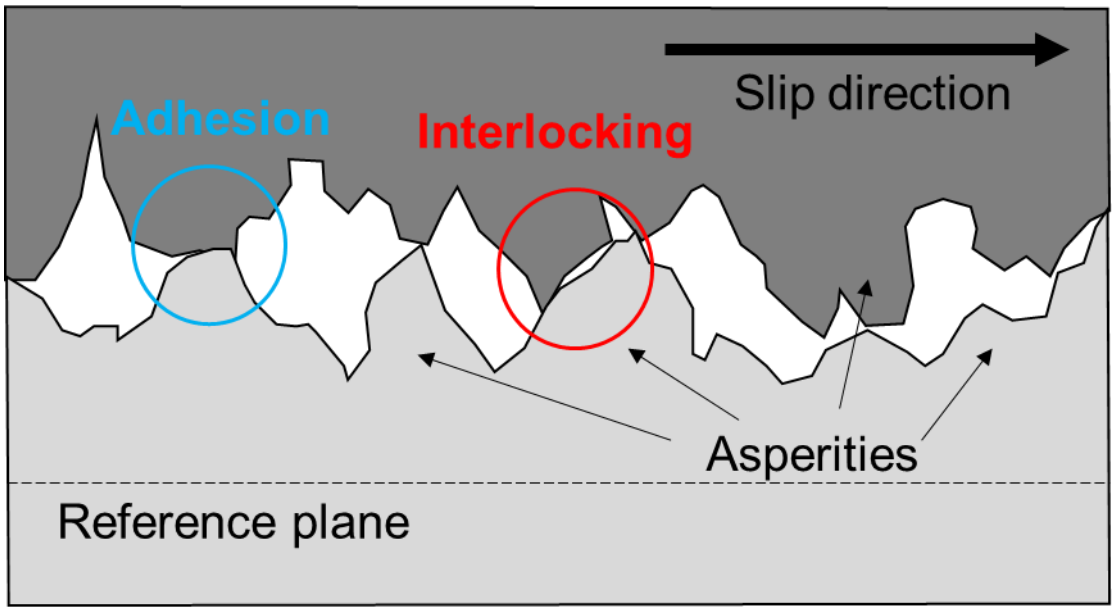

Figure 5.17: *Schematic diagram of the interactions of contact asperities during frictional sliding experiments. After Zhou et al. (2021).*

In this discussion, the role of surface roughness and normal stress on frictional behaviour is discussed considering the two aforementioned asperity interaction mechanisms.

5.4.1.2 Surface roughness

Results show that unstable stick-slip is more readily generated on smoother surfaces, which is shown through the higher frequency of large stick-slips and lower recurrence intervals, in agreement with similar studies (Bouissou et al., 1999; Morad et al., 2022; Zhou et al., 2021). This is due to differences in the real contact area of asperities: smoother faults have smaller variations in asperity amplitude and size than rougher surfaces (Figures 5.15c and 5.15d). Consequently, the real contact area of asperities of smoother fault systems is larger than that of rougher systems (Bouissou et al., 1999; Dieterich and Kilgore, 1994). Stable sliding was only observed for the roughest surface (125 μm) at 30 MPa (test PMMA_120_30). Moreover, at 50 MPa, stable sliding was only observed for the two roughest surfaces (125 and 18.3 μm). Stick-slip is commonly preceded by pre-seismic slip (where slip accelerates) at 30 and 50 MPa for the smoothest surfaces. Interestingly, during test PMMA_1200_30, large stick-slips evolve into quasi-stable sliding at 0.9 mm displacement, but then stick-slip restarts at 1.8 mm load point displacement. All these observations suggest that fault surface roughness affects the accumulation of elastic strain energy. In test PMMA_1200_30, results suggest that elastic strain energy increased during quasi-stable sliding until sufficient elastic strain energy was accumulated to restart stick-slip. Accumulation may have occurred due to increased contact hold time, which may have enhanced asperity adhesion.

5.4.1.3 Normal stress

In general, the stress drop and recurrence interval of large stick-slips increases as normal stress increases. Stress drop and recurrence interval are anti-correlated (i.e. the lower the recurrence interval, the higher the average stress drop), as observed in similar studies (Zhou et al., 2021). At 30 MPa normal stress, faults are observed to slide unstably with significant pre-seismic slip and quasi-stable sliding. Increasing normal stress to 40 MPa enhances the generation of large stick-slip, reducing the amount of quasi-stable sliding. However, increasing normal stress to 50 MPa suppresses stick-slip instability for the roughest surfaces (125 and 18.3 μm). These results suggest that normal stress plays a key role in controlling frictional behaviour. At a critical high normal stress (50 MPa), stick-slip instability in PMMA can be suppressed, in agreement with frictional tests with Westerly granite (Harbord et al., 2017).

It should be noted that the interplay between surface roughness and normal stress will affect the real area of contact of asperities, adding complexity. Test PMMA_800_50 had lower-than-expected stress drops and recurrence intervals which coincides with relatively high levels of pre-seismic slip. If the experiment were able to be lengthened, perhaps frictional behaviour would evolve from stick-slip with pre-seismic slip, to quasi-stable slip and ultimately, stable slip,

5.4.2 Pre-seismic slip and stability

Similarly to Chapter 4, pre-seismic slip preceding large stick-slips generally increases with increasing load point displacement. Pre-seismic slip partially releases accumulated strain energy, reducing the stress drops of large stick-slips (Cattania and Segall, 2019). Moreover, tests conducted at 30 MPa had the most pre-seismic slip. This is in agreement with Byerlee and Summers (1975) who found that pre-seismic slip decreased with increased confining pressure in triaxial compression tests with intact granite. They also suggested that in nature, aseismic creep should dominate in low stress environments (i.e. the shallow crust) in releasing tectonic stress while at higher normal stresses (deeper crust; seismogenic zone), stress is more likely to be relieved by sudden earthquake slip.

As discussed in the previous chapter (Chapter 4, Section 4.4.2), time-dependent healing, based on rate-and-state friction, states that increased healing results in an increase in the real area of contact of asperities. As pre-seismic slip and fault stability generally increase with displacement, rate-and-state friction parameters must evolve with slip. As the system stabilises, system stiffness k decreases towards critical stiffness k_c (Chapter 4, Equation 4.15). This means that the difference between the direct and evolution effect $(a - b)$ must decrease with slip, critical slip distance D_c must increase with slip, or a combination of both must occur. Marone and Cox (1994) found that for rough surfaces, $(a - b)$ started as positive and became negative with cumulative slip and D_c increased. For smooth surfaces $(a - b)$ remained negative, decreasing slightly while D_c remained the same. Additionally, Marone and Kilgore (1993) suggested that D_c increases with increasing gouge layer thickness. While there is evidence of increased gouge following frictional sliding experiments from infilled grooves observed in EBSD images (Figure 5.15), further study of PMMA rate-and-state parameters is required for quantification of $(a - b)$ and D_c. Nevertheless, the results of this study suggest that evolution of rate-and-state parameters with cumulative slip throughout the experiments brings frictional systems towards stability, causing stick-slip instability to transition towards stick-slips with increased pre-seismic slip, quasi-stable slip and eventually, stable sliding.

5.4.3 Evolution of stick-slip seismic source properties – are they actually evolving?

A question that remains is whether the observed variation in the source properties (seismic moment, corner frequency and source radius) of large stick-slips is due to actual source property variation or Brune model fitting, which may not be suitable for stick-slip events due to fundamental differences in source geometry. Comparing local magnitude (based on the amplitude of measured P-waves) to moment magnitude (based on Brune model spectral fitting), there is a moderate correlation between the two parameters. This suggests that moment magnitude

derived from using the Brune model does give a general indication of the earthquake size, although it is less reliable than the local magnitude. Scatter in this relation could either be due to the Brune model being unsuitable for these events or due to actual variation in other source properties, such as rupture velocity, source radius or stress drop.

In Chapter 4, source radius and rupture velocity were discussed as potentially scaling with average fault displacement (and therefore seismic moment). However, this does not appear to be the case in this study. Comparing events of similar moment magnitude (but vastly different local magnitude), PMMA_1200_30_006 and PMMA_120_30_003, displacement spectra visually appear to show a depletion of high-frequency content for the former event (Figure 5.11). This suggests that at least some of the observed variation in source radius or rupture velocity is due to actual variation in source properties rather than limitations in using the Brune model. If this is the case, then the observed variability in source radius or rupture velocity across experiments suggests that source radius and rupture velocity do not scale with average fault displacement. While both changes in source radius and rupture velocity were monitored, it is more likely that changes in rupture velocity are the reason for changes in corner frequency than source radius. Corner frequency is inversely proportional to rise time, the duration of the source pulse. If the duration of the pulse decreases, this is most likely due to a faster rupture rather than source geometry, meaning that Hypothesis C (Chapter 4, Section 4.4.3) is the most likely. However, knowing that the real contact area of asperities of smoother fault systems is larger than that of rougher systems, an increase in asperity length is also possible meaning that a combination of changes to both source radius and rupture velocity is conceivable.

While normal stress appears to have very little effect on average rupture velocity, in general, stick-slip events on smoother surfaces have lower rupture velocity. Large stick-slip events with lower rupture velocity also tend to have high amounts of pre-seismic slip relative to fault displacement during slip and more precursory events. Combining these observations with stability considerations in the previous section, results suggest that as frictional behaviour transitions from unstable stick-slip towards more stable regimes (quasi-stable sliding and slow precursory events), the corner frequency of events decreases (rupture velocity decreases; Kaproth and Marone, 2013; Leeman et al., 2016; McLaskey and Yamashita, 2017). Moreover, smoother surfaces promote more quasi-stable behaviour, leading to stick-slips with lower corner frequencies (lower rupture velocity). It may be assumed that smoothness increases with cumulative slip, due to the observation of infilled grooves in EBSD images, though further study of post-experimental surfaces should be carried out to characterise roughness quantitatively. These results support the findings of Renard et al. (2020) who found through imaging of fault slip

using 4D synchrotron Z-ray microtomography that smoother surfaces deformed mainly by slow slip with striations along the slip plane and less off-fault damage than rougher faults.

Future work should investigate the source properties of precursory events, including acoustic emissions (AEs) which precede and follow large stick-slips. Due to the smaller magnitude of AEs, they should be fully contained within the size of the sample, which should allow more accurate Brune model fitting and derivation of source properties to be more reliable.

5.4.4 Implications for natural faults

The results presented in this chapter demonstrate the influence of surface roughness and normal stress on frictional stability, which has much importance for earthquake nucleation and source property characterisation. While dynamic rupture and coseismic weakening of friction enable ruptures to propagate on frictionally stable fault segments (Noda and Lapusta, 2013), earthquake nucleation is limited to segments that promote frictional instability. In these segments, friction and loading conditions enable frictional stability. The results of this study indicate that surface roughness plays a crucial role in the development of frictional stability. Moreover, the interplay between surface roughness and normal stress generates complex frictional behaviour with slip, ranging from unstable stick-slip, quasi-stable sliding and stable sliding in a single experiment.

Other frictional sliding experiments have shown that roughness and normal stress affect frictional stability in materials ranging from granite to marble (Aubry et al., 2020; Dresen et al., 2020; Harbord et al., 2017; Morad et al., 2022; Zhou et al., 2021). Several seismological studies have also suggested that fault geometry affects earthquake behaviour (e.g. Allmann and Shearer, 2007; Choy and Kirby, 2004; Ma et al., 2001; Wang and Bilek, 2011), but the effects are widely debated (Abercrombie, 2021). Therefore, this study has relevance for natural faulting and earthquake source property estimation.

Table 5.2 summarises the key relationships between measured variables and source parameters in this chapter, including where they agree and differ with other studies.

Table 5.2: *Summary of key relationships between measured properties with comparison to other studies (+ = agrees with study, - = disagrees with study).*

Property	Observations	Comparison to other studies
Roughness	As roughness decreases, unstable stick-slip more readily generated	+ Bouissou et al. (1999), Morad et al. (2022), Zhou et al. (2021)
	As roughness decreases, rupture velocity decreases	
	As roughness decreases, pre-seismic slip and precursory events increase	
	As roughness decreases, corner frequency decreases	+ Kaproth and Marone (2013), Leeman et al. (2016), McLaskey and Yamashita, (2017)
	Roughness decreases with cumulative slip	+ Renard et al. (2020)
Normal stress	Stress drop of large stick-slips increases as normal stress increases	+ Zhou et al. (2021)
	Recurrence of large stick-slips decreases as normal stress increases	+ Zhou et al. (2021)
	Increasing normal stress to 50 MPa suppresses stick-slip for rough surfaces	+ Harbord et al. (2017)
	Tests at 30 MPa have the most pre-seismic slip	+ Byerlee and Summers (1975)
Pre-seismic slip	Increases with cumulative displacement	+ Shreedharan et al. (2020)

5.5 Conclusion

To conclude, stick-slip instability is controlled by both surface roughness and normal stress. Sliding stabilises as normal stress increases, transitioning from unstable stick-slip to quasi-stable and stable sliding, in line with previous studies (Harbord et al., 2017; Morad et al., 2022; Okubo and Dieterich, 1984; Yamashita et al., 2018). Gradual stabilisation with increased cumulative slip is a consistent observation across experiments, and this coincides with a decrease in static stress drop, average fault displacement and seismic moment. Moreover, the number of slow, small precursory stick-slip events increases with slip and decreases with increased roughness and normal stress. While limited inferences can be made about estimates of the source properties (seismic moment, corner frequency, source radius and rupture velocity), comparing moment magnitude to local magnitude and events of similar magnitude suggests that there is variation in source properties. While it was suggested in Chapter 4 that source radius may scale with fault displacement, there is little evidence of this. Instead, lower rupture velocity is related to stick-slip events with high levels of pre-seismic slip and precursory events.

The results presented in this chapter emphasise the key roles of roughness, normal stress and fault evolution in the nucleation of stick-slip instabilities. Findings have implications for natural

fault stability and earthquake source properties, as changes in frictional behaviour are associated with changes in source properties of radiated wavefields.

5.6 APPENDIX

5.6.1 Examples of shear-calibrated force measurements $\boldsymbol{F_{strain}}$ (grey line) used to calculate stress drops of large stick-slips in tests a) PMMA_400_50, b) PMMA_800_30 and c) PMMA_1200_30.

Force gauge data F outlined by coloured lines.

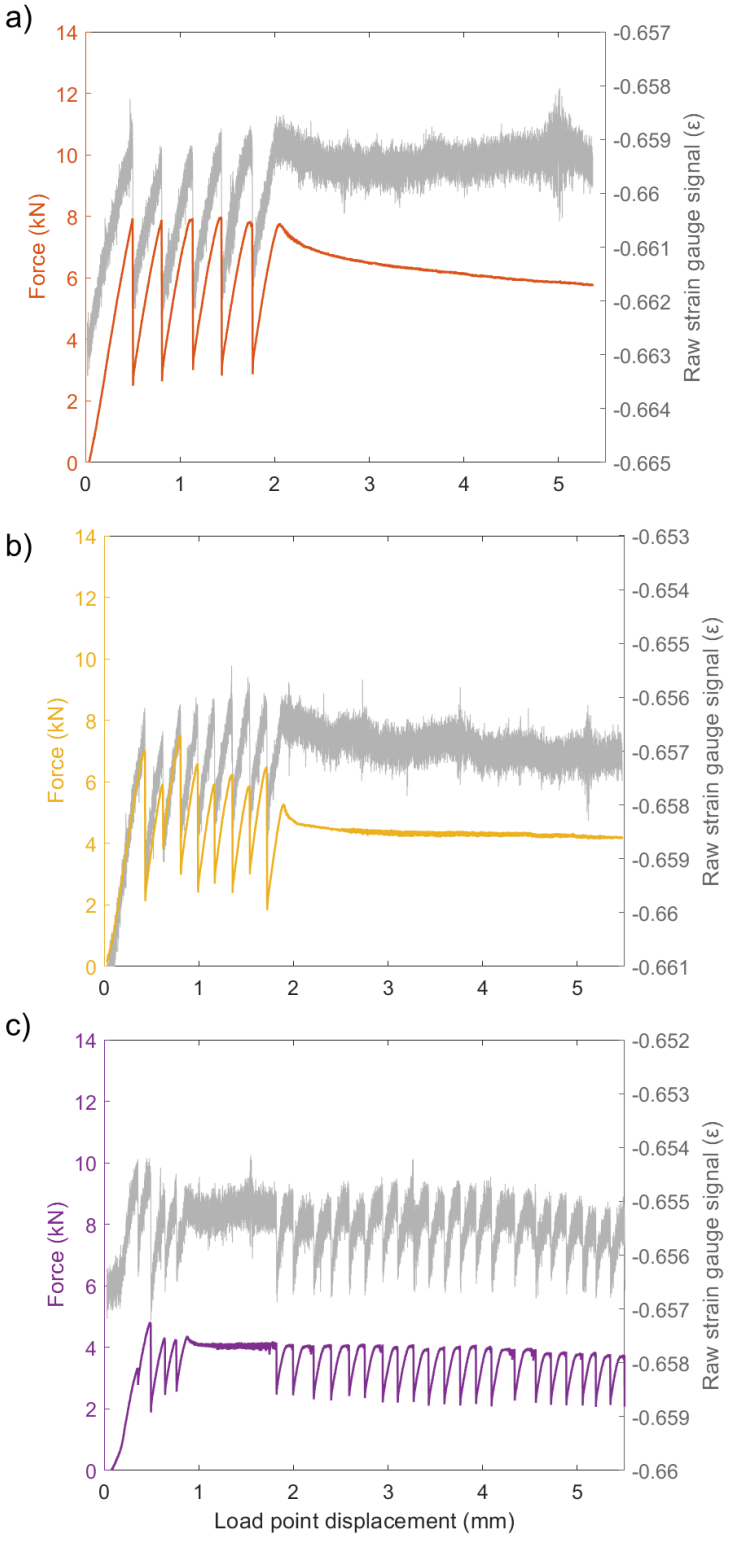

5.6.2 Values used for stick-slip picking for each experiment using code *find_stickslip_v4.m*.

Experiment Name	slength	smin (mm)	tmin (s)	llimit (mm)	ulimit (mm)	stol
PMMA_120_30	5	0.75	0.01	0	5.5	0.97
PMMA_120_40	5	0.75	0.01	0	5.5	0.97
PMMA_120_50	5	0.75	0.01	0	5.5	0.97
PMMA_400_30	5	0.75	0.01	0	5.5	0.97
PMMA_400_40	5	0.75	0.01	0	5.5	0.97
PMMA_400_50	5	0.75	0.01	0	5.5	0.97
PMMA_800_30	5	0.75	0.01	0	5.5	0.97
PMMA_800_40	5	0.75	0.01	0	5.5	0.97
PMMA_800_50	5	0.75	0.01	0	5.5	0.97
PMMA_1200_30	5	0.75	0.01	0	5.5	0.97
PMMA_1200_40	2	0.75	0.01	0	5.5	0.97
PMMA_1200_50	5	0.75	0.01	0	5.5	0.97

5.6.3 Table of mean and range of large stick-slips' stress drops, durations and recurrence intervals for each experiment.

Experiment Name	Mean stress drop (MPa)	Range stress drop (MPa)	Mean duration (s)	Range duration (s)	Mean recurrence interval (s)	Range recurrence interval (s)
PMMA_120_30	3.75	3.41	0.611	0.4	166	435
PMMA_120_40	8.15	2.97	0.436	0.3	284	50.7
PMMA_120_50	12.1	3.33	1.60	1.1	N/A	N/A
PMMA_400_30	6.29	3.57	0.384	0.3	235	85.5
PMMA_400_40	7.88	5.89	0.224	0.2	243	107
PMMA_400_50	8.62	0.508	0.340	0.2	316	22.3
PMMA_800_30	4.63	1.91	0.325	0.2	184	12.4
PMMA_800_40	6.54	6.44	0.279	0.4	187	180
PMMA_800_50	4.00	5.42	0.277	0.3	134	49.8
PMMA_1200_30	3.42	3.95	0.312	0.2	172	124
PMMA_1200_40	5.56	1.43	0.230	0.2	174	31.7
PMMA_1200_50	7.11	2.37	0.283	0.3	199	59.5

6 THESIS SUMMARY AND SUGGESTION FOR FUTURE WORK

The overarching aim of this thesis was to understand how changes to frictional properties affect earthquake source properties. To do this, I evaluated the source properties of laboratory-generated stick-slip, which facilitates an assessment of validity of seismic source models for our laboratory system. The nature of the wider problem of earthquake source property estimation was presented in Chapter 1. Chapter 2 summarised the equipment and methods applied in this thesis. Chapters 3, 4 and 5 were presented as individual pieces of work. Chapter 3 describes how the piezoelectric sensors within the seismic sample assembly, used in laboratory frictional sliding experiments, are calibrated to remove path and instrument effects (instrument-apparatus response) from radiated wavefields. Chapter 4 discusses how the internal instrument-apparatus responses derived in Chapter 3 can be removed from seismic waves radiated during spontaneous laboratory stick-slip to obtain source properties such as stress drop and seismic moment. Chapter 5 extends the use of this method further, investigating how roughness and normal stress affects the source properties of stick-slip. In this final chapter, the key findings of this thesis are summarised and related to each other. The implications of these findings are then brought into the context of the nature of the problem, as presented in Chapter 1. Specifically, faults exhibit structural complexity that is not yet encapsulated in source models and problems remain in estimating the source properties of small-to-medium earthquakes. The wider implications of this work for source characterisation, crustal earthquakes and seismic hazard analysis are then discussed, with suggestions made to show how this work can be developed in future studies.

6.1 SUMMARY OF RESULTS

In Chapter 1, it was stated that it is unclear how earthquake source properties vary with physical parameters such as earthquake depth (normal stress) and fault heterogeneity (e.g. fault material, roughness and damage). In nature, a range of slip behaviour, from aseismic creep to earthquake slip, is observed but is sometimes difficult to relate to particular fault properties and source properties. The advantages of laboratory studies of fault friction were discussed, with the ability to simulate natural fault behaviour using carefully controlled conditions. However, seismic acquisition systems used in laboratory experiments are routinely uncalibrated, initially only providing limited information on measured seismic waves (i.e. relative instead of absolute time histories). Fault heterogeneity resulting from roughness was highlighted to play a role in earthquake nucleation. Moreover, normal stress is key to earthquake nucleation as it reduces both the effective stiffness and critical nucleation length on the fault (Passelègue et al., 2013). Laboratory analogues for earthquakes, stick-slip, were proposed as suitable for assessing source characterisation for a range of frictional sliding experiments in varying conditions.

Chapter 3 addressed the issue of uncalibrated piezoelectric sensors within the seismic sample assembly, which are used in laboratory frictional sliding experiments, by applying the absolute acoustic calibration method (McLaskey et al., 2015). This enabled the combined path and instrument response (internal instrument-apparatus response) of piezoelectric acoustic sensors held within the top and bottom platens of the seismic sample assembly to be derived. Ball bearings of different diameters and materials (steel and ceramic) are dropped onto the platens' surfaces to obtain instrument-apparatus responses with a broad frequency range. The internal instrument-apparatus response describes how the path and instrument responses of the seismic assembly modify the wavefield of internal sources across a frequency range of 150 Hz – 300 kHz (Abercrombie, 2021; Lanzano et al., 2017; Sahakian et al., 2019). The method of combining individual instrument-apparatus responses was modified from an enveloping method used by McLaskey et al. (Baltay et al., 2010) to averaging using the median. This is due to the median returning bootstrapped estimates and ball drop spectra with improved accuracy. Results are compared to the calibration of a steel plate of similar thickness to observe how geometrical differences affect the instrument-apparatus responses. The low-frequency amplitudes of the internal instrument-apparatus responses of all three (top and bottom platen, and steel plate) vary significantly. The complex geometry of the seismic assembly and differences in the surface areas of the piezoelectric crystals in the top and bottom platens of the seismic assembly were considered reasonable explanations for this variance (McLaskey and Glaser, 2012). Additionally, the effect of applying the Pulser Amplifier System (PAS) was investigated, with observations highlighting that amplifiers act as high-pass filters, making high frequencies clearer. The minimum event magnitude for the seismic acquisition system was calculated to be $M_w = -7.75$, smaller than the minimum event size measured by McLaskey et al. (2015). Following the completion of absolute acoustic calibration, the internal instrument-apparatus responses can be removed from seismic signals measured using the seismic assembly during stick-slip in frictional sliding experiments. This can lead to more reliable estimation of key seismological properties such as corner frequency and average rupture velocity.

Chapter 4 removes the internal instrument-apparatus responses derived in Chapter 3 to seismic waves radiated during spontaneous laboratory stick-slip. A single direct shear experiment on poly(methyl methacrylate) (PMMA) is carried out to understand how fault property evolution with slip results in systematic changes to seismic source properties, with no changes to strain rate or confining pressure. PMMA is a useful analogue material for frictional sliding experiments as it is around 20 times more compliant than crustal rocks, generating events with a smaller nucleation length (~ mm vs cm; Bouissou et al., 1999). Moreover, the experiment tested the validity of spectral modelling of the source spectra of large stick-slips using the Brune (1970)

model. This was achieved by comparing seismic estimates with mechanical measurements of source properties, namely seismic moment and static stress drop. Both mechanical data (stress vs load point displacement) and seismic source property estimates indicated an evolution in fault behaviour with slip. The stress drop and seismic moment of large stick-slips decreased with cumulative fault slip, with later events exhibiting more small, slow precursor events with smaller stress drops and quasi-stable slip. However, there were discrepancies between seismic and mechanical estimates of stress drop and seismic moment. This was attributed to the unsuitability of the Brune model for source property estimation for large stick-slips (Wu and McLaskey, 2019). Estimates of the seismic moment using the top and bottom internal instrument-apparatus responses have a good fit, suggesting that absolute acoustic calibration is a robust method for acoustic sensor calibration. Pre-seismic slip, defined as the total slip between the minimum interseismic shear stress and peak shear stress), also increases with slip. Increased stability with slip potentially reflects an evolution in rate-and-state parameters with cumulative slip, which may take the system towards the stability boundary (Marone, 1998a; Rice and Ruina, 1983; Ruina, 1983; Voisin et al., 2007). Precursors to large stick-slips were shown to accelerate towards the initiation of stick-slip with a $1/t$ relationship, suggesting a positive feedback between creep and foreshocks (Cattania and Segall, 2021). Although the Brune model may not be suitable for modelling large stick-slips, the decrease in seismic moment and stress drop was consistently observed in both mechanical and seismic data. This coincided with systematic decreases in corner frequency, interpreted as decrease in average rupture velocity, an increase in source radius, or perhaps a combination of both. Three hypotheses were proposed for the observed trends and discrepancies in source properties: A) limited variation in corner frequency, with the decrease in f_0 an 'apparent' decrease due to model bias, which reduces f_0 with M_0; B) observed variation in corner frequency is due to changes in source radius (source radius is not necessarily equivalent to fault rupture area A; Equation 4.7), which may scale with fault displacement; C) observed variation in corner frequency is due to changes in average rupture velocity, which may scale with fault displacement. A combination of both Hypothesis B and C is also a possibility. Experiments that produce a wider magnitude and range of laboratory seismic events were proposed to test the three hypotheses.

Chapter 5 investigated the effects of roughness and normal stress on frictional stability and source properties of laboratory stick-slips. Throughout 12 frictional sliding experiments using roughened PMMA, a broad range of frictional stability, from unstable stick-slip to intermediate quasi-stable sliding and stable sliding, was observed. Similarly to Chapter 4, frictional behaviour typically stabilised with slip, coinciding with decreases in stress drop, average fault displacement and seismic moment (Harbord et al., 2017; Morad et al., 2022; Okubo and Dieterich, 1984;

Yamashita et al., 2018). The number of precursory events increased with cumulative slip and decreases with increased roughness and normal stress. To account for issues with using the Brune model to estimate source properties from source spectra, the local magnitude M_L was compared to moment magnitude M_W (Aki, 1967; Hanks and Kanamori, 1979; Richter, 1935). While M_L and M_W scaled, there was significant scatter around the linear fit which indicates that observed variations in source properties were significant. This is because significant differences in M_L and M_W scaling are related to differences in physical source properties such as low or high stress drop or corner frequency (Ristau, 2009). Consequently, Hypotheses B and C above were tested by comparing source radius and average rupture velocity with slip, respectively. It was determined that Hypothesis C, which assumes that observed changes in corner frequency are due to rupture velocity, is the most likely explanation for observations. A wide range of average rupture velocities, from 600 – 1180 m/s, are observed, with lower rupture velocity associated with stick-slip events with high levels of pre-seismic slip and precursory events. Consequently, stick-slip events on smoother faults are more likely to have lower rupture velocities and slow slip (Renard et al., 2020). SEM-based electron backscatter diffraction (EBSD) imaging demonstrated how surface roughness changes following slip. Features such as grooves infilled with wear gouge, striations in approximately the direction of shear and damage indicate roughness evolution with slip, with clear destruction of initial surface roughness features. This implies that cumulative slip smooths the surface, which supports the hypothesis that increased smoothing and potentially wear modify rate-and-state parameters and take the system towards the stability boundary (Marone, 1998a; Rice and Ruina, 1983; Ruina, 1983; Voisin et al., 2007).

Bringing together Chapters 4 and 5, it is clear that the initial conditions of a fault (normal stress and roughness) significantly impact subsequent frictional sliding behaviour and source properties. Moreover, variation in frictional sliding behaviour with slip is reflected by variation in source properties. The general decrease in corner frequency and rupture velocity with load point displacement (at 30 MPa and 50 MPa), i.e. Hypothesis C, is strengthened by the observations of systematic depletion of high-frequency radiation and radiated energy with slip in Chapter 4.

6.2 IMPLICATIONS FOR CRUSTAL EARTHQUAKES

Typically, crustal faults can be considered as comprising three different sections: the country rock, the damage zone and the fault core (Figure 6.1; Chester and Logan, 1986; Faulkner, Lewis and Rutter, 2003; Mitchell and Faulkner, 2008; Faulkner et al., 2010).). Strain is predominately localised to powder rock in fault cores (usually much smaller than 1 m wide) which are surrounded by a fracture network, known as the damage zone (around 10's – 100's m wide).

These structures are commonly hosted within a protolith of comparatively intact rock, known as the country rock.

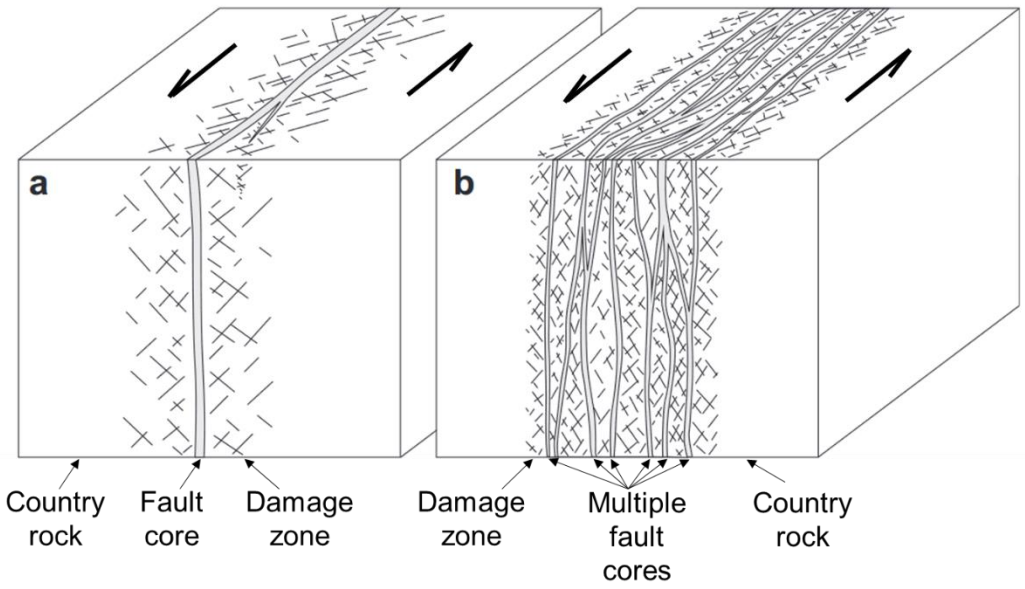

Figure 6.1: *Typical fault zone structures in quartzo-feldspathic rocks for a) a single fault core surrounded by a fractured damage zone and b) multiple fault cores which enclose lenses of a fractured protolith. After Chester and Logan (1986); Faulkner et al. (2003); Mitchell and Faulkner (2008); Faulkner et al. (2010).*

The topography (or roughness) of fault slip surfaces has been investigated across a range of different length scales (Candela et al., 2012). Spectral analysis of fault slip surfaces using microscopy for laboratory-scale samples and LiDAR and photogrammetric techniques for field-scale samples has shown that surfaces are self-affine (Mandelbrot, 1985) across a broad range of scales (Bistacchi et al., 2011; Brodsky et al., 2016; Candela et al., 2012; Harbord et al., 2017; Power et al., 1988). Surface roughness is thought to control the nature of frictional contact in crustal fault zones (Dieterich and Kilgore, 1994; Scholz, 1998; Yoshioka and Scholz, 1989). Therefore, fault roughness has been considered as potentially affecting frictional sliding behaviour, with numerical models demonstrating the effect of roughness on both static and dynamic frictional resistance (Fang and Dunham, 2013). Experimental studies of roughness have observed the effect it has on rate-and-state parameters (Harbord et al., 2017; Marone and Cox, 1994) and nucleation length (Ohnaka and Shen, 1999; Okubo and Dieterich, 1984). Nevertheless, very few experimental studies have considered the effect of fault heterogeneity, including roughness, on earthquake source properties.

The results of this study contribute to the ongoing work on understanding the impact of fault roughness on seismicity. The observation of increased stress drop with increased normal stress directly agrees with previous experimental work (Harbord et al., 2017; Okubo and Dieterich, 1984). The general stabilisation of slip at high (50 MPa) normal stress is supported by the findings

of Brace and Kohlstedt (1980), who related this to increased asperity interlocking. Moreover, the finding that rougher surfaces exhibit more instability than smoother surfaces is supported by experimental and modelling studies (Morad et al., 2022; Yamashita et al., 2018; Zhou et al., 2021). Previous studies on geometric complexity and roughness have shown that slip on immature, rougher faults generates a higher degree of source mechanism heterogeneity than mature, smoother faults (Bailey et al., 2010; Goebel et al., 2014; Powers and Jordan, 2010). In this study, the roughest faults generally produce stick-slips with the widest range of stress drop and seismic moment (Appendix 5.6.3). If fault roughness decreases with cumulative slip and age (Choy and Kirby, 2004; Mitchell and Faulkner, 2008; Sagy et al., 2007), the results of this study suggest that more mature, smoother faults are associated with smoother stress fields, lower stress drops and are overall more stable, in agreement with displacement-length earthquake data (Manighetti et al., 2007) and aftershock distribution modelling (Perrin et al., 2021). Perrin et al. (2021) found that earthquake stress drop decreases with cumulative fault displacement due to the narrowing of the shear deformation zone with cumulative slip and fault smoothing.

Modelling studies have found that quasi-static slip is expected during earthquake nucleation (Dieterich, 1992; Kaneko and Lapusta, 2008; Noda et al., 2013; Rubin and Ampuero, 2005; Tal et al., 2018). However, slip behaviour on natural faults is often inconsistent with nucleation models. For example, Kato et al. (2012) found that small earthquakes preceding the M_W 7.3 foreshock before the 2011 Tohoku earthquake migrated towards the rupture initiation point of the M_W 9.0 mainshock. They proposed that this migration of seismicity was driven by precursory slow slip on the fault, but they also found that slip did not exhibit the power-law acceleration predicted (Bouchon et al., 2013; Jones and Molnar, 1979). While Kato et al. (2016) observed accelerating seismic and aseismic slip preceding the M_W 8.2 2014 Iquique, Chile earthquake, slip evolution was more episodic and irregular when compared to observed laboratory processes (Harbord et al., 2017; Ohnaka and Kuwahara, 1990; Okubo and Dieterich, 1984). In this study, irregular pre-seismic slip was observed, with period-doubling and chaotic recurrence, which has been outlined in laboratory experiments (Gu and Wong, 1994), numerical modelling (Gu et al., 1984) and in nature (Veedu and Barbot, 2016). This study has implications for observations of periodic, chaotic and double earthquake recurrence intervals as it indicates that frictional fault properties control this behaviour (Shelly, 2010).

6.3 IMPLICATIONS FOR SEISMIC HAZARD

The dependence of ground motion prediction models on regional structural heterogeneity continues to be an area of active research. Regional variations in stress fields due to fault structure and maturity can lead to differences in stress drop estimates (Allmann and Shearer,

2007; Goertz-Allmann and Edwards, 2014). Radiguet et al. (2009) found that earthquakes on rougher, immature faults can produce ground motions 1.5 times larger than those produced on more mature, smoother faults, which strengthens the findings of this thesis. Structural maturity is likely to have a significant role in strong ground motion variability. As structural maturity can be estimated *a priori* (before an event) and independently of knowledge of both past and future earthquakes, it is an independent parameter which can be included in ground motion models (Douglas and Edwards, 2016; Radiguet et al., 2009). Incorporating structural maturity into ground motion models reduce bias and variability inherent in ergodic approaches, where such features are unknowingly mixed.

The findings of this study could contribute to the development of a fault maturity parameter or adjustment factor to be used in GMPEs (Douglas and Edwards, 2016; Kotha et al., 2020; Radiguet et al., 2009). For example, Guo et al. (2023) analysed geological measurements (e.g. rupture segmentation and fault slip) for 34 strike-slip earthquakes ($M_W \geq 6$) and found measurements to correlate with rupture velocity and aftershock productivity. They also found that radiated energy decreased with fault maturity, which supports the results of this thesis. Guo et al. (2023) suggest that if empirical relationships between the observed maturity of faults and earthquake source properties can be established, then this can provide insight to the geological complexity of fault systems where surface measurements are inaccessible. In this case, empirical relations can be used to improve hazard assessment using earthquake source properties estimated from regional, large earthquakes. This offers the possibility of developing a fault maturity parameter to classify recorded ground motion and enable fault behaviour to be classified into fault maturity classes (e.g. immature, moderately mature and mature; Radiguet et al., 2009). The results of this thesis can be used to "ground-truth" empirical relations such as these in order to understand the underlying physical mechanisms behind variations in each maturity class.

6.4 SUGGESTIONS FOR FUTURE WORK

Several different directions of work could be pursued following this thesis. Building on from the results of Chapter 3, which found amplifiers to act as high-pass filters enhancing high-frequency signals, further work should aim to detect greater numbers of acoustic emissions (AEs) that precede and follow large stick-slip events. Work must be done to reduce the level of low-frequency noise produced by the servo-control system, which makes detecting these small events difficult. If significant (> 100) numbers of AEs can be detected, the magnitude-frequency distribution (Gutenberg and Richter, 1944) can be determined. As absolute acoustic calibration has already been carried out on the seismic acquisition system, the absolute (rather than relative) seismic moment of events can be determined. It would be interesting to see if spectral fitting

found any variations in AE source properties with slip, roughness and normal stress, as observed in the results of this thesis. For example, Goebel et al., (2017) found that rougher faults had higher b-values, more heterogenous focal mechanisms and more spatially distributed seismicity than smoother faults. Foreshock and aftershock AE events could be quantified to determine whether physical processes hypothesised in natural earthquakes are observed, such as pre-slip and cascade processes for foreshocks and decreasing event rate following Omori's law for aftershocks (Acosta et al., 2019; Lei, 2003).

Alternative source models such as the Haskell (1964), Madariaga (1976) and Sato and Hirasawa (1973) models could be compared to investigate whether they are more appropriate for estimating the source properties of large stick-slips. Haskell's (1964) model assumes a rectangular fault, which reflects the geometry of simulated faults used to generate large stick-slip events. While the model has limited use at high frequencies due to problematic features such as potential infinite energy release and the inter-penetration of matter (Madariaga, 2009), it would still be useful to compare source properties estimates using this model with the Brune model. Considering that observed changes in corner frequency are mostly likely due to changes in rupture velocity, Madariaga's (1976) model (which assumes a circular rupture that expands at a constant rupture velocity) could be more appropriate to model source parameter variation. The Madariaga model derives stress drop estimates that are around 5.5 times smaller than Brune model estimates, assuming the same shear wave velocity (Dong and Papageorgiou, 2002; Kaneko and Shearer, 2014). This further motivates future investigation of this problem and comparison to mechanical estimates of stress drop.

Moreover, further aspects of fault heterogeneity such as using different fault materials (such as clay and quartz gouges or slabs of different crustal rocks) should be explored. Bedford et al., (2022) found that $(a - b)$ (Dieterich, 1992) values were consistently lower in heterogeneous than homogenous simulated faults, showing reduced stability. Monitoring of stick-slip and AE waveforms during frictional sliding experiments of mixed fault material gouges would demonstrate how heterogeneity affects seismicity. This could quantify smaller-scale effects on source properties which are not currently included in present earthquake source and rupture models, improving understanding of how the evolution of fault rock heterogeneity in complex fault zones affects key properties such as stress drop and rupture velocity.

Considering that fault maturity has been shown to impact source properties in both laboratory experiments (this study) and in nature, further spectral modelling of recorded earthquake waveforms from mature and immature faults should be carried out. It would be interesting to compare stress drop estimates in faults considered as mature and immature to determine whether observations of lower stress drops on more mature faults are reflected in spectral

modelling of earthquakes. Incorporating a fault maturity index into ground motion models could be a way of reducing uncertainty in peak ground motion, with laboratory results reported in this study contributing towards the development of this index, alongside modelling and field studies (Douglas and Edwards, 2016; Kotha et al., 2020; Manighetti et al., 2007; Radiguet et al., 2009).

7 REFERENCES

Abercrombie, R., Mori, J., 1994. Local observations of the onset of a large earthquake: 28 June 1992 Landers, California. Bulletin of the Seismological Society of America 84, 725–734.

Abercrombie, R.E., 2021. Resolution and uncertainties in estimates of earthquake stress drop and energy release. Philosophical Transactions of the Royal Society A: Mathematical, Physical and Engineering Sciences 379. https://doi.org/10.1098/rsta.2020.0131

Abercrombie, R.E., 2015. Investigating uncertainties in empirical Green's function analysis of earthquake source parameters. Journal of Geophysical Research: Solid Earth 120, 4263–4277. https://doi.org/10.1002/2015JB011984

Abercrombie, R.E., 1995a. Earthquake source scaling relationships from −1 to 5 ML using seismograms recorded at 2.5-km depth. Journal of Geophysical Research: Solid Earth 100, 24015–24036. https://doi.org/10.1029/95JB02397

Abercrombie, R.E., 1995b. Earthquake source scaling relationships from −1 to 5 ML using seismograms recorded at 2.5-km depth. Journal of Geophysical Research: Solid Earth 100, 24015–24036. https://doi.org/10.1029/95JB02397

Abercrombie, R.E., Bannister, S., Ristau, J., Doser, D., 2017. Variability of earthquake stress drop in a subduction setting, the Hikurangi Margin, New Zealand. Geophysical Journal International 208, 306–320. https://doi.org/10.1093/gji/ggw393

Abercrombie, R.E., Rice, J.R., 2005. Can observations of earthquake scaling constrain slip weakening? Geophysical Journal International 162, 406–424. https://doi.org/10.1111/j.1365-246X.2005.02579.x

Abercrombie, R.E., Trugman, D.T., Shearer, P.M., Chen, X., Zhang, J., Pennington, C.N., Hardebeck, J.L., Goebel, T.H.W., Ruhl, C.J., 2021. Does Earthquake Stress Drop Increase With Depth in the Crust? Journal of Geophysical Research: Solid Earth 126, e2021JB022314. https://doi.org/10.1029/2021JB022314

Acosta, M., Passelègue, F.X., Schubnel, A., Madariaga, R., Violay, M., 2019. Can Precursory Moment Release Scale With Earthquake Magnitude? A View From the Laboratory. Geophysical Research Letters 46, 12927–12937. https://doi.org/10.1029/2019GL084744

Aki, K., 1967. Scaling law of seismic spectrum. Journal of Geophysical Research (1896-1977) 72, 1217–1231. https://doi.org/10.1029/JZ072i004p01217

Aki, K., 1966. Generation and Propagation of G Waves from the Niigata Earthquake of June 16, 1964.: Part 2. Estimation of earthquake moment, released energy, and stress-strain drop from the G wave spectrum. 東京大學地震研究所彙報= Bulletin of the Earthquake Research Institute, University of Tokyo 44, 73–88.

Aki, K., Reasenberg, P., DeFazio, T., Tsai, Y.-B., 1969. Near-field and far-field seismic evidences for triggering of an earthquake by the Benham explosion. Bulletin of the Seismological Society of America 59, 2197–2207. https://doi.org/10.1785/BSSA0590062197

Aki, K., Richards, P.G., 1980. Quantitative seismology: Theory and Methods. Freeman, San Francisco, California.

Allen, M.J., 2017. Physicochemical evolution of an active plate boundary fault ; the Alpine Fault , New Zealand : insight from the Deep Fault Drilling Project 306.

Allen, M.J., Tatham, D., Faulkner, D.R., Mariani, E., Boulton, C., 2017. Permeability and seismic velocity and their anisotropy across the Alpine Fault, New Zealand: An insight from laboratory measurements on core from the Deep Fault Drilling Project phase 1 (DFDP-1). Journal of Geophysical Research: Solid Earth 122, 6160–6179. https://doi.org/10.1002/2017JB014355

Allmann, B.P., Shearer, P.M., 2009. Global variations of stress drop for moderate to large earthquakes. Journal of Geophysical Research: Solid Earth 114. https://doi.org/10.1029/2008JB005821

Allmann, B.P., Shearer, P.M., 2007. Spatial and temporal stress drop variations in small earthquakes near Parkfield, California. Journal of Geophysical Research 112.

Ampuero, J.-P., Rubin, A.M., 2008. Earthquake nucleation on rate and state faults – Aging and slip laws. Journal of Geophysical Research: Solid Earth 113. https://doi.org/10.1029/2007JB005082

Anderson, J.G., Hough, S., 1984. A model for the shape of the fourier amplitude spectrum of acceleraton at high frequencies. Bulletin of the Seismological Society of America 74, 1969–1993.

Andrews, D.J., 1986. Objective Determination of Source Parameters and Similarity of Earthquakes of Different Size, in: Earthquake Source Mechanics, Geophysical Monograph Series. pp. 259–267. https://doi.org/10.1029/GM037p0259

Andrews, D.J., 1976. Rupture velocity of plane strain shear cracks. Journal of Geophysical Research 81, 5679–5687.

Anthony, J.L., Marone, C., 2005. Influence of particle characteristics on granular friction. Journal of Geophysical Research: Solid Earth 110. https://doi.org/10.1029/2004JB003399

Ashman, I.R., Faulkner, D.R., 2023. The Effect of Clay Content on the Dilatancy and Frictional Properties of Fault Gouge. Journal of Geophysical Research: Solid Earth 128, e2022JB025878. https://doi.org/10.1029/2022JB025878

Atkinson, G.M., 1993. Earthquake source spectra in eastern North America. Bulletin of the Seismological Society of America 83, 1778–1798. https://doi.org/10.1785/BSSA0830061778

Atkinson, G.M., Boore, D.M., 1998. Evaluation of models for earthquake source spectra in eastern North America. Bulletin of the Seismological Society of America 88, 917–934. https://doi.org/10.1785/BSSA0880040917

Aubry, J., Passelègue, F.X., Escartín, J., Gasc, J., Deldicque, D., Schubnel, A., 2020. Fault Stability Across the Seismogenic Zone. Journal of Geophysical Research: Solid Earth 125, e2020JB019670. https://doi.org/10.1029/2020JB019670

AZoM, n.d. Properties: Stainless Steel - Grade 420 (UNS S42000) [WWW Document]. AZoM.com. URL https://www.azom.com/properties.aspx?ArticleID=972 (accessed 5.23.23).

Bailey, I.W., Ben-Zion, Y., Becker, T.W., Holschneider, M., 2010. Quantifying focal mechanism heterogeneity for fault zones in central and southern California. Geophysical Journal International 183, 433–450. https://doi.org/10.1111/j.1365-246X.2010.04745.x

Bakun, W.H., Aagaard, B., Dost, B., Ellsworth, W.L., Hardebeck, J.L., Harris, R.A., Ji, C., Johnston, M.J.S., Langbein, J., Lienkaemper, J.J., Michael, A.J., Murray, J.R., Nadeau, R.M., Reasenberg, P.A., Reichle, M.S., Roeloffs, E.A., Shakal, A., Simpson, R.W., Waldhauser, F., 2005. Implications for prediction and hazard assessment from the 2004 Parkfield earthquake. Nature 437, 969–974. https://doi.org/10.1038/nature04067

Baltay, A., Ide, S., Prieto, G., Beroza, G.C., 2011. Variability in earthquake stress drop and apparent stress. Geophysical Research Letters 38.

Baltay, A., Prieto, G., Beroza, G.C., 2010. Radiated seismic energy from coda measurements and no scaling in apparent stress with seismic moment. Journal of Geophysical Research: Solid Earth 115. https://doi.org/10.1029/2009JB006736

Baltay, A.S., Hanks, T.C., Abrahamson, N.A., 2017. Uncertainty, variability, and earthquake physics in ground-motion prediction equations. Bulletin of the Seismological Society of America 107, 1754–1772. https://doi.org/10.1785/0120160164

Barenblatt, G.I., 1962. The Mathematical Theory of Equilibrium Cracks in Brittle Fracture, in: Dryden, H.L., von Kármán, Th., Kuerti, G., van den Dungen, F.H., Howarth, L. (Eds.), Advances in Applied Mechanics. Elsevier, pp. 55–129. https://doi.org/10.1016/S0065-2156(08)70121-2

Bedford, J.D., 2017. The kinetics and mechanics of a dehydrating system and the deformation of porous rock.

Bedford, J.D., Faulkner, D.R., 2021. The Role of Grain Size and Effective Normal Stress on Localization and the Frictional Stability of Simulated Quartz Gouge. Geophysical Research Letters 48. https://doi.org/10.1029/2020GL092023

Bedford, J.D., Faulkner, D.R., Lapusta, N., 2022. Fault rock heterogeneity can produce fault weakness and reduce fault stability. Nature Communications 13, 326. https://doi.org/10.1038/s41467-022-27998-2

Beeler, N., Kilgore, B., McGarr, A., Fletcher, J., Evans, J., Baker, S.R., 2012. Observed source parameters for dynamic rupture with non-uniform initial stress and relatively high fracture energy. Journal of Structural Geology 38, 77–89. https://doi.org/10.1016/j.jsg.2011.11.013

Beeler, N.M., Tullis, T.E., Blanpied, M.L., Weeks, J.D., 1996. Frictional behavior of large displacement experimental faults. Journal of Geophysical Research: Solid Earth 101, 8697–8715. https://doi.org/10.1029/96JB00411

Beeler, N.M., Tullis, T.E., Weeks, J.D., 1994. The roles of time and displacement in the evolution effect in rock friction. Geophysical research letters 21, 1987–1990.

Ben-David, O., Cohen, G., Fineberg, J., 2010. The Dynamics of the Onset of Frictional Slip. Science 330, 211–214. https://doi.org/10.1126/science.1194777

Benioff, H., 1964. Earthquake Source Mechanisms. Science 143, 1399–1406. https://doi.org/10.1126/science.143.3613.1399

Ben-Zion, Y., Ampuero, J.P., 2009. Seismic radiation from regions sustaining material damage, in: Geophysical Journal International. pp. 1351–1356. https://doi.org/10.1111/j.1365-246X.2009.04285.x

Ben-Zion, Y., Eneva, M., Liu, Y., 2003. Large earthquake cycles and intermittent criticality on heterogeneous faults due to evolving stress and seismicity. Journal of Geophysical Research: Solid Earth 108. https://doi.org/10.1029/2002JB002121

Ben-Zion, Y., Sammis, C.G., 2003. Characterization of fault zones. Pure and Applied Geophysics 160, 677–715. https://doi.org/10.1007/PL00012554

Berg, E.J., 1936. Heaviside's Operational Calculus as Applied to Engineering and Physics. McGraw-Hill book Company, Incorporated.

Berlincourt, D., 1971. Piezoelectric Crystals and Ceramics, in: Mattiat, O.E. (Ed.), Ultrasonic Transducer Materials, Ultrasonic Technology. Springer US, Boston, MA, pp. 63–124. https://doi.org/10.1007/978-1-4757-0468-6_2

Beroza, G.C., Ellsworth, W.L., 1996. Properties of the seismic nucleation phase. Tectonophysics, Seismic Source Parameters: From Microearthquakes to Large Events 261, 209–227. https://doi.org/10.1016/0040-1951(96)00067-4

Bevington, P., Robinson, D.K., 2003. Data Reduction and Error Analysis for the Physical Sciences. McGraw-Hill Education.

Bhattacharya, P., Rubin, A.M., Bayart, E., Savage, H.M., Marone, C., 2015. Critical evaluation of state evolution laws in rate and state friction: Fitting large velocity steps in simulated fault gouge with time-, slip-, and stress-dependent constitutive laws. Journal of Geophysical Research: Solid Earth 120, 6365–6385.

Bilek, S.L., Lay, T., 1999. Rigidity variations with depth along interplate megathrust faults in subduction zones. Nature 400, 443–446. https://doi.org/10.1038/22739

Bistacchi, A., Ashley Griffith, W., Smith, S.A.F., di Toro, G., Jones, R., Nielsen, S., 2011. Fault Roughness at Seismogenic Depths from LIDAR and Photogrammetric Analysis. Pure and Applied Geophysics 168, 2345–2363. https://doi.org/10.1007/s00024-011-0301-7

Blake, O.O., 2011. Seismic transport properties of fractured rocks.

Blanke, A., Kwiatek, G., Goebel, T.H.W., Bohnhoff, M., Dresen, G., 2021. Stress drop–magnitude dependence of acoustic emissions during laboratory stick-slip. Geophysical Journal International 224, 1371–1380. https://doi.org/10.1093/gji/ggaa524

Boatwright, J., 1980. A spectral theory for circular seismic sources; simple estimates of source dimension, dynamic stress drop, and radiated seismic energy. Bulletin of the Seismological Society of America 70, 1–27. https://doi.org/10.1785/BSSA0700010001

Boatwright, J., Fletcher, J.B., Fumal, T.E., 1991. A general inversion scheme for source, site, and propagation characteristics using multiply recorded sets of moderate-sized earthquakes. Bulletin of the Seismological Society of America 81, 1754–1782. https://doi.org/10.1785/BSSA0810051754

Boitnott, G.N., Biegel, R.L., Scholz, C.H., Yoshioka, N., Wang, W., 1992. Micromechanics of rock friction 2: Quantitative modeling of initial friction with contact theory. Journal of Geophysical Research: Solid Earth 97, 8965–8978. https://doi.org/10.1029/92JB00019

Bolotskaya, E., Hager, B.H., 2022. A 1D Spring-Slider Model with a Simple Poly-Linear Failure Law Produces Rich Variations in Slip Behavior. Bulletin of the Seismological Society of America 112, 2795–2811. https://doi.org/10.1785/0120220052

Bolton, D.C., Shreedharan, S., McLaskey, G.C., Rivière, J., Shokouhi, P., Trugman, D.T., Marone, C., 2022. The High-Frequency Signature of Slow and Fast Laboratory Earthquakes. Journal of Geophysical Research: Solid Earth 127, e2022JB024170. https://doi.org/10.1029/2022JB024170

Bommer, J.J., Scherbaum, F., 2005. Capturing and Limiting Groundmotion Uncertainty in Seismic Hazard Assessment, in: Gülkan, P., Anderson, J.G. (Eds.), Directions in Strong Motion Instrumentation, Nato Science Series: IV: Earth and Environmental Sciences. Springer-Verlag, Berlin/Heidelberg, pp. 25–40. https://doi.org/10.1007/1-4020-3812-7_2

Boore, D.M., 2003. Simulation of ground motion using the stochastic method. Pure and Applied Geophysics 160, 635–676. https://doi.org/10.1007/PL00012553

Boore, D.M., Atkinson, G.M., 1992. Source spectra for the 1988 Saguenay, Quebec, earthquakes. Bulletin of the Seismological Society of America 82, 683–719. https://doi.org/10.1785/BSSA0820020683

Bouchon, M., Durand, V., Marsan, D., Karabulut, H., Schmittbuhl, J., 2013. The long precursory phase of most large interplate earthquakes. Nature Geosci 6, 299–302. https://doi.org/10.1038/ngeo1770

Bouissou, S., Petit, J.-P., Barquins, M., 1999. Stress drop and contact stiffness measured from stick-slip experiments on PMMA-PMMA friction. Tribology Letters 7, 61–65. https://doi.org/10.1023/A:1019152832763

Bowden, F.P., Bowden, F.P., Tabor, D., 2001. The friction and lubrication of solids. Oxford university press.

Bowden, F.P., Tabor, D., 1958. The Friction and Lubrication of Solids. Clarendon Press, Oxford.

Bowden, F.P., Tabor, D., Taylor, G.I., 1939. The area of contact between stationary and moving surfaces. Proceedings of the Royal Society of London. Series A. Mathematical and Physical Sciences 169, 391–413. https://doi.org/10.1098/rspa.1939.0005

Bowers, D., Hudson, J.A., 1999. Defining the scalar moment of a seismic source with a general moment tensor. Bulletin of the Seismological Society of America 89, 1390–1394. https://doi.org/10.1785/BSSA0890051390

Brace, W.F., Byerlee, J.D., 1966. Stick-Slip as a Mechanism for Earthquakes. Science 153, 990–992.

Brace, W.F., Kohlstedt, D.L., 1980. Limits on lithospheric stress imposed by laboratory experiments. Journal of Geophysical Research: Solid Earth 85, 6248–6252. https://doi.org/10.1029/JB085iB11p06248

Bracewell, R.N., 2000. The Fourier Transform and applications. McGraw Hill 1–10.

Brener, E.A., Bouchbinder, E., 2021. Unconventional singularities and energy balance in frictional rupture. Nature communications 12, 2585.

Brodsky, E.E., Kirkpatrick, J.D., Candela, T., 2016. Constraints from fault roughness on the scale-dependent strength of rocks. Geology 44, 19–22. https://doi.org/10.1130/G37206.1

Brown, S.R., Scholz, C.H., 1985. Broad bandwidth study of the topography of natural rock surfaces. Journal of Geophysical Research: Solid Earth 90, 12575–12582. https://doi.org/10.1029/JB090iB14p12575

Brune, J.N., 1979. Implications of earthquake triggering and rupture propagation for earthquake prediction based on premonitory phenomena. Journal of Geophysical Research: Solid Earth 84, 2195–2198.

Brune, J.N., 1970. Tectonic Stress and the Spectra of Seismic Shear Waves from Earthquakes. Journal of Geophysical Research 75, 4997–5009.

Brune, J.N., Allen, C.R., 1967. A low-stress-drop, low-magnitude earthquake with surface faulting: The Imperial, California, earthquake of March 4, 1966. Bulletin of the Seismological Society of America 57, 501–514. https://doi.org/10.1785/BSSA0570030501

Byerlee, J., 1978. Friction of Rocks, in: Byerlee, J.D., Wyss, M. (Eds.), Rock Friction and Earthquake Prediction, Contributions to Current Research in Geophysics (CCRG). Birkhäuser, Basel, pp. 615–626. https://doi.org/10.1007/978-3-0348-7182-2_4

Byerlee, J., Mjachkin, V., Summers, R., Voevoda, O., 1978. Structures developed in fault gouge during stable sliding and stick-slip. Tectonophysics 44, 161–171. https://doi.org/10.1016/0040-1951(78)90068-9

Byerlee, J., Summers, R., 1976. A note on the effect of fault gouge thickness on fault stability. International Journal of Rock Mechanics and Mining Sciences & Geomechanics Abstracts 13, 35–36. https://doi.org/10.1016/0148-9062(76)90226-6

Byerlee, J.D., 1970. The mechanics of stick-slip. Tectonophysics 9, 475–486. https://doi.org/10.1016/0040-1951(70)90059-4

Byerlee, J.D., Summers, R., 1975. Stable sliding preceding stick-slip on fault surfaces in granite at high pressure. Pure and Applied Geophysics PAGEOPH 113, 63–68. https://doi.org/10.1007/BF01592899

Campbell, L.R., Menegon, L., Fagereng, Å., Pennacchioni, G., 2020. Earthquake nucleation in the lower crust by local stress amplification. Nature Communications 11, 1322. https://doi.org/10.1038/s41467-020-15150-x

Candela, T., Renard, F., Bouchon, M., Brouste, A., Marsan, D., Schmittbuhl, J., Voisin, C., 2009. Characterization of fault roughness at various scales: Implications of three-dimensional high resolution topography measurements. Pure and Applied Geophysics 166, 1817–1851. https://doi.org/10.1007/s00024-009-0521-2

Candela, T., Renard, F., Bouchon, M., Schmittbuhl, J., Brodsky, E.E., 2011. Stress Drop during Earthquakes: Effect of Fault Roughness Scaling. Bulletin of the Seismological Society of America 101, 2369–2387. https://doi.org/10.1785/0120100298

Candela, T., Renard, F., Klinger, Y., Mair, K., Schmittbuhl, J., Brodsky, E.E., 2012. Roughness of fault surfaces over nine decades of length scales. Journal of Geophysical Research: Solid Earth 117, 1–30. https://doi.org/10.1029/2011JB009041

Cao, T., Aki, K., 1986. Effect of slip rate on stress drop. Pure and Applied Geophysics PAGEOPH 124, 515–529. https://doi.org/10.1007/BF00877214

Cattania, C., Segall, P., 2021. Precursory Slow Slip and Foreshocks on Rough Faults. Journal of Geophysical Research: Solid Earth 126, 1–20. https://doi.org/10.1029/2020JB020430

Cattania, C., Segall, P., 2019. Crack Models of Repeating Earthquakes Predict Observed Moment-Recurrence Scaling. Journal of Geophysical Research: Solid Earth 124, 476–503. https://doi.org/10.1029/2018JB016056

Chester, F.M., Logan, J.M., 1986. Implications for mechanical properties of brittle faults from observations of the Punchbowl fault zone, California. Pure and applied geophysics 124, 79–106.

Choy, G.L., Kirby, S.H., 2004. Apparent stress, fault maturity and seismic hazard for normal-fault earthquakes at subduction zones. Geophysical Journal International 159, 991–1012. https://doi.org/10.1111/j.1365-246X.2004.02449.x

Cimpanu, C., 2020. GitHub to replace “master” with alternative term to avoid slavery references. ZDNET.

Cocco, M., Bizzarri, A., 2002. On the slip-weakening behavior of rate- and state dependent constitutive laws. Geophysical Research Letters 29, 11-1-11–4. https://doi.org/10.1029/2001GL013999

Cocco, M., Tinti, E., Cirella, A., 2016. On the scale dependence of earthquake stress drop. J Seismol 20, 1151–1170. https://doi.org/10.1007/s10950-016-9594-4

Das, S., 2007. The Need to Study Speed. Science 317, 905–906.

Deichmann, N., 1997. Far-field pulse shapes from circular sources with variable rupture velocities. Bulletin of the Seismological Society of America 87, 1288–1296. https://doi.org/10.1785/BSSA0870051288

Di Toro, G., Han, R., Hirose, T., De Paola, N., Nielsen, S., Mizoguchi, K., Ferri, F., Cocco, M., Shimamoto, T., 2011. Fault lubrication during earthquakes. Nature 471, 494–498. https://doi.org/10.1038/nature09838

Dieterich, J.H., 1992. Earthquake nucleation on faults with rate-and state-dependent strength. Tectonophysics 221, 115–134.

Dieterich, J.H., 1986. A model for the nucleation of earthquake slip. Earthquake source mechanics 37, 37–47.

Dieterich, J.H., 1979a. Modeling of rock friction: 1. Experimental results and constitutive equations. Journal of Geophysical Research: Solid Earth 84, 2161–2168. https://doi.org/10.1029/JB084iB05p02161

Dieterich, J.H., 1979b. Modeling of rock friction: 2. Simulation of preseismic slip. Journal of Geophysical Research: Solid Earth 84, 2169–2175. https://doi.org/10.1029/JB084iB05p02169

Dieterich, J.H., 1978. Time-dependent friction and the mechanics of stick-slip. pure and applied geophysics 116, 790–806.

Dieterich, J.H., 1972. Time-dependent friction in rocks. Journal of Geophysical Research (1896-1977) 77, 3690–3697. https://doi.org/10.1029/JB077i020p03690

Dieterich, J.H., Kilgore, B., 1996. Implications of fault constitutive properties for earthquake prediction. Proceedings of the National Academy of Sciences 93, 3787–3794. https://doi.org/10.1073/pnas.93.9.3787

Dieterich, J.H., Kilgore, B.D., 1994. Direct Observation of Frictional Contacts: New Insights for State-dependent Properties. PAGEOPH 143, 283–302.

Dong, G., Papageorgiou, A.S., 2002. Seismic Radiation from a Unidirectional Asymmetrical Circular Crack Model, Part I: Constant Rupture Velocity. Bulletin of the Seismological Society of America 92, 945–961. https://doi.org/10.1785/0120000283

Douglas, J., Edwards, B., 2016. Recent and future developments in earthquake ground motion estimation. Earth-Science Reviews 160, 203–219. https://doi.org/10.1016/j.earscirev.2016.07.005

Dresen, G., Kwiatek, G., Goebel, T., Ben-Zion, Y., 2020. Seismic and Aseismic Preparatory Processes Before Large Stick–Slip Failure. Pure Appl. Geophys. 177, 5741–5760. https://doi.org/10.1007/s00024-020-02605-x

Dunn, Z., Yeary, M., Fulton, C., 2014. Frequency-dependent power amplifier modeling and correction for distortion in wideband radar transmissions. Midwest Symposium on Circuits and Systems 61–64. https://doi.org/10.1109/MWSCAS.2014.6908352

Duparré, A., Ferre-Borrull, J., Gliech, S., Notni, G., Steinert, J., Bennett, J.M., 2002. Surface characterization techniques for determining the root-mean-square roughness and power spectral densities of optical components. Appl. Opt. 41, 154–171. https://doi.org/10.1364/AO.41.000154

Ellsworth, W.L., Beroza, G.C., 1995. Seismic Evidence for an Earthquake Nucleation Phase. Science 268, 851–855. https://doi.org/10.1126/science.268.5212.851

Eshelby, J.D., 1957. The determination of the elastic field of an ellipsoidal inclusion, and related problems. Proc. R. Soc. Lond. A 241, 376–396. https://doi.org/10.1098/rspa.1957.0133

Fang, Z., Dunham, E.M., 2013. Additional shear resistance from fault roughness and stress levels on geometrically complex faults. Journal of Geophysical Research: Solid Earth 118, 3642–3654. https://doi.org/10.1002/jgrb.50262

Faulkner, D.R., Armitage, P.J., 2013. The effect of tectonic environment on permeability development around faults and in the brittle crust. Earth and Planetary Science Letters 375, 71–77. https://doi.org/10.1016/j.epsl.2013.05.006

Faulkner, D.R., Jackson, C.A.L., Lunn, R.J., Schlische, R.W., Shipton, Z.K., Wibberley, C.A.J., Withjack, M.O., 2010. A review of recent developments concerning the structure, mechanics and fluid flow properties of fault zones. Journal of Structural Geology 32, 1557–1575. https://doi.org/10.1016/j.jsg.2010.06.009

Faulkner, D.R., Lewis, A.C., Rutter, E.H., 2003. On the internal structure and mechanics of large strike-slip fault zones: Field observations of the Carboneras fault in southeastern Spain. Tectonophysics 367, 235–251. https://doi.org/10.1016/S0040-1951(03)00134-3

Fieseler, C., Mitchell, C.A., Pyrak-Nolte, L.J., Kutz, J.N., 2022. Characterization of Acoustic Emissions From Analogue Rocks Using Sparse Regression-DMDc. Journal of Geophysical Research: Solid Earth 127, e2022JB024144. https://doi.org/10.1029/2022JB024144

Freund, L.B., 1972. Crack propagation in an elastic solid subjected to general loading—II. Non-uniform rate of extension. Journal of the Mechanics and Physics of Solids 20, 141–152. https://doi.org/10.1016/0022-5096(72)90007-5

Gao, C., Kuhlmann-Wilsdorf, D., Makel, D.D., 1993. Fundamentals of stick-slip. Wear 162, 1139–1149.

Goebel, T.H.W., Candela, T., Sammis, C.G., Becker, T.W., Dresen, G., Schorlemmer, D., 2014. Seismic event distributions and off-fault damage during frictional sliding of saw-cut surfaces with pre-defined roughness. Geophysical Journal International 196, 612–625. https://doi.org/10.1093/gji/ggt401

Goebel, T.H.W., Kwiatek, G., Becker, T.W., Brodsky, E.E., Dresen, G., 2017. What allows seismic events to grow big?: Insights from b-value and fault roughness analysis in laboratory stick-slip experiments. Geology 45, 815–818. https://doi.org/10.1130/G39147.1

Goebel, T.H.W., Sammis, C.G., Becker, T.W., Dresen, G., Schorlemmer, D., 2015. A Comparison of Seismicity Characteristics and Fault Structure Between Stick–Slip Experiments and Nature. Pure and Applied Geophysics 172, 2247–2264. https://doi.org/10.1007/s00024-013-0713-7

Goertz-Allmann, B.P., Edwards, B., 2014. Constraints on crustal attenuation and three-dimensional spatial distribution of stress drop in Switzerland. Geophysical Journal International 196, 493–509. https://doi.org/10.1093/gji/ggt384

Goldsmith, W., 2001. Impact. Courier Corporation, Dover, New York.

Goldstein, J.I., Newbury, D.E., Echlin, P., Joy, D.C., Fiori, C., Lifshin, E., 1981. Image Formation in the Scanning Electron Microscope, in: Goldstein, J.I., Newbury, D.E., Echlin, P., Joy, D.C., Fiori, C., Lifshin, E. (Eds.), Scanning Electron Microscopy and X-Ray Microanalysis: A Text for Biologist, Materials Scientist, and Geologists. Springer US, Boston, MA, pp. 123–204. https://doi.org/10.1007/978-1-4613-3273-2_4

Goldstein, J.I., Newbury, D.E., Echlin, P., Joy, D.C., Romig, A.D., Lyman, C.E., Fiori, C., Lifshin, E., 1992. Coating and Conductivity Techniques for SEM and Microanalysis, in: Goldstein, J.I., Newbury, D.E., Echlin, P., Joy, D.C., Romig, A.D., Lyman, C.E., Fiori, C., Lifshin, E. (Eds.), Scanning Electron Microscopy and X-Ray Microanalysis: A Text for Biologists, Materials Scientists, and Geologists. Springer US, Boston, MA, pp. 671–740. https://doi.org/10.1007/978-1-4613-0491-3_13

Goodfellow, S.D., Young, R.P., 2014. A laboratory acoustic emission experiment under in situ conditions. Geophysical Research Letters 41, 3422–3430. https://doi.org/10.1002/2014GL059965

Griffith, A.A., 1921. The Phenomena of Rupture and Flow in Solid. Philosophical transactions of the royal society of london. Series A, containing papers of a mathematical or physical character 221, 163–198.

Gu, J.-C., Rice, J.R., Ruina, A.L., Tse, S.T., 1984. Slip motion and stability of a single degree of freedom elastic system with rate and state dependent friction. Journal of the Mechanics and Physics of Solids 32, 167–196. https://doi.org/10.1016/0022-5096(84)90007-3

Gu, Y., Wong, T.-F., 1994. Nonlinear Dynamics of the Transition from Stable Sliding to Cyclic Stick-Slip in Rock, in: Nonlinear Dynamics and Predictability of Geophysical Phenomena. American Geophysical Union (AGU), pp. 15–35. https://doi.org/10.1029/GM083p0015

Guo, H., Lay, T., Brodsky, E.E., 2023. Seismological Indicators of Geologically Inferred Fault Maturity. Journal of Geophysical Research: Solid Earth 128, e2023JB027096. https://doi.org/10.1029/2023JB027096

Gutenberg, B., Richter, C.F., 1944. Frequency of earthquakes in California. Bulletin of the Seismological society of America 34, 185–188.

Gutenberg, B., Richter, C.F., 1941. Seismicity of the Earth. Geological Society of America. Special Papers 1–126.

Han, J., Nguyen, C., 2002. A new ultra-wideband, ultra-short monocycle pulse generator with reduced ringing. IEEE Microwave and Wireless Components Letters 12, 206–208. https://doi.org/10.1109/LMWC.2002.1009996

Hanks, T.C., 1979. b values and ω−γ seismic source models: Implications for tectonic stress variations along active crustal fault zones and the estimation of high-frequency strong ground motion. Journal of Geophysical Research: Solid Earth 84, 2235–2242. https://doi.org/10.1029/JB084iB05p02235

Hanks, T.C., 1977. Earthquake Stress Drops, Ambient Tectonic Stresses and Stresses That Drive Plate Motions, in: Wyss, M. (Ed.), Stress in the Earth, Contributions to Current Research in Geophysics (CCRG). Birkhäuser, Basel, pp. 441–458. https://doi.org/10.1007/978-3-0348-5745-1_28

Hanks, T.C., Kanamori, H., 1979. A moment magnitude scale. Journal of Geophysical Research: Solid Earth 84, 2348–2350. https://doi.org/10.1029/JB084iB05p02348

Hanks, T.C., Wyss, M., 1972. The use of body-wave spectra in the determination of seismic-source parameters. Bulletin of the Seismological Society of America 62, 561–589. https://doi.org/10.1785/BSSA0620020561

Harbord, C.W.A., 2018. Earthquake nucleation, rupture and slip on rough laboratory faults. Durham University. https://doi.org/10.1080/1331677X.2014.947132

Harbord, C.W.A., Nielsen, S.B., De Paola, N., Holdsworth, R.E., 2017. Earthquake nucleation on rough faults. Geology 45, 931–934. https://doi.org/10.1130/G39181.1

Haskell, N.A., 1969. Elastic displacements in the near-field of a propagating fault. Bulletin of the Seismological Society of America 59, 865–908.

Haskell, N.A., 1966. Total energy and energy spectral density of elastic wave radiation from propagating faults. Part II. A statistical source model. The Bulletin of the Seismological Society of America 56, 125–140. https://doi.org/10.1785/BSSA0560010125

Haskell, N.A., 1964. Total energy and energy spectral density of elastic wave radiation from propagating faults. Bulletin of the Seismological Society of America 54, 1811–1841. https://doi.org/10.1785/BSSA05406A1811

Hoummady, M., Campitelli, A., Wlodarski, W., 1997. Acoustic wave sensors: design, sensing mechanisms and applications. Smart Materials and Structures 6, 647. https://doi.org/10.1088/0964-1726/6/6/001

Hsu, N.N., 1985. Dynamic Green's functions of an infinite plate-A computer program.

Huang, Y., Ampuero, J.P., Helmberger, D.V., 2016. The potential for supershear earthquakes in damaged fault zones - theory and observations. Earth and Planetary Science Letters 433, 109–115. https://doi.org/10.1016/j.epsl.2015.10.046

Hunter, S.C., 1957. Energy absorbed by elastic waves during impact. Journal of the Mechanics and Physics of Solids 5, 162–171.

Hutchings, I.M., 2016. Leonardo da Vinci's studies of friction. Wear 360–361, 51–66. https://doi.org/10.1016/j.wear.2016.04.019

Ida, Y., 1972. Cohesive force across the tip of a longitudinal-shear crack and Griffith's specific surface energy. Journal of Geophysical Research 77, 3796–3805. https://doi.org/10.1029/jb077i020p03796

Ide, S., 2003. Apparent break in earthquake scaling due to path and site effects on deep borehole recordings. Journal of Geophysical Research: Solid Earth 108, 2271.

Ide, S., Beroza, G.C., Shelly, D.R., Uchide, T., 2007. A scaling law for slow earthquakes. Nature 447, 76–79. https://doi.org/10.1038/nature05780

Ikari, M.J., Ito, Y., Ujiie, K., Kopf, A.J., 2015. Spectrum of slip behaviour in Tohoku fault zone samples at plate tectonic slip rates. Nature Geoscience 8, 870–874. https://doi.org/10.1038/ngeo2547

Imanishi, K., Ellsworth, W.L., 2006. Source Scaling Relationships of Microearthquakes at Parkfield, CA, Determined Using the SAFOD Pilot Hole Seismic Array, in: Earthquakes: Radiated Energy and the Physics of Faulting. American Geophysical Union (AGU), pp. 81–90. https://doi.org/10.1029/170GM10

IRIS, n.d. Fault: Normal [WWW Document]. IRIS. URL https://www.iris.edu/hq/inclass/animation/fault_normal (accessed 6.8.23).

Irwin, G.R., 1957. Analysis of Stresses and Strains Near the End of a Crack Traversing a Plate. Journal of Applied Mechanics 24, 361–364. https://doi.org/10.1115/1.4011547

Itasca Consulting Ltd, 2017. Acoustic Emission System Test Report and User Guide.

Jia, B., Gao, Z., Han, X., Jin, J., Zhang, J., 2020. Experimental analysis of the stick-slip characteristics of faults at different loading rates. PLoS ONE 15, e0231464. https://doi.org/10.1371/journal.pone.0231464

Johnson, P.A., Ferdowsi, B., Kaproth, B.M., Scuderi, M., Griffa, M., Carmeliet, J., Guyer, R.A., Le Bas, P.Y., Trugman, D.T., Marone, C., 2013. Acoustic emission and microslip precursors to stick-slip failure in sheared granular material. Geophysical Research Letters 40, 5627–5631. https://doi.org/10.1002/2013GL057848

Johnson, T., Wu, F.T., Scholz, C.H., 1973. Source parameters for stick-slip and for earthquakes. Science 179, 278–279. https://doi.org/10.1126/science.179.4070.278

Johnson, T.L., Scholz, C.H., 1976. Dynamic properties of stick-slip friction of rock. Journal of Geophysical Research (1896-1977) 81, 881–888. https://doi.org/10.1029/JB081i005p00881

Johnston, M.J.S., Borcherdt, R.D., Linde, A.T., Gladwin, M.T., 2006. Continuous Borehole Strain and Pore Pressure in the Near Field of the 28 September 2004 M 6.0 Parkfield, California, Earthquake: Implications for Nucleation, Fault Response, Earthquake Prediction, and Tremor. Bulletin of the Seismological Society of America 96, S56–S72. https://doi.org/10.1785/0120050822

Jones, L.M., Molnar, P., 1979. Some characteristics of foreshocks and their possible relationship to earthquake prediction and premonitory slip on faults. Journal of Geophysical Research: Solid Earth 84, 3596–3608. https://doi.org/10.1029/JB084iB07p03596

Kammer, D.S., McLaskey, G.C., 2019. Fracture energy estimates from large-scale laboratory earthquakes. Earth and Planetary Science Letters 511, 36–43. https://doi.org/10.1016/j.epsl.2019.01.031

Kanamori, H., 2004. Static and Dynamic Scaling Relations for Earthquakes and Their Implications for Rupture Speed and Stress Drop. Bulletin of the Seismological Society of America 94, 314–319. https://doi.org/10.1785/0120030159

Kanamori, H., 1977. The energy release in great earthquakes. Journal of Geophysical Research (1896-1977) 82, 2981–2987. https://doi.org/10.1029/JB082i020p02981

Kanamori, H., Anderson, D.L., 1975. Theoretical basis of some empirical relations in seismology. Bulletin of the Seismological Society of America 65, 1073–1095. https://doi.org/10.1785/BSSA0650051073

Kanamori, H., Brodsky, E.E., 2004. The physics of earthquakes. Reports on Progress in Physics 67, 1429–1496. https://doi.org/10.1088/0034-4885/67/8/R03

Kanamori, H., Rivera, L., 2004. Static and Dynamic Scaling Relations for Earthquakes and Their Implications for Rupture Speed and Stress Drop. Bulletin of the Seismological Society of America 94, 314–319.

Kanamori, H., Ross, Z.E., Rivera, L., 2020. Estimation of radiated energy using the KiK-net downhole records—old method for modern data. Geophysical Journal International 221, 1029–1042. https://doi.org/10.1093/gji/ggaa040

Kaneko, Y., Lapusta, N., 2008. Variability of earthquake nucleation in continuum models of rate-and-state faults and implications for aftershock rates. Journal of Geophysical Research: Solid Earth 113. https://doi.org/10.1029/2007JB005154

Kaneko, Y., Shearer, P.M., 2014. Seismic source spectra and estimated stress drop derived from cohesive-zone models of circular subshear rupture. Geophysical Journal International 197, 1002–1015. https://doi.org/10.1093/gji/ggu030

Kaproth, B.M., Marone, C., 2013. Slow earthquakes, preseismic velocity changes, and the origin of slow frictional stick-slip. Science 341, 1229–1232. https://doi.org/10.1126/science.1239577

Karner, S.L., Marone, C., 2001. Fractional restrengthening in simulated fault gouge: Effect of shear load perturbations. Journal of Geophysical Research: Solid Earth 106, 19319–19337. https://doi.org/10.1029/2001JB000263

Kato, A., Fukuda, J., Kumazawa, T., Nakagawa, S., 2016. Accelerated nucleation of the 2014 Iquique, Chile Mw 8.2 Earthquake. Sci Rep 6, 24792. https://doi.org/10.1038/srep24792

Kato, A., Obara, K., Igarashi, T., Tsuruoka, H., Nakagawa, S., Hirata, N., 2012. Propagation of slow slip leading up to the 2011 M(w) 9.0 Tohoku-Oki earthquake. Science 335, 705–708. https://doi.org/10.1126/science.1215141

Kazimi, A.A., Mackenzie, C.A., 2016. The economic costs of natural disasters, terrorist attacks, and other calamities: An analysis of economic models that quantify the losses caused by disruptions, in: 2016 IEEE Systems and Information Engineering Design Symposium (SIEDS). Presented at the 2016 IEEE Systems and Information Engineering Design Symposium (SIEDS), IEEE, Charlottesville, VA, pp. 32–37. https://doi.org/10.1109/SIEDS.2016.7489322

Keylis-Borok, V., 1959. On estimation of the displacement in an earthquake source and of source dimensions. Annali di Geofisica 12, 205–214.

Kilgore, B.D., McGarr, A., Beeler, N.M., Lockner, D.A., 2017. Earthquake Source Properties From Instrumented Laboratory Stick-Slip, in: Fault Zone Dynamic Processes, Geophysical Monograph Series. pp. 151–169. https://doi.org/10.1002/9781119156895.ch8

Konno, K., Ohmachi, T., 1998. Ground-motion characteristics estimated from spectral ratio between horizontal and vertical components of microtremor. Bulletin of the Seismological Society of America 88, 228–241.

Kostrov, B.V., 1974. Seismic moment and enengy of earthquakes, and the seismic flow of rock, Izv. Acad. Sci. USSR. Phys. Solid Earth 1, 23–44.

Kostrov, B.V., 1964. Selfsimilar problems of propagation of shear cracks. Journal of Applied Mathematics and Mechanics 28, 1077–1087. https://doi.org/10.1016/0021-8928(64)90010-3

Kotha, S.R., Weatherill, G., Bindi, D., Cotton, F., 2020. A regionally-adaptable ground-motion model for shallow crustal earthquakes in Europe. Bull Earthquake Eng 18, 4091–4125. https://doi.org/10.1007/s10518-020-00869-1

Kulesa, A., Krzywinski, M., Blainey, P., Altman, N., 2015. Points of Significance: Sampling distributions and the bootstrap. Nature Methods 12, 477–478. https://doi.org/10.1038/nmeth.3414

Lam, N., 2023. A review of stochastic earthquake ground motion prediction equations for stable regions. Int J Adv Eng Sci Appl Math 15, 1–14. https://doi.org/10.1007/s12572-022-00325-0

Lambert, V., Lapusta, N., 2020. Rupture-dependent breakdown energy in fault models with thermo-hydro-mechanical processes. Solid Earth 11, 2283–2302.

Lambert, V., Lapusta, N., Faulkner, D., 2021. Scale dependence of earthquake rupture prestress in models with enhanced weakening: Implications for event statistics and inferences of fault stress. Journal of Geophysical Research: Solid Earth 126, e2021JB021886.

Langbein, J., Borcherdt, R., Dreger, D., Fletcher, J., Hardebeck, J.L., Hellweg, M., Ji, C., Johnston, M., Murray, J.R., Nadeau, R., Rymer, M.J., Treiman, J.A., 2005. Preliminary Report on the 28 September 2004, M 6.0 Parkfield, California Earthquake. Seismological Research Letters 76, 10–26. https://doi.org/10.1785/gssrl.76.1.10

Lanzano, G., Pacor, F., Luzi, L., D'Amico, M., Puglia, R., Felicetta, C., 2017. Systematic source, path and site effects on ground motion variability: the case study of Northern Italy. Bulletin of Earthquake Engineering 15, 4563–4583. https://doi.org/10.1007/s10518-017-0170-2

Lapusta, N., Rice, J.R., 2002. Nucleation of rate and state frictional instability under non-uniform loading, in: AGU Fall Meeting Abstracts. pp. S61E-05.

Laughton, M.A., Warne, D.F., 2004. Electrical Engineer's Reference Book. Newnes.

Lee, R.L., Bradley, B.A., Stafford, P.J., Graves, R.W., Rodriguez-Marek, A., 2020. Hybrid broadband ground motion simulation validation of small magnitude earthquakes in Canterbury, New Zealand. Earthquake Spectra 36, 673–699. https://doi.org/10.1177/8755293019891718

Leeman, J.R., Marone, C., Saffer, D.M., 2018. Frictional Mechanics of Slow Earthquakes. Journal of Geophysical Research: Solid Earth 123, 7931–7949. https://doi.org/10.1029/2018JB015768

Leeman, J.R., Saffer, D.M., Scuderi, M.M., Marone, C., 2016. Laboratory observations of slow earthquakes and the spectrum of tectonic fault slip modes. Nature Communications 7, 1–6. https://doi.org/10.1038/ncomms11104

Lei, X., 2003. How do asperities fracture? An experimental study of unbroken asperities. Earth and Planetary Science Letters 213, 347–359. https://doi.org/10.1016/S0012-821X(03)00328-5

Lei, X., Masuda, K., Nishizawa, O., Jouniaux, L., Liu, L., Ma, W., Satoh, T., Kusunose, K., 2004. Detailed analysis of acoustic emission activity during catastrophic fracture of faults in rock. Journal of Structural Geology 26, 247–258. https://doi.org/10.1016/S0191-8141(03)00095-6

Li, B.Q., Casanova, M., Einstein, H.H., 2022. Laboratory study of fracture initiation and propagation in Barre granite under fluid pressure at stress state close to failure. Journal of Rock Mechanics and Geotechnical Engineering. https://doi.org/10.1016/j.jrmge.2022.06.011

Linde, A.T., Sacks, I.S., 2002. Slow earthquakes and great earthquakes along the Nankai trough. Earth and Planetary Science Letters 203, 265–275. https://doi.org/10.1016/S0012-821X(02)00849-X

Linker, M.F., Dieterich, J.H., 1992. Effects of variable normal stress on rock friction: Observations and constitutive equations. Journal of Geophysical Research: Solid Earth 97, 4923–4940. https://doi.org/10.1029/92JB00017

Liu, Y., Rice, J.R., 2007. Spontaneous and triggered aseismic deformation transients in a subduction fault model. Journal of Geophysical Research: Solid Earth 112. https://doi.org/10.1029/2007JB004930

Lockner, D., 1993. The role of acoustic emission in the study of rock fracture. International Journal of Rock Mechanics and Mining Sciences and 30, 883–899. https://doi.org/10.1016/0148-9062(93)90041-B

Lockner, D.A., Okubo, P.G., 1983. Measurements of frictional heating in granite. Journal of Geophysical Research: Solid Earth 88, 4313–4320. https://doi.org/10.1029/JB088iB05p04313

Love, A.E.H., 1927. A Treatise on the Mathematical Theory of Elasticity. Cambridge Univeristy Press, London. https://doi.org/10.1038/105511a0

Ma, K.-F., Mori, J., Lee, S.-J., Yu, S.B., 2001. Spatial and Temporal Distribution of Slip for the 1999 Chi-Chi, Taiwan, Earthquake. Bulletin of the Seismological Society of America 91, 1069–1087. https://doi.org/10.1785/0120000728

Madariaga, R., 2009. Seismic source theory, in: Kanamori, H., Schubert, G. (Eds.), Earthquake Seismology (Treatise on Geophysics). Elsevier, Amsterdam, pp. 59–82. https://doi.org/10.1016/B978-044452748-6.00061-4

Madariaga, R., 1979. On the relation between seismic moment and stress drop in the presence of stress and strength heterogeneity. Journal of Geophysical Research: Solid Earth 84, 2243–2250. https://doi.org/10.1029/JB084iB05p02243

Madariaga, R., 1976. Dynamics of an Expanding Circular Fault. The Journal of Geology 66, 639–666. https://doi.org/10.1086/622062

Mandelbrot, B.B., 1985. Self-Affine Fractals and Fractal Dimension. Phys. Scr. 32, 257. https://doi.org/10.1088/0031-8949/32/4/001

Manighetti, I., Campillo, M., Bouley, S., Cotton, F., 2007a. Earthquake scaling, fault segmentation, and structural maturity. Earth and Planetary Science Letters. https://doi.org/10.1016/j.epsl.2006.11.004

Manighetti, I., Campillo, M., Bouley, S., Cotton, F., 2007b. Earthquake scaling, fault segmentation, and structural maturity. Earth and Planetary Science Letters 253, 429–438. https://doi.org/10.1016/j.epsl.2006.11.004

Margenau, H., 1939. Van der waals forces. Rev. Mod. Phys. 11, 1–35. https://doi.org/10.1103/RevModPhys.11.1

Marone, C., 1998a. Laboratory-Derived Friction Laws and Their Application To Seismic Faulting. Annual Review of Earth and Planetary Sciences 26, 643–696. https://doi.org/10.1146/annurev.earth.26.1.643

Marone, C., 1998b. The effect of loading rate on static friction and the rate of fault healing during the earthquake cycle. Nature 391, 69–72. https://doi.org/10.1038/34157

Marone, C., Cox, S.J.D., 1994. Scaling of rock friction constitutive parameters: The effects of surface roughness and cumulative offset on friction of gabbro. PAGEOPH 143, 359–385. https://doi.org/10.1007/BF00874335

Marone, C., Kilgore, B., 1993. Scaling of the critical slip distance for seismic faulting with shear strain in fault zones. Nature 362, 618–621. https://doi.org/10.1038/362618a0

Marty, S., Passelègue, F.X., Aubry, J., Bhat, H.S., Schubnel, A., Madariaga, R., 2019. Origin of High-Frequency Radiation During Laboratory Earthquakes. Geophysical Research Letters 46, 3755–3763. https://doi.org/10.1029/2018GL080519

Marty, S, Passelègue, F.X., Aubry, J., Bhat, H.S., Schubnel, A., Madariaga, R., 2019. Origin of high-frequency radiation during laboratory earthquakes. Geophysical Research Letters. https://doi.org/10.1029/2018GL080519

McGarr, A., 2012. Relating stick-slip friction experiments to earthquake source parameters. Geophysical Research Letters 39, 1–5. https://doi.org/10.1029/2011GL050327

McLaskey, G.C., 2019. Earthquake Initiation From Laboratory Observations and Implications for Foreshocks. Journal of Geophysical Research: Solid Earth 124, 12882–12904. https://doi.org/10.1029/2019JB018363

McLaskey, G.C., Glaser, S.D., 2012. Acoustic emission sensor calibration for absolute source measurements. Journal of Nondestructive Evaluation 31, 157–168. https://doi.org/10.1007/s10921-012-0131-2

McLaskey, G.C., Glaser, S.D., 2011. Micromechanics of asperity rupture during laboratory stick slip experiments. Geophysical Research Letters 38, 1–5. https://doi.org/10.1029/2011GL047507

McLaskey, G.C., Glaser, S.D., 2010. Hertzian impact: Experimental study of the force pulse and resulting stress waves. The Journal of the Acoustical Society of America 128, 1087. https://doi.org/10.1121/1.3466847

McLaskey, G.C., Kilgore, B.D., 2013. Foreshocks during the nucleation of stick-slip instability. Journal of Geophysical Research: Solid Earth 118, 2982–2997. https://doi.org/10.1002/jgrb.50232

McLaskey, G.C., Kilgore, B.D., Lockner, D.A., Beeler, N.M., 2014. Laboratory Generated M -6 Earthquakes. Pure and Applied Geophysics 171, 2601–2615. https://doi.org/10.1007/s00024-013-0772-9

McLaskey, G.C., Lockner, D.A., 2016. Calibrated Acoustic Emission System Records M -3.5 to M -8 Events Generated on a Saw-Cut Granite Sample. Rock Mechanics and Rock Engineering 49, 4527–4536. https://doi.org/10.1007/s00603-016-1082-1

McLaskey, G.C., Lockner, D.A., 2014. Preslip and cascade processes initiating laboratory stick slip. Journal of Geophysical Research : Solid Earth 119, 6323–6336.

McLaskey, G.C., Lockner, D.A., Kilgore, B.D., Beeler, N.M., 2015. A robust calibration technique for acoustic emission systems based on momentum transfer from a ball drop. Bulletin of the Seismological Society of America 105, 257–271. https://doi.org/10.1785/0120140170

McLaskey, G.C., Yamashita, F., 2017. Slow and fast ruptures on a laboratory fault controlled by loading characteristics. Journal of Geophysical Research: Solid Earth 122, 3719–3738. https://doi.org/10.1002/2016JB013681

Mei, C., Wu, W., 2021. Fracture asperity evolution during the transition from stick slip to stable sliding. Philosophical Transactions of the Royal Society A: Mathematical, Physical and Engineering Sciences 379, 20200133. https://doi.org/10.1098/rsta.2020.0133

Mitchell, T.M., Faulkner, D.R., 2008. Experimental measurements of permeability evolution during triaxial compression of initially intact crystalline rocks and implications for fluid flow in fault zones. Journal of Geophysical Research: Solid Earth 113, 1–16. https://doi.org/10.1029/2008JB005588

Mooney, C.Z., Duval, R.D., 1993. Bootstrapping: A nonparametric approach to statistical inference, Sage University Paper series on Quantitative Applications in the Social Sciences. Sage, Newbury Park, CA.

Morad, D., Sagy, A., Tal, Y., Hatzor, Y.H., 2022. Fault roughness controls sliding instability. Earth and Planetary Science Letters 579, 117365. https://doi.org/10.1016/j.epsl.2022.117365

Moradian, Z., Einstein, H.H., Ballivy, G., 2016. Detection of Cracking Levels in Brittle Rocks by Parametric Analysis of the Acoustic Emission Signals. Rock Mechanics and Rock Engineering 49, 785–800. https://doi.org/10.1007/s00603-015-0775-1

Mori, T., Tobita, Y., Okimura, T., 2012. The damage to hillside embankments in Sendai city during The 2011 off the Pacific Coast of Tohoku Earthquake. Soils and Foundations 52, 910–928. https://doi.org/10.1016/j.sandf.2012.11.011

Mueller, C.S., 1985. Source pulse enhancement by deconvolution of an empirical Green's function. Geophysical Research Letters 12, 33–36.

Müller, M., 2018. Micromechanical Broadband Vibration Amplitude-Amplifier for Microseismic and Acoustic Emission Detection.

Noda, H., Lapusta, N., 2013. Stable creeping fault segments can become destructive as a result of dynamic weakening. Nature 493, 518–521. https://doi.org/10.1038/nature11703

Noda, H., Nakatani, M., Hori, T., 2013. Large nucleation before large earthquakes is sometimes skipped due to cascade-up—Implications from a rate and state simulation of faults with hierarchical asperities. Journal of Geophysical Research: Solid Earth 118, 2924–2952. https://doi.org/10.1002/jgrb.50211

Ohnaka, M., 2000. A Physical Scaling Relation Between the Size of an Earthquake and its Nucleation Zone Size. Pure appl. geophys. 157, 2259–2282. https://doi.org/10.1007/PL00001084

Ohnaka, M., 1992. Earthquake source nucleation: A physical model for short-term precursors. Tectonophysics 211, 149–178. https://doi.org/10.1016/0040-1951(92)90057-D

Ohnaka, M., 1973. Experimental Studies of Stick-Slip and Their Application to the Earthquake Source Mechanism. Journal of Physics of the Earth 21, 285–303. https://doi.org/10.4294/jpe1952.21.285

Ohnaka, M., Kuwahara, Y., 1990. Characteristic features of local breakdown near a crack-tip in the transition zone from nucleation to unstable rupture during stick-slip shear failure. Tectonophysics, Earthquake Source Processes 175, 197–220. https://doi.org/10.1016/0040-1951(90)90138-X

Ohnaka, M., Shen, L., 1999. Scaling of the shear rupture process from nucleation to dynamic propagation: Implications of geometric irregularity of the rupturing surfaces. Journal of Geophysical Research: Solid Earth 104, 817–844. https://doi.org/10.1029/1998JB900007

Okubo, K., Bhat, H.S., Rougier, E., Marty, S., Schubnel, A., Lei, Z., Knight, E.E., Klinger, Y., 2019. Dynamics, Radiation, and Overall Energy Budget of Earthquake Rupture With Coseismic

Off-Fault Damage. Journal of Geophysical Research: Solid Earth 124, 11771–11801. https://doi.org/10.1029/2019JB017304

Okubo, P.G., 1989. Dynamic rupture modeling with laboratory-derived constitutive relations. Journal of Geophysical Research: Solid Earth 94, 12321–12335.

Okubo, P.G., Dieterich, J.H., 1986. State Variable Fault Constitutive Relations for Dynamic Slip, in: Earthquake Source Mechanics, Geophysical Monograph Series. pp. 25–35. https://doi.org/10.1029/GM037p0025

Okubo, P.G., Dieterich, J.H., 1984. Effects of physical fault properties on frictional instabilities produced on simulated faults. Journal of Geophysical Research: Solid Earth 89, 5817–5827. https://doi.org/10.1029/JB089iB07p05817

Oppenheim, A.V., Willsky, A.S., Young, I.T., 1983. Signals and systems. Prentice-Hall, Englewood Cliffs, New Jersey.

Orowan, E., 1960. Chapter 12: Mechanism of Seismic Faulting, in: Griggs, D., Handin, J. (Eds.), Rock Deformation (A Symposium). Geological Society of America, p. 0. https://doi.org/10.1130/MEM79-p323

Ostapchuk, A.A., Morozova, K.G., 2020. On the Mechanism of Laboratory Earthquake Nucleation Highlighted by Acoustic Emission. Scientific Reports 10, 1–8. https://doi.org/10.1038/s41598-020-64272-1

Paglialunga, F., Passelègue, F.X., Brantut, N., Barras, F., Lebihain, M., Violay, M., 2022. On the scale dependence in the dynamics of frictional rupture: Constant fracture energy versus size-dependent breakdown work. Earth and Planetary Science Letters 584, 117442.

Palmer, A.C., Rice, J.R., 1973. The growth of slip surfaces in the progressive failure of over-consolidated clay. Proceedings of the Royal Society of London. A. Mathematical and Physical Sciences 332, 527–548. https://doi.org/10.1098/rspa.1973.0040

Papadopoulos, G.A., Charalampakis, M., Fokaefs, A., Minadakis, G., 2010. Strong foreshock signal preceding the L'Aquila (Italy) earthquake (M_w 6.3) of 6 April 2009. Natural Hazards and Earth System Sciences 10, 19–24. https://doi.org/10.5194/nhess-10-19-2010

Papazachos, B.C., 1973. The time distribution of the reservoir-associated foreshocks and its importance to the prediction of the principal shock. Bulletin of the Seismological Society of America 63, 1973–1978.

Passelègue, F.X., Schubnel, A., Nielsen, S., Bhat, H.S., Madariaga, R., 2013. From Sub-Rayleigh to Supershear Ruptures During Stick-Slip Experiments on Crustal Rocks. Science 340, 2–6. https://doi.org/10.1126/science.1235637

Paterson, M.S., Wong, T.F., 2005. Experimental rock deformation - The brittle field. Experimental Rock Deformation - The Brittle Field 1–347. https://doi.org/10.1007/b137431

Patton, F.D., 1966. Multiple Modes of Shear Failure In Rock. Presented at the 1st ISRM Congress, OnePetro.

Perrin, C., Waldhauser, F., Scholz, C.H., 2021. The Shear Deformation Zone and the Smoothing of Faults With Displacement. Journal of Geophysical Research: Solid Earth 126, e2020JB020447. https://doi.org/10.1029/2020JB020447

Pourahmadi, M., 1984. Taylor Expansion of and Some Applications. The American Mathematical Monthly 91, 303–307. https://doi.org/10.1080/00029890.1984.11971411

Power, W.L., Tullis, T.E., Weeks, J.D., 1988. Roughness and wear during brittle faulting. Journal of Geophysical Research: Solid Earth 93, 15268–15278. https://doi.org/10.1029/JB093iB12p15268

Powers, P.M., Jordan, T.H., 2010. Distribution of seismicity across strike-slip faults in California. Journal of Geophysical Research: Solid Earth 115. https://doi.org/10.1029/2008JB006234

Rabinowicz, E., 1958. The intrinsic variables affecting the stick-slip process. Proceedings of the Physical Society 71, 668–675. https://doi.org/10.1088/0370-1328/71/4/316

Rabinowicz, E., 1951. The Nature of the Static and Kinetic Coefficients of Friction. Journal of Applied Physics 22, 1373–1379. https://doi.org/10.1063/1.1699869

Radiguet, M., Cotton, F., Manighetti, I., Campillo, M., Douglas, J., 2009. Dependency of Near-Field Ground Motions on the Structural Maturity of the Ruptured Faults. Bulletin of the Seismological Society of America 99, 2572–2581. https://doi.org/10.1785/0120080340

Reasenberg, P.A., 1999. Foreshock occurrence before large earthquakes. Journal of Geophysical Research: Solid Earth 104, 4755–4768. https://doi.org/10.1029/1998JB900089

Reed, J., 1985. Energy losses due to elastic wave propagation during an elastic impact impact. Journal of Physics D: Applied Physics 18, 2329–2337.

Renard, F., McBeck, J., Cordonnier, B., 2020. Competition between slow slip and damage on and off faults revealed in 4D synchrotron imaging experiments. Tectonophysics 782–783, 228437. https://doi.org/10.1016/j.tecto.2020.228437

Rice, J.R., 1993. Spatio-temporal complexity of slip on a fault. Journal of Geophysical Research: Solid Earth 98, 9885–9907.

Rice, J.R., Lapusta, N., Ranjith, K., 2001. Rate and state dependent friction and the stability of sliding between elastically deformable solids. Journal of the Mechanics and Physics of Solids 49, 1865–1898. https://doi.org/10.1016/S0022-5096(01)00042-4

Rice, J.R., Ruina, A.L., 1983. Stability of Steady Frictional Slipping. Journal of Applied Mechanics 50, 343–349. https://doi.org/10.1115/1.3167042

Rice, J.R., Sammis, C.G., Parsons, R., 2005. Off-Fault Secondary Failure Induced by a Dynamic Slip Pulse. Bulletin of the Seismological Society of America 95, 109–134. https://doi.org/10.1785/0120030166

Rice-Birchall, E., Faulkner, D.R., Bedford, J.D., 2021. The manufacture, mechanical properties, and microstructural analysis of synthetic quartz-cemented sandstones. International Journal of Rock Mechanics and Mining Sciences 146, 104869. https://doi.org/10.1016/j.ijrmms.2021.104869

Richter, C.F., 1935. An instrumental earthquake magnitude scale*. Bulletin of the Seismological Society of America 25, 1–32. https://doi.org/10.1785/BSSA0250010001

Ristau, J., 2009. Comparison of Magnitude Estimates for New Zealand Earthquakes: Moment Magnitude, Local Magnitude, and Teleseismic Body-Wave Magnitude. Bulletin of the Seismological Society of America 99, 1841–1852. https://doi.org/10.1785/0120080237

Rivière, J., Lv, Z., Johnson, P.A., Marone, C., 2018. Evolution of b-value during the seismic cycle: Insights from laboratory experiments on simulated faults. Earth and Planetary Science Letters 482, 407–413. https://doi.org/10.1016/j.epsl.2017.11.036

Roeloffs, E.A., 2006. Evidence for Aseismic Deformation Rate Changes Prior to Earthquakes. Annual Review of Earth and Planetary Sciences 34, 591–627. https://doi.org/10.1146/annurev.earth.34.031405.124947

Romanet, P., Bhat, H.S., Jolivet, R., Madariaga, R., 2018. Fast and Slow Slip Events Emerge Due to Fault Geometrical Complexity. Geophysical Research Letters 45, 4809–4819. https://doi.org/10.1029/2018GL077579

Rosakis, A.J., Xia, K., Lykotrafitis, G., Kanamori, H., 2007. Dynamic Shear Rupture in Frictional Interfaces: Speeds, Directionality, and Modes, in: Treatise on Geophysics. Elsevier, pp. 183–213. https://doi.org/10.1016/B978-0-444-53802-4.00072-5

RS Pro, 2023. RS Pro ARBITRARY/FUNCTION WAVEFORM GENERATOR SDG800 SERIES.

Rubin, A.M., Ampuero, J.-P., 2005. Earthquake nucleation on (aging) rate and state faults. Journal of Geophysical Research: Solid Earth 110. https://doi.org/10.1029/2005JB003686

Ruina, A., 1983. Slip instability and state variable friction laws. Journal of Geophysical Research: Solid Earth 88, 10359–10370. https://doi.org/10.1029/JB088iB12p10359

Sagy, A., Brodsky, E.E., Axen, G.J., 2007. Evolution of fault-surface roughness with slip. Geology 35, 283–286. https://doi.org/10.1130/G23235A.1

Sahakian, V.J., Baltay, A., Hanks, T.C., Buehler, J., Vernon, F.L., Kilb, D., Abrahamson, N.A., 2019. Ground Motion Residuals, Path Effects, and Crustal Properties: A Pilot Study in Southern California. Journal of Geophysical Research: Solid Earth 124, 5738–5753. https://doi.org/10.1029/2018JB016796

Sato, H., 1977. Some Precursors Prior to Recent Great Earthquakes Along the Nankai Trough. Journal of Physics of the Earth 25, S115–S121. https://doi.org/10.4294/jpe1952.25.Supplement_S115

Sato, H., Hirasawa, T., 1973. Body wave spectra from propagating shear cracks. Journal of Physics of the Earth 21, 415–431. https://doi.org/10.4294/jpe1952.21.415

Scherbaum, F., 1990. Combined inversion for the three-dimensional Q structure and source parameters using microearthquake spectra. Journal of Geophysical Research: Solid Earth 95, 12423–12438. https://doi.org/10.1029/JB095iB08p12423

Scholz, C., Molnar, P., Johnson, T., 1972. Detailed studies of frictional sliding of granite and implications for the earthquake mechanism. Journal of Geophysical Research (1896-1977) 77, 6392–6406. https://doi.org/10.1029/JB077i032p06392

Scholz, C.H., 2019. The Mechanics of Earthquakes and Faulting, 3rd ed. Cambridge University Press, Cambridge.

Scholz, C.H., 1998. Earthquakes and friction laws. Nature 391, 37–42. https://doi.org/10.1038/34097

Scholz, C.H., Engelder, J.T., 1976. The role of asperity indentation and ploughing in rock friction — I: Asperity creep and stick-slip. International Journal of Rock Mechanics and Mining Sciences & Geomechanics Abstracts 13, 149–154. https://doi.org/10.1016/0148-9062(76)90819-6

Scuderi, M.M., Carpenter, B.M., Marone, C., 2014. Physicochemical processes of frictional healing: Effects of water on stick-slip stress drop and friction of granular fault gouge. Journal of Geophysical Research: Solid Earth 119, 4090–4105. https://doi.org/10.1002/2013JB010641

Scuderi, M.M., Marone, C., Tinti, E., Di Stefano, G., Collettini, C., 2016. Precursory changes in seismic velocity for the spectrum of earthquake failure modes. Nature Geoscience 9, 695–700. https://doi.org/10.1038/ngeo2775

Segall, P., 2010. Fault Friction, in: Earthquake and Volcano Deformation. Princeton University Press, pp. 332–371.

Selvadurai, P.A., 2019. Laboratory Insight Into Seismic Estimates of Energy Partitioning During Dynamic Rupture: An Observable Scaling Breakdown. Journal of Geophysical Research: Solid Earth 124, 11350–11379. https://doi.org/10.1029/2018JB017194

Selvadurai, P.A., Glaser, S.D., 2017. Asperity generation and its relationship to seismicity on a planar fault: A laboratory simulation. Geophysical Journal International 208, 1009–1025. https://doi.org/10.1093/gji/ggw439

Shearer, P.M., Prieto, G.A., Hauksson, E., 2006. Comprehensive analysis of earthquake source spectra in southern California. Journal of Geophysical Research: Solid Earth 111. https://doi.org/10.1029/2005JB003979

Shelly, D.R., 2010. Periodic, Chaotic, and Doubled Earthquake Recurrence Intervals on the Deep San Andreas Fault. Science 328, 1385–1388. https://doi.org/10.1126/science.1189741

Shibazaki, B., Matsu'ura, M., 1998. Transition process from nucleation to high-speed rupture propagation: Scaling from stick-slip experiments to natural earthquakes. Geophysical Journal International 132, 14–30. https://doi.org/10.1046/j.1365-246x.1998.00409.x

Shibazaki, B., Matsu'ura, M., 1992. Spontaneous processes for nucleation, dynamic propagation, and stop of earthquake rupture. Geophysical Research Letters 19, 1189–1192.

Shreedharan, S., Bolton, D.C., Rivière, J., Marone, C., 2020. Preseismic Fault Creep and Elastic Wave Amplitude Precursors Scale With Lab Earthquake Magnitude for the Continuum of Tectonic Failure Modes. Geophysical Research Letters 47, e2020GL086986. https://doi.org/10.1029/2020GL086986

Siman-Tov, S., Aharonov, E., Sagy, A., Emmanuel, S., 2013. Nanograins form carbonate fault mirrors. Geology 41, 703–706. https://doi.org/10.1130/G34087.1

Singh, S.K., Ordaz, M., 1994. Seismic energy release in Mexican subduction zone earthquakes. Bulletin of the Seismological Society of America 84, 1533–1550. https://doi.org/10.1785/BSSA0840051533

Singh, S.K., Suárez, G., 1988. Regional variation in the number of aftershocks (mb ≧ 5) of large, subduction-zone earthquakes (Mw ≧ 7.0). Bulletin of the Seismological Society of America 78, 230–242.

Starr, A.T., 1928. Slip in a crystal and rupture in a solid due to shear. Mathematical Proceedings of the Cambridge Philosophical Society 24, 489–500. https://doi.org/10.1017/S0305004100014626

Stein, S., Wysession, M., 1991. An Introduction to Seismology, Earthquakes, and Earth Structure. John Wiley & Sons, Incorporated, Hoboken, UNITED KINGDOM.

Strasser, F.O., Abrahamson, N.A., Bommer, J.J., 2009. Sigma: Issues, Insights, and Challenges. Seismological Research Letters 80, 40–56. https://doi.org/10.1785/gssrl.80.1.40

Stump, B.W., Johnson, L.R., 1977. The determination of source properties by the linear inversion of seismograms. Bulletin of the Seismological Society of America 67, 1489–1502. https://doi.org/10.2307/1779766

Summers, R., Byerlee, J., 1977. A note on the effect of fault gouge composition on the stability of frictional sliding. International Journal of Rock Mechanics and Mining Sciences & Geomechanics Abstracts 14, 155–160. https://doi.org/10.1016/0148-9062(77)90007-9

Tal, Y., Hager, B.H., Ampuero, J.P., 2018. The Effects of Fault Roughness on the Earthquake Nucleation Process. Journal of Geophysical Research: Solid Earth 123, 437–456. https://doi.org/10.1002/2017JB014746

Tan, W., Liu, J., Chen, T., Marquez, H.J., 2006. Comparison of some well-known PID tuning formulas. Computers & Chemical Engineering 30, 1416–1423. https://doi.org/10.1016/j.compchemeng.2006.04.001

Teunissen, P., 1990. Nonlinear least squares. Manuscripta Geodaetica 15, 137–150.

THK, n.d. Examples of Selecting a Ball Screw.

Thompson, B.D., Young, R.P., Lockner, D.A., 2009. Premonitory acoustic emissions and stick-slip in natural and smooth-faulted Westerly granite. Journal of Geophysical Research: Solid Earth 114, 1–14. https://doi.org/10.1029/2008JB005753

Tinti, E., Fukuyama, E., Piatanesi, A., Cocco, M., 2005. A kinematic source-time function compatible with earthquake dynamics. Bulletin of the Seismological Society of America 95, 1211–1223. https://doi.org/10.1785/0120040177

Tinti, E., Scuderi, M.M., Scognamiglio, L., Di Stefano, G., Marone, C., Collettini, C., 2016. On the evolution of elastic properties during laboratory stick-slip experiments spanning the transition from slow slip to dynamic rupture. Journal of Geophysical Research: Solid Earth 121, 8569–8594. https://doi.org/10.1002/2016JB013545

Tobin, H., Ito, H., Behrmann, J., Hickman, S., Kimura, G., 2007. Introduction to Special Issue: IODP-ICDP Workshop examines challenges of fault zone drilling. Scientific Drilling Special Issue No. 1, 5–16.

Trugman, D.T., Ross, Z.E., 2019. Pervasive Foreshock Activity Across Southern California. Geophysical Research Letters 46, 8772–8781. https://doi.org/10.1029/2019GL083725

Udias, A., Madariaga, R., Buforn, E., Udias, A., Madariaga, R., Buforn, E., 2014a. Earthquakes and fault motion, in: Source Mechanisms of Earthquakes. pp. 1–21. https://doi.org/10.1017/cbo9781139628792.002

Udias, A., Madariaga, R., Buforn, E., Udias, A., Madariaga, R., Buforn, E., 2014b. Point source models 4.1., in: Source Mechanisms of Earthquakes. pp. 63–89.

Udias, A., Madariaga, R., Buforn, E., Udias, A., Madariaga, R., Buforn, E., 2014c. Simple dynamic models 9.1., in: Source Mechanisms of Earthquakes. pp. 189–204.

UN DESA, 2022. The Sustainable Development Goals Report 2022. UN DESA, New York, USA.

U.S. Geological Survey, 2023. Latest Earthquakes [WWW Document]. USGS. URL https://earthquake.usgs.gov/earthquakes/map/?extent=-80.29793,78.75&extent=84.16085,641.25&range=search&baseLayer=ocean&timeZone=utc&help=interface&search=%7B%22name%22:%22Search%20Results%22,%22params%22:%7B%22starttime%22:%222022-01-01%2000:00:00%22,%22endtime%22:%222023-06-07%2023:59:59%22,%22minmagnitude%22:4.5,%22orderby%22:%22time%22%7D%7D (accessed 6.7.23).

Vassiliou, M.S., Kanamori, H., 1982. The energy release in earthquakes. Bulletin of the Seismological Society of America 72, 371–387. https://doi.org/10.1785/BSSA0720020371

Veedu, D.M., Barbot, S., 2016. The Parkfield tremors reveal slow and fast ruptures on the same asperity. Nature 532, 361–365. https://doi.org/10.1038/nature17190

Venkataraman, A., Kanamori, H., 2004. Effect of directivity on estimates of radiated seismic energy. Journal of Geophysical Research: Solid Earth 109.

Voisin, C., Grasso, J.-R., Larose, E., Renard, F., 2008. Evolution of seismic signals and slip patterns along subduction zones: Insights from a friction lab scale experiment. Geophysical Research Letters 35. https://doi.org/10.1029/2008GL033356

Voisin, C., Renard, F., Grasso, J.-R., 2007. Long term friction: From stick-slip to stable sliding. Geophysical Research Letters 34. https://doi.org/10.1029/2007GL029715

Walsh, J.B., 1971. Stiffness in faulting and in friction experiments. Journal of Geophysical Research (1896-1977) 76, 8597–8598. https://doi.org/10.1029/JB076i035p08597

Wang, K., Bilek, S.L., 2011. Do subducting seamounts generate or stop large earthquakes? Geology 39, 819–822. https://doi.org/10.1130/G31856.1

Wang, W., Scholz, C.H., 1995. Micromechanics of rock friction: 3. Quantitative modeling of base friction. Journal of Geophysical Research: Solid Earth 100, 4243–4247. https://doi.org/10.1029/94JB02915

Wang, W., Scholz, C.H., 1994. Micromechanics of the velocity and normal stress dependence of rock friction. PAGEOPH 143, 303–315. https://doi.org/10.1007/BF00874333

Widder, D.V., 2015. Laplace Transform (PMS-6). Princeton University Press, Princeton.

Wirth, E., Sahakian, V., Wallace, L., Melnick, D., 2022. The occurrence and hazards of great subduction zone earthquakes. Nature Reviews Earth & Environment 3. https://doi.org/10.1038/s43017-021-00245-w

Wu, B.S., McLaskey, G.C., 2019. Contained Laboratory Earthquakes Ranging From Slow to Fast. Journal of Geophysical Research: Solid Earth 124, 10270–10291. https://doi.org/10.1029/2019JB017865

Wu, S., Li, T., Ge, H., Wang, X., Li, N., Zou, Y., 2019. Shear-tensile fractures in hydraulic fracturing network of layered shale. Journal of Petroleum Science and Engineering 183, 106428. https://doi.org/10.1016/j.petrol.2019.106428

Wyss, M., Brune, J.N., 1967. The Alaska earthquake of 28 March 1964: A complex multiple rupture. Bulletin of the Seismological Society of America 57, 1017–1023.

Wyss, M., Molnar, P., 1972. Efficiency, stress drop, apparent stress, effective stress, and frictional stress of Denver, Colorado, earthquakes. Journal of Geophysical Research (1896-1977) 77, 1433–1438. https://doi.org/10.1029/JB077i008p01433

Xia, K., Rosakis, A.J., Kanamori, H., 2004. Laboratory Earthquakes: The Sub-Rayleigh-to-Supershear Rupture Transition. Science 303, 1859–1862. https://doi.org/10.1126/science.1094022 ARTICLE

Yamashita, F., Fukuyama, E., Xu, S., Kawakata, H., Mizoguchi, K., Takizawa, S., 2021. Two end-member earthquake preparations illuminated by foreshock activity on a meter-scale laboratory fault. Nature Communications 12, 4302. https://doi.org/10.1038/s41467-021-24625-4

Yamashita, F., Fukuyama, E., Xu, S., Mizoguchi, K., Kawakata, H., Takizawa, S., 2018. Rupture preparation process controlled by surface roughness on meter-scale laboratory fault. Tectonophysics 733, 193–208. https://doi.org/10.1016/j.tecto.2018.01.034

Yoshioka, N., Scholz, C.H., 1989. Elastic properties of contacting surfaces under normal and shear loads: 1. Theory. Journal of Geophysical Research: Solid Earth 94, 17681–17690. https://doi.org/10.1029/JB094iB12p17681

Zayas, J.M., 1986. Experimental determination of the coefficient of drag of a tennis ball. American Journal of Physics 54, 622–625. https://doi.org/10.1119/1.14519

Zhang, Y., An, Y., Long, F., Zhu, G., Qin, M., Zhong, Y., Xu, Q., Yang, H., 2021. Short-Term Foreshock and Aftershock Patterns of the 2021 Ms 6.4 Yangbi Earthquake Sequence. Seismological Research Letters 93, 21–32. https://doi.org/10.1785/0220210154

Zhou, X., He, Y., Shou, Y., 2021. Experimental investigation of the effects of loading rate, contact roughness, and normal stress on the stick-slip behavior of faults. Tectonophysics 816, 229027. https://doi.org/10.1016/j.tecto.2021.229027

Zhou, X., Shou, Y., Yang, L., He, Y., 2020. Stick-slip failure in heterogeneous sheared fault with a variety of fault roughness. Physics of the Earth and Planetary Interiors 309. https://doi.org/10.1016/j.pepi.2020.106587

8 PUBLICATION ASSOCIATED WITH THE PHD

Brotherson, L. 2021. Simulating earthquakes with laboratory experiments. Nature Reviews Earth & Environment 2, 3, 164, doi: 10.1038/s43017-021-00151-1.

RESEARCH HIGHLIGHTS

Check for updates

Nature Reviews Earth & Environment | https://doi.org/10.1038/s43017-021-00151-1 | Published online 15 February 2021

TOOLS OF THE TRADE

Simulating earthquakes with laboratory experiments

Rapid urbanisation is increasing the risk of seismic hazards to human populations, therefore understanding the origin and mechanics of earthquakes is becoming ever more important. The most uncertain term in earthquake models used in the insurance industry is the earthquake source term, which represents the area of slip during earthquakes and controls their magnitude and frequency. Therefore, understanding earthquake source properties is crucial for understanding earthquake rupture and damage. Lab experiments are advantageous as we can generate analogues of earthquakes under carefully controlled conditions and measure their properties to a higher spatiotemporal resolution than in the field.

Laboratory frictional sliding experiments are useful analogues for natural earthquake behaviour and, in particular, for understanding earthquake nucleation and source properties. Previous studies have shown that acoustic emissions from laboratory earthquakes have extremely similar seismic signals to natural earthquakes. For example, acoustic emission waveforms visually resemble earthquake seismograms (with P and S arrivals) and acoustic emission magnitudes obey the Gutenberg-Richter relation for earthquakes. To generate a laboratory earthquake, samples of rock analogues such as Perspex are directly sheared using a triaxial deformation apparatus. Perspex is a useful analogue because it behaves similarly to rocks in terms of fracturing and friction, but more easily produces acoustic emissions due to its lower elastic moduli. The normal stress and sliding velocity applied to the samples can be carefully controlled in the laboratory to resemble upper crustal conditions, where earthquakes naturally occur. Spontaneous stick slip motion and associated acoustic emissions are measured using acoustic sensors. By using classic seismology techniques on the acoustic emissions, such as back-projection and waveform modelling, the source properties of laboratory-generated earthquakes, such as the corner frequency and stress drop, can be estimated.

Credit: image courtesy of Gary Coughlan

Combining results from laboratory simulations and earthquake seismology can reduce the uncertainty in earthquake source properties, which are widely used in seismic hazard modelling. Frictional sliding experiments can further aid understanding of how earthquake source properties vary under different geological settings, which can be simulated and carefully controlled in the laboratory, and thus lower the overall uncertainty in seismic hazard analysis. To further advance understanding of earthquake mechanics, future multidisciplinary research should focus on including fault complexities such as fault roughness and fracture networks into earthquake models.

Louisa Brotherson
Department of Earth, Ocean and Ecological Sciences, University of Liverpool, Liverpool, UK
e-mail: L.Brotherson@liverpool.ac.uk

Competing interests
The author declares no competing interests.